

QUANTIFICATION OF TRANSMISSION LOSS PROCESSES ALONG THE LETABA RIVER

Report to the
Water Research Commission

by

ES Riddell, JM Nel, S Gokool, C Jarman, R Raubenheimer, T Strydom, A Swemmer
South African Environmental Observation Network, Groundwater Consulting Services,
Centre for Water Resources Research, University of KwaZulu-Natal, South African National Parks

WRC Report No. 2338/1/17

ISBN 978-1-4312-0931-6

November 2017

Obtainable from

Water Research Commission

Private Bag X03

Gezina, 0031

orders@wrc.org.za or download from www.wrc.org.za

This report emanates from a project entitled: Quantification of transmission losses along the Letaba River for improved delivery of environmental water requirements (ecological reserve) (Project No. K5/2338)

DISCLAIMER

This report has been reviewed by the Water Research Commission (WRC) and approved for publication. Approval does not signify that the contents necessarily reflect the views and policies of the WRC, nor does mention of trade names or commercial products constitute endorsement or recommendation for use.

Printed in the Republic of South Africa

©Water Research Commission

EXECUTIVE SUMMARY

Background

The Letaba River system in north-eastern South Africa is an example of a fully allocated catchment with a semi-arid climate, which requires efficient management of all water resources demands. Most available water resources in this system have already been exploited, but progress is being made to implement *ecological reserve* or environmental water requirements (EWRs) in the catchment as required under the National Water Act (Act 36 of 1998). This has important bearing for providing ecosystem goods and services in the Lower Groot Letaba River and the Kruger National Park (KNP). This progress stems from the implementation of an adaptive operational water resources management system using a hydrological model to inform catchment managers how and when to make releases from upstream dams. However, one of the challenges with this system has been to account for suspected losses of water between upstream storage and downstream EWR target gauges. These losses may be described as *transmission losses*.

The timing of the project also coincided with a severe El Niño-induced drought. This allowed for novel insights into interactions between river flow, and geohydrological and atmospheric drivers during periods of extremely low flow.

Study objectives

The aim of this study was to provide a detailed hydrological processes definition of a 10 km river reach along the Lower Groot Letaba to improve the hydrological understanding of the system and inform operational water resources management of the system. The river reach studied traverses of agricultural land being developed by emerging farmers before entering small protected areas upstream of the KNP. The project attempted to close the gap in knowledge on the Letaba River's hydrology with the following objectives:

1. Quantify transmission losses along a reach of the Groot Letaba River.
2. Incorporate transmission losses into real-time modelling systems, thus improving the delivery of EWRs.
3. Develop a cost-effective method to upscale the transmission loss parameters using hydrometrics coupled with remote sensing and an integrated surface water/groundwater interaction model.
4. Develop regional parameters for transmission losses to enable application to other river systems in the South African Lowveld.
5. Contribute to the development of a long-term research site for studying riparian zone hydrology, hydrogeology and river ecology.

Methodology

The study was conducted on a 10 km stretch of the Lower Groot Letaba River, with the Letaba Ranch Weir forming the downstream boundary of the study reach. Data collection commenced in April 2014 with collection of baseline data on river hydrology, geophysical characterisation of the study site and hydrocensus of water use. The groundwater/surface water interaction component of the study required continuous monitoring of the groundwater phreatic surface and hydraulic characterisation of aquifer properties. To achieve this, 29 boreholes were installed along four transects that ran perpendicular to the river channel. A comprehensive hydrological processes determination was then conducted between April 2015 and November 2016, which quantified groundwater/surface water interaction through hydraulic characterisation of the multi-piezometer borehole network. Water level data was used to generate hydraulic gradients between both the unconsolidated (shallow) and hard rock (deep) aquifer(s) and the northern and southern banks of the river over time. This data was also used to define a robust conceptual model of geohydrological processes between the aquifer and the river.

Evapotranspiration (total transpiration + evaporation = ET) was determined for the riparian zone in 2015 and 2016, during periods when the active channel was accessible (winter and spring). This coincided with the low flow management period in this river system. Daily ET values with satisfactory spatial resolution were derived from a novel downscaling procedure using linear regression to blend coarse spatial resolution MODIS imagery (at a daily time step) with high-spatial but low-temporal resolution Landsat imagery. The downscaled, modelled actual ET was cross-referenced with *in situ* measurements of daily ET using an eddy covariance system. Furthermore, a new methodology was devised to address one of the major limitations associated with implementing the Surface Energy Balance System (SEBS) model in an environment where ET is constrained by low water availability. The ET analysis was augmented by stable isotope analysis of ^{18}O and ^2H to differentiate water sources used by the dominant riparian vegetation of the study reach.

Measured hydrological data was then integrated into a numeric groundwater flow model to calculate the dominant elements of the water balance at the scale of the study area, and estimate transmission losses.

Results

Initial modelling of ET using SEBS produced poor results – especially for a site with sparse riparian vegetation (outside the protected area where reed beds were heavily grazed). This was overcome by introducing an evaporative scaling factor for SEBS (SEBS_{ESF}), which corrected for the underestimation of the sensible heat flux in the surface energy balance. Average winter (May–July) and typical maximum spring (August–October) ET within the riparian zone was estimated to be approximately 3 mm/day and 7 mm/day respectively. Daily ET measured within the protected areas was found to be higher than an upstream site surrounded by farmland, which apparently was due to high levels of cattle grazing in the riparian zone. The ET was significantly greater in 2016 than in 2015, although intra-annual variability was similar for both years. While rainfall for both 2015 and 2016 was similar and well below average, the greater ET in 2016 was due to an isolated rainfall event in March 2016, which apparently enhanced ET well into the dry season.

Stable isotope analysis of xylem water of riparian trees and shrubs revealed that these plants predominantly took up soil water rather than groundwater or river water. However, both trees and shrubs become more dependent on surface water (sampled in channel) and groundwater (from riparian zone boreholes) as the dry season progressed, with the combined contribution of these sources totalling approximately 16% of plant water use. Stable isotope analysis of xylem water of reeds (*Phragmites mauritianus*) showed that surface water contributed approximately 75% of their daily water use (assuming that soil water in the upper 30 cm is actually surface water). Considering the density of reeds distributed along the river reach studied, it was concluded that reeds are the primary pathway for transmission losses via ET.

The groundwater/surface water interaction analyses revealed a throughflow system of the regional aquifer to the river from the south to the north, for the upstream (western) section of the study site, which was located within the agricultural areas. The reverse of this pattern was evident further downstream. In the most eastern part of the study site within the protected areas, there were potential gains from the regional aquifer to the river. However, this pattern was complicated by the river's interactions with the shallow/unconsolidated aquifer, which appears to have a predominantly negative gradient away from the river during low flows. Bank-full recharge events also occurred during a major peak flow in March 2016. The Lower Letaba River is therefore both a geohydrologically losing and gaining river depending on the spatial scale of analysis.

The numerical model for the study was run using MODFLOW-USG under steady-state conditions. Two distinct recharge and evaporative zones were incorporated, which were informed by the conceptual model. Simulations applied a constant head-well as the upstream boundary condition as simulation of the river inflow (at the Mahale Weir), with downstream drain as the river outflow (Letaba Ranch gauging

weir) under realistic low flow scenarios (0.5 m³/s, 1 m³/s, and 1.5 m³/s inflow) and a typical median peak flow scenario (23 m³/s inflow). Modelled transmission losses for these scenarios were as follows:

Inflow (m ³ /s)	Loss over reach (m ³ /day)	Loss over reach (m ³ /s)	Transmission loss (% of inflow)	Extrapolated transmission loss* (m ³ /s)
0.5	1 400	0.016	3.24	0.10
1.0	2 750	0.032	3.18	0.20
1.5	4 500	0.052	3.47	0.33
23.0	50 000	0.579	2.52	3.64

*Letaba Ranch (B8H008) to next upstream gauge Prieska, B8H017 (a distance of 44 km), assuming similar hydrogeological and ecohydrological conditions to the study site.

Model results indicated a generally linear relationship between inflow and transmission losses. This can be explained by the head-driven process between the river and the surrounding aquifer, which is based on the observed hydraulic characteristics (the shallower unconsolidated aquifer around the river channel generally had a greater hydraulic conductivity than the deeper hard rock). Assuming similar hydrogeological and ecohydrological characteristics of the riparian zone upstream as far as the next upstream gauge, an approximate 20% transmission loss occurs over a 44 km reach of the river. Unfortunately, since the commencement of this study, the gauging in the Letaba River has deteriorated and the next upstream weir (Prieska Weir) is no longer operational. It is therefore not currently possible to verify this estimate.

While higher flow rates were found to induce higher transmission losses (due to bank storage processes), the influence of total evaporation in the study area should not be discounted. Based on representative flow rates, there was a deficit in the water balance for both winter and summer scenarios of the numerical model. Evaporative losses were estimated to reduce the flow in the river by 3.07% and 5.22%, for summer and winter respectively. The losses are in the same order of magnitude as the losses calculated from the measured and modelled ET. Simulated losses for winter and extreme summer conditions were approximately 1.37 mm·d⁻¹ and 2.34 mm·d⁻¹, while downscaled ET values were 1.31 mm·d⁻¹ and 2.38 mm·d⁻¹, respectively.

Management impacts

The study has given new insight into the hydrological processes that give rise to transmission losses in the semi-arid Letaba River system. While most studies in the region suggest that transmission losses are a significant component of the water budget, recent studies of other perennial rivers of the South African Lowveld indicate that these rivers typically gain from the regional groundwater system at lower altitudes, albeit with losses to ET. In some cases, this has led to a reduction in actual losses modelled for operational purposes. This study has revealed that the Letaba River system may not conform to this model (at least at the scale studied) and is therefore anomalous in terms of regional management.

These findings are of critical importance for effective management of the system in the future – especially considering the recent gazettement of the Letaba Management Class and the mandatory EWRs that must now be implemented. The table that follows depicts the low flow assurance rules for median (60th percentile) and extreme low flows (90th percentile), as gazetted¹ for implementation prior to and proceeding the construction of the Nwamitwa Dam (to be constructed upstream of the study site). This table reveals that if median target flows are achieved at Prieska without the dam, then target flows would be achieved at Letaba Ranch even with 20% transmission loss. However, during a drought, such as the one experienced in 2015 and 2016, a >20% shortfall would occur at Letaba Ranch (based on the gazetted rule for Prieska) for the 90th percentile flow assurance.

¹ Government Gazette No. 40531, 30 December 2016.

C Class Low Flow Assurance		EWR4 Letaba Ranch B8H008		EWR3 Prieska B8H017		Difference	
		90%	60%	90%	60%	90%	60%
Prior to Nwamitwa Dam	Oct	0.497	0.597	0.254	0.806	-0.243	0.209
	Nov	0.082	0.583	0.259	0.738	0.177	0.155
	Dec	0.085	0.595	0.463	0.819	0.378	0.224
	Jan	0.277	0.828	0.532	1.087	0.255	0.259
	Feb	0.448	2.118	0.619	2.484	0.171	0.366
	Mar	0.571	1.094	0.744	1.400	0.173	0.306
	Apr	0.595	1.083	0.720	1.261	0.125	0.178
	May	0.597	0.597	0.343	0.800	-0.254	0.203
	Jun	0.586	0.598	0.168	0.742	-0.418	0.144
	Jul	0.530	0.597	0.139	0.632	-0.391	0.035
	Aug	0.597	0.597	0.067	0.529	-0.530	-0.068
	Sep	0.594	0.598	0.221	0.698	-0.373	0.100
	Post-Nwamitwa Dam		90%	60%	90%	60%	90%
Oct		0.523	0.554	1.092	1.222	0.569	0.668
Nov		0.498	0.629	0.994	1.253	0.496	0.624
Dec		0.497	0.773	1.035	1.302	0.538	0.529
Jan		0.616	3.589	1.248	3.983	0.632	0.394
Feb		0.733	5.264	1.421	5.323	0.688	0.059
Mar		0.788	3.781	1.461	4.474	0.673	0.693
Apr		0.679	1.517	1.318	2.500	0.639	0.983
May		0.688	1.354	1.338	2.195	0.650	0.841
Jun		0.669	1.129	1.339	1.856	0.670	0.727
Jul		0.650	0.945	1.274	1.626	0.624	0.681
Aug		0.605	0.778	1.226	1.431	0.621	0.653
Sep		0.552	0.632	1.160	1.306	0.608	0.674

Project conclusions, objectives and recommendations

The study has detailed key hydrological processes that result in transmission losses in the Groot Letaba River, and has met the primary objective of the study. Long-term monitoring at study site will advantageous to reduce the assumptions and related uncertainties that had to be factored into the analysis. Continued academic investment, as envisaged in the development of a South African Environmental Observation Network Hydrological Observatory at the site, should reduce these uncertainties and further improve the management of the Letaba system and delivery of EWRs in Lower Letaba. To this end, it would be advantageous to integrate the MODFLOW routines developed in this study into any future operational model modifications or redevelopment.

One of the shortcomings of the project was that data was not integrated into the operational model for the Letaba system (Objective 2). However, subsequent to the final gazetting of the management class in the system that occurred after this project began, the catchment requires a whole new model. Furthermore, gauging stations upstream of Letaba Ranch (such as Prieska Weir and others) need to be operationalised to provide input data for such a model.

Finally, some additional impacts of the study are expected in the short-term based on the data of post-graduate students who are completing their work on the project.

Capacity building

One PhD student (University of KwaZulu-Natal), one Master's student (University of the Free State), and one Honours student (University of KwaZulu-Natal) were capacitated in this project. Several other students have gained research experience from the project through site visits and short internships, which involved assisting with data collection and analysis at various stages. Furthermore, many environmental monitors of the South African National Parks Biodiversity Social Projects Division gained experiential learning while assisting with data collection on the project.

ACKNOWLEDGEMENTS

The research in this non-solicited project was initiated, managed and funded by the Water Research Commission (WRC), for whose assistance we are sincerely grateful. The project would also not have been possible had it not been for additional funding and services: The Department of Water and Sanitation Limpopo drilling division for the borehole drilling campaigns during 2015; additional time and resources of Groundwater Consulting Services (GCS) personnel; and student funding provided by the South African Environmental Observation Network (SAEON). The SAEON also provided some of capital equipment (level loggers and weather stations), the use of a drone for capturing aerial imagery, the use of a field technician, as well as accommodation, office space and transport for students. We also gratefully acknowledge the Department of Geography and Environmental Studies, University of Stellenbosch, for providing SUDEM data for the study area. The Council for Scientific and Industrial Research is kindly acknowledged for loaning of field equipment during the eddy covariance campaign, as is Engineering and Exploration Geophysical Services during the geophysics campaign.

Special thanks go to: the staff of SAEON, Mr Rion Lerm; GCS, Mr Raymond Minnaar; South African National Parks (SANParks), Mr Annoit Mashale; and IWR Water Resources, Mr Stephen Mallory and Dr Tendai Sawunyama, for their assistance and inputs during the project. Special thanks also to Ms Anna-Lisa Vicente and Mr Angelo Johnson of the University of Western Cape who assisted with the geohydrological modelling during their internship projects.

Members of the Reference Group (below) are thanked for their time and invaluable expertise:

- Dr Brilliant Petja (Chairperson) WRC
- Dr Chris Moseki (Chairperson former) WRC
- Ms Celiwe Ntuli Department of Water and Sanitation
- Mr Isaac Nyatlo Department of Water and Sanitation
- Dr Alistair Clulow University of KwaZulu-Natal
- Ms Kershani Chetty University of KwaZulu-Natal
- Dr Bill Pitman Independent Researcher
- Miss Samantha Tjaden WRC

The following people provided valuable assistance in the field:

Environmental Monitors:

Andile Ndzamba, Masana Htimani, Salvation Shikwambani, Peska Nkuna, Dipuo Ramalepe, Mosa Mokgalaka, Ponisiwani Mathebula, Hlanganani Mabunda, Evidence Shikwambani, Queen Malatji, Solani Maswanganyi, Rahab Mohale, Peace Nkuna, Elma Mashale, Raina Ramoshaba, Lassie Mokgalaka, Elijah Masango, Sharon Ngobeni, Ntsako Makhubele, Jako Lombard and Gladness Khosa.

Students:

Kgetho Mashile, Kinsley Manyama, Angel Mavasa, Delina Chipape, Rinaldar Mochemi and Oliver Stirzaker.

TABLE OF CONTENTS

EXECUTIVE SUMMARY	iii
ACKNOWLEDGEMENTS	viii
TABLE OF CONTENTS	ix
LIST OF FIGURES	xi
LIST OF TABLES	xv
ABBREVIATIONS	xvi
1 INTRODUCTION	1
2 LITERATURE REVIEW	3
2.1 Environmental Water Requirements.....	3
2.2 Transmission Losses	3
2.3 Incorporating the Total Evaporation Process into Streamflow Transmission Loss Estimation Procedures.....	4
3 OBJECTIVES	6
4 STUDY SITE: THE LETABA RIVER SYSTEM	7
4.1 Climate.....	7
4.2 Hydrology and Geomorphology	7
4.3 Land Use Activities	8
4.4 Letaba Water Supply System – Status Quo	8
4.5 History and Present Operating Rules	10
4.6 Transmission Loss Study Site	12
4.7 Study Site Set-up: River Hydrology and Hydrochemistry	13
4.8 Study Site Set-up: Riparian Eco-Hydrology Through Stable Isotopes	16
4.9 Study Site Set-up: Hydrocensus.....	17
4.10 Study Site Set-up: Precipitation	19
4.11 Study Site Set-up: Geophysical Surveys	20
4.12 Study Site Set-up: Groundwater Piezometric Monitoring Network.....	27
4.13 Study Site Set-up: Vegetation Characterisation & Total Evaporation	30
4.14 Micrometeorological and energy flux measurements	30
4.14.1 The simplified SEBS.....	34
4.14.2 SEBS modifications	34
4.14.3 Spatial downscaling of satellite-derived total evaporation.....	35
4.14.4 Determining the distribution of vegetation biomass and identifying land uses.....	39
4.14.5 Riparian vegetation water use	41
5 RESULTS	43
5.1 Hydrogeological Characterisation.....	43
5.1.1 Transect 1.....	43
5.1.2 Transect 2.....	46
5.1.3 Transect 3.....	52
5.1.4 Transect 4.....	54
5.1.5 Dolerite dyke transect.....	58
5.1.6 Summary	59
5.2 Groundwater Hydraulic Gradient Distribution	59
5.3 Initial Transmission Loss Estimation	65
5.4 Updated Conceptual Model: Groundwater/Surface Water Interaction	68

5.4.1	Assessing peak flow transmission losses	68
5.4.2	Groundwater flow direction from hydraulic heads	72
5.4.3	Conceptual model.....	76
5.5	Stable Isotopes in the Riparian Zone	80
5.5.1	Isotopic composition of rainfall	80
5.5.2	Isotopic composition of riparian zone water	80
5.5.3	Proportional contribution of potential water sources to plant water use during transpiration 82	
5.6	Total Evaporation.....	85
5.6.1	Inter-annual comparison of EC_{ET} for 2015 and 2016	85
5.6.2	A comparison of satellite-derived evaporative fraction (EF) and ET against EF and ET measured in situ for the period 17 June to 22 October 2015	86
5.6.3	A comparison of downscaled and infilled ET against ET measured in situ from 17 June to 22 October 2015	88
5.6.4	A comparison of satellite-derived ET against EC_{ET} from 19 May to 11 November 2016 .	92
5.6.5	Discussion	94
5.6.6	Estimation of losses due to ET	100
6	NUMERICAL FLOW MODEL.....	102
6.1	Objective of the Model	102
6.2	Governing Equations	102
6.3	Boundary Conditions	103
6.4	Construction of the Finite Difference Grid	105
6.5	Vertical Discretization	105
6.6	Input Parameters	106
6.7	Aquifer Hydraulic Conductivity.....	106
6.8	Recharge	106
6.9	Evapotranspiration.....	107
6.10	Time Discretization	108
6.11	Flow Rates.....	108
6.12	Model Results	108
6.12.1	Evaluation of river flows.....	108
6.12.2	Transmission losses	113
6.12.3	Water Balances	115
7	CONCLUSIONS	116
8	REFERENCES	119
	Appendix I: Letaba River Transmissions Losses Maps.....	123
	Appendix II: Magnetic Surveys.....	127

LIST OF FIGURES

Figure 1: The Letaba Catchment with major dams and EWR sites according to the WRCS (DWA, 2013)	7
Figure 2: Hydrology of the Letaba Catchment at B8H008 (Letaba Ranch) using flow duration curves	8
Figure 3: Status of present water allocation in the Letaba Catchment, 2014 (total allocated includes commercial agriculture, industrial and domestic requirements).....	9
Figure 4: Compliance with the ecological reserve at Letaba EWR4 (Pollard et al., 2012).....	10
Figure 5: Operating rule for EWR4 (columns), mean daily flow (lines) for EWR4, comparing existing SPATSIM model with recently gazetted EWRs.....	11
Figure 6: Delineation of the study site between B8H007 (Mahale) and B8H008 and the location of geophysics transects over two different land uses.....	12
Figure 7: Typical river channel morphology at study site: braided alluvial channel	13
Figure 8: Typical river channel morphology at study site: bedrock controls	13
Figure 9: Mahale Weir (left) and Letaba Ranch Weir (right).....	14
Figure 10: Letaba River between Mahale and Letaba Ranch	14
Figure 11: Longitudinal hydrochemical surveys of the Letaba River between Mahale and Letaba Ranch.....	15
Figure 12: Location of the six sampling regions across a portion of the Groot Letaba River incorporating the three geomorphological zones categorized in this study	16
Figure 13: Mbaula Village and Mthimkhulu Reserve in relation to the study site	17
Figure 14: Agricultural water use hydrocensus at study site	18
Figure 15: Rainfall measured for the 2015–2016 hydrological year within the study site (Mahale, Mthimkulu) and at nearby village north of the site (Phalaubeni)	19
Figure 16: Locations of geophysics transects across the farms.....	20
Figure 17: LF001 geophysical pseudosection	21
Figure 18: LF002 geophysical pseudosection	21
Figure 19: LF003 geophysical pseudosection	22
Figure 20: LF004 geophysical pseudosection	22
Figure 21: LF005 geophysical pseudosection	23
Figure 22: LF006 Geophysical pseudosection	23
Figure 23: Locality of the geophysics surveys in the protected areas along the Groot Letaba.....	24
Figure 24: LM001 geophysical pseudosection	24
Figure 25: LM002 geophysical pseudosection	25
Figure 26: LM003 geophysical pseudosection	25
Figure 27: LM004 geophysical pseudosection	26
Figure 28: LM005 geophysical pseudosection	26
Figure 29: LM006 geophysical pseudosection	27
Figure 30: Groundwater piezometric monitoring network at the Letaba River transmission losses study site as of February 2016 (with transect numbers)	28
Figure 31: Location of the eddy covariance system and the general land cover distribution for Transect 1 and Transect 2	32
Figure 32: Installation of the eddy covariance system in channel with location of sensors	33
Figure 33: A UAV survey conducted of the Letaba River study site around the eddy covariance installation area during November 2015.....	34
Figure 34: Schematic of the downscaling with linear regression approach methodology to create a daily continuous MSR total evaporation data set.....	37
Figure 35: An illustration of SEBS total evaporation derived using MODIS and Landsat data for 7 July 2015.....	38

Figure 36: Distribution of vegetation biomass and classification of land uses based upon NDVI for the region between Mahale and Letaba Ranch Weirs on 21 June 2015	40
Figure 37: Fluid log of LF002A	43
Figure 38: Fluid log of LF002B	44
Figure 39: Fluid log of LF0021	44
Figure 40: Fluid log of LF004A	45
Figure 41: Fluid log of LF004B	46
Figure 42: Fluid log of LF0031A	46
Figure 43: Fluid log of LF0031B	47
Figure 44: Fluid log of LF003A	48
Figure 45: Fluid log of LF003B	48
Figure 46: Fluid log of LF005A	49
Figure 47: Fluid log of LF005B	50
Figure 48: Fluid log of LF005C	50
Figure 49: Fluid log of LF0051A	51
Figure 50: Fluid log of LF0051B	52
Figure 51: Fluid log of LR002A	53
Figure 52: Fluid log of LR004A	53
Figure 53: Fluid log of LR004B	54
Figure 54: Fluid log of LR0011A	55
Figure 55: Fluid log of LR001A	55
Figure 56: Fluid log of LR005A	56
Figure 57: Fluid log of LR005B	57
Figure 58: Fluid log of LR003	57
Figure 59: Fluid log of LRW001	58
Figure 60: Fluid log LRW002	59
Figure 61: Cross-section plot of transect LF004 to LF002, February 2016	60
Figure 62: Cross-section plot of transect LF0051 to LF0031, February 2016	61
Figure 63: Cross-section plot of transect LR004 to LR002, February 2016	62
Figure 64: Cross-section plot of transect LR005 to LR001, February 2016	63
Figure 65: Cross-section plot of transect LR005 to LR0011, February 2016	64
Figure 66: Assumed river reaches between Mahale and Letaba Ranch Weirs associated with geohydrological transects	66
Figure 67: Time series of potential gains/losses along the study site (related to deep hard rock aquifer)	67
Figure 68: Time series of potential gains/losses along the study site (related to shallow unconsolidated aquifer)	68
Figure 69: Key responses to March 2016 rain and peak flow along Transect 1 (stream stages plotted against datum at upstream and downstream sites for reference)	69
Figure 70: Key responses to March 2016 rain and peak flow along Transect 2 (stream stages plotted against datum at upstream and downstream sites for reference)	70
Figure 71: Key responses to March 2016 rain and peak flow along Transect 3 (stream stages plotted against datum at upstream and downstream sites for reference)	71
Figure 72: Key responses to March 2016 rain and peak flow along Transect 4 (stream stages plotted against datum at upstream and downstream sites for reference)	71
Figure 73: Borehole and river heads before the flood event (30 November 2015)	73
Figure 74: Borehole and river heads before the flood event (15 February 2016)	73

Figure 75: Borehole and river heads after the flood event (28 March 2016)	74
Figure 76: Borehole and river heads after the flood event (8 August 2016)	74
Figure 77: Groundwater-streamflow processes across dolerite dyke.....	75
Figure 78: Conceptual model of cross-section LF004–LF002 (Transect 1 – see Figure 30).....	76
Figure 79: Conceptual model of cross-section LF005–LF003 (Transect 2 – see Figure 30).....	77
Figure 80: Conceptual model of cross-section LR005–LR003 (Transect 4 – see Figure 30).....	77
Figure 81: Conceptual model of cross-section LR004–LR002 (Transect 3 – see Figure 30).....	78
Figure 82: Conceptual model of geohydrological process connectivity along the Groot Letaba River study site ..	79
Figure 83: Stable isotopes of rainfall during the study period against GMWL (left) and time series (right)	80
Figure 84: A plot of the relationship between $\delta^2\text{H}$ and $\delta^{18}\text{O}$ values for all the study samples	81
Figure 85: A plot of the relationship between $\delta^2\text{H}$ and $\delta^{18}\text{O}$ simple end member values for all study samples.....	83
Figure 86: A comparison of ET_0 and EC_{ET} for 2015 and 2016	86
Figure 87: A comparison of the SEBS_0 and SEBS_{ESF} derived ET against EC_{ET} from 17 June to 22 October 2015	87
Figure 88: A comparison of the K_{Cact} ET estimates derived from the implementation of the SEBS_0 and SEBS_{ESF} against EC_{ET} from 17 June to 22 October 2015	89
Figure 89: A comparison of the downscaled ET estimates derived from the implementation of SEBS_0 and SEBS_{ESF} against EC_{ET} from 17 June to 22 October 2015	91
Figure 90: A comparison of the SEBS_0 and SEBS_{ESF} derived ET against EC_{ET} from 19 May to 11 November 2016	92
Figure 91: A comparison of solar radiation for 2015 and 2016 from 17 June to 17 October	96
Figure 92: A comparison of nett radiation for 2015 and 2016 from 17 June to 17 October	97
Figure 93: A comparison of VPD for 2015 and 2016 from 17 June to 17 October	97
Figure 94: A comparison of temperature for 2015 and 2016 from 17 June to 17 October	98
Figure 95: A comparison of the SEBS_{ESF} derived ET against EC_{ET} within acceptable accuracy ranges from 19 May to 11 November 2016.....	100
Figure 96: Model area, unstructured grid and steady-state water levels of the Letaba groundwater model (head = above mean sea level)	104
Figure 97: A picture representing the aerial view of the finite difference grid	105
Figure 98: NW–SE and NE–SW cross-section through grid at the Letaba Catchment site showing grid and layer definition used in numerical model.....	105
Figure 99: A south–north cross-section displaying the two layers of different hydraulic conductivities	106
Figure 100: A model representation of two recharge zones (farms and reserves)	107
Figure 101: A model representation of the two ET zones (farms and reserves)	107
Figure 102: A model representation of the hydraulic head distribution under medium flow conditions (1 ℓ/s).....	108
Figure 103: Model 1: Response of Letaba River against distance with a flow rate of 43 200 m^3/day (0.5 m^3/s) .	110
Figure 104: Model 2: Response of Letaba River against distance with a flow rate of 86 400 m^3/day (1 m^3/s)....	110
Figure 105: Model 3: Response of Letaba River against distance with a flow rate of 129 600 m^3/day (1.5 m^3/s)	111
Figure 106: Model 4: Response of Letaba River against distance with a flow rate of 2 000 000 m^3/day (23 m^3/s)	111
Figure 107: Model 5: Response of Letaba River under realistic summer conditions at 0.5 m^3/s	112
Figure 108: Model 6: Response of Letaba River in winter conditions at 0.5 m^3/s	112
Figure 109: Model 7: Response of Letaba River in extreme summer conditions at 0.5 m^3/s	113
Figure 110: Graph indicating transmission losses of the Letaba River against topography	113
Figure 111: Graph indicating transmission losses of the Letaba River against distance	114

Figure 112: Geology of the site illustrating the dominant geology and dykes.....	123
Figure 113: The dominant soil types and perennial/non-perennial streams	124
Figure 114: Topocadastral map of the study site delineating farms, ranches and rural communities	125
Figure 115: Topographical map of the study site	126
Figure 116: Combined geophysical interpretation LF001	128
Figure 117: Combined geophysical interpretation LF002.....	129
Figure 118: Combined geophysical interpretation LF003.....	130
Figure 119: Combined geophysical interpretation LF004.....	131
Figure 120: Combined geophysical interpretation LF005.....	132
Figure 121: Combined geophysical interpretation LF006.1	133
Figure 122: Combined geophysical interpretation LF006.2.....	134
Figure 123: Combined geophysical interpretation LR001	135
Figure 124: Combined geophysical interpretation LR002	136
Figure 125: Combined geophysical interpretation LR003	137
Figure 126: Combined geophysical interpretation LR004	138
Figure 127: Combined geophysical interpretation LR005	139
Figure 128: Combined geophysical interpretation LR006	140

LIST OF TABLES

Table 1: Management class and water availability in the Letaba Catchment	11
Table 2: Mahale Weir low flow rating	14
Table 3: Co-ordinates for the six sampling regions distributed across a portion of the Groot Letaba River along which 13 individual tree species were sampled.....	16
Table 4: Details of boreholes located on Mthimkhulu Reserve	18
Table 5: Hydrocensus information from July 2015 survey.....	19
Table 6: Transmission losses study site borehole drilling information.....	29
Table 7: Percentage cover of the dominant landcover classes within each of the sites in which the measuring tower was situated	31
Table 8: Identification of features within a satellite image based upon their respective NDVI values.....	39
Table 9: Hydraulic characteristics of boreholes at study site.....	65
Table 10: Transmission loss parameters determined for the Letaba River study site comparing wet season (15 February 2016) with dry season (16 September 2016).....	67
Table 11: Average contribution of sources to plant water uptake investigation period (May to October 2017)	83
Table 12: Contribution of sources to plant water uptake under different environmental conditions (during each field campaign), estimated at the 50 th percentile	83
Table 13: Average contribution of sources to plant water uptake at each sampling location during the period of investigation (May to Oct 2017).....	84
Table 14: Average contribution of sources to individual plant species during the period of investigation (May to October 2017)	84
Table 15: Statistical comparison of ET_0 and EC_{ET} for 2015 and 2016.....	85
Table 16: Statistical comparison of $SEBS_0$ and $SEBS_{ESF}$ EF estimates derived using Landsat and MODIS against EC_{EF} from 17 June to 22 October 2015.....	86
Table 17: Statistical comparison of $SEBS_0$ and $SEBS_{ESF}$ ET estimates derived using Landsat and MODIS against EC_{EF} from 17 June to 22 October 2015.....	88
Table 18: Statistical comparison of the K_{Cact} ET estimates against EC_{ET} from 17 June to 22 October 2015	89
Table 19: Statistical comparison of the K_{Cact} ET estimates against EC_{ET} from 17 June to 22 October 2015	91
Table 20: Statistical comparison of $SEBS_0$ and $SEBS_{ESF}$ ET estimates derived using Landsat and MODIS against EC_{EF} for the period 19 May to 11 November 2016.....	92
Table 21: Statistical comparison of K_{Cact} ET estimates against EC_{ET} from 19 May to 11 November 2016.....	93
Table 22: Statistical comparison of the K_{Cact} ET estimates against EC_{ET} from 17 June to 22 October 2015	94
Table 23: ANOVA test at 95% confidence interval, comparing changes in 2015 and 2016 climatic drivers of ET	96
Table 24: Estimated losses due to ET ($3 \text{ mm}\cdot\text{d}^{-1}$) and open water evaporation in winter	101
Table 25: Estimated losses due to ET ($5 \text{ mm}\cdot\text{d}^{-1}$) and open water evaporation in summer.....	101
Table 26: Estimated losses due to ET ($7 \text{ mm}\cdot\text{d}^{-1}$) and open water evaporation in summer.....	101
Table 27: Identification of the real-world local boundaries and the adopted model boundary conditions	103
Table 28: Values of horizontal and vertical hydraulic conductivities.....	106
Table 29: Four values of the flow rates per category	108
Table 30: Input parameters for the constructed seven models	109
Table 31: Water balances for the seven models	115

ABBREVIATIONS

ANOVA	Analysis of Variance
BBM	Building Block Method
CLN	Connected Linear Network
CSR	Coarse Spatial Resolution
CVFD	Control Volume Finite Difference
DWA	Department of Water Affairs
DWS	Department of Water and Sanitation
EC	Electrical Conductivity
EC _{EF}	Eddy Covariance Evaporative Fraction
EC _{ET}	Eddy Covariance Evapotranspiration
EF	Evaporative Fraction
ERT	Electrical Resistivity Tomography
ESF	Environmental Stress Factor
ET	Evapotranspiration
EWR	Environmental Water Requirement
FAO	Food and Agriculture Organization
FDC	Flow Duration Curve
GLeWaP	Groot Letaba Water Development Project
GMWL	Global Meteoric Water Line
GWF	Groundwater Flow
HTR	High Temporal Resolution
IFR	In-stream Flow Requirement
K	Hydraulic Conductivity
K _{Cact}	
KNP	Kruger National Park
LMWL	Local Meteoric Water Line
LWUA	Letaba Water User Association
MAD	
MAP	Mean Annual Precipitation
MAR	Mean Annual Run-off
MOSA	Middle Olifants South Africa
MSR	Moderate Spatial Resolution
NDVI	Normalized Difference Vegetation Index
NE/SW	North-east/South-west
NIR	Near Infrared
NW	North-west
NWA	South Africa's National Water Act
OWRM	Operational Water Resources Management
RMSE	Root Mean Square Error
RVE	Relative Volume Error
SAEON	South African Environmental Observation Network
SANParks	South African National Parks
SE	South-east
SEL	
SEBS	Surface Energy Balance System
SEBS _{ESF}	Evaporative Scaling Factor for SEBS
SPATSIM	Spatial and Time Series Information Modelling
T	Transmissivity
UAV	Unmanned Aerial Vehicle
VPD	Vapour Pressure Deficit
VSMOW	Vienna Standard Mean Oceanic Water
WRC	Water Research Commission
WRCS	Water Resources Classification System

1 INTRODUCTION

This deliverable report stems from the non-solicited Water Research Commission (WRC) research project K5/2338 titled:

Quantification of transmission processes along the Letaba River for improved delivery of environmental water requirements (EWR) (Ecological Reserve)

This report provides a detailed hydrological processes definition of groundwater/surface water interaction and energy balance processes contributing to total evaporation along the riparian zone of a 10 km reach of the lower Groot Letaba River in north-eastern South Africa.

The rationale for this study being that the perennial rivers flowing through the arid and semi-arid parts of South Africa are all said to be closing, with water abstractions exceeding, or close to exceeding, supply (e.g. Molle et al., 2010). Environmental water requirements (EWRs) or 'ecological reserve' flows were shown to be deteriorating in many catchments of the South African Lowveld during the latter decades of the 20th century due to significant land use changes and loose governance of water resources (Pollard & Du Toit, 2011a). This despite EWRs being the only 'right' to water in addition to the Basic Human Needs reserve under South Africa's National Water Act (NWA) (South Africa, Act 36 of 1998).

Intensive management of their flows through the efficient management of water abstraction and dam outflows is critical to ensure that all water users continue to receive adequate allocations at a good assurance of supply, while still meeting the specified ecological reserve. Efficient management in turn requires a complete quantification of the hydrological processes that significantly affect river flows. Rainfall inputs, dam releases and water abstractions are relatively easy to quantify, and are currently being used to manage flows in river operations. Meanwhile, channel losses resulting from outflows from river systems remain a key gap and have limited the effectiveness of flow management to date.

The Letaba River system in north-eastern South Africa provides a good case study of this situation, with water use abstractions often exceeding available supply (DWA, 2006; Pollard & Du Toit 2011b). This in combination with infrastructural developments and land conversion in the catchment, such as dams, have meant that flows in the Letaba no longer resemble natural flows (Katambara & Ndiritu, 2010). This situation has improved somewhat following the formalisation of consensus-based operational river management (Pollard & Du Toit, 2011a; Riddell et al., 2014). In the Letaba Catchment, this resulted from the development of river-operating rules linked to releases from the Tzaneen Dam, where flow releases are monitored by the downstream Kruger National Park (KNP) through a Strategic Adaptive Management feedback mechanism with dam operators (McLoughlin et al., 2011).

The Letaba system operating rules were developed by the Department of Water Affairs (DWA) in 2006 and are facilitated using a real-time ecological reserve implementation model, namely, the Spatial and Time Series Information Modelling (SPATSIM) (Hughes et al., 2008, Sawunyama & Hughes, 2010). It was recognized within this development that any method for implementing the ecological reserve must account for different water resource development and supply situations. These can be divided into situations where a water manager has control over the flow rates in the channel through controlled releases from reservoir storage (which is the case in Letaba system where releases are made from Tzaneen Dam), and those where the manager has no control. It was agreed that the first step in implementing the SPATSIM modelling system and associated feedbacks (within an adaptive management framework) would be to implement the relevant operating rules and initiate a network of communication feedbacks between the KNP and dam operators (McLoughlin et al, 2011). The system was in operation from 2009 to 2012 until problems occurred with running SPATSIM. One of the identified problem areas is that of channel losses, which include potential alluvial channel, riparian and/or floodplain recharge, and evapotranspiration (ET); hereafter, we refer to these in combination as transmission losses. On the Groot Letaba, these transmission losses have been an area of considerable uncertainty due to their impacts on releases emanating from the Tzaneen Dam – meaning that the

specified reserve flows are often not met adequately at the Letaba Ranch (B8H008) monitoring weir close to the KNP (e.g. DWAF, 2010) and aquatic biomonitoring site (EWR4). In the DWA (2006) reserve determination study on Letaba, these transmission losses were estimated to be between 8% and 50% of the channel inflow.

While the SPATSIM real-time ecological reserve sub-model is still being used on the Letaba system, there have been some changes within the Letaba Catchment since the original proposal for K5-2338 was submitted in 2013. These changes are:

- The Letaba system now forms part of the Olifants Water Management Area.
- The Letaba system has now seen a finalisation of the Water Resources Classification System (WRCS), which has seen the gazetting of the lower Groot Letaba as a Management Class II, C Recommended Ecological Category river. Importantly, the EWRs have increased from those presently implement through SPATSIM.
- A concomitant part of the WRCS was the distinction of operationalising EWRs prior to and post-commissioning of the new Nwamitwa Dam.
- The updated national water resources availability assessment (Bailey & Pitman, 2012) study has now been completed, which reveals a significant reduction in the mean annual run-off (MAR) for the Letaba system under present catchment conditions.
- Hydrometric streamflow gauging in the Letaba River has deteriorated significantly over the past few years, which means that there is no accurate flow gauging along a >90 km stretch of river between Letsitele (B8H009) and Letaba Ranch (B8H008).

To this end, it is critical to improve the data inputs to any model used to operationalise the system moving forward as it quite clear that the system is fully allocated, and that efficiency is key. Therefore, by determining the actual rather than estimated transmission losses in a semi-arid system such as Letaba, the uncertainty associated with operational decision-making will be reduced significantly. Hence, it is expected that the results of this study will be used to:

- Change and update the operating rules: There is a need to adjust the operating rules, and determine when to impose restrictions, thus making sure that the system is sustainable. This is necessary to provide transparent but accurate information to inform river operations decision-making in a consensus-driven manner. To this end, it is a pre-requisite to improve data inputs such as dam levels, river flows and rainfall.
- Establish the reliability and integrity of the data on an ongoing basis, which include the accurate determination of transmission losses, which reduce the impact of releases from the controlling dam, to determine water release 'tolerances'.

2 LITERATURE REVIEW

2.1 Environmental Water Requirements

Due to the regulation of flow by dams, excessive water abstraction, the discharge of effluent in river systems and increasing water demands, it is critical that the EWRs be determined for all major rivers (Malan & Day, 2003). This EWR has to be an active rather than passive component of water resources management (Poff et al., 2009). An EWR refers to the flow needed by a river to sustain a healthy ecosystem. Typically, this EWR is determined to mimic the components of a river's natural flow variability, considering the magnitude, frequency, timing, duration, rate of change, and predictability of flow events (Arthington et al., 2006). There is a global concern about the deterioration of water quality in rivers, and it has been acknowledged that the decline in river health is highly influenced by changes in river flows (O'Keeffe, 2008).

EWR flows are being negatively affected by significant changes in land use and poor water resource governance (Pollard & Du Toit, 2011b), which means that EWRs have been notoriously difficult to implement. In order to meet the determined EWRs as well as to ensure that all water users receive their allocated water supplies, dedicated flow management is required through the efficient management of water abstraction, effluent discharge and dam outflows. In South Africa, this is termed 'operational water resources management' (OWRM). However, for OWRM to be truly effective, it is required that the hydrological processes that affect river flows is quantified. Transmission processes, namely, losses and gains of surface water from a river channel, are key knowledge gaps that currently undermine effective water allocation and management.

Until the early 2000s, the EWRs of South African rivers used the Building Block Method (BBM) (King & Louw, 1998). At that time, BBM was called in-stream flow requirements (IFRs), which represented the highly variable nature of the country's rivers. The BBM process defines a set of monthly (daily average) flow blocks that should be applied during normal/maintenance years as well as a set that should be applied during drought years (Hughes, 2001). However, Hughes (1999) also emphasized that IFRs are not sufficient to be incorporated into the type of water resource systems models that are used in South Africa. The argument was that IFRs do not provide the necessary temporally dynamic information on the frequency of occurrence, or assurance levels, of the different flows. A way to overcome this was to use flow duration curves (FDCs) instead of actual flow values that display the full range of river discharges from low flows to flood events. These now form the hydrological basis of reserve determination studies, which generate FDCs as site-specific flow assurance rules. These assurance rules are then typically implemented/monitored at hydrometric flow gauges [typically operated by the Department of Water and Sanitation (DWS)] close to EWR biomonitoring sites. Through the national WRCS, as mandated in the NWA, a river will be classified through a public participation process. A class of river and associated assurance rules are gazetted as the future management and operating scenario for a river system.

2.2 Transmission Losses

Globally, transmission losses are also known as *channel*, *river* or *water losses*. Transmission loss can be defined as a reduction in the volume of flow in a river/stream channel system between upstream and downstream points (Cataldo et al., 2010; Hughes & Sami, 1992; Lane, 1990; Shanafield & Cook, 2014; Walters, 1990). The reduction in the flow volume between the upstream and downstream points is attributed to the loss of water through three natural processes (Cataldo et al., 2010):

- Total evaporation in the riparian zone and open water evaporation from the river channel.
- Evaporation or infiltration of water stored in channel depressions or the flood plain.
- Recharge of groundwater as water infiltrates the stream channel, its banks or the floodplain.

Walters (1990) describes transmission losses as the reduction in river flow due to evaporation and infiltration to the riverbed, riverbanks and even the adjacent floodplain. Boroto and Görgens (2003) describe transmission losses as storage recharge in alluvial channel beds or alluvial banks, and as

evaporation and ET; direct evaporation from the water body surface; deep groundwater recharge and during extreme climatic events as losses to floodplain flows. Water lost via infiltration may either percolate to recharge aquifers or will return to the river downstream and contribute to the flow (Hacker, 2005). Sharp and Saxton (1962) as cited by Hacker (2005) propose that the key factors influencing transmission losses are:

- The size and sequence of floods.
- The geology and soils of the valley.
- The gradient, depth, size, continuity, meander, and number of channels.
- Riparian and phreatophytic vegetation along the channel and in the valleys.
- Soil frost conditions.
- Depth to the water table.
- Soil moisture content.
- Gross and gravitational pore space in the soil.
- Manmade structures and alterations.
- Antecedent and current rainfall.
- The content and nature of sediment in the stream flow.

Transmission loss can be a significant contributing process to the water balance of river systems, particularly in arid and semi-arid environments (Cataldo et al., 2010; Costelloe et al., 2003; Hughes & Sami, 1992; Hughes et al., 2008; Huang et al., 2015; Lange, 2005; Shanafield & Cook, 2014). Therefore, to ensure effective water management and water provision in these environments, it is critical to understand transmission losses considering that it is a key component of the water balance or hydrological budget (Gu & Deutschman, 2001).

Transmission losses have been well documented for arid and semi-arid environments around the world, but there remains a paucity of studies in southern Africa (Hughes et al., 2008). While transmission losses have yet to be properly quantified for any South African river, they are estimated to be high for perennial rivers flowing through arid and semi-arid areas, such as the Letaba system. According to Hacker (2005), transmission losses are amplified in arid or semi-arid regions where the water table is very deep and predominantly lower than the water level in a channel. Boroto & Görgens (2003) predicted that up to 30% of the Limpopo River's mass balance may be allocated to transmission losses due to ET and recharge to aquifer storage. Everson (2001) quantified losses due to ET between two gauged sites on the Sabie River to be 0.32 m³/s in low flow months – a significant proportion of total available flow considering that low flows range from 0–5 m³/s (Pollard & Du Toit, 2011a).

A similar figure has been noted for alluvial transmission losses in semi-arid regions of north-east Brazil (Costa et al., 2013). More recently, a figure of 10% has been used in the Lower Olifants (DWA, 2011). In the Letaba River Reserve Determination Study conducted by DWAF (2006), transmission losses were estimated to be between 8% and 50% of the channel inflow. Quantitative investigations of transmission losses are therefore necessary to calculate flows in a river and appropriately allocate water for different users (Gu & Deutschman, 2001).

2.3 Incorporating the Total Evaporation Process into Streamflow Transmission Loss Estimation Procedures

Even though there are various factors that have been identified to influence the transmission loss process, only a select few parameters have been successfully incorporated into transmission loss estimation techniques (Hacker, 2005). Run-off volume, velocity, river channel geometry and characteristics of the channel bed material are among the most commonly used factors for transmission loss estimation procedures (Hacker, 2005). Ultimately, the choice of factors used for transmission loss estimation procedures is controlled by the characteristics of the study site and the availability of data (Cataldo et al., 2004). However, one of the factors that is seldom included or adequately represented in transmission loss estimation procedures is the total evaporation process.

It is often the case that total evaporation is ignored or inadequately represented in the transmission loss estimation procedures, even though it has been identified as a contributing process to transmission loss (Cataldo et al., 2010; Hacker, 2005; Shanafield & Cook, 2014). Research and transmission loss estimation techniques have tended to focus more on the flow reduction in relation to infiltration (Cataldo et al., 2010; Hacker, 2005; Shanafield & Cook, 2014). This is largely due to most transmission loss in most ephemeral rivers occurring as a result of infiltration-based losses (Cataldo et al., 2010).

Although infiltration-based losses may contribute relatively more to transmission loss, the absolute losses resulting from total evaporation cannot be discounted. This is particularly pertinent to environments where total evaporation is a considerably large component of the water cycle (Everson, 2001; Hacker, 2005; McKenzie, 2001; Shanafield & Cook, 2014). According to Shanafield and Cook (2014), all processes that influence transmission loss need to be quantified in order to fully understand the magnitude and effects of transmission losses.

The accurate quantification of hydrological processes, such as the role of riparian total evaporation and open water evaporation, must be acknowledged and accounted for to model transmission loss successfully.

3 OBJECTIVES

Hughes et al. (2008) note that there have been very few direct studies of channel transmission losses in southern Africa; this despite it being a significant component of river water balances in the region. Hughes et al. (2008) also acknowledge that while the process of river losses into alluvial aquifers (recharge to the aquifer) is reasonably understood (e.g. Görgens & Boroto, 2003), it has often eluded the water resources modellers to quantify such losses. Furthermore, it is even suspected that losses in hard rock terrains underlying many of the regions rivers (such as the Letaba) are significant due to the highly fractured nature of the material of bedrock channels. Thus, transmission losses from non-alluvial rivers can also be substantial. To this end, the project had the following aims:

1. Quantify transmission losses along a reach of the Groot Letaba River.
2. Incorporate transmission losses into real-time modelling systems, thus improving the delivery of EWRs.
3. Develop a cost-effective method to upscale the transmission loss parameters using hydrometrics coupled with remote sensing and an integrated surface water/groundwater interaction model.
4. Develop regional parameters for transmission losses to enable application to other river systems in the South African Lowveld.
5. Contribute to the development of a long-term research site for studying riparian zone hydrology, hydrogeology and river ecology.

Specific objectives were:

1. Determine EWR real-time implementation model uncertainties due to transmission loss parameterization.
2. Select river reaches under various geological/hydrogeological settings where transmission losses need to be determined.
3. Select river reaches under various land management types where transmission losses need to be determined.
4. Quantify abiotic mechanisms for transmission losses in these reaches through groundwater/surface water interaction determination.
5. Quantify biotic mechanisms for transmission losses in these reaches through determination of actual ET losses in the riparian zone.
6. Upscale the quantified processes through extrapolation with remote sensing, geophysical, hydrochemical and modelling techniques.
7. Develop accurate transmission loss parameters and incorporate in real-time reserve implementation models.
8. Where possible, provide added value by transcribing the findings to other rivers in the Lowveld.

4 STUDY SITE: THE LETABA RIVER SYSTEM

The Letaba River catchment is located in the Limpopo Province of South Africa. It extends over an area of approximately 13 400 km² (Moon & Heritage, 2001). It is delineated by the Drakensberg Escarpment in the west extending into the low-lying Lowveld in the east (Figure 1). The catchment can be divided into the Klein Letaba sub-catchment in the north and the Groot Letaba sub-catchment in the south. Downstream of the Middle Letaba Dam, the Middle Letaba River flows into the Klein Letaba, which drains into the Groot Letaba River at the KNP boundary. According to Heritage et al. (2001), nearly three-quarters of the catchment is underlain by granitic and gneiss geological formations, whereas the east is dominated by volcanic formations derived from the Karoo sequence basalts. Due to the presence of granites, weathered zones are shallow, and soils have a sandy soil texture. There are numerous diabase dykes across the catchment, with many intercepting the Letaba River upstream of the KNP.

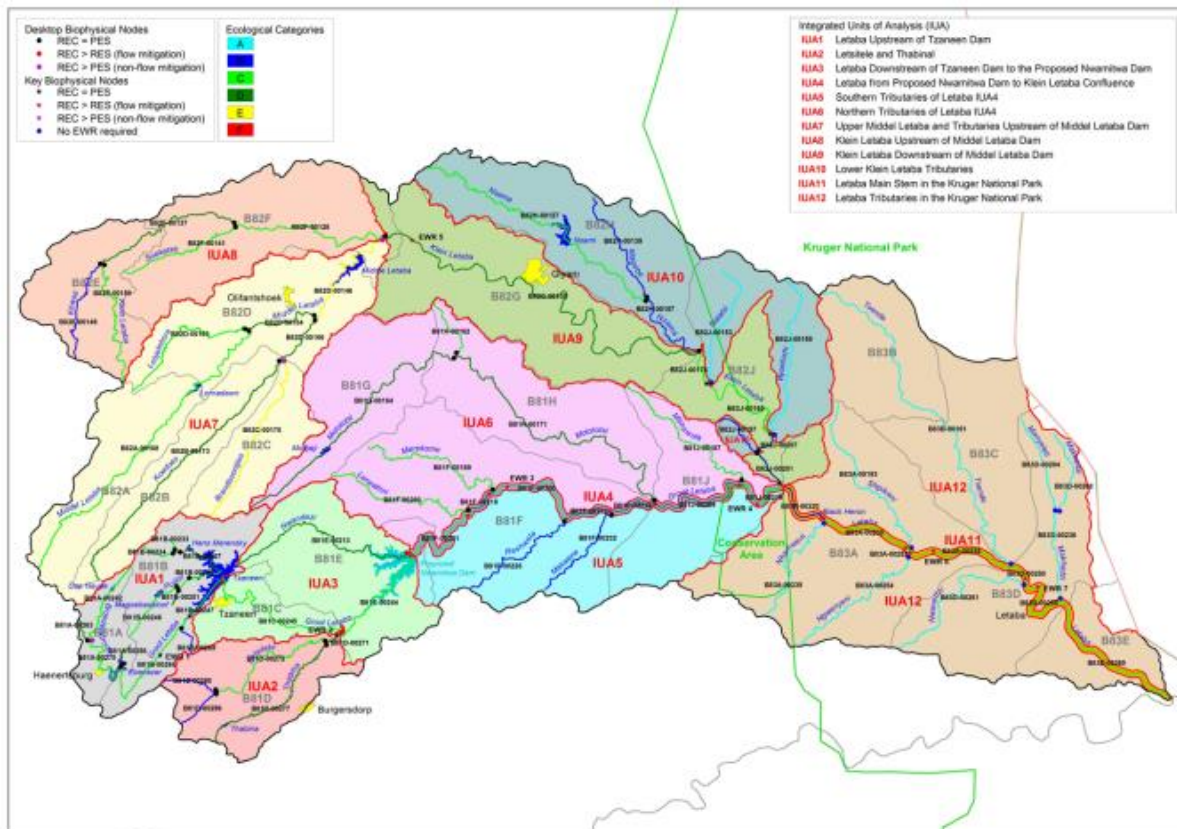


Figure 1: The Letaba Catchment with major dams and EWR sites according to the WRCS (DWA, 2013)

4.1 Climate

The climate across the catchment is considered semi-arid and varies since it extends across high-altitude mountainous areas in the west and the low-lying areas of the Lowveld in the east. Generally, summers are wet and hot whereas winter conditions are dry and mild. The mean annual precipitation (MAP) in the catchment is approximately 612 mm, of which more than 60% is captured in only 6% of the total area, namely, the mountainous region in the west (WRC, 2001). In particular, 500–1800 mm of rainfall falls in the western mountainous areas whereas the east receives 450–700 mm (Moon & Heritage, 2001). According to the WRC (2001), mean annual evaporation is estimated to be 1669 mm.

4.2 Hydrology and Geomorphology

There are more than 20 major dams located in the Letaba Catchment (WRC, 2001). The Letaba River is the tributary of the Olifants River just upstream of the Mozambican border. The Molototsi River and Klein Letaba are the major tributaries contributing to the Letaba River. The macro-channel of the river

may be described as bedrock-bounded (Van Niekerk et al., 1995; cited by Heritage et al., 2001). The channel is further characterised by steep bedrock including cascading boulder rapids with sporadic waterfalls (WRC, 2001). Further downstream in sections with gentler gradients, cobble riffles occur before changing to an alluvial channel type as it approaches the KNP (WRC, 2001). Deep pools may be found all along the Letaba River. There are a number of different morphological units due to varying sediment distribution along the Letaba River (Heritage et al., 2001). The hydrology of the system is dominated by low flows as seen in Figure 2. The figure also compares the Letaba Rivers hydrology over three recent severe drought events.

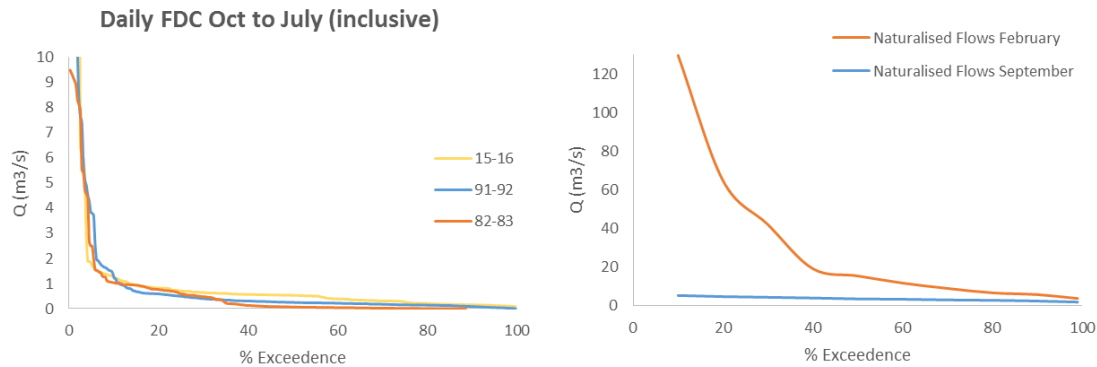


Figure 2: Hydrology of the Letaba Catchment at B8H008 (Letaba Ranch) using flow duration curves (left: comparing three major drought periods; right: natural hydrology wettest month versus driest month)

4.3 Land Use Activities

Throughout the Letaba Catchment, land use is dominated by commercial agriculture, afforestation, densely populated rural communities with informal, rain-fed agriculture, and protected areas in the eastern section of the catchment (Pollard & Du Toit, 2011a). The Letaba Catchment is home to intense, commercial agricultural activities where citrus, tropical fruits and vegetables are the most commonly farmed produce (Pollard & Du Toit, 2011a). Since the headwaters in the western section of the catchment are under commercial forestry, water resources are already under stress due to the additional demand of water supply for irrigators downstream. The upper reaches of the catchment are generally regarded as being in good condition, but it deteriorates further downstream due to natural salinization and nutrient enrichment by anthropogenic influences (Pollard & Du Toit, 2011a).

The water supply schemes in the catchment currently consists of numerous small to major dams for storage, bulk water pipelines and extensive canal networks (Pollard & Du Toit, 2011a). More than a decade ago, Vlok and Engelbrecht (2000) noted that the Tzaneen Dam allocated 103.9 million m³/a to irrigators, 8.4 million m³/a to households and industry, and 14.7 million m³/a to environmental flows. However, the water that was allocated exceeded available supply because Tzaneen Dam could only yield 98 million m³/a (Vlok & Engelbrecht, 2000). Situations such as these highlight the magnitude of poor water management strategies in a stressed catchment such as Letaba.

4.4 Letaba Water Supply System – Status Quo

Katambara and Ndiritu (2010) have identified that flows in the Letaba River no longer resemble natural flows due to infrastructural developments including large dams such as the Magoebaskloof, Ebenezer and Tzaneen dams.

In terms of water resources planning, we often speak of catchments along with their associated infrastructure as *water supply systems*. The Letaba River is one such system that uses water from the Groot, Middle and Klein Letaba rivers and their tributaries. In the Middle and Klein Letaba rivers, there are a number of borehole supply schemes and water supply schemes using the Middle Letaba and Nsami dams. In the Groot Letaba, water is supplied for bulk domestic use to towns such as Polokwane

(inter-basin transfer), Tzaneen and rural communal areas. These use the Dap Naudè, Ebenezer, Magoebaskloof, Vergelegen, Hans Merensky, Tzaneen, Thabina and Modjadji dams. However, the surface water resources within the entire Letaba Catchment are extensively developed (Figure 3).

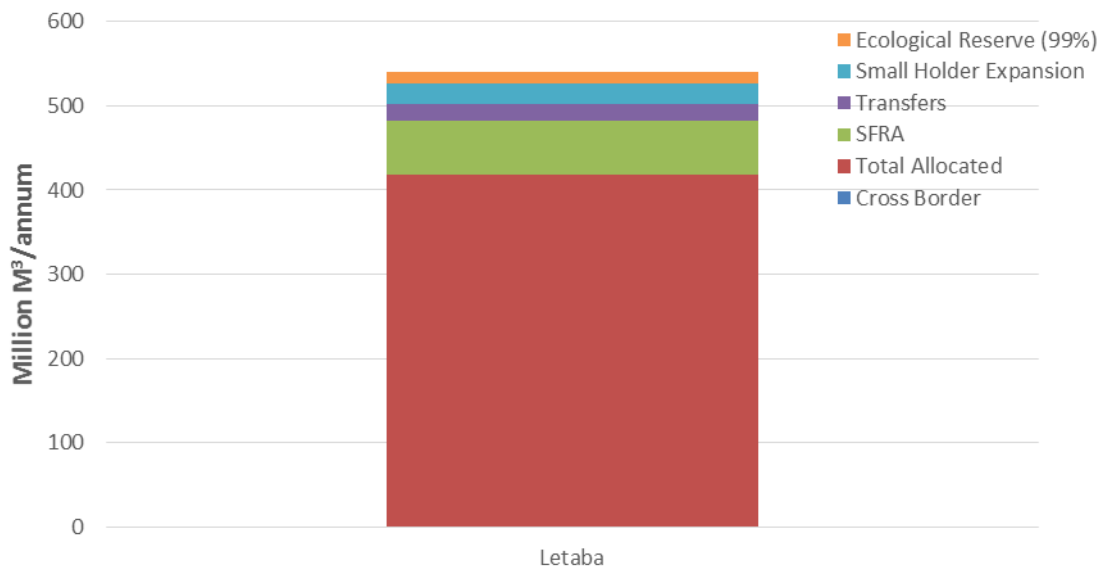


Figure 3: Status of present water allocation in the Letaba Catchment, 2014 (total allocated includes commercial agriculture, industrial and domestic requirements)

Faced with water shortages of increasing severity and frequency over the years, the main consumptive users of water have from time to time competed for the limited supplies and experienced significant levels of restrictions. This has resulted in the degradation of the riverine ecosystem. The water resources of the Groot Letaba are not sufficient to meet all its requirements all the time (DWA, 2014). The recent water resources reconciliation for the Letaba system (DWA, 2014) included among others the following advice to be implemented to achieve water resources management sustainability in this catchment up to 2040:

- Excess water from Ebenezer Dam should be allocated to users in the Groot Letaba system by augmenting the Tzaneen Dam. No further augmentation is possible via inter-basin transfer to other areas (e.g. Polokwane).
- Water conservation/water demand management must be implemented in this catchment with immediate effect from both the domestic and industrial sector.
- Continue with the implementation of the Groot Letaba Water Development Project (GLeWaP) that includes:
 - Raising of Tzaneen Dam by 3 m to improve the assurance of supply to the users.
 - A new major storage dam on the Groot Letaba River just downstream of the Nwanedi River confluence at the site known as Nwamitwa, with first water stored by 2019.
 - Resulting from Nwamitwa, develop a bulk water supply scheme to serve rural communities without adequate water supplies.
- Importantly (and demonstrating the added value of the WRC project K5-2338), use Nwamitwa Dam to start delivering water according the ecological water resources requirements gazetted in the WRCS process for the Letaba.

Furthermore, large transmission losses were identified during the GLeWaP and other studies on the lower reaches of the Letaba River. It has previously not been possible to estimate these losses as no acceptable gauging stations existed in this part of the Letaba, and because the current water resources assessment model (WRSM2000/Pitman model) only specifies transmission losses as a monthly value. Also, the sluice of the weir at Prieska (B8H017) has been open since the 1996 floods due to a tree being stuck in the sluice gate. This already might account for the perceived losses on its own. The Prieska Weir issue should be resolved by either continuously measuring the flow from the leaking sluice or by destroying the Prieska Weir.

Pollard et al. (2012) showed through a historical (contextual) assessment of compliance with the ecological reserve that during the period of major water resource development (1960–1994) in the Groot Letaba, meeting the present day assurance rules close to the KNP at EWR4 (using a 'C/D' class assurance determined prior to the WRCS process), that there was typically above 40% non-compliance with the ecological reserve, which is especially noticeable in the dry winter months (May–October) (Figure 4). However post-1994, the situation had begun to improve where non-compliance ranged between 20% and 30%. It was noted in this study that this catchment had seen continuous effort to improve water resources management since 1994. This was attributed to close interaction between the operator of Tzaneen Dam and commercial agriculture through the Letaba Water Users Association (LWUA) and, then more recently, with the KNP monitoring flows near the western boundary, who initially started to benchmark flows at 0.6 m³/s in the absence of a comprehensive reserve study.

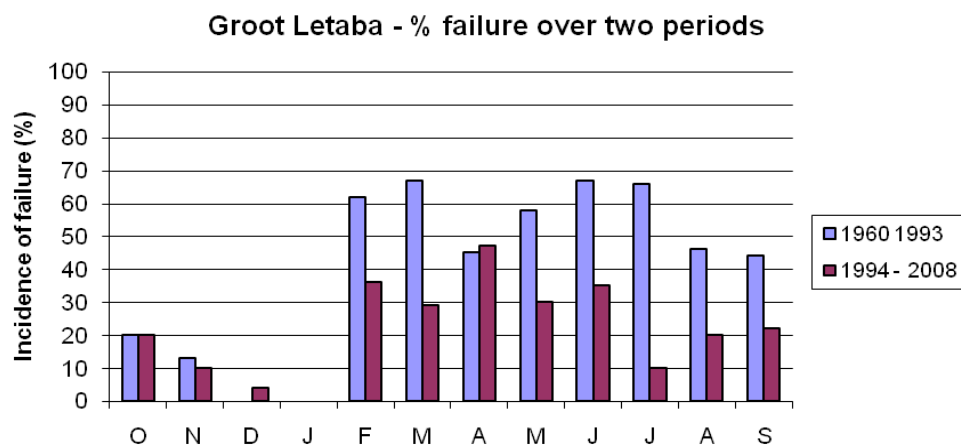


Figure 4: Compliance with the ecological reserve at Letaba EWR4 (Pollard et al., 2012)

4.5 History and Present Operating Rules

The Tzaneen Dam was completed in 1976. By 1977, the Tzaneen Dam started to fill with an annual allocation of 130 Mm³ while its full supply is 156 Mm³ with a firm yield of 50 Mm³. History has demonstrated the stresses that the Tzaneen Dam is meant to endure. For instance, in the droughts of the late 1980s and early 1990s, the Tzaneen Dam capacity effectively dropped to below 5%; in 1995, it dried out completely. The short drought from 2004–2005 also saw its storage drop significantly. In general, the dam is at 0–10% capacity approximately 14% of the time; the dam is above 90% capacity close to 20% of the time.

The wet cycles in the Letaba region are about 20 years apart, which needed to be factored into the management of the dam. The history of constraints on the system meant that new operating practices had to be implemented for the sustainable utilisation of the dam. This is mainly to provide the citrus orchards in Tzaneen area with a permanent supply of water (otherwise plants die, and it takes 4–5 years before citrus can become productive again, which is a significant risk for the local economy). Therefore, early restrictions were brought in to the operations from 2006 (water years starts from 1 April to end of March), which allowed accrual of storage in the dam; something that has not occurred previously.

The DWS operating rules for the Tzaneen Dam plan for annual losses of 30% downstream, while 10–15% of the dam is reserved for domestic and industrial use. If the dam reaches the 15% level, then there is a 100% curtailment to irrigators. Meanwhile, irrigators through the LWUA implement their own voluntary operating rule: at 95–100% capacity, then there is 100% assurance of supply to irrigators; below 95% capacity, 50% curtailment on 1 April, and for each month thereafter they add a further 5% curtailment. For example, May would be 55%, until you get to 70% curtailment. These steep restrictions allow the LWUA to manage for large storage depletion in the dam.

Meanwhile it is assumed that the tributaries in the system make significant inflows that allow the reserve to be met and to meet the needs of the run-of-river users downstream. However, if the tributaries are not flowing, then the Tzaneen Dam needs to release on average about 6 Mm³; if they are flowing, then about 2 Mm³ is released in order to meet requirements at Letaba Ranch (EWR4).

The comprehensive reserve determination through the WRCS process has proposed the lower reaches of the lower Groot Letaba to be a Management Class II with a C class reserve (Table 1). The implication of this is high-assurance rule flows that must be implemented in the present day operating scenario (Figure 5), although it is acknowledged that this will only be fully achievable following the construction of Nwamitwa Dam, wherein a new EWR rule applies.

Table 1: Management class and water availability in the Letaba Catchment (Drainage Region Olifants: B8), MAR data from WR2012 study

	Management Class	REC	Catchment Area (km ²)	nMAR ¹	revised nMAR ²		EWR Mm ³ /a		
					Natural MAR	Present Day MAR	70% assurance	99% assurance	% of nMAR at 99% assurance
Letaba	II	C	13677	679.6	636	342	36	13	2

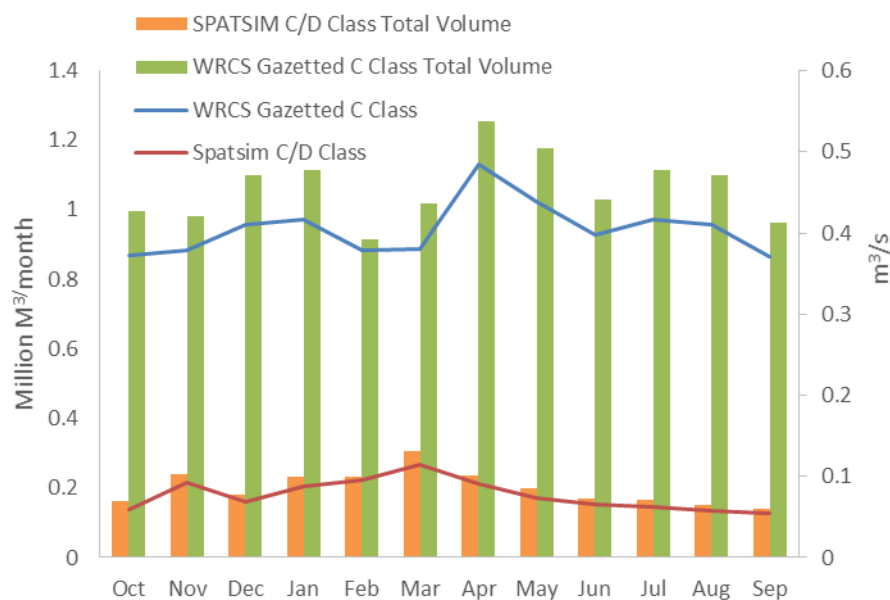


Figure 5: Operating rule for EWR4 (columns), mean daily flow (lines) for EWR4, comparing existing SPATSIM model with recently gazetted EWRs

4.6 Transmission Loss Study Site

The Letaba River Transmission Loss study site is situated along the lower end of the Groot Letaba River just before the river enters the KNP. The site is bounded on the upstream side by the defunct Mahale Weir (B8H007²) and on the downstream side by the Letaba Ranch Weir (B8H008) as can be seen in Figure 6.

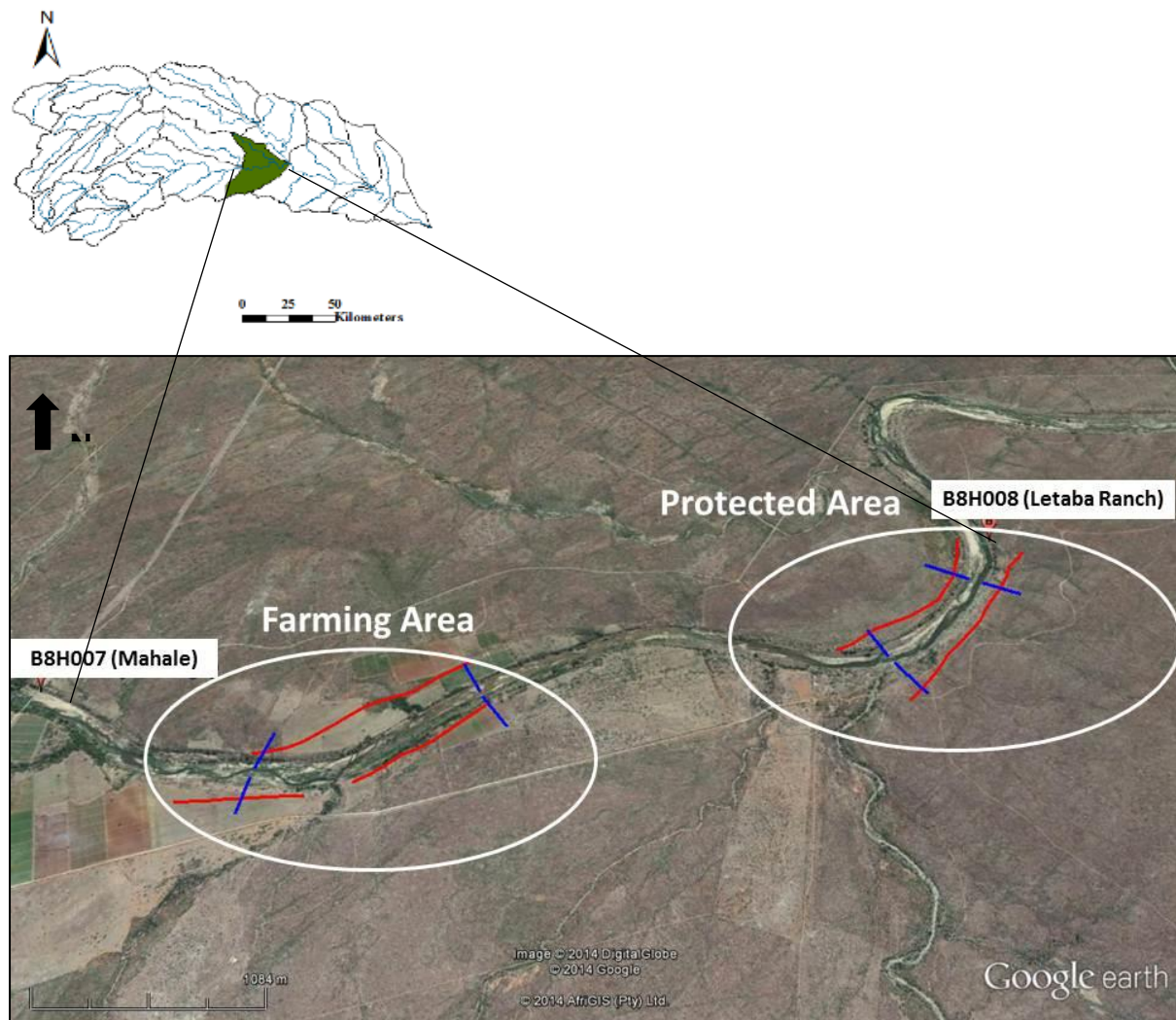


Figure 6: Delineation of the study site between B8H007 (Mahale) and B8H008 and the location of geophysics transects over two different land uses

Between these two gauges, the river first traverses agricultural areas under tenure by emerging farmers schemes in the west before traversing protected areas (the community-owned Mthimkhulu Reserve on the northern bank, and the provincial Letaba Ranch Game Reserve on the southern bank). Appendix I gives detailed site description maps on the local lithology, soils, stream networks, topography and topocadastral features. The river morphology consists of two dominant types, namely, sandy braided alluvial system most dominant in the west with increasing occurrence of bedrock controls (dykes) in the east (Figure 7 and Figure 8).

² This is not a gauging weir as it was constructed as a river crossing/abstraction weir although registered on the DWS hydrometry database.



Figure 7: Typical river channel morphology at study site: braided alluvial channel



Figure 8: Typical river channel morphology at study site: bedrock controls

4.7 Study Site Set-up: River Hydrology and Hydrochemistry

The study used the two river gauges for mass-balance purposes (Figure 9). Primary flow data was available from the DWS HYDSTRA database for the downstream Letaba Ranch B8H008³. Meanwhile, the Mahale Weir (B8H007) was ungauged. Therefore, it was fitted with a Solinst™ Levelogger to determine stage height and a rating was attempted. However, the structure of the weir wall was such that it was not suitable for a full rating. However, for most of the period of interest (during low flows

³ [https://www.dwa.gov.za/hydrology/Verified/HyData sets.aspx?Station=B8H008&SiteDesc=RIV](https://www.dwa.gov.za/hydrology/Verified/HyData%20sets.aspx?Station=B8H008&SiteDesc=RIV)

during winter and spring), the river did not flow over the weir. When the Levellogger data showed a constant stage, this was taken to mean no overflow of the weir wall but simply continued discharge through two low flow sluices. The following rating was determined for these sluices, which allowed for reasonable gauging of low flows:

Table 2: Mahale Weir low flow rating

	Flow at weir pipes (m/s)	Pipe diameter (m)	Discharge (m ³ /s)	Total discharge (m ³ /s)
Pipe 1	3.4	0.3	0.24	0.50
Pipe 2	3.7	0.3	0.26	



Figure 9: Mahale Weir (left) and Letaba Ranch Weir (right)

Longitudinal hydrochemistry surveys of the river channel were conducted three times during the study. The first such survey in November 2014 (Figure 11) alluded to groundwater discharge into the river as the electrical conductivity of the river freshened out further downstream into the protected areas. It is at the point where the river electrical conductivity increases in the November 2014 survey that the river may appear to intersect the regional groundwater flow path. It is expected that paleo-floodplain alluvium⁴ is the conduit for an unconfined aquifer in this region that relinquished water to the river as accruals during the early part of the study period. However, as drought conditions persisted during the study, it appeared that these contributions diminished, resulting in stable electrical conductivity throughout the longitudinal river profile by the April 2016 survey.



Figure 10: Letaba River between Mahale and Letaba Ranch

⁴ As suggested by the geophysics study

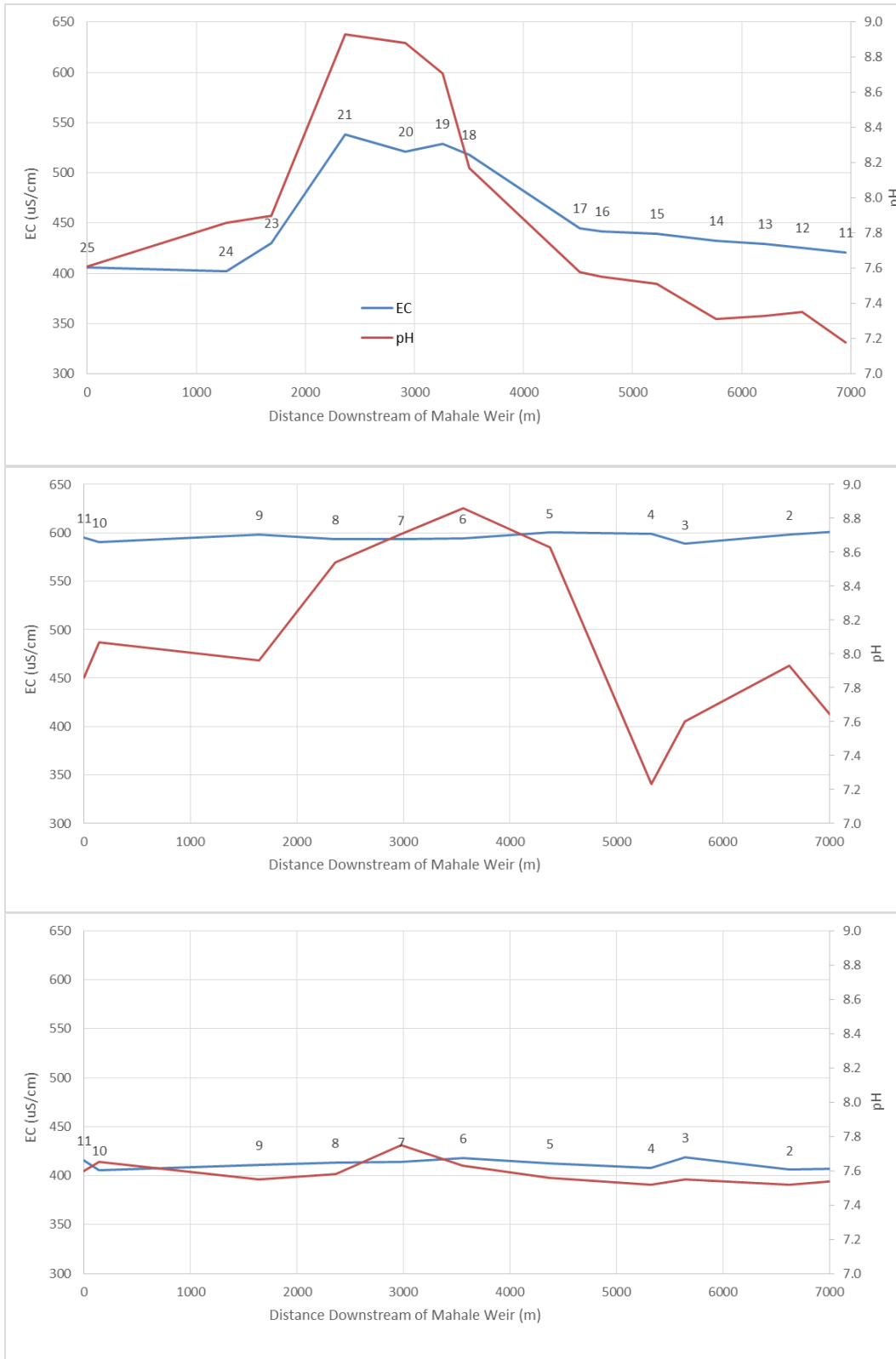


Figure 11: Longitudinal hydrochemical surveys of the Letaba River between Mahale and Letaba Ranch on 24 November 2014 (top) using *in situ* measurements on 27 October 2015 (middle) and 14 April 2016 (bottom) using samples analysed by the MOSA Mobile Laboratory⁵

⁵ Work funded by the Middle Olifants South Africa (MOSA) project, BMBF, Germany

4.8 Study Site Set-up: Riparian Eco-Hydrology Through Stable Isotopes

The study undertook to determine potential hydrological connectivity between surface water and groundwater using stable isotope analysis and furthermore distinguish whether riparian zone vegetation uses either of these water sources, and the temporal variation thereof. There were 46 individual trees from the following species:

- Ten *Ficus sycomorus*.
- Eight *Phalaenopsis violacea*.
- Ten *Diospyros mespiliformis*.
- Three *Colophospermum mopane*.
- Three *Cercidium microphyllum*.
- Five *Guiera senegalensis*.
- Five *Ziziphus mucronata*.
- Two *Phragmites mauritianus*.

These trees, which were distributed among six sampling regions across a portion of the Groot Letaba River incorporating the three geomorphological zones categorized in this study, were sampled for stable isotope analysis. These sampling regions were categorized according to their respective locations with regards to Letaba Farm (20 trees) and Letaba Ranch (26 trees). The co-ordinates and a Google Earth illustration of the sampling regions are given in Table 3 and Figure 12, respectively.

Table 3: Co-ordinates for the six sampling regions distributed across a portion of the Groot Letaba River along which 13 individual tree species were sampled

Sampling Point	Description	Latitude	Longitude
1	Letaba Farm near stream northern bank	23.669	31.017
2	Letaba Farm near stream southern bank	23.670	31.019
3	Letaba Farm near stream northern bank	23.675	31.005
4	Letaba Ranch near stream northern bank	23.662	31.047
5	Letaba Ranch within river channel	23.659	31.049
6	Letaba Ranch near stream southern bank	23.662	31.049

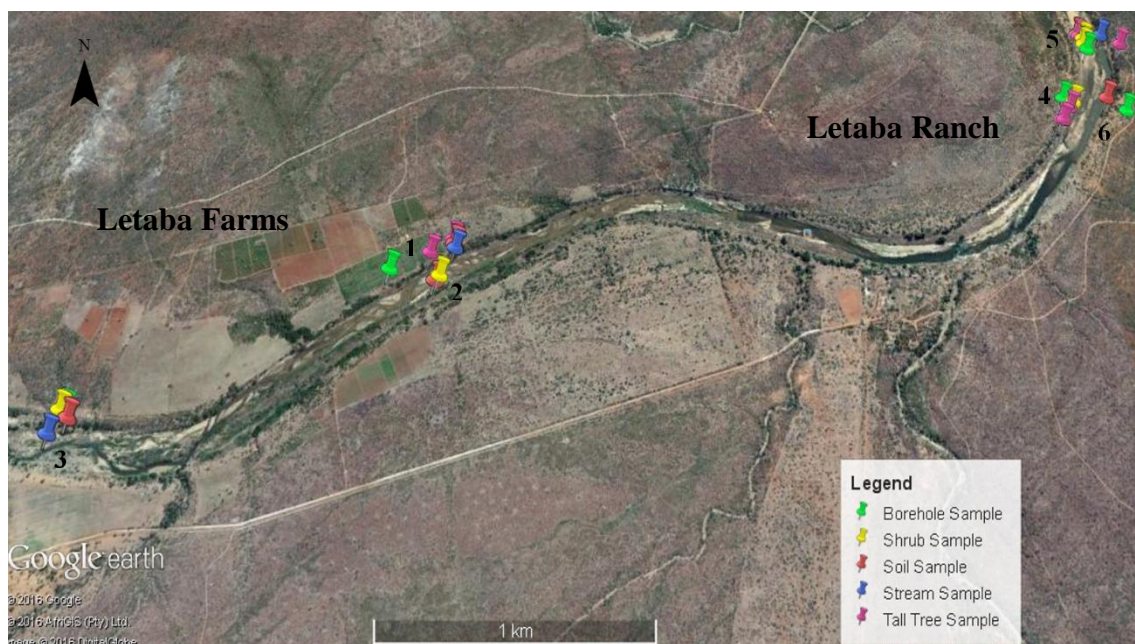


Figure 12: Location of the six sampling regions across a portion of the Groot Letaba River incorporating the three geomorphological zones categorized in this study

4.9 Study Site Set-up: Hydrocensus

An initial hydrocensus was performed during May 2014 in a local community just north of the study site. The hydrocensus was conducted to provide some indication of the local hydrochemistry in the surrounding area and to establish how dependent local communities were on groundwater for domestic and small-scale irrigation supply. The data provided in the sub-section that follow stem from an initial hydrocensus conducted north in Mbaula and on a local reserve, Mthimkhulu (Figure 13).

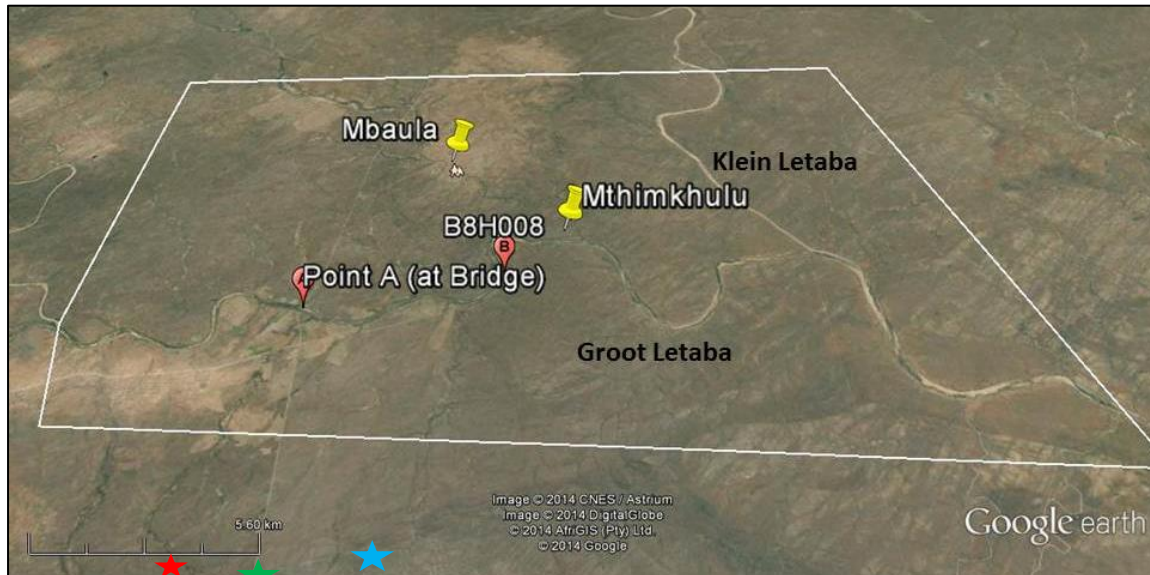


Figure 13: Mbaula Village and Mthimkhulu Reserve in relation to the study site

Mbaula

A total of 37 boreholes were identified in Mbaula. However, hydrochemistry variables were only measured in 32 of these due to owners/operators not being available to switch on the pumps to obtain a water sample. Boreholes in Mbaula were drilled to an average depth of 50 m. Of the 32 boreholes, the average pH in Mbaula was 7.19, while the average groundwater temperature was 24.44°C. Groundwater measured in nine of these boreholes was extremely saline resulting in out-of-range electrical conductivity values. In 16 of these boreholes, the electrical conductivity ranged from 12–19 mS/cm. In less than 22% of the boreholes measured (i.e. only seven boreholes), groundwater was very fresh with a low electrical conductivity ranging from 1–2 mS/cm. It is likely that these boreholes were drilled along dykes where preferential pathways act as conduits for fresh surface water to recharge aquifers.

Mthimkhulu

There are six boreholes located throughout the Mthimkhulu Reserve, of which only five could be accessed for recording (Table 4). Not all these boreholes are pumped actively. At the inactive boreholes, a bailer was submerged to collect a water sample for hydrochemistry measurements.

In general, the groundwater observed on Mthimkhulu is similar to that measured around Mbaula, which provides a decent indication of the local hydrochemistry in the area. Borehole WP021, which was drilled up to 100 m to supply water for a guest lodge along the Groot Letaba (just upstream of the Groot and Klein Letaba confluence), has good quality water.

Table 4: Details of boreholes located on Mthimkhulu Reserve

Bore-hole ID	Status	Activity (e.g. domestic, farming)	Borehole depth (m)	Water level (m)	pH	Electrical conductivity (mS/cm)	Temp. (°C)	Total dissolved solids (ppt)
WP019	Active	Domestic	?	Covered				
WP020	Not always	Domestic, watering hole	50	10.21	6.9	14.75	26.2	7.36
WP021	Not active	Domestic	100	21.96	6.26	0.50	27.6	0.25
WP022	Not active	Domestic, watering hole	30	2.32	6.9	13.33	25.6	6.71
WP023	Active	Domestic, lodge	60	10.97	7	15.50	20.2	7.64

Additional hydrocensus information

Although no formal hydrocensus was been completed on these farms, correspondence with the farmers provided additional hydrocensus information. The farm represented by the red star in Figure 13 has seven boreholes on the property, but only one of these are actively used to supply water for household use. Crops are irrigated directly from the Groot Letaba River. The farm represented by the green star irrigates using both groundwater and a direct supply from the river. The exact number of boreholes on this property is still uncertain. The farm represented by a blue star (as well as the farm directly opposite the river) does not have any boreholes drilled on the property since it irrigates daily using water directly from the Groot Letaba.

River abstraction

Direct abstractions from the river occur within the study site – especially in the farming portion. While all the farms use drip irrigation and abstractions should be relatively low, the total amount needed to be quantified to properly understand differences in flow between the two weirs. The results of this survey suggest relatively low direct river abstraction (Figure 14 and Table 5), with an estimated mean daily abstraction of 52 m³.

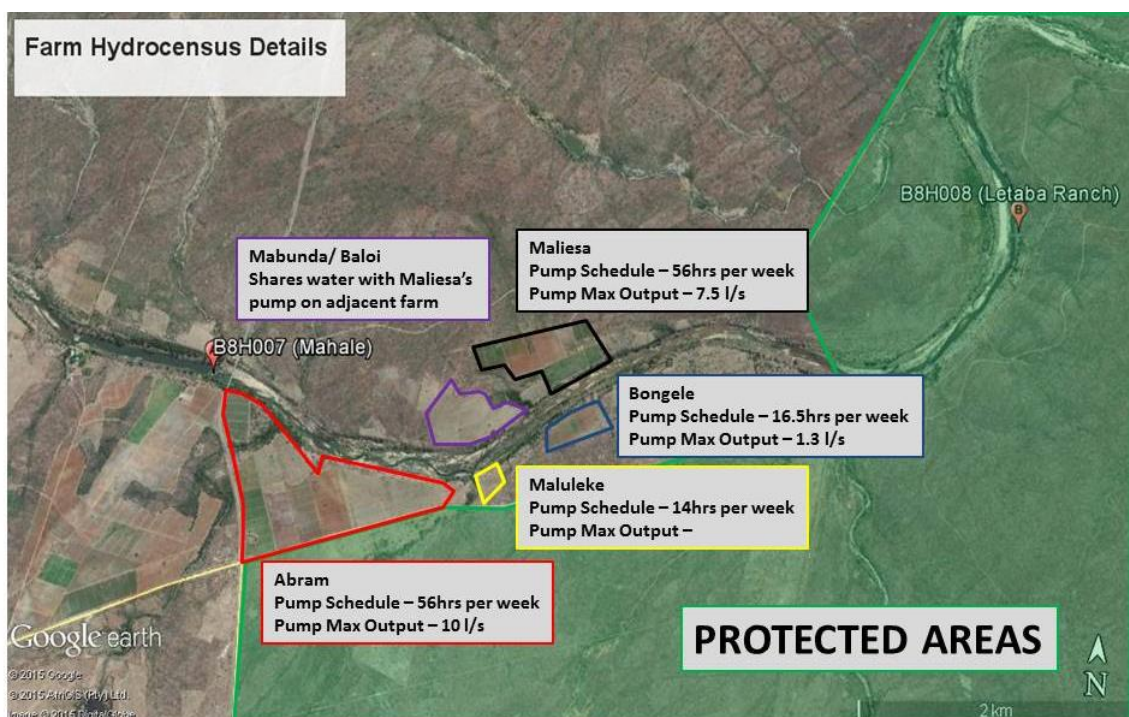


Figure 14: Agricultural water use hydrocensus at study site

Table 5: Hydrocensus information from July 2015 survey

Farm name	Bank	No. boreholes	Farming scale	Pump max. capacity (l/s)	Pumping schedule (hours/week)	Estimated volume per day (ℓ)
Abram	Southern	0	Commercial	10.0	56.0	28 800
Maliesa	Northern	4	Commercial	7.5	56.0	21 600
Mabunda	Northern	0	Commercial			
Bongele	Southern	5	Commercial	1.3	16.5	1 103
Maluleke	Southern	0	Commercial	1.0	14.0	720
			Potential Abstractions per day (ℓ)			52 223
				m³/day		52

4.10 Study Site Set-up: Precipitation

Rainfall data was collected during the study period from three Davis Vantage Pro weather stations situated within the study site at Mahale farm (adjacent to Mahale Weir B8H007), Mthimkulu (within the Mbaula reserve), and Phalaubeni, which is a village 6 km to the north. As can be seen in Figure 15, the study period was marked by extremely low rainfall from 1 June 2015 onwards. No more than 180 mm rain was received over the study period, and a significant proportion of this was from a single event in March 2016. Up until that date, only 73 mm had been recorded for the rain season.

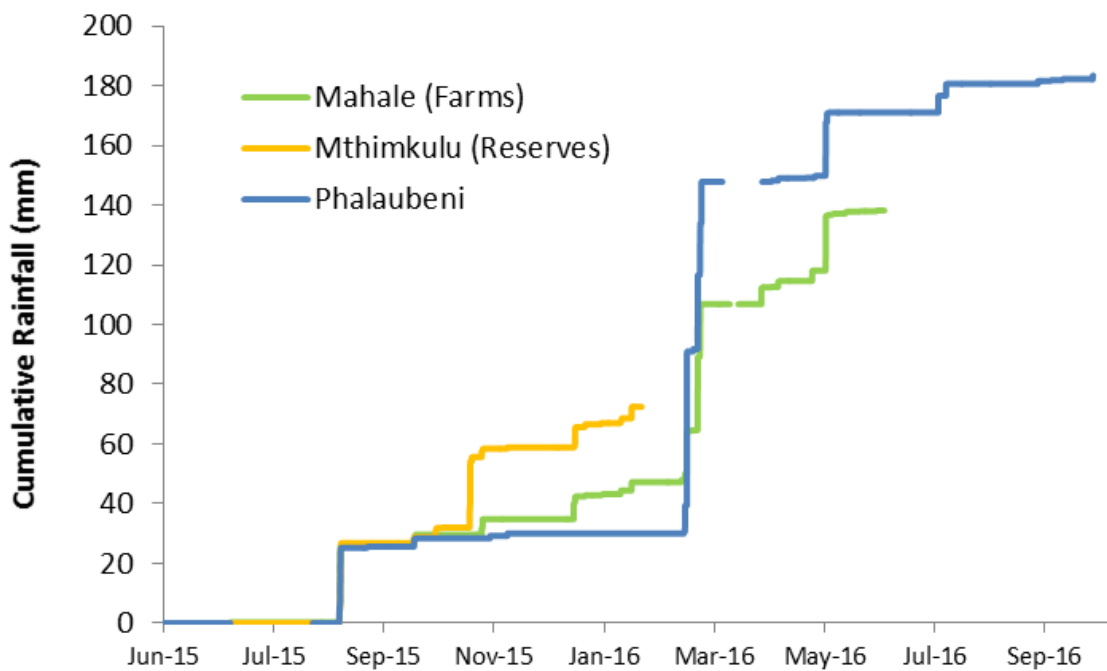


Figure 15: Rainfall measured for the 2015–2016 hydrological year within the study site (Mahale, Mthimkulu) and at nearby village north of the site (Phalaubeni)

4.11 Study Site Set-up: Geophysical Surveys

Geophysical survey techniques were conducted to obtain valuable information of the subsurface geology using the commonly applied electrical resistivity tomography (ERT). This is a common geophysics technique used in water resource and geomorphological studies (Robinson et al., 2008). According to Loke (1999), this technique provides a reliable account of the bedrock and lithological distribution within catchments since detailed measurements of the subsurface resistivity distribution is obtained based on known geological resistivity ranges.

Resistivity values are influenced by soil/rock properties, water content and salinity. Studies by Kongo et al. (2007), Riddell et al. (2010), Uhlenbrook et al. (2005) and Wenninger et al. (2008) have shown how the ERT method could be successfully applied in hydrological investigations in southern Africa. The purpose here was to extensively survey the subsurface resistivity distribution along the river and to identify ideal locations for drilling the boreholes required for monitoring groundwater/surface water interaction. These surveys were conducted over two different land uses, i.e. farming areas and protected areas (Figure 16), as described in the sub-sections that follow.

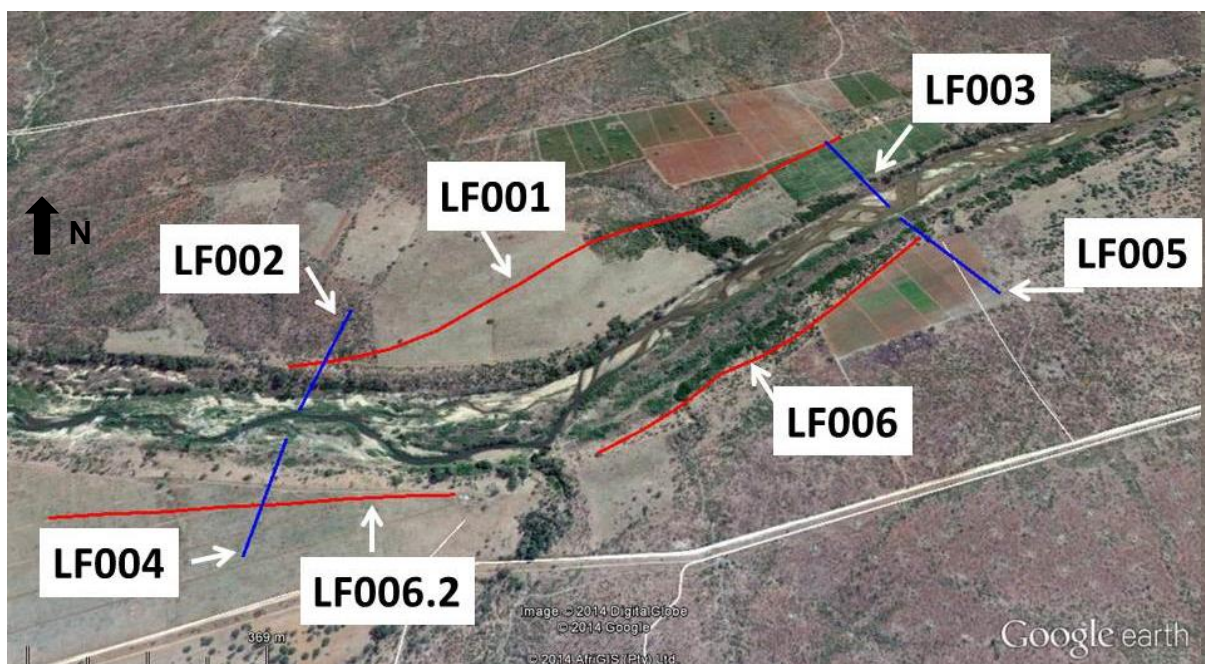
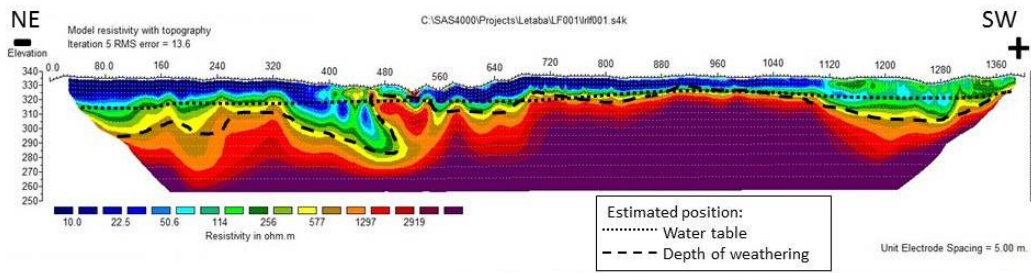


Figure 16: Locations of geophysics transects across the farms

Farming area

Two geophysics transects were surveyed on both sides of the river running in parallel from east to west (red lines). These surveys used a minimum electrode spacing of 5 m using the Schlumberger array in order to measure deep resistivity profiles (~70 m). The blue transects represent surveys that ran perpendicularly across the river. These surveys also used a Schlumberger array with minimum electrode spacing of 2.5 m for shallower resistivity profiles (~35 m). Ideally, these perpendicular transects would have ran from one bank to the opposite bank. However, due to accessibility constraints, surveys had to split with each transect beginning in the riverbed and progressing upwards toward the riverbank. The results and interpretations are depicted from Figure 17 to Figure 22.

Letaba Farms: LF001

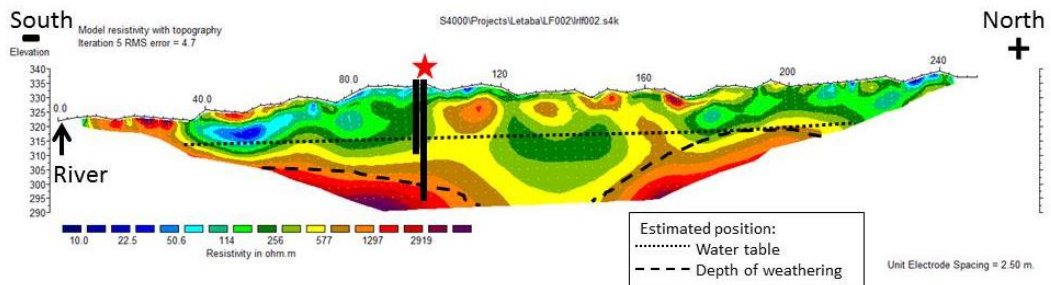


- Runs parallel to river channel (in a south-west direction)
- Evidence of tributary between 400m and 550m ~ negative weathering
- Shallow weathering 500-1100m



Figure 17: LF001 geophysical pseudosection

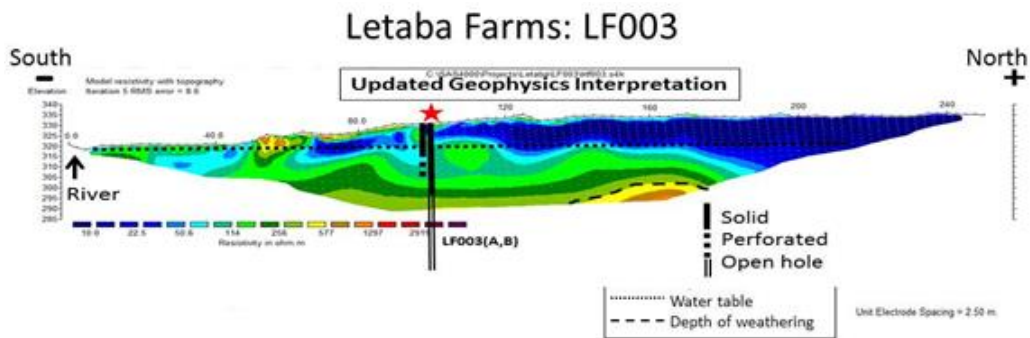
Letaba Farms: LF002



- Runs perpendicular to river channel
- A relatively flat water table
- Proposed borehole drilling location at ± 100 m.



Figure 18: LF002 geophysical pseudosection

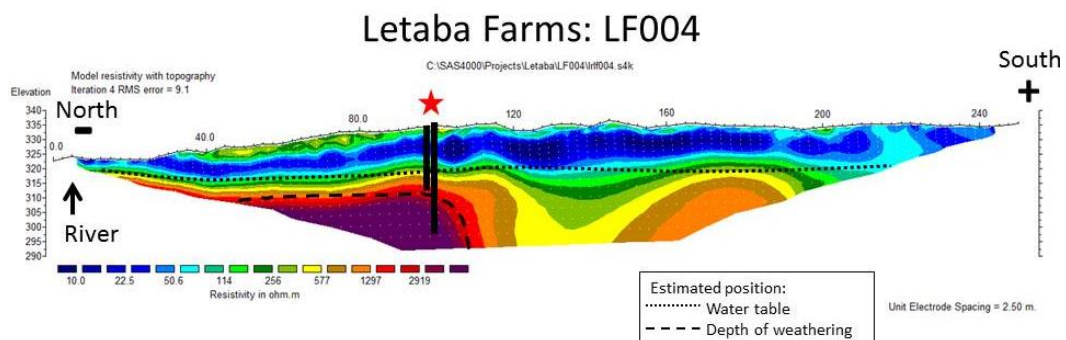


- Runs perpendicular to river channel
- Deep weathering (>25m)
- Proposed borehole drilling location at ± 100m (at edge of farm).



Initially it was assumed that there was a deep water table at around 30m. However, since the boreholes have been drilled it has been verified that it was in fact a shallow water table at around 11m which happens to be the level of the water in the adjacent Letaba River about 100m away.

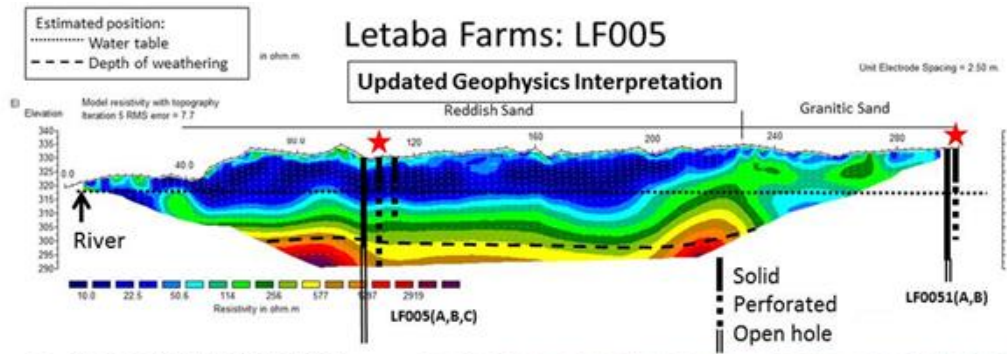
Figure 19: LF003 geophysical pseudosection



- Runs perpendicular to river channel (from north to south)
- Shallow weathering (± 10m) closer to river
- Proposed borehole drilling location at ± 100m.



Figure 20: LF004 geophysical pseudosection

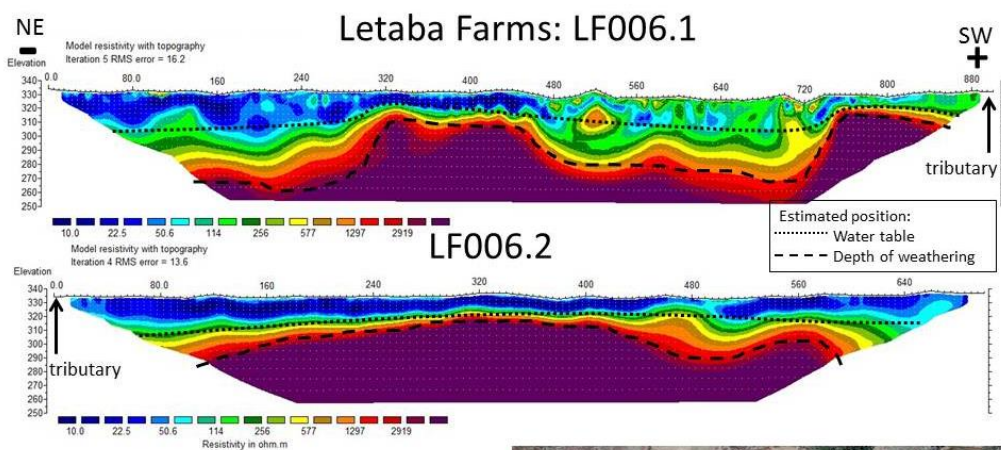


- Runs perpendicular to river channel (north to south)
- Groundwater flow direction towards the river
- Red sands up to roughly 230m; likely river deposition on floodplains.
- Typical granitic soils from 240m onwards.
- Proposed borehole drilling location at ± 110m (at edge of farm)



Initially the water table was assumed to be at a depth of about 25m. After the boreholes were installed, the water table has been verified at a depth of 12m (LF005A,B,C) and 15m (LF0051A,B). This is, however, a flat water table extending from the river to a distance of about 300m away. In addition, the borehole logs confirm the initial finding that the reddish sands are indeed part of historical river deposition on a floodplain up to roughly 230m with coarse granitic soils beyond 240m from the river. Also, the depth of weathering was slightly deeper than originally assumed.

Figure 21: LF005 geophysical pseudosection



- Runs parallel to river channel (in a south-west direction)
- LF006.1- Deep sands at 0-280m and 470-750m
- LF006.2 – similar floodplain sediment with no distinct structures
- Large tributary to the Letaba intercepts between LF006.1 and LF006.2 at ± 900m



Figure 22: LF006 Geophysical pseudosection

Protected areas

Geophysics surveys were set up in an identical design in the protected area downstream of the farming area. Two transects were surveyed on both sides of the river running in parallel from east to west (red lines) as can be seen in Figure 23. The transect on the northern bank was spaced 2.5 m short and 5 m long; the transect on the southern bank was spaced 5 m short and 10 m long. The blue transects represent surveys that ran perpendicularly to the river. These surveys were spaced 2.5 m short and 5 m long for shallower resistivity profiles (~35 m). The results of these surveys and their interpretations are given from Figure 24 to Figure 29.

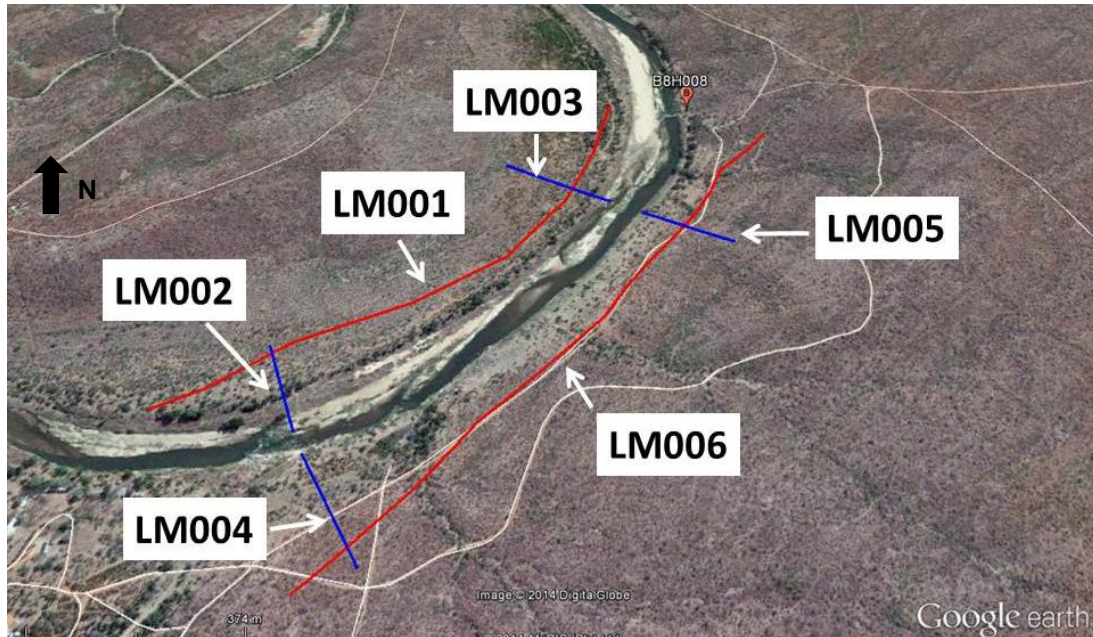


Figure 23: Locality of the geophysics surveys in the protected areas along the Groot Letaba

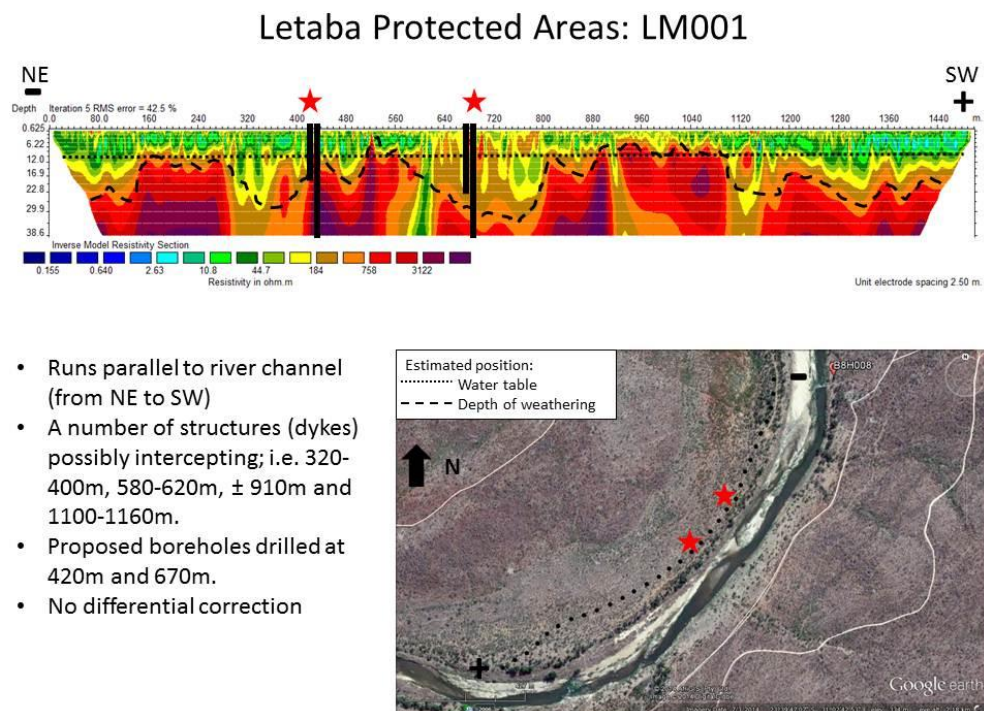
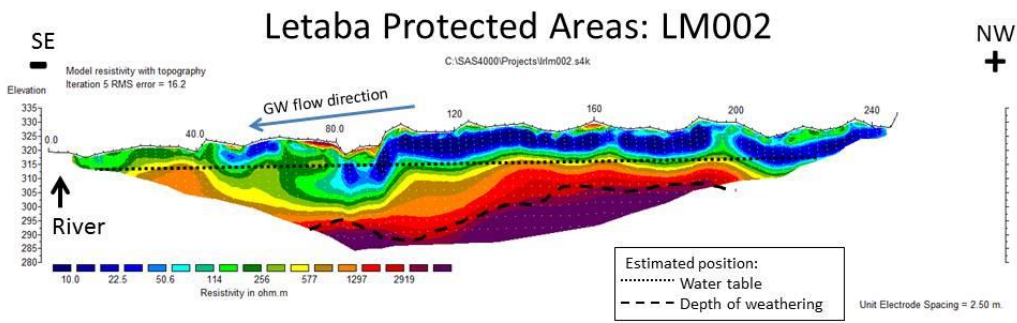


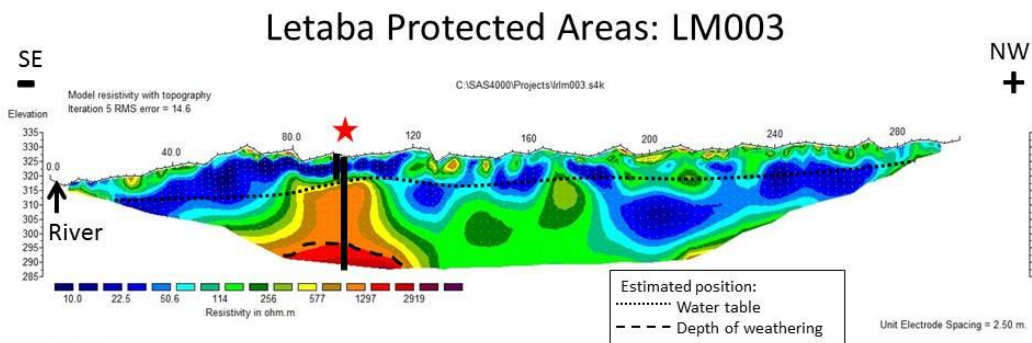
Figure 24: LM001 geophysical pseudosection



- Runs perpendicular to river channel
- Possible groundwater contribution to streamflow from bank.



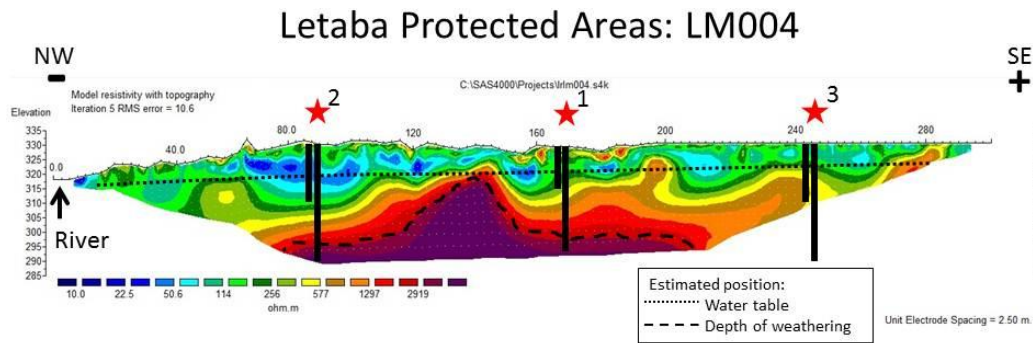
Figure 25: LM002 geophysical pseudosection



- Runs perpendicular to river channel starting in river channel
- Deep weathering after 120m to depths up (>35m)
- Proposed borehole drilling location at ± 100 m



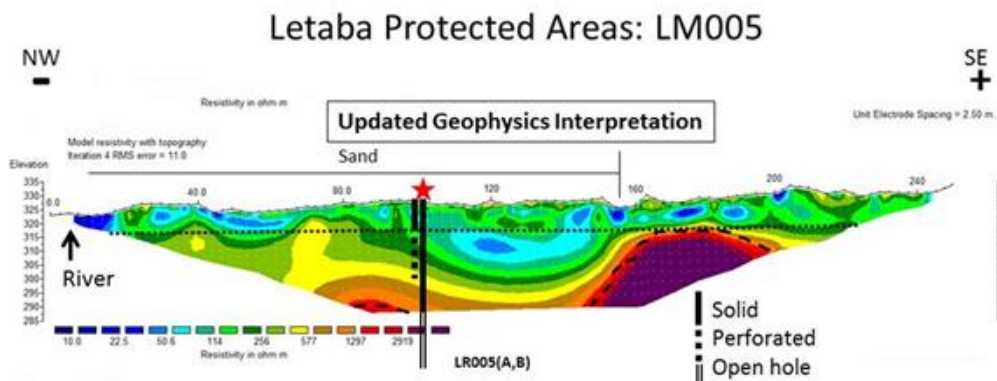
Figure 26: LM003 geophysical pseudosection



- Runs perpendicular to river channel (from north to south)
- Structure identified at $\pm 150\text{m}$ possibly having a damming effect on groundwater flow from the south towards the river.
- Proposed borehole drilling locations at $\pm 170\text{m}$, 90m and 250m (in order of priority)



Figure 27: LM004 geophysical pseudosection

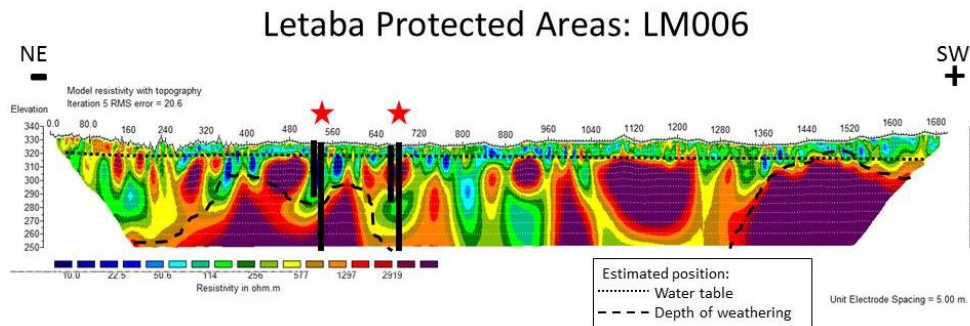


- Runs perpendicular to river channel from river in a SE direction
- Deep sands closer to river; possibly part of alluvial aquifer
- Proposed borehole drilling location at $\pm 100\text{m}$



After drilling boreholes LR005 (A,B), the water table was confirmed to be at roughly the same depth as estimated from the initial geophysics surveys. Likewise, weathering was confirmed at a depth of around 38m where the boreholes were installed. Initial interpretation of the resistivity profiles concluded the presence of deep sands close to river which was thought to be part of an alluvial aquifer. This has been confirmed by the borehole logs with the presence of coarse sands till a depth of about 20m.

Figure 28: LM005 geophysical pseudosection



- Runs parallel to river channel in a South-westerly direction
- Shallow water table estimated
- A number of structures identified; i.e. 240m, 550m, 670m, 800m and between 1270-1350m.
- Both geophysics and aerial imagery suggests presence of more dykes on the southern side of Letaba River (i.e. Letaba Ranch).
- Proposed boreholes to be drilled at 550m and 670m.



Figure 29: LM006 geophysical pseudosection

In addition, magnetic surveys were conducted along the geophysics transects (results in Appendix II). Results correlated well with the ERT data. In most cases, the same intrusions identified during the geophysics surveys were observed in the magnetic surveys, as well as additional details regarding structure width, depth, direction and dip. In general, several structures were identified that struck parallel to the Letaba River with a general strike direction of north-east/south-west (NE/SW). Initial field observations, geophysics and Google Earth™ imagery alluded to a higher density of dyke intrusions downstream in the protected areas than the farming areas. This was confirmed by the magnetic surveys that recorded at least two NE/SW striking structures running parallel to river located north-west of Letaba River and at least one NE/SW striking structure running parallel to river located south-east of Letaba River.

4.12 Study Site Set-up: Groundwater Piezometric Monitoring Network

The drilling of the piezometric borehole network by the DWS, Limpopo Drilling Division, at the Letaba transmission losses study site commenced in June 2015 with the first borehole complete on 4 June 2015. Initially, the drilling campaign focused on the western side of the project area within the farms before moving east to the protected areas. In total 29 boreholes were drilled. The network comprising paired piezometric boreholes drilled into shallow weathered material and deep fractured hard rock is depicted in Figure 30 and detailed in Table 6.

This campaign used the guidance of the geophysics to identify suitable drilling sites within and adjacent to the riparian zone. Furthermore, two boreholes were drilled either side of the dolerite dyke within the main river channel close to the Letaba Ranch gauging weir (B8H008) to characterise the longitudinal hydraulic gradient across this geological structure. The majority if these boreholes were fitted with Solinst™ Levellogger for continuous monitoring and routinely dip-read manually.

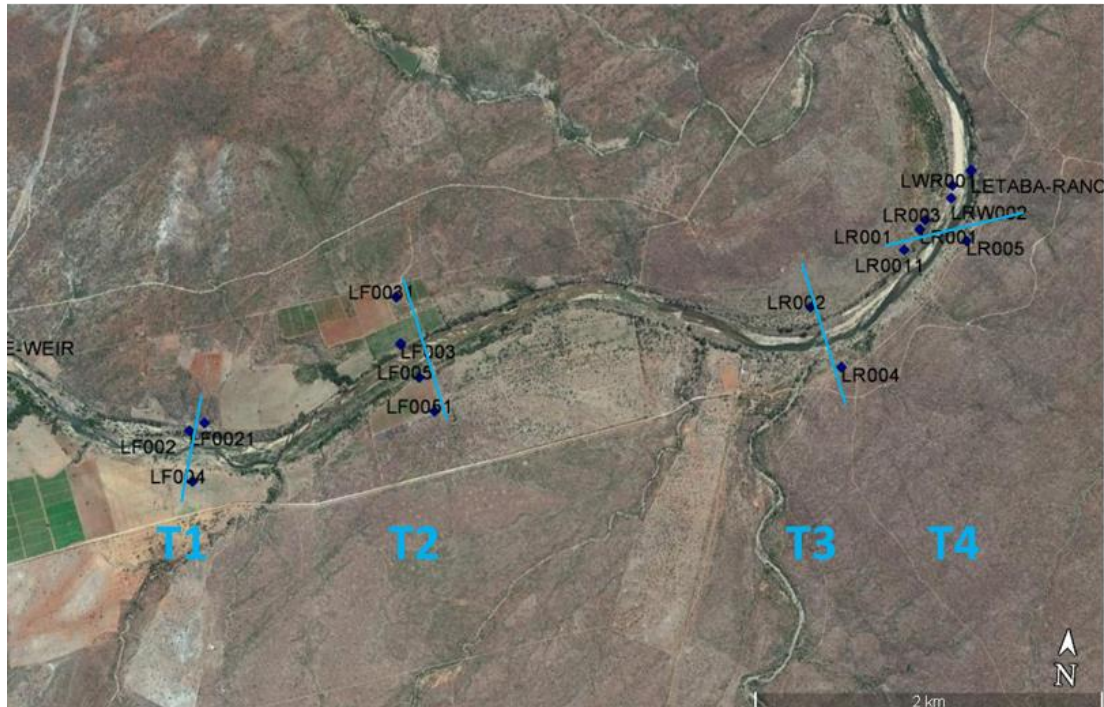


Figure 30: Groundwater piezometric monitoring network at the Letaba River transmission losses study site as of February 2016 (with transect numbers)

Aquifer tests were performed to determine the hydraulic properties transmissivity (T) and hydraulic conductivity (K) of an aquifer. Single-borehole aquifer tests were conducted for this purpose, which included pump and slug tests as described by Kruseman and De Ridder (1994).

The Cooper–Jacob (1946) equation (Equation 1) was applied to determine the T values using a pump test. Slug test data was analysed using the Bouwer and Rice (1976, Equation 2) method to determine T or K .

$$\text{Equation 1} \quad Sc(r, t) = S(r, t) - \frac{S^2(r, t)}{2D}$$

Where:

- $Sc(r, t)$ is corrected drawdown (m);
- $S(r, t)$ is observed drawdown (m); and
- $2D$ is the saturated thickness (m) prior to pumping.

$$\text{Equation 2} \quad K = \frac{rc^2 \ln\left(\frac{R_e}{r_w}\right) 1}{2L} \ln \frac{y_0}{y_t}$$

Where:

- K is the hydraulic conductivity;
- r_c is inside radius of piezometer if water level is above perforated area;
- R_e is the effective radius over which y is dissipated;
- r_w is the horizontal distance from well centre to original aquifer (radius of casing plus thickness of gravel pack); and
- the term $\frac{1}{t} \ln \frac{y_0}{y_t}$ is obtained from the best fitting straight line in a plot of $\ln y$ against t .

Borehole fluid logging was used to provide undisturbed *in situ* borehole parameters of specific conductance, temperature and pH with depth serving as spatial baseline data across the catchment. A Yellow Spring Inc. Sonde multi-parameter *in situ* monitoring device was used for this purpose at two-second intervals in order to record these parameters at ~0.25 m depth intervals.

Table 6: Transmission losses study site borehole drilling information

	Site Name	Site Description	Latitude	Longitude	Altitude (m)	Depth (m)	Solid Casing Depth (m)	Casing height (m)	Date completed	Initial Water Level (m)	Strike (m)	Blow Out yield (l/s)	EC (uS/cm)	
Farms	LF002A	Mabunda/Baloi	-23.674299259	31.005508751	332.816	60	6	0.51	08/10/2015	11.51	11	1		
	LF002 B	Mabunda/Baloi	-23.674297937	31.005498881	332.966	15	6	0.58	10/09/2015	11.78	11	0.4	864	
	LF0021	Mabunda/Baloi in river	-23.674764519	31.004662622	329.940	24	6	0.63	01/11/2015	8.26				
	LF003 A	Maliesa's Farm	-23.669515034	31.016633354	332.840	72	36	0.7	25/05/2015	10.97	15	0.3	1740	
	LF003 B	Maliesa's Farm	-23.669519698	31.016568496	328.683	20	14	0.8	01/06/2015	10.76	12	<0.5	1446	
	LF003C	Maliesa's Farm	-23.669494574	31.016672592	333.985			Dry						
	LF0031 A	Maliesa's Farm	-23.667002914	31.016215720	333.183	60	24	0.22	25/05/2015	12.95	21	3	1518	
	LF0031 B	Maliesa's Farm	-23.667069700	31.016260718	335.904	20	6	0.255	26/06/2015	12.68	19	1	2535	
	LF004 A	Abram's Farm	-23.677412130	31.005063317	337.243	72	24	0.43	22/10/2015	13.385	25	0.5	3413	
	LF004 B	Abram's Farm	-23.677413088	31.005053265	338.883	15	10	0.46	23/10/2015	13.39	12	0.5	3996.00	
	LF005 A	Bongele,s Farm	-23.671245070	31.017841574	328.391	72	30	0.29	04/06/2015	12.33	32	0.5	2800	
	LF005 B	Bongele,s Farm	-23.671308501	31.017884338	330.151	42	6	0.305	09/06/2015	12.15	13	<0.5	3354	
	LF005 C	Bongele,s Farm	-23.671222963	31.017831282	332.179	18	6	0.345	14/07/2015	10.97	13	0.5	3074	
	LF0051 A	Bongele,s Farm	-23.673002919	31.018831950	328.978	54	36	0.54	11/06/2015	14.29	25/40	1.5	1446	
	LF0051 B	Bongele,s Farm	-23.673047435	31.018857310	327.363	30	6	0.36	25/06/2015	14.26	16	1	1393	
reserves	LR001 A	Mthimkhulu	-23.661769123	31.046823055	328.039	60	30	0.46	03/09/2015	10.35	10	0.5	5600 - 7000	
	LR001 B	Mthimkhulu	-23.661764275	31.046805745	330.826	12	6	0.355	08/09/2015	11.93	10		>10 000	
	LR0011 A	Mthimkhulu	-23.662934730	31.045922747	324.700	72	24	0.3	14/09/2015	10.3	10	0.1	>10 200	
	LR0011 B	Mthimkhulu	-23.662913645	31.045961774	331.089	10	6	0.315	15/09/2015	10.15	10		11 100	
	LR002 A	Mthimkhulu	-23.666323042	31.040506466	330.907	42	24	0.43	28/09/2015	10.59	25	0.5	2478.00	
	LR002 B	Mthimkhulu	-23.666330049	31.040511463	329.536	10	6	DRY	01/10/2015					
	LR003	Mthimkhulu. Tercias BH	-23.661232653	31.047126602	326.855	10	4	0.355	26/09/2015	Initially dry		0	0	5595
	LR004 A	Letaba Ranch	-23.669463099	31.042411630	327.109	54	30	0.57	02/12/2015					
	LR004 B	Letaba Ranch	-23.669447874	31.042414074	326.388	24	0	0.505	03/12/2015					
	LR005 A	Letaba Ranch	-23.662268314	31.049551881	327.444	60	42	0.265	09/07/2015	8.95	25/38/50	5.7	1740	
	LR005 B	Letaba Ranch	-23.662269810	31.049502905	328.971	24	6	0.56	13/07/2015	8.94	19	1.8	1580	
	LRW001	Mthimkhulu in river	-23.659273246	31.048663193	316.063	12	0	0.35	26/11/2015	1.23	5	0.2		
	LRW002	Mthimkhulu in river	-23.659964290	31.048604409	317.902	6	0	0.52	30/11/2015	1	4	0.2		
LR006	Mthimkhulu Near camp					75	0		24/11/2015					

The nomenclature used for these boreholes are: Letaba Farms (LF), Letaba Reserves (LR), Letaba River Water (in channel, LRW) followed by a number (e.g. 001). Where two numerals are used, it implies that the borehole was drilled away from the riparian zone (e.g. 0031).

Note also that these boreholes were manually dip-read once a week and that 15 have been equipped with Solinst™ Leveloggers for continuous hourly monitoring.

4.13 Study Site Set-up: Vegetation Characterisation & Total Evaporation

This study proposed the implementation of the Surface Energy Balance System (SEBS) (Su, 2002) model to quantify riparian ET. The implementation of SEBS makes allowance for the relatively timeous and cost-effective quantification of ET, which can prove to be invaluable for OWRM.

Two major challenges that are limiting factors to the modelling of ET using this model are:

- The trade-off between the spatial and temporal resolution of available imagery (Singh et al., 2014).
- The accuracy of the model and the requisite data used to capture hydrological processes (Seneviratne et al., 2010). Previous studies have proposed potential solutions to the abovementioned limitations through the application of downscaling/disaggregation techniques and the integration of scaling factors (Gokmen et al., 2012; Hong et al., 2011; Li et al., 2015; Pardo et al., 2014; Wu et al., 2014).

While these techniques may offer feasible solutions to improve the modelling of ET in SEBS, it is essential that any uncertainty that these techniques introduce to the ET estimate is understood and quantified. For this purpose, a one-sensor eddy covariance system was installed within the study area to validate the ET estimates acquired from implementing SEBS, as well as the proposed techniques mentioned above.

4.13.1 Micrometeorological and energy flux measurements

A measuring tower was installed within the study area to measure energy fluxes, as well as all meteorological variables required to describe the ecosystem of the measuring site in detail. The system was alternated between two positions within the river channel of the Groot Letaba River during the drier low flow periods of the study (June–October 2015 and May–October 2016) between the Mahale (23.669 S; 30.991 E) and Letaba Ranch Weirs (23.658 S; 31.047 E) as illustrated in Figure 31.

During the 2015 field campaign, the measuring tower was first installed at a point upstream of Mahale Weir within the river channel (Site 1) to measure from 17 June to 13 August 2015. The measuring tower was then moved approximately 1.2 km further upstream (Site 2) and measurements were acquired from 21 August to 22 October 2015. The same procedure was repeated for the 2016 field. The measuring tower was first installed at Site 1 and measured from 18 May to 25 July 2016. The measuring tower was then moved approximately 2.0 km further upstream from the 2015 Site 2 position and measurements were acquired from 27 July to 17 October 2016.

The channel morphology remained unchanged within this 3.2 km reach; therefore, the eddy covariance ET (EC_{ET}) estimates acquired at these locations were considered to be characteristic of the morphological river reach.

The measuring tower, which incorporated a one-sensor eddy covariance system, was equipped with a CSAT 3-D sonic anemometer (approximately 1.5 m above the *P. mauritanus*) that measured the sonic air temperature, wind speed and direction. The anemometer was connected to a CR3000 data logger and measurements were taken with a sampling frequency of 10 Hz. The averages of these high frequency measurements (from instantaneous data) were then used to compute a half-hourly sensible heat flux.

Meteorological instrumentation and energy balance sensors were used to provide measurements of nett radiation, a computed soil heat flux density, soil temperature, relative humidity, horizontal wind speed and wind direction, solar radiation and rainfall. Observations were made every 10 seconds and the appropriate statistical outputs were stored on a data logger (CR23 X, Campbell Scientific Inc., Logan, UT, USA) at 10-minute intervals. These values were then used to compute the daily estimates.

The instrumentation consisted of:

- Two Kipp & Zonen NR Lite2 Net radiometers installed at approximately 1.0 m above the bare soil surface and vegetation, respectively, to provide representative and integrated estimates of R_n above these surfaces.
- A Licor LI200X Pyranometer, RM Young wind sentry, and a Texas Tipping Bucket rain gauge (0.1 mm).
- Six Hukseflux HFP01 soil heat flux plates (installed approximately 0.08 m below the soil surface).
- Three pairs of soil temperature averaging probes (installed at 0.02 m and 0.06 m below the surface).
- Two CS616 soil water reflectometers (approximately 0.08 m below the soil surface).

The soil heat flux was determined as the weighted average of the computed soil heat flux for bare soil, vegetation and open water heat flux (Gokool et al., 2016).

The average integrated estimates of R_n above the bare soil and vegetation surfaces, the computed sensible heat flux and the weighted average of the computed soil heat flux were then used to determine the latent heat flux as a residual of the shortened energy balance equation, which is given as:

$$\text{Equation 3} \quad R_n = G_o + H + \lambda E$$

Where:

R_n ;
 G_o ;
 H ; and
 λE .

The rationale for situating the measuring tower at these two locations was to capture the ET associated with distinctive land cover compositions and environmental conditions in a riparian environment. The dominant landcover classes present in this riparian environment within the river channel are *P. mauritanus*, bare soils and open water. Table 7 provides an approximation of the percentage cover for each of the aforementioned land cover classes within each of the sites, with the value for *P. mauritanus* representing percentage canopy cover.

Table 7: Percentage cover of the dominant landcover classes within each of the sites in which the measuring tower was situated

Land Cover class	Site 1	Site 2
<i>P. mauritanus</i>	40%	60%
Bare soils	40%	20%
Open water	20%	20%

There was a higher cover of *P. mauritanus* at Site 2, where livestock (cattle) are allowed to graze within the river channel. Site 2 was situated within a pristine protected area where livestock are prevented from grazing. Although buffalo and elephant graze this area, their densities are significantly lower than the cattle.

The situation of the measuring tower at the 2016 site, which is approximately 2.0 km further upstream from the position of the 2015 Site 2, was due to the removal of an electric fence that previously separated Site 2 from Site 1. Consequently, this area no longer represent a pristine protected area as livestock are no longer prevented from grazing in this region. Therefore, the system was moved to the 2016 Site 2, which had a similar characterisation to the 2015 Site 2.

Changes in environmental conditions during the period of measurement, such as seasonal and climatic changes from winter to summer that influence environmental stress conditions, may have also contributed the higher cover at Site 2. While these two locations are situated within the same

morphological reach, their respective evaporative surfaces are different in their basal and canopy cover, and their soil moisture status. Due to these differences, the situation of the measuring tower at these two locations provides the ideal platform to assess the performance of implementing SEBS for a riparian environment characterised by distinctive land cover compositions and environmental conditions in a semi-arid region.

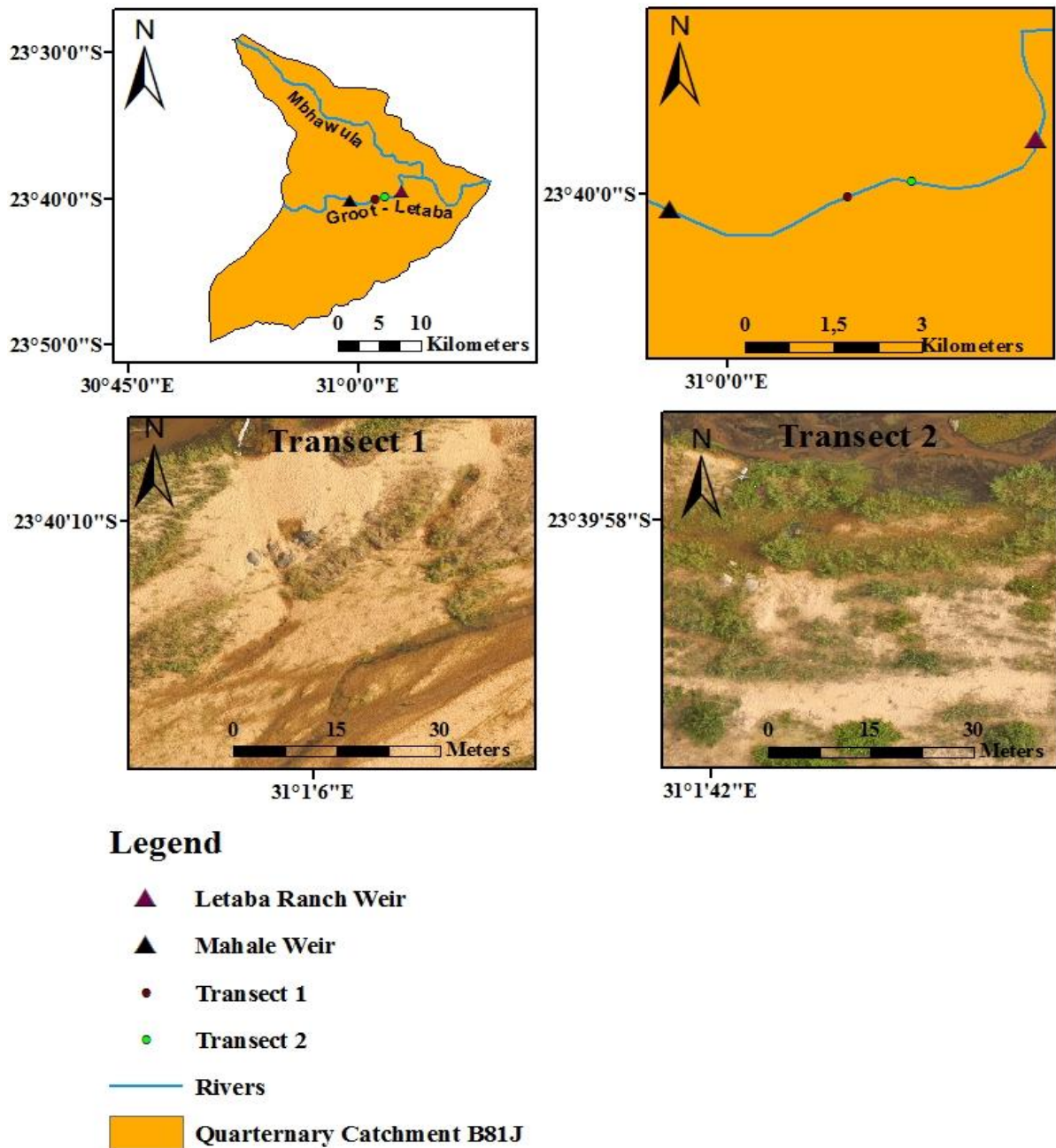


Figure 31: Location of the eddy covariance system and the general land cover distribution for Transect 1 and Transect 2

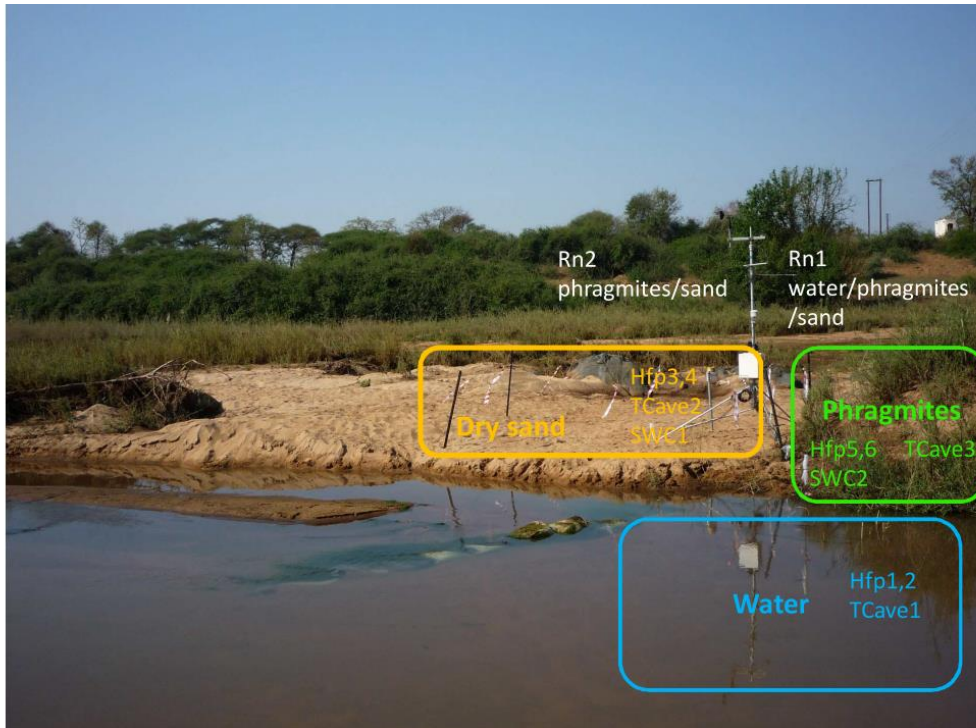


Figure 32: Installation of the eddy covariance system in channel with location of sensors

The weighting of the soil heat flux density was determined as follows for Transect 1:

- 20% water contribution.
- 40% for bare soil.
- 40% for vegetation.

The weighting of soil heat flux density was determined as follows for Transect 2:

- 20% water contribution.
- 20% for bare soil.
- 60% for vegetation.

The percentage contribution used for the aforementioned weighting was determined from a visual assessment of the study site through a field survey and using imagery captured from a DJI Phantom 3 Advanced unmanned aerial vehicle (UAV). These images were captured at a 5 cm resolution by an on-board 12 megapixel DJI camera at an altitude of 120 m above ground level. An orthophoto was then created using the Open Drone Map Software (<https://github.com/OpenDroneMap/OpenDroneMap>) as can be seen in Figure 33.

The EC_{ET} measurements taken during these periods were used to validate the ET estimates derived from satellite earth observation data. Thirteen Clear-sky Landsat (7 and 8) Level 1 Geotiff products (16-day temporal resolution) as well as 114 MODIS Level 1 B Terra images (daily temporal resolution) from 17 June to 22 October 2015 were selected to estimate ET using the SEBS model.

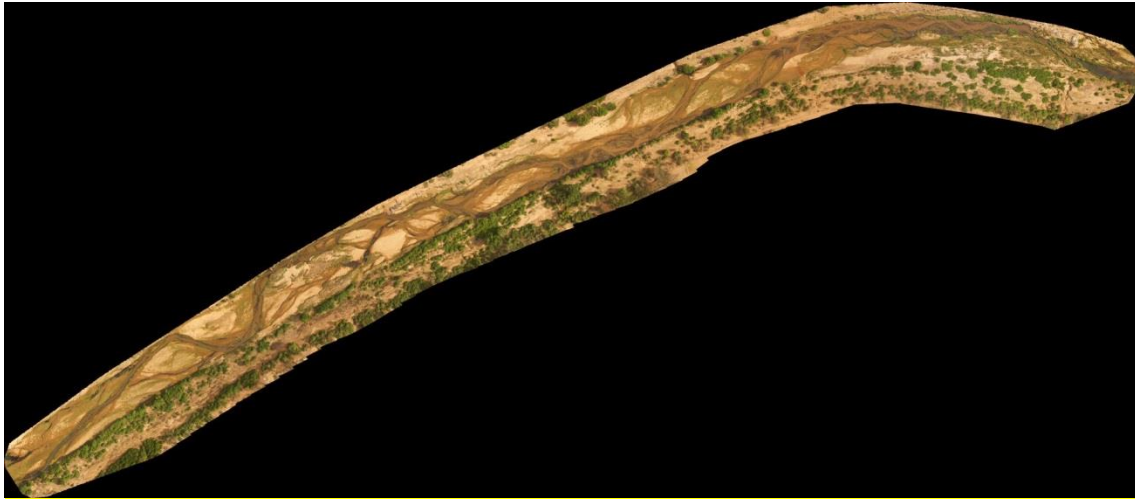


Figure 33: A UAV survey conducted of the Letaba River study site around the eddy covariance installation area during November 2015

4.13.2 The simplified SEBS

The SEBS model was selected for application in this study as it has been extensively applied for the estimation of regional fluxes and ET. The SEBS model has been shown to provide accurate estimates of ET and terrestrial heat fluxes (Jarmain et al., 2009; Yang et al., 2010; Zhuo et al., 2014). The principle is that SEBS estimates atmospheric turbulent fluxes using both satellite earth observation and spatially representative meteorological data (Liou & Kar, 2014; Pardo et al., 2014; Su, 2002).

The model consists of a suite of tools to estimate land surface physical parameters from spectral reflectance and radiance (Su et al., 1999), a comprehensive model for the approximation of the roughness length of heat transfer (Su et al., 2001) and an innovative procedure for the estimation of the evaporative fraction on the basis of the energy balance at limiting cases (Su, 2002). The model applies the shortened surface energy balance equation to partition the available energy into sensible and latent heat flux density. The daily ET is estimated, assuming the evaporative fraction remains constant throughout the day (Su, 2002).

SEBS was therefore applied in this study using satellite earth observation data acquired from open access imagery derived from Landsat (7 and 8) and MODIS to estimate ET for the riparian zone along the Letaba River. The spatial resolution of the SEBS ET estimate is dependent on the spatial resolution of the thermal band (Alidoost et al., 2015; Su, 2002); therefore, the study was limited to the spatial resolution of these open access products.

Moderate spatial resolution (MSR) imagery acquired by Landsat (7 and 8) provides thermal bands at a spatial resolution of 60 m and 100 m, respectively, which are resampled to 30 m and possess a temporal resolution of 16 days (USGS, 2015). However, data can be obtained with an eight-day gap between consecutive data acquisitions, if data from both Landsat 7 and 8 is available and used (USGS, 2015). Coarse spatial resolution (CSR) imagery acquired by MODIS provides thermal bands at a spatial resolution of 1 km at a daily temporal resolution.

4.13.3 SEBS modifications

According to Seneviratne et al. (2010), satellite-based ET estimation approaches often overestimate ET in areas of arid and semi-arid climatic regimes in which the availability of water is limiting ET. Studies undertaken by Timmermans and Meijerink (1999), Lubczynski and Gurwin (2005) and Van der Kwast et al. (2009) in these environments, have shown that satellite-based ET estimation models may overestimate ET in the magnitude of $0.50 \text{ mm}\cdot\text{d}^{-1}$ to $3.00 \text{ mm}\cdot\text{d}^{-1}$, as a result of an underestimation of the sensible heat flux (H).

The inferior performance of these models can largely be attributed to their inability to adequately account for the influence of soil moisture and physical characteristics of vegetation during the estimation of fluxes (Gokmen et al., 2012; Pardo et al., 2014; Wu et al., 2014; Li et al., 2015). The influence of soil moisture and vegetation on fluxes are implicitly encompassed in input variables, which ignore their direct impact on ET estimates (Gokmen et al., 2012; Li et al., 2015; Wu et al., 2014). While the aforementioned approach may be suitable for environmental settings where the available energy is limiting ET (such as in the high latitude regions), it may prove to be inadequate where water availability is the principle limiting factor to ET (Seneviratne et al., 2010). Hence, satellite-based ET modelling necessitates an improvement for the estimation of fluxes for different land covers experiencing conditions of water stress (Wu et al., 2014).

In this particular study, the $SEBS_0$ formulation was first implemented and validated against EC_{ET} measurements during the dry season in 2015 (17 June to 13 August 2015) to assess if the conditions experienced in the study area would influence the performance of the model. The results of these investigations indicated that comparisons between the $SEBS_0$ formulation and EC_{ET} measurements were generally poor – especially for an environmental setting dominated by sparse vegetation coverage and drier soils (Site 1). To address this limitation, the integration of a scaling factor that can be applied to the evaporative fraction estimated in SEBS was proposed. This scaling factor can be computed from *in situ* measurements of the Food and Agriculture Organization (FAO) Penman–Monteith reference evaporation and ET, which is given as:

$$\text{Equation 4} \quad ESF = \frac{ET_a}{ET_{ref}}$$

Where:

ESF can be defined as an environmental stress factor (Allen et al., 2005);

ET_a is the ET measured *in situ* ($\text{mm}\cdot\text{d}^{-1}$); and

ET_{ref} is the grass reference evaporation determined using the FAO Penman–Monteith reference evaporation approach ($\text{mm}\cdot\text{d}^{-1}$).

Based on the approach detailed in Pardo et al. (2014), the ESF can be used to adjust the evaporative fraction estimated in SEBS to obtain a new evaporative fraction. Once the new evaporative fraction has been determined, it can be applied in conjunction with the Rn and Go previously determined in $SEBS_0$, to estimate the daily ET.

4.13.4 Spatial downscaling of satellite-derived total evaporation

In order to obtain a complete daily MSR ET record for the riparian zone along the Letaba Rive, for the measurement study period at a MSR, a combination of two approaches were followed:

- An output downscaling with linear regression downscaling approach (Hong et al., 2011).
- An infilling approach using $K_{c_{act}}$ (Santos et al., 2008) and Penman–Monteith reference ET to infill missing data.

The application of downscaling procedures is used to facilitate the amalgamation of the advantages of high temporal resolution (HTR) imagery with MSR imagery. Bierkens et al. (2000) and Liang (2004) define downscaling as the increase in spatial resolution resulting from the disaggregation of the original data set. Downscaling procedures attempt to restore spatial variations at a particular scale by assuming the values at the larger scale represent the average of the values at the smaller scale (Bierkens et al., 2000).

The procedure results in an increase in the number of pixels within an image, with the output of each pixel representing a smaller area (Hong et al., 2011). According to Ha et al. (2013) and Spiliotopolous et al. (2013), downscaling procedures can be broadly classified into two categories, namely:

- Scale-based traditional downscaling.
- Pan sharpening or data fusion techniques.

In this study, a relatively simplistic downscaling procedure predicated upon the linear regression [discussed in Hong et al. (2011)] was tested to provide total evaporation estimates at an MSR with HTR. It has been shown by Hong et al. (2011) and Spiliotopolous et al. (2013) to provide results within acceptable limits.

The regression approach disaggregates CSR imagery by applying a linear regression between two CSR images to a preceding or subsequent MSR image covering the same area of interest (Hong et al., 2011). It is assumed that the linear relationship between CSR imagery remains valid between MSR imagery (Hong et al., 2011).

In order to create a daily continuous MSR total evaporation data set for the period of investigation in this study, a linear regression was initially applied between two consecutive MODIS total evaporation estimates generated (M_1 and M_2) using the SEBS model to obtain regression coefficients. These coefficients were then applied to the Landsat total evaporation image (L_1) generated using the SEBS model for the same date as the first MODIS total evaporation image (M_1). This was done in order to generate a total evaporation image (L_2) at the Landsat spatial resolution for the same date as the subsequent MODIS total evaporation image (M_2).

This procedure was repeated; however, the linear regression was then performed between the MODIS total evaporation image for Day 1 (M_1) and the MODIS total evaporation image for Day 3 (M_3) to obtain regression coefficients. These coefficients were then applied to the Landsat total evaporation image (L_1) obtained for the same date as the first MODIS total evaporation image (M_1). This was done in order to generate a total evaporation image (L_3) at the Landsat spatial resolution for the same date as the subsequent MODIS total evaporation image (M_3).

This procedure was systematically repeated until a new Landsat Level 1 GeoTIFF product was available. Once this product was available, the abovementioned procedure was repeated. Figure 33 and Figure 34 provide schematic representations of the abovementioned process to better understand how the daily continuous MSR total evaporation data set was generated and also gives an example of a downscaled total evaporation map generated for this study.

Bhattarai et al. (2015) note that the procedures discussed in Hong et al. (2011) have not yet been applied to obtain a seasonal continuous MSR total evaporation data set. Therefore, the results of the investigations conducted in this study can provide valuable insight on the suitability of applying the linear regression approach to generate continuous MSR total evaporation data set on a daily time step.

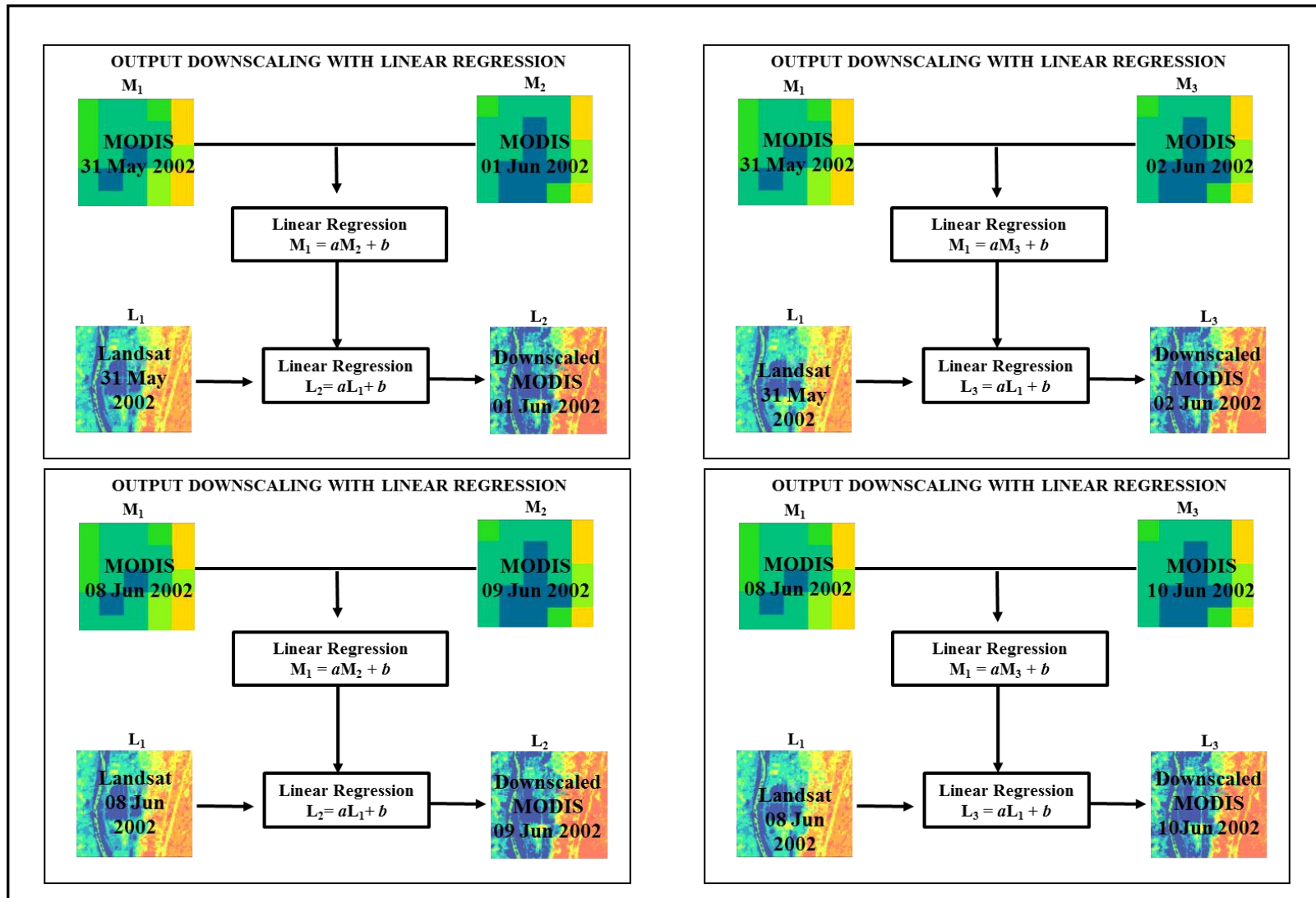


Figure 34: Schematic of the downscaling with linear regression approach methodology to create a daily continuous MSR total evaporation data set, where a and b are the linear regression coefficients and L_2 and L_3 are the subsequent spatially downscaled total evaporation maps at the Landsat resolution (adapted from Hong et al., 2011)

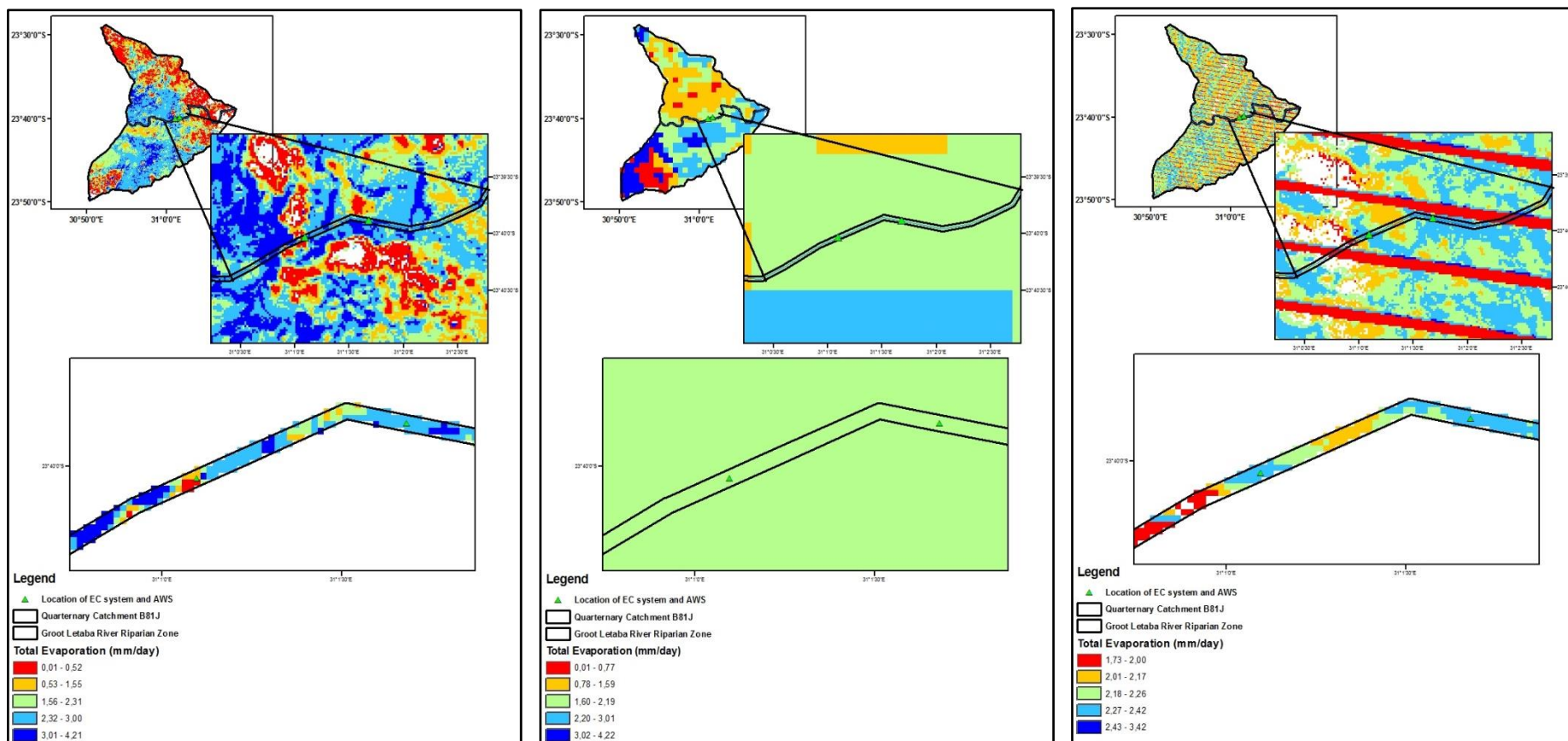


Figure 35: An illustration of SEBS total evaporation derived using MODIS and Landsat data for 7 July 2015: a) SEBS total evaporation map derived using Landsat, b) SEBS total evaporation map derived using MODIS, and c) Downsampled total evaporation derived using linear regression

4.13.5 Determining the distribution of vegetation biomass and identifying land uses

A vegetation/vegetative index can be used to quantify the biomass and/or the plant vigour within a pixel of a satellite image. The index may be computed using various satellite reflectance bands that are sensitive to biomass and plant vigour. One of the most commonly applied vegetation indices is the normalized difference vegetation index (NDVI) (Ramsey et al., 2004).

The NDVI has been adopted to analyse satellite earth observation data *viz.* to assess if the region/feature being observed contains actively growing vegetation or not (Ghorbani et al., 2012). The behaviour of plant species across the electromagnetic spectrum is understood fairly well. As a result, NDVI information can be derived from satellite earth observation data by analysing the satellite bands that highlight the greatest responses between vegetation and radiation. The satellite bands that are the most responsive to the interactions between vegetation and radiation are the red and near-infrared (NIR) bands of the electromagnetic spectrum (Ghorbani et al., 2012).

The reflectance of radiation in the visible portion of the electromagnetic spectrum (400–700 nm) is low due to the absorption of light energy by chlorophyll in actively growing green vegetation. The reflectance of radiation in the NIR portion of the electromagnetic spectrum is high due to the multiple scattering of light by plant leaf tissues (Zhang et al., 2011).

The algorithm used to derive the NDVI is given as:

$$\text{Equation 5} \quad NDVI = \frac{(\text{NIR Band} - \text{Red Band})}{(\text{NIR Band} + \text{Red Band})}$$

The difference between the red and NIR bands provides an indication of the amount of vegetation present in the region/feature being observed. The greater the difference between the red and NIR bands, the greater the amount of vegetation present and vice versa (Ghorbani et al., 2012).

Numerous vegetation studies have used the NDVI for wide ranging applications *inter alia* estimating crop yields, pasture performance, vegetation health and biomass (Muskova et al., 2008; Petorelli et al., 2005). Furthermore, the NDVI technique generally allows for the identification of various features within a satellite image such as areas that possess dense vegetation or has no vegetation coverage (bare soil and rock), water bodies and ice.

The identification of a feature is based upon the NDVI value it possesses within the range of –1 to 1 (Holme et al., 1987). Table 8 provides a general representation of the features that may be identified in an image based upon their respective NDVI values.

Table 8: Identification of features within a satellite image based upon their respective NDVI values

NDVI Value	Feature
NDVI < 0	Water body
0.1 < NDVI < 0.2	Bare soil
0.2 < NDVI < 0.3	Sparse vegetation cover
0.3 < NDVI < 0.5	Moderate vegetation cover
NDVI > 0.6	Dense vegetation cover

The NDVI was calculated for the region between Mahale and Letaba Ranch Weirs utilising the red and NIR bands of a Landsat 8 image obtained for 21 June 2015. These values were then used in conjunction with knowledge of the study area to identify the density distribution of vegetation and to broadly classify land use. These are represented in Figure 36. It should be noted that this classification is a very simplistic representation of the land uses that are present in the study area.

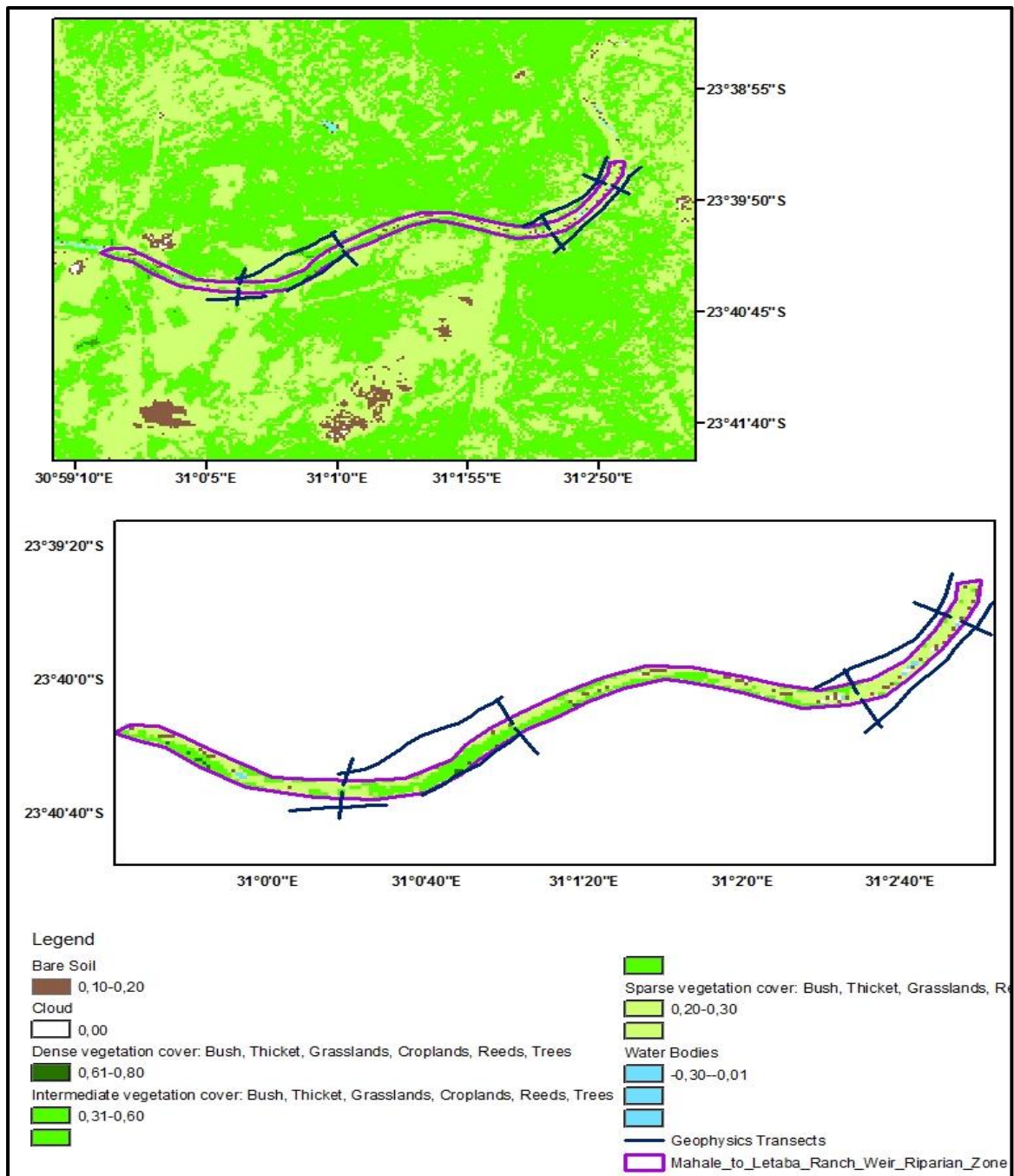


Figure 36: Distribution of vegetation biomass and classification of land uses based upon NDVI for the region between Mahale and Letaba Ranch Weirs on 21 June 2015

Although Landsat 8 data is provided at a spatial resolution of 30 m, classifying land use and land cover at this resolution may be too broad. It can be difficult to determine the distribution of individual species without detailed *a priori* knowledge regarding the location and distribution of individual plant species observed in the satellite image. Furthermore, the presence of cloud within Figure 36 may have contributed to an incorrect identification of features. The land uses represented in Figure 36 were broadly classified into five categories, including:

- Water bodies.
- Bare soil.
- Sparse vegetation cover consisting of shrubs, thicket, reeds and grassland.
- Moderate vegetation cover consisting of shrubs, thicket, reeds, croplands, grassland and trees.
- Dense vegetation cover consisting of shrubs, thicket, reeds, croplands, grassland and trees.

Each component of the total evaporation process (i.e. evaporation of intercepted water, soil water evaporation and transpiration) is either directly or indirectly affected by the type, distribution and density of vegetation in a specified area. Therefore, the classification of vegetation species and distribution facilitates an improved understanding of total evaporation estimates and may hold added significance when other factors which influence total evaporation are relatively stable.

4.13.6 Riparian vegetation water use

The water use of riparian vegetation was also characterised for selected riparian species during the study period using stable isotopes to determine their potential utilisation of groundwater, surface water or soil water. These were collected at the locations in

Sampling procedure

Twig, soil, stream and groundwater samples were collected on three sampling occasions during the 2016 dry season (May, August and October), which are representative of the late autumn, late winter and mid spring seasons, respectively in the study area. During this period (from May to October), the study area usually experiences drier conditions and low flows. Twig samples of mature wood approximately 0.3 cm to 1.0 cm in diameter and 4.0 cm to 7.0 cm in length were collected from the 46 individual trees. These samples were collected from randomized locations from each tree and the bark was removed immediately. The samples were then stored in small airtight glass vials. Soil samples at depths of 30 cm, 60 cm, 100 cm and 140 cm were collected concurrently with the twig samples. The soil samples were obtained using a hand auger. They were then transferred and sealed into airtight 500 ml plastic bottles.

Stream samples from the Groot Letaba River were collected at Sampling Points 1, 3 and 6 and stored in airtight 500 ml plastic bottles. Groundwater samples were collected from five boreholes situated adjacent to the active river channel at Sampling Points 1, 3, 4 and 5, as well as from a borehole situated within the active river channel at Sampling Point 6.

These samples were then stored in airtight 500 ml plastic bottles. The stream and groundwater samples were later transferred into small glass vials. The various samples collected in field were then stored in a fridge prior to analysis over the following days.

In addition to the aforementioned samples, 13 rainfall samples from 15 November 2015 to 19 May 2016 were collected and analysed. The $\delta^2\text{H}$ and $\delta^{18}\text{O}$ values for these precipitation events were then used to construct a local meteoric water line (LMWL) for our study site. The $\delta^2\text{H}$ and $\delta^{18}\text{O}$ values for twig, soil, stream and groundwater were then plotted and compared relative to this LMWL.

The ^2H and ^{18}O contents of rainfall, stream and groundwater samples were measured using a Los Gatos Research DLT-100 Liquid Water Isotope Analyser. Water from the xylem and soils was extracted using an open manifold system that facilitated removal of non-condensable gases and potential organic contaminants. The ^2H and ^{18}O contents of the xylem water and soil water were measured using a Picarro L1102-i CRDS Analyser (Picarro, Santa Clara, California, USA). The overall analytical precision of the spectrometers was less than 2 permil (0.002%) for ^2H and less than 0.3 permil (0.0003%) for ^{18}O .

The ^2H and ^{18}O of the various samples (^2H and ^{18}O) were expressed in delta notation relative to the Vienna Standard Mean Oceanic Water (VSMOW), as:

$$\text{Equation 6} \quad \delta = \left(\frac{R_{\text{sample}}}{R_{\text{standard}}} - 1 \right) 1000$$

Where:

δ (‰) represents the deviation from the VSMOW (can be positive or negative depending if the isotopic concentration of the sample is enriched or depleted relative to the source);

R_{sample} and R_{standard} are the ratio of the heavy to light isotopes ($^2\text{H}/^1\text{H}$ and $^{18}\text{O}/^{16}\text{O}$) in the sample and the standard, respectively.

The stable isotope mixing model package in R

The Simmr Bayesian mixing model, which is freely available, was used to identify the potential sources of water used by the vegetation in the study area. According to Ma and Song (2016), there has been limited application of Bayesian mixing models to determine the water uptake characteristics of plant species. However, these models have several advantages over conventional linear mixing models such as being able to quantify the proportional contribution of water sources to the plant, accounting for uncertainties associated with the sources, and allowing for the input of isotope data from multiple sources.

In this particular study, the potential sources of water used by the vegetation was considered to be soil water at the different sampling depths, groundwater and stream water. This decision was based on the $\delta^2\text{H}$ and $\delta^{18}\text{O}$ relationship identified for each of the xylem samples.

The Simmr package has been designed to solve mixing equations for stable isotope data using a Bayesian statistical framework (Parnell & Inger, 2016). The package requires three sets of input data as a minimum to determine the proportions of water used from a particular source, which includes (Parnell and Inger and Inger, 2016):

- The mixture ($\delta^2\text{H}$ and $\delta^{18}\text{O}$ of the xylem water).
- The mean $\delta^2\text{H}$ and $\delta^{18}\text{O}$ for the various sources.
- The standard deviations of $\delta^2\text{H}$ and $\delta^{18}\text{O}$ for the various sources.

According to Parnell and Inger (2016), any number of isotopes and observations can be used during the implementation of Simmr.

The package implements a Markov Chain Monte Carlo function to repeatedly estimate the proportions of the various sources in the mixture and determine the values that best fit the mixture data (Parnell & Inger, 2016). The initial estimates obtained from this procedure are usually poor and are discarded as part of the burn-in phase (initial phase). The subsequent iterations are then used to determine the best estimates of the source proportions according to the data and model. Convergence diagnostics can then be used to check if the model has run correctly. Parnell and Inger (2016) note that it can take thousands of iterations to depart from the initial guesses.

5 RESULTS

5.1 Hydrogeological Characterisation

Two rounds of fluid logging were conducted across the groundwater piezometric network; the first being November 2015 (prior to the onset of extreme drought wet season conditions), which were followed in August 2016 (thus following the rain season, of which there was only one significant event in March 2016). These will be described on a transect by transect basis (Figure 30).

5.1.1 Transect 1

LF002A (farms, regional, deep)

There is almost no difference in the temperature profile of LF002A (Figure 37), although there is a steady decrease in both profiles with depth. This takes place because of the inflow of fresh water from the top to the bottom of the borehole. The inflow occurs because boreholes will form a preferential pathway for water percolating to and through the groundwater system, thus the warm water from the surface will cool down as it moves to the bottom of the borehole. There is also an increase in the electrical conductivity between the periods, which is expected due to extremely low rainfall input and evaporation. The result therefore is very little water reaching the saturated zone of the aquifer. The electrical conductivity also increases to the bottom of the borehole as the heavier salt water and debris from pumping settle at the bottom. The fractures are again indicated at a similar depth of 30 m, 35 m and 45 m with a sharp and sudden increase in conductivity.

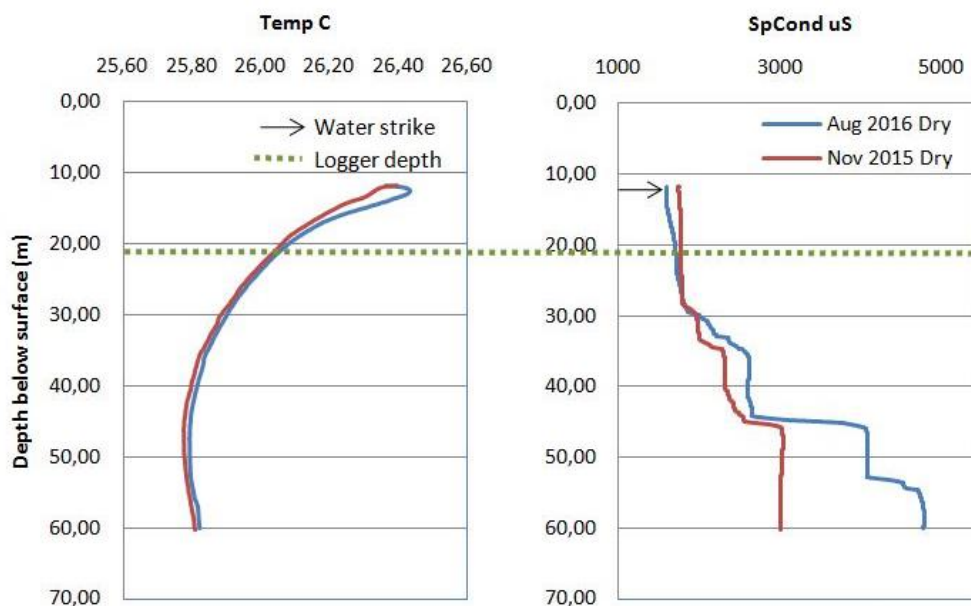


Figure 37: Fluid log of LF002A

LF002B (farms, regional, shallow)

LF002B (Figure 38) shows a slight increase with temperature in the dryer and warmer conditions of August 2016. Once again it indicates an inflow of fresh water at the top, similar to the deeper borehole LF002A. A small fracture is again indicated through the sudden increase in electrical conductivity and the small temperature change at 12.8 m where warmer water flows into the borehole.

LF002A and LF002B are located on the fringes of the riparian zone located on the northern bank of the farms. They are situated on a transect that shows a loss to the northern bank from LF004A/B to LF0021 to LF002A/B (Transect 1), thus we expected to observe flow in these boreholes.

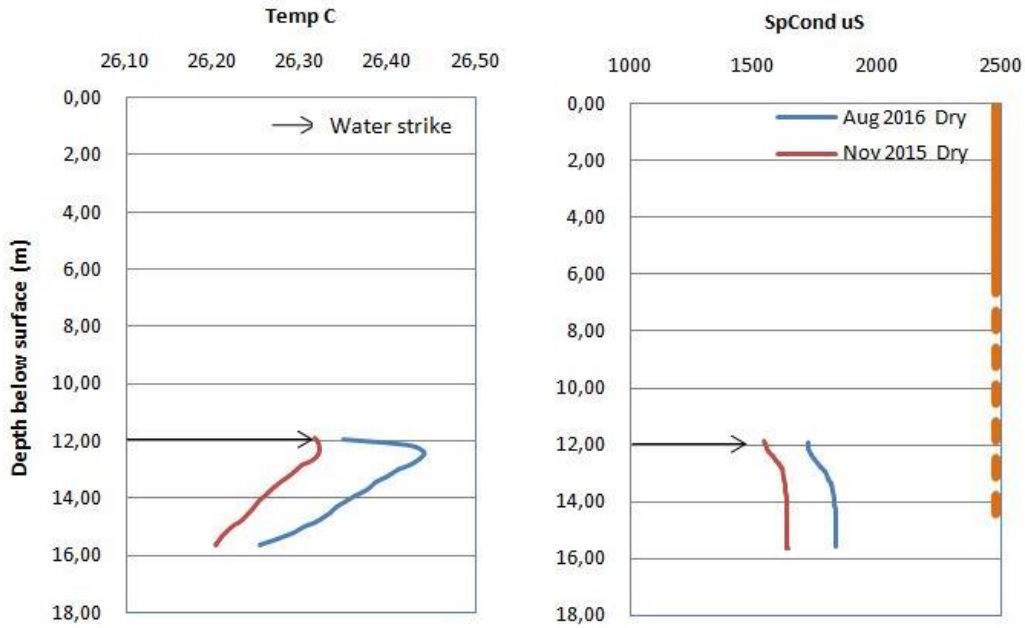


Figure 38: Fluid log of LF002B

LF0021 (Farms, riparian, shallow)

The temperature within borehole LF0021 (Figure 39) is warmer in August 2016. The temperature also decreases with depth to around 18 m where it stabilises, indicating increased flow within the aquifer. This indicates that more water is moving through the unconsolidated zone and into the borehole, especially after the March 2016 flood and rainfall events. In addition, the electrical conductivity displays an expected increase in August from the dryer and warmer conditions. Numerous small fractures are indicated by the electrical conductivity at 13 m, 15 m, 18 m and 21 m.

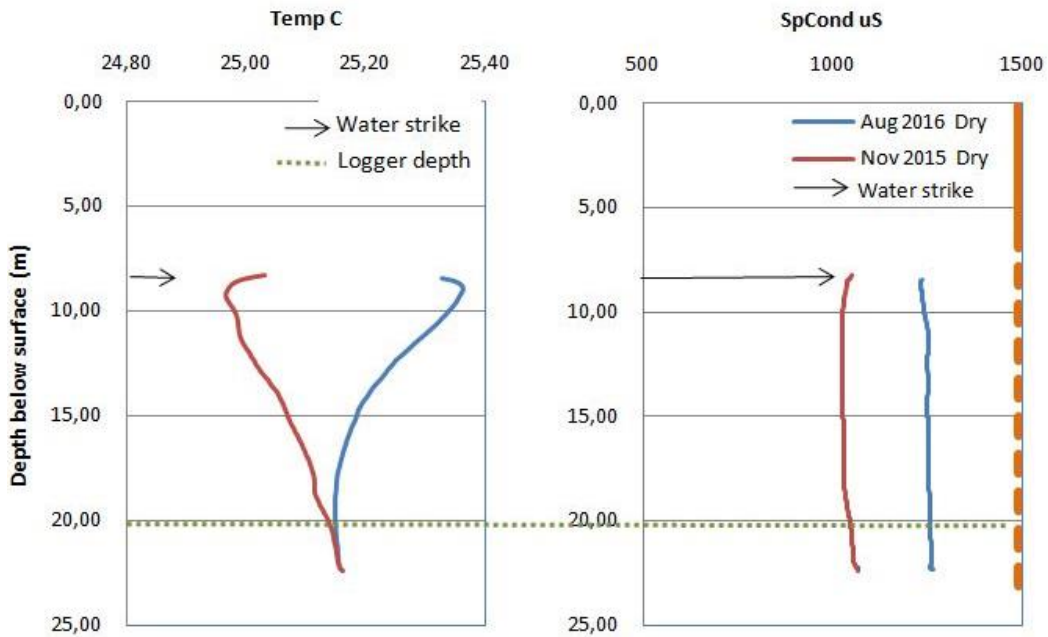


Figure 39: Fluid log of LF0021

LF004A (farms, regional, deep)

The temperature displays a steady increase with depth in both periods (Figure 40). While the temperature profile is similar between the two periods, the conductivity displays a sharp increase after 49 m. This indicates that there is significant inflow occurring from water flowing through the unconsolidated zone, but rather from numerous small fractures within the deep consolidated aquifer. The temperature will thus only increase to the bottom where these fractures bring in warmer and high electrical conductivity water. The end of the solid casing is displayed at 24 m with a sharp increase in conductivity. The numerous small fractures are indicated by the increase in temperature and electrical conductivity at 35 m, 53 m, 64 m and 67 m.

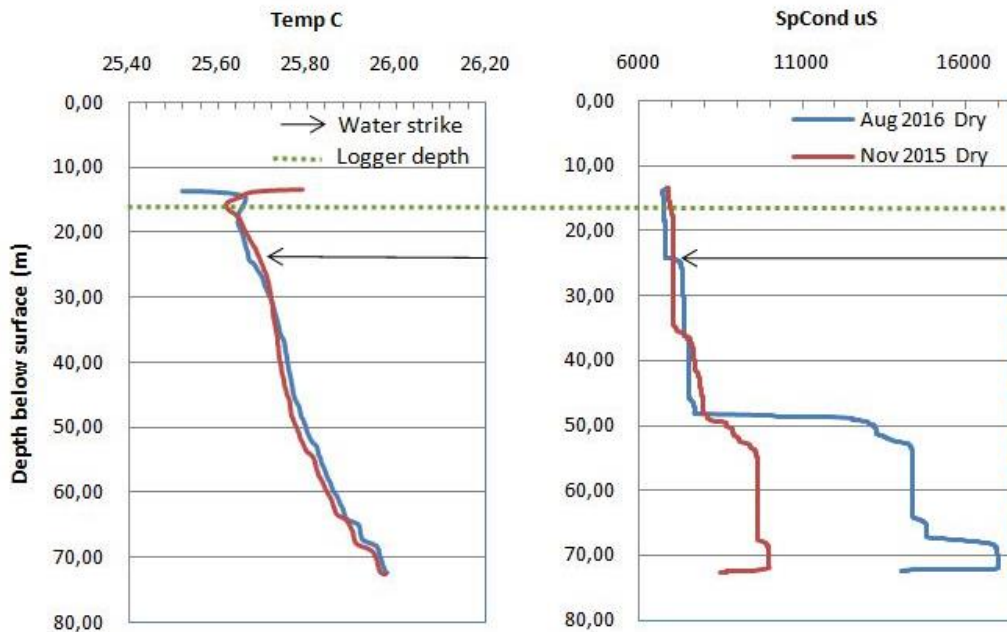


Figure 40: Fluid log of LF004A

LF004B (farms, regional, shallow)

LF004B (Figure 41) shows an increase in temperature with depth in the dryer August 2016 period, which contrasts the other shallow boreholes, namely, LF003B and LF002B. This indicates that fresh warm water is not flowing in from the unconsolidated zone, but rather from a fracture – similar to the deep borehole LF004A. The electrical conductivity is surprisingly high within this borehole. It is lower in the dry season than in the wet season, which again contrasts with the boreholes described previously. The fracture also surprisingly indicates low electrical conductivity water flowing in at 15 m. The reason for this is that the fracture could possibly be influenced by water from agricultural activities or a high electrical conductivity profile from contamination during drilling.

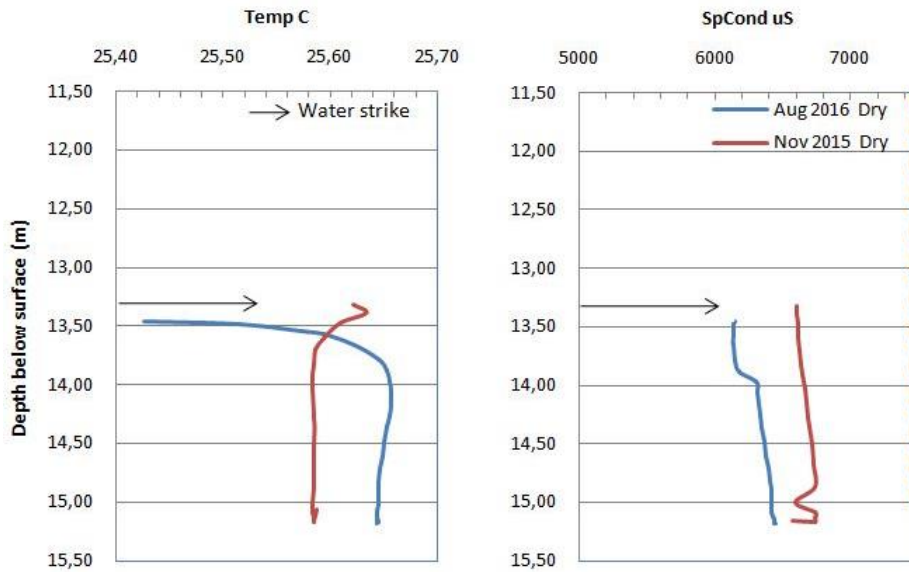


Figure 41: Fluid log of LF004B

5.1.2 Transect 2

LF0031A (farms, regional, deep)

LF0031A displays a similar profile in conductivity and temperature between the two periods (Figure 42). The temperature shows an increase with depth indicating that no flow is coming from the unconsolidated zone but rather from a fracture, which is similar to LF004A. At 20 m, there is a sudden increase in temperature and electrical conductivity, although this is still located within the solid casing, thus indicating a leak in backfill. At 25 m, there is another increase in temperature and electrical conductivity that is located exactly where the solid casing stops. This indicates the end of the solid casing as the restricted flow within the solid casing will lower the temperature. The electrical conductivity will also be lower as the only movement will be heavier salt water moving down the borehole. At 26 m, a fracture is indicated by the increase in electrical conductivity and temperature as warm high electrical conductivity water enters through the fracture.

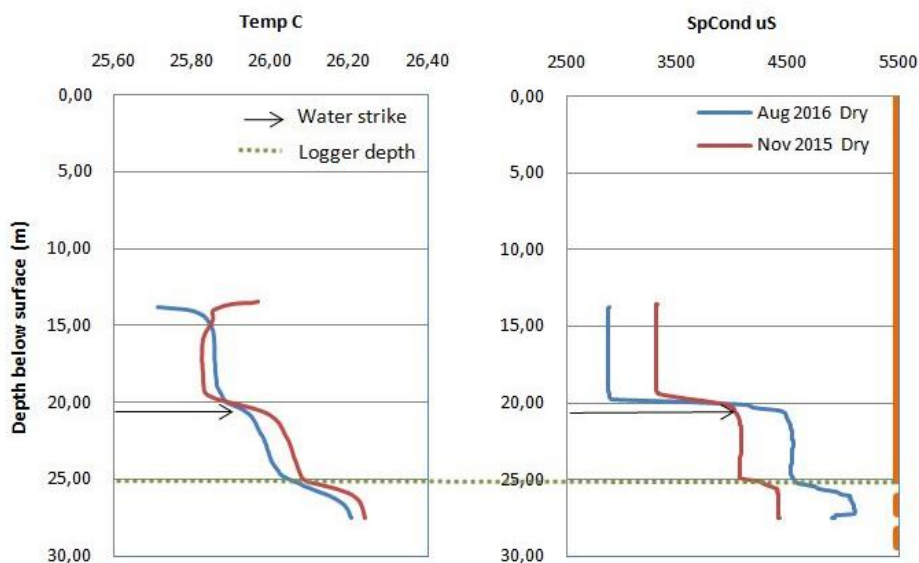


Figure 42: Fluid log of LF0031A

LF0031B (farms, regional, shallow)

As expected, the temperature and electrical conductivity are higher in August 2016 due to the consistently dry and warm conditions during the monitoring period (Figure 43). The temperature indicates some inflow from the unconsolidated zone within August. The fracture is indicated by the temperature curve change, which is also observed in the November 2015 temperature log with a sudden increase in temperature at 17 m. The electrical conductivity supports the temperature with a sudden increase in electrical conductivity at 17 m. Low inflow from the unconsolidated zone was expected at these boreholes. The deeper borehole indicates no inflow from the unconsolidated zone, thus suggesting that the two aquifers are separated from each other.

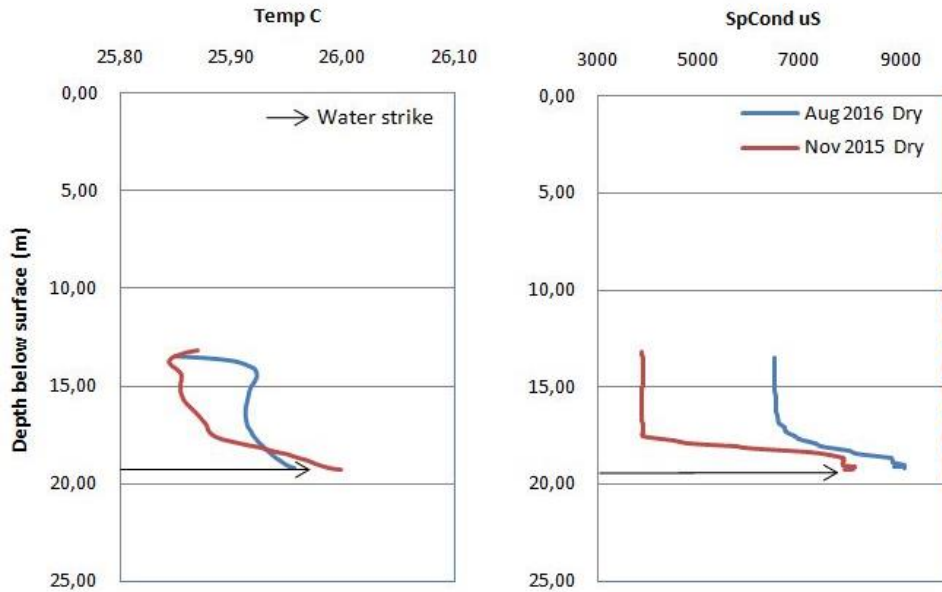


Figure 43: Fluid log of LF0031B

LF003A (farms, riparian, deep)

The temperature in LF003A shows no difference between the periods (Figure 44). The inflow of fresher water is again depicted by the decrease in temperature with depth similar to the previous boreholes. The conductivity is again slightly higher in the dryer winter period. Two big fractures are displayed at 23 m and 33 m, although these are within the solid casing and might indicate a leakage within the solid casing. Numerous very small fractures are indicated further down the borehole by subtle increases in electrical conductivity.

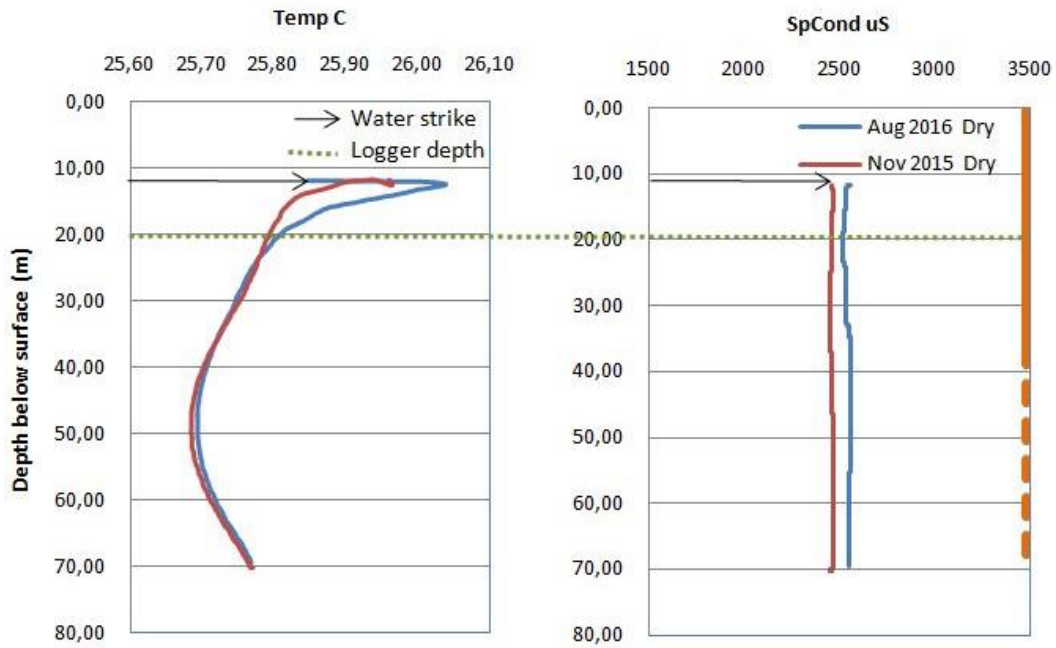


Figure 44: Fluid log of LF003A

LF003B (farms, riparian, shallow)

There is a surface inflow suggested in Figure 45, which is depicted by the decrease in temperature with depth. The conductivity displays a similar profile between the two seasons with a sharp increase after 15 m where the solid casing ends. A fracture is indicated by the temperature with a small increase at 19 m, as well as the electrical conductivity with a sudden increase. Most of the fractures are indicated by an increase in temperature and electrical conductivity. LF003A and LF003B are riparian boreholes located on the northern bank of the farm area.

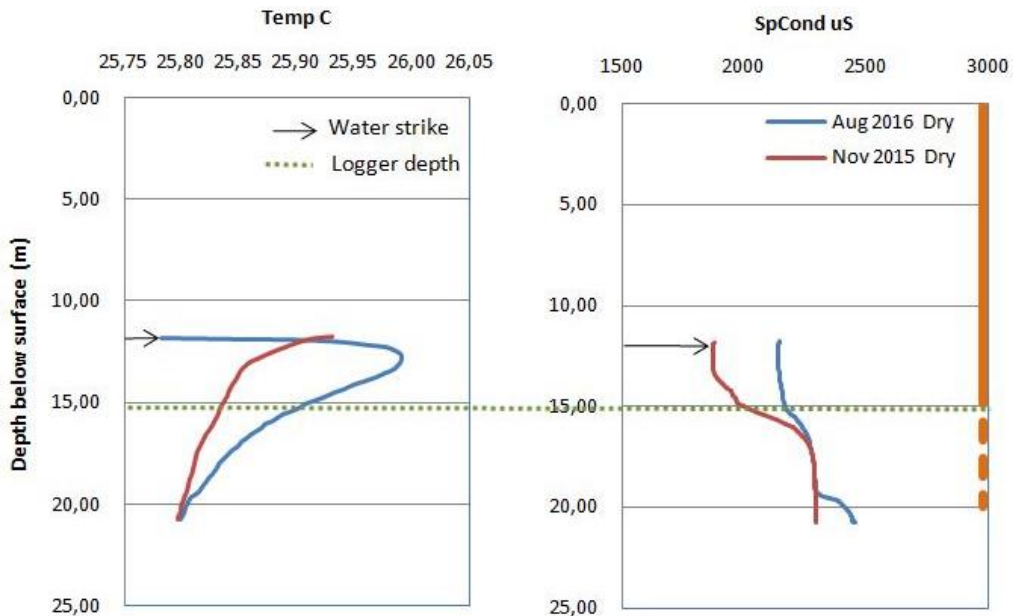


Figure 45: Fluid log of LF003B

LF005A (farms, riparian, deep)

LF005A (Figure 46) displays a similar temperature profile between the two monitoring periods with the suggested inflow of fresh water near the top of the borehole, and a decrease in temperature toward the bottom of the borehole until a large fracture is obtained. The electrical conductivity displays the end of the solid casing at 30 m with fractures indicated at 44 m and 62 m by the sudden increase in electrical conductivity within both periods. The lower electrical conductivity during August 2016 is due to the location of the borehole as LF005A is located on the southern bank of Transect 2 on the farms area within the riparian zone just south of the river. The lower electrical conductivity is likely due to the contribution from the river (especially after the March 2016 flood), which lowered the electrical conductivity through mixing.

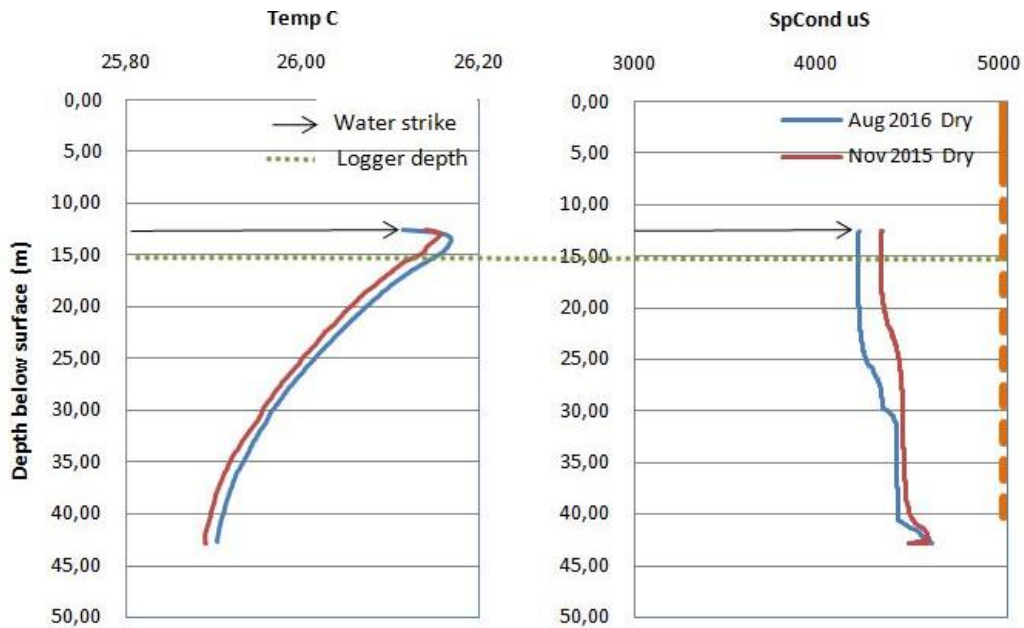


Figure 46: Fluid log of LF005A

LF005B (farms, riparian, shallow)

The temperature of borehole LF005B (Figure 47) displays the decrease with depth from the inflow of fresh water from the unconsolidated zone, as was seen in LF005A. The temperature is similar between the two periods and the conductivity also displays a relatively similar profile. Fractures are indicated at 30 m and 40 m with an increase in electrical conductivity and temperature. The fracture at 40 m within LF005B is indicated by a sudden increase in conductivity, which is similar to a fracture within LF005A (located only 5 m away) at 44 m. This indicates that both boreholes intersect the same fracture at around 40 m. When the temperatures of the two boreholes are compared, it is clear that the temperature drops to around 40 m where there is a large fracture. This provides more evidence that water is moving through the unconsolidated zone down the borehole (preferential flow path) and into the fractures.

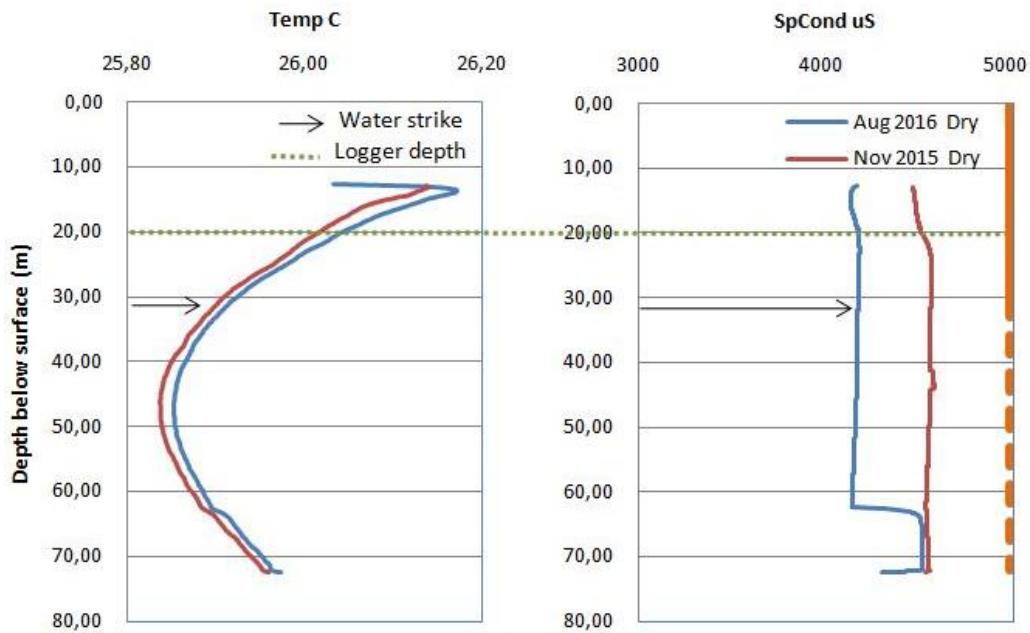


Figure 47: Fluid log of LF005B

LF005C (farms, riparian, shallow)

Only one fluid log LF005C (Figure 48) was conducted as very little water was found within the borehole in the initial November 2015 survey. The borehole displays an increase in temperature to the bottom, which indicates flow within the fracture zone and no flow from the unconsolidated zone. The electrical conductivity displays a definite fracture at 13.5 m with a slight decrease. This is suggested by the high electrical conductivity profile around 6000 uS, which is similar to LF004B. Both boreholes are very shallow with less than 1.7 m of water, thus evaporation within the borehole will have a bigger effect on its electrical conductivity. The result is a borehole with very high electrical conductivity, which ultimately displays a decrease in electrical conductivity at the fracture.

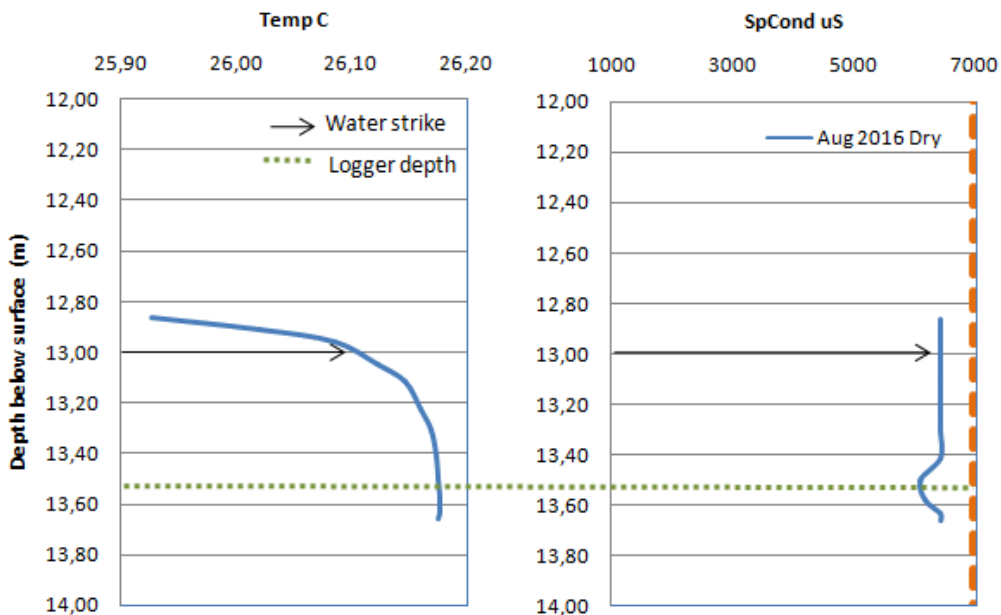


Figure 48: Fluid log of LF005C

LF0051A (farms, regional, deep)

The temperature profile is similar between the two periods (Figure 49), with the normal decrease with depth that indicates fresh water flowing in from the top of the borehole to the bottom. This is expected as LF0051A/B is located on the southern bank of Transect 2 with the lowest hydraulic heads of all the boreholes on this transect. Thus, we would expect the inflow of groundwater from the unconsolidated zone ultimately as the river is losing water to the southern bank. This should also lower the electrical conductivity as fresher groundwater from the river is entering the borehole. The lowering of the electrical conductivity can clearly be seen in both periods supporting the theory. A sudden increase in electrical conductivity at 25 m indicates that the solid casing has a perforation at this point. The end of the solid casing can be seen at 36 m with a small increase in both electrical conductivity temperature.

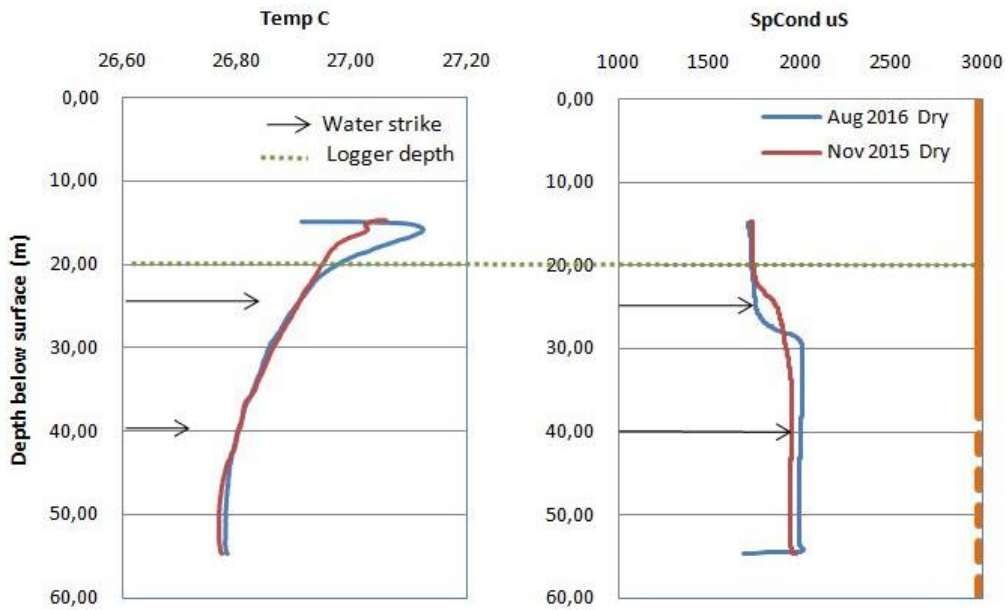


Figure 49: Fluid log of LF0051A

LF0051B (farms, regional, shallow)

The temperature displays a decrease with depth (Figure 50) caused by the inflow of groundwater from the unconsolidated zone from the top to the bottom of the borehole, or a prominent fracture. The temperature and conductivity as expected are higher in August 2016. A fracture is indicated at 26 m (where the temperature starts to stabilise) by a sudden increase in electrical conductivity and temperature, supported by the electrical conductivity increase in the August 2016 fluid log.

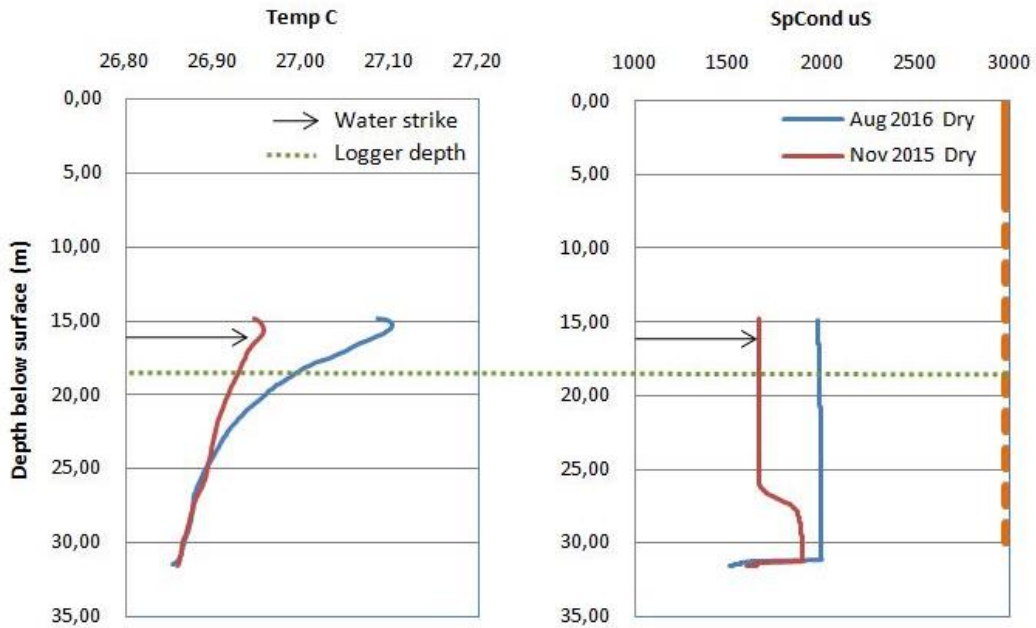


Figure 50: Fluid log of LF0051B

5.1.3 Transect 3

LR002A (protected area, regional, deep)

In LR002A, a temperature decrease is shown with depth (Figure 51), which indicates the inflow of fresher water from the unconsolidated zone at the top of the borehole to the bottom or prominent fracture. As expected, there was a slightly higher temperature in August 2016. Two fractures were observed with the increase of temperature and electrical conductivity. The first larger fracture sits at 28 m where both electrical conductivity profiles indicated the fracture. This is confirmed by the temperature decrease that stabilises beyond this depth. The second fracture is much smaller observed at 32 m. The November 2015 electrical conductivity only displays a straight line from 28 m, when the borehole is pumped for hydraulic testing for extensive periods.

LR002A is a deep borehole situated on the northern bank of the protected area. It has the highest hydraulic head of Transect 3 and shows that water is moving from the northern bank to the southern bank. The borehole did, however, display the recharge from the unconsolidated zone, indicating that water is moving through this zone toward the river.

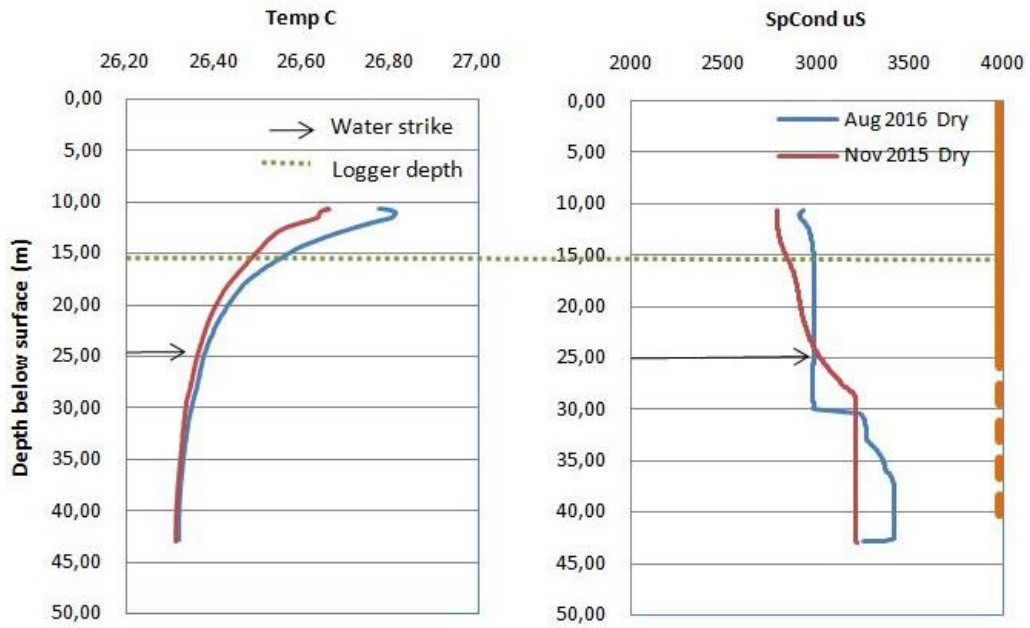


Figure 51: Fluid log of LR002A

LR004A (protected area, regional, deep)

Only one fluid log is available for LR004A (Figure 52), as the borehole has not yet been drilled by November 2015. The electrical conductivity displays no prominent fractures, although the casing is indicated at the correct 30 m with a sudden increase in electrical conductivity. The temperature did, however, display a very small fracture at 35 m.

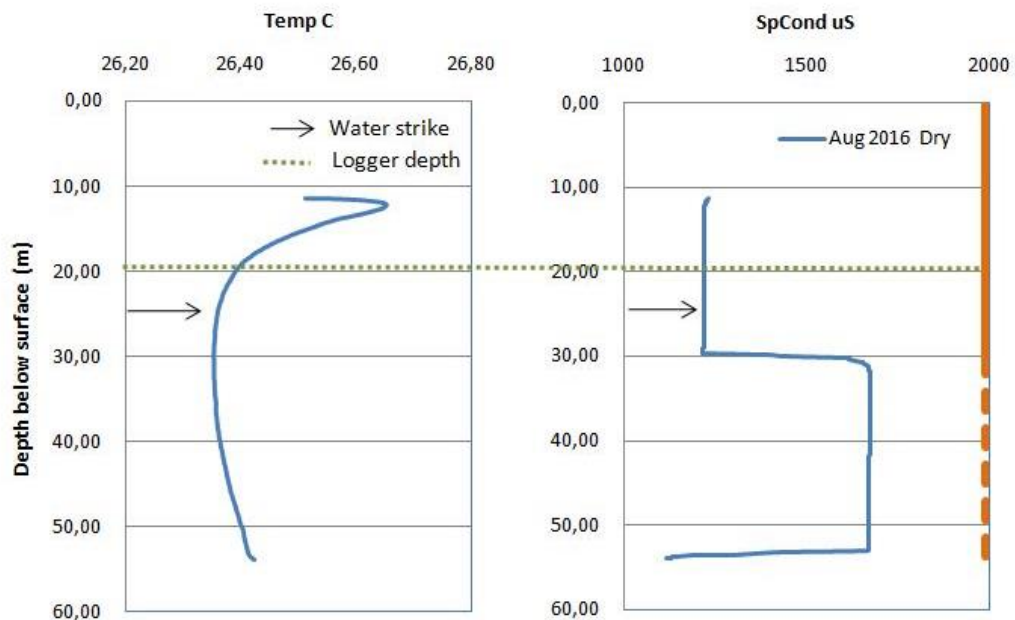


Figure 52: Fluid log of LR004A

LR004B (protected area, regional, shallow)

Figure 53 shows a decrease in temperature with depth displaying the similar inflow as most of the boreholes with fresh water flowing in at the top to the bottom of the borehole or prominent fracture. The electrical conductivity displays only one fracture at 24 m with a small increase in electrical conductivity. The temperature indicates the exact same profile up to 24 m, where the fracture is located in LF004A. This is also where the water strike occurred. Thus, it can be assumed that both boreholes intersected the same fracture and that both boreholes are receiving water from the unconsolidated zone.

LR004A and LR004B are located on the southern bank of the protected area. They have the lowest hydraulic heads of Transect 3 and had a quick reaction to the March 2016 flood event. This indicates that water is being lost from the river in the direction of the boreholes. The electrical conductivity supports this theory by displaying a relatively low electrical conductivity overall when compared to the opposite riverbank at LR002A. The inflow of water through the unconsolidated zone in both boreholes also suggests that the water from the river is being lost to the aquifer around these boreholes as water moves through the unconsolidated zone.

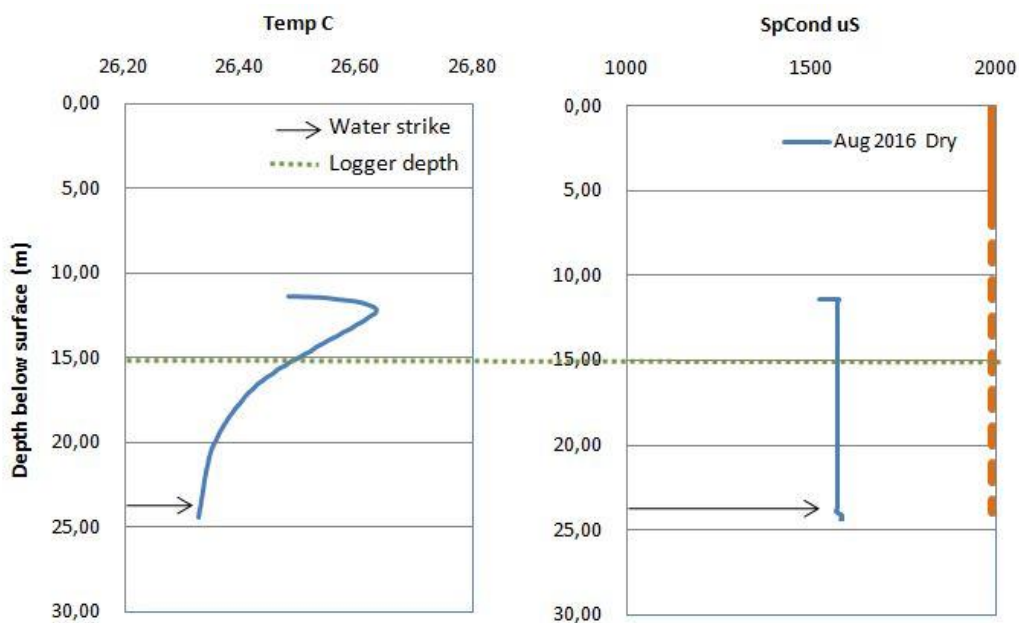


Figure 53: Fluid log of LR004B

5.1.4 Transect 4

LR0011A (protected area, riparian, deep)

The temperature displays a decrease with depth from the inflow of fresh water at the top with almost no difference in temperature between the periods (Figure 54). The first 20 m shows a slightly higher temperature, which indicates warm fresh water is entering the borehole from the unconsolidated zone. The electrical conductivity was much lower in August 2016. The cause is most likely the influence of the March flood, as LR0011A is situated within the riparian zone on the northern bank and is displaying a quick response to the flood event. Fractures were indicated at 32 m and 47 m with an increase in temperature and electrical conductivity as the warm high electrical conductivity water enters the borehole.

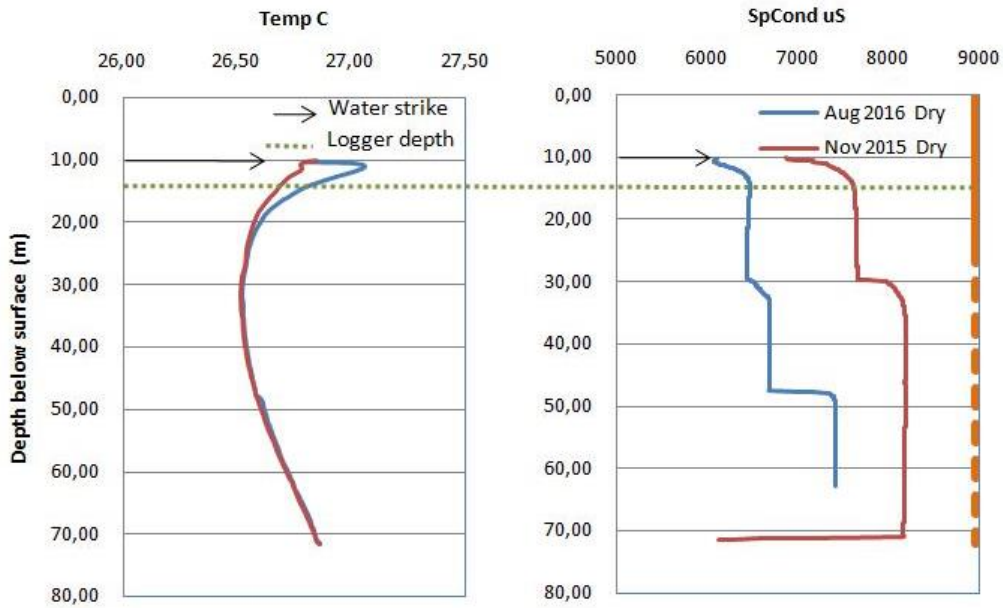


Figure 54: Fluid log of LR0011A

LR001A (protected area, riparian, deep)

No significant difference is found between the temperatures of the two periods (Figure 55). The decrease in temperature with depth found in most of the boreholes is also displayed in LR001A, which indicates inflow from the unconsolidated zone. The temperature shows a definitive increase at 21 m with a slight change in the electrical conductivity, which indicates a perforation leak in the solid casing.

Numerous small fractures were indicated at 35 m, 42 m, 47 m and 50 m through the increases in temperature and electrical conductivity. A lower electrical conductivity is observed in August 2016. LR001A is located within the riparian zone on Transect 4, which displayed a very quick response to the March 2016 flood event. The result was mixing of fresher low electrical conductivity river water, ultimately lowering the electrical conductivity profile of the aquifer around LR001A.

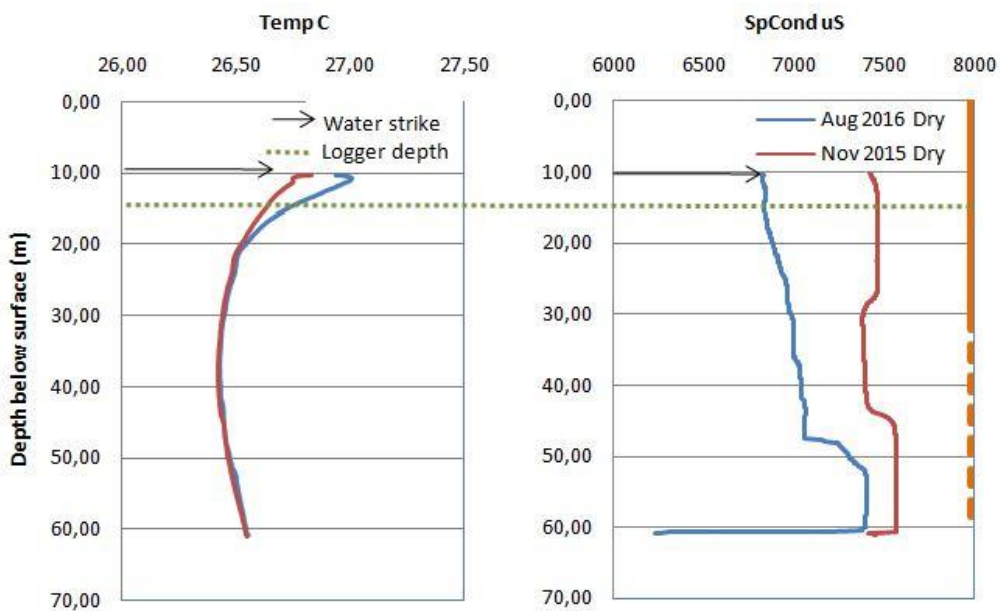


Figure 55: Fluid log of LR001A

LR005A (protected area, regional, deep)

The temperature displays an anticipated decrease with depth due to the inflow of fresh water at the top (Figure 56). The temperature and electrical conductivity remain similar over the two periods with both indicating a perforation leak in the solid casing at 20 m. Only one prominent fracture was indicated at 57 m.

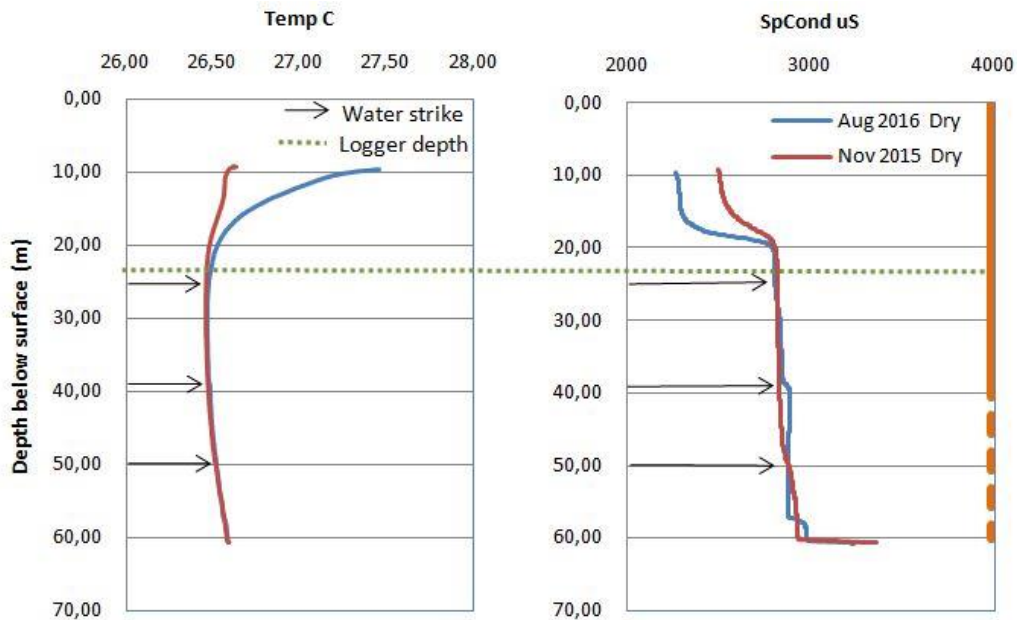


Figure 56: Fluid log of LR005A

LR005B (protected area, riparian, shallow)

The temperature in August 2016 displays an increase in temperature as anticipated for this dry and warm period (Figure 57). The temperature decreases with depth indicating water flowing in from the unconsolidated zone. The temperature starts to stabilise around 16 m, and stabilises at around 20 m. Two fractures are confirmed with a slight increase of electrical conductivity at 16 m and 20 m.

The decreases in temperature from both boreholes show that groundwater is moving through the unconsolidated zone, as well as the deep fractured aquifer toward the river. The slightly lower electrical conductivity within the top 25 m shows that the water that moves into the aquifer is lower in electrical conductivity and fresher than the high electrical conductivity groundwater within the fractures. This lowering of electrical conductivity could also be the effect of the March 2016 flood contributions to the aquifer, as both boreholes had a delayed reaction to the flood.

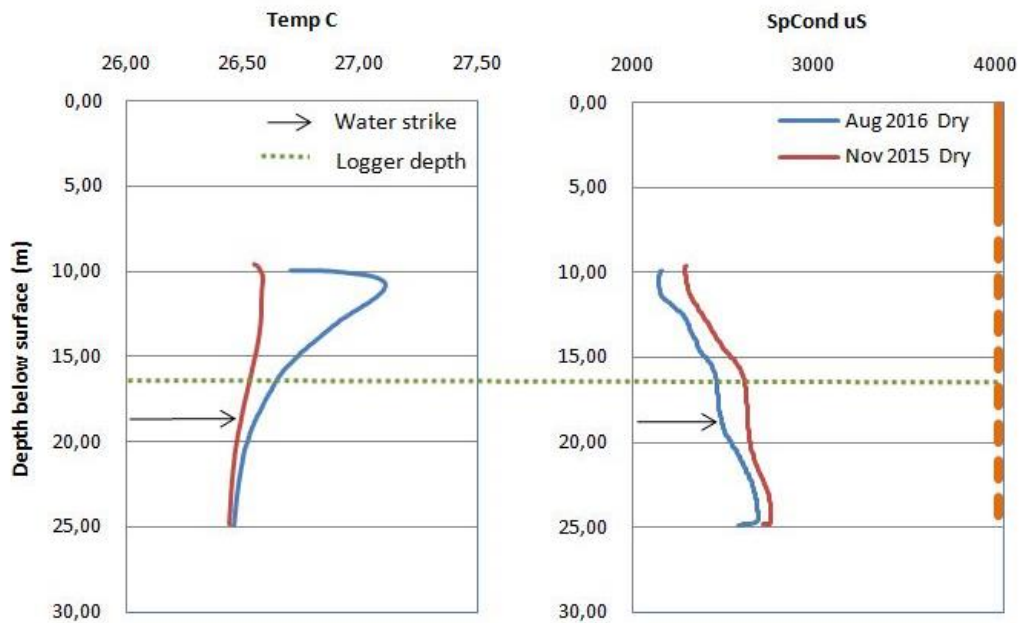


Figure 57: Fluid log of LR005B

LR003 (protected area, riparian, shallow)

Only one fluid log is available for LR003 (Figure 58), because it never had a water strike and was initially dry. The inflow of groundwater from the unconsolidated zone can be seen in the temperature log with a decrease to the bottom of the borehole. The electrical conductivity is extremely high – it increases to 16 000 uS and displays no fractures. This indicates no flow through the borehole, with only flow into the borehole from the top.

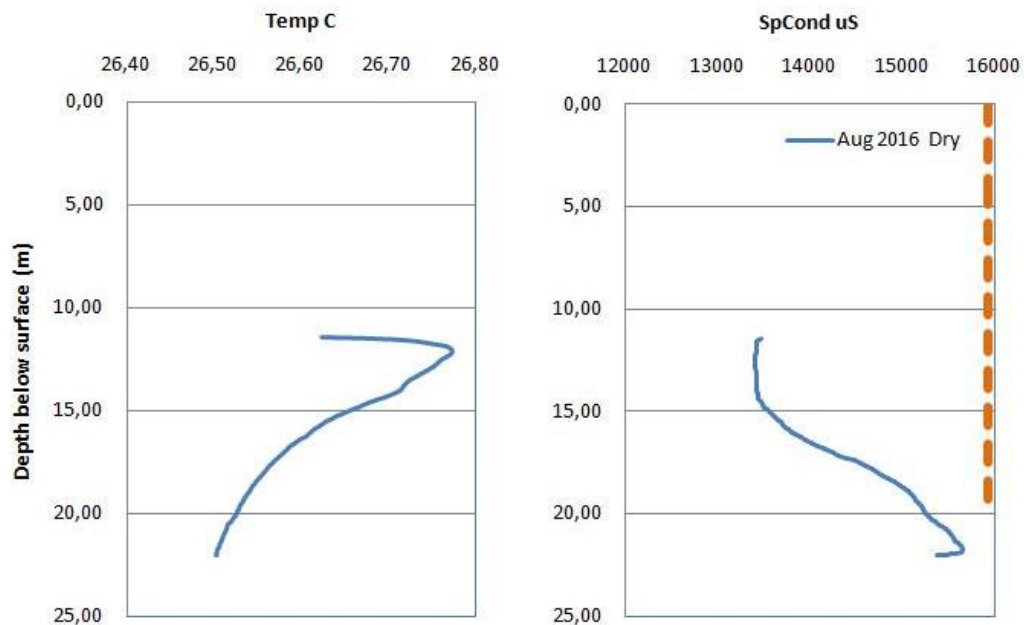


Figure 58: Fluid log of LR003

5.1.5 Dolerite dyke transect

LRW001 (protected area, riverbed, shallow)

Only one fluid log is available for LRW001 (Figure 59), because the borehole was only drilled in November 2015. The temperature increases with depth, which indicates that no water is moving through the unconsolidated zone, but only through the fracture. The fracture is indicated with an increase in both conductivity and temperature at 8 m as the warmer and high electrical conductivity water flows into the borehole from the fracture.

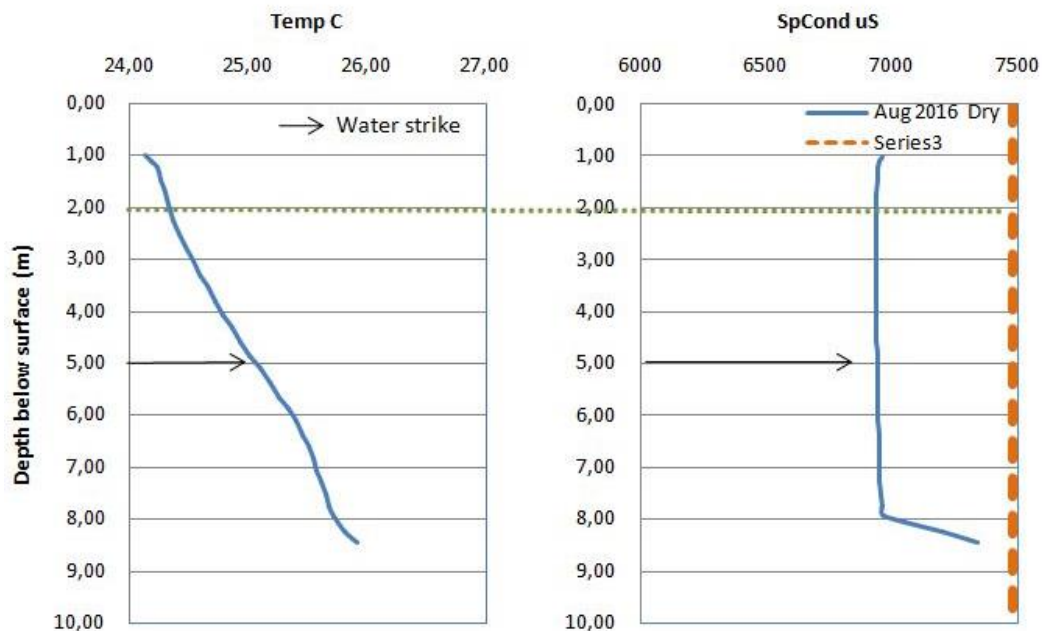


Figure 59: Fluid log of LRW001

LRW002 (protected area, riverbed, shallow)

Only one fluid log is available for LRW002 (Figure 60), because the borehole was only drilled in November 2015. The temperature increases with depth, which indicates that no water is moving through the unconsolidated zone, but only through the fracture. The fracture is indicated by an increase in temperature at 4.6 m.

LRW001 is located within the Letaba River streambed on the northern side (downstream) of a large dolerite dyke (with a small dam wall on top of it) running through the river, ultimately connecting with the Letaba weir. This causes a damming of the river water and groundwater. LRW002 was purposefully drilled on the southern side (upstream) of this dolerite dyke to determine the processes and water movement across it.

LRW001 indicates a very high electrical conductivity of 7000 uS, which is anticipated as no contact occurs with water from the river. The temperature slowly increases from 24°C to 26°C in a relatively straight line, which indicates no inflow of groundwater from the unconsolidated zone, but only from the fracture. This is supported by the high increase in electrical conductivity at the fracture.

LRW002 displays a much lower temperature and electrical conductivity. The reason for this is that the dolerite dyke blocks the water forcing the river water to move alongside the dyke in the direction of the Letaba Ranch gauging weir (north-east). This forces the colder river water to flow into LRW002. The result will be a lower temperature and electrical conductivity with the borehole. This can clearly be seen with the cold river water flowing in at 21°C, which slowly increases to the warmer groundwater flowing in the fracture. The electrical conductivity is also evidence of this with LRW002 displaying a low electrical

conductivity of 1500 uS. The only anomaly is the electrical conductivity should be higher at the fracture of 4.6 m, although this can be explained by the low electrical conductivity river water flowing and diluting the high electrical conductivity from the fracture.

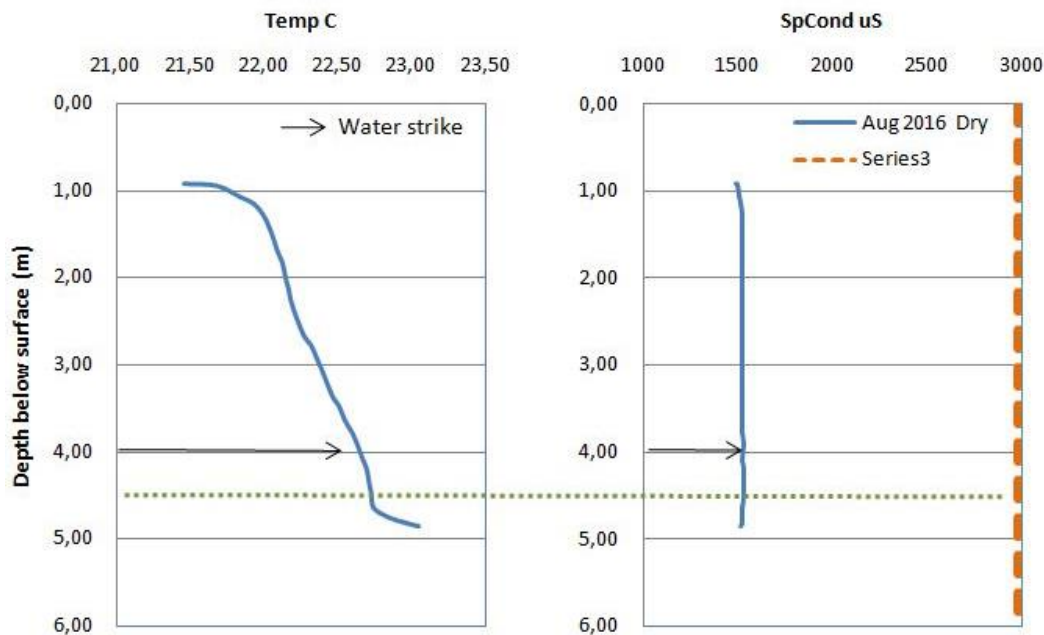


Figure 60: Fluid log LRW002

5.1.6 Summary

The high difference in electrical conductivity between the two periods show that the aquifer is strongly dependent on rainfall events – especially regional boreholes that are located outside the riparian zone of the river (e.g. LF0031, LF0051). The large effect the March 2016 flood event had on riparian zone, as well as sections where the river was losing water to the groundwater system, was evident and displayed the interconnectedness of the river and the groundwater system.

5.2 Groundwater Hydraulic Gradient Distribution

As an example, the following section plots the water levels as observed on 15 February 2016 in a cross-section relating to the position of the river. Included are the final values for K and T in order to build an interpretation of *potential* losses or gains to the Letaba River from the surrounding aquifer(s). This data is then used to derive a cumulative time series of potential gains/losses between the river and the surrounding aquifer along the entire river reach.

Figure 61 shows the most upstream transect with the hydraulic gradient showing a potential groundwater flow from south (LF004) to north (LF002). The T values show that there is a high flow within the shallow fractured aquifer from the north, although this is lower in the deep hard rock aquifer. After intersecting with the river, the T values suggest a slight loss to the river but a greater loss to the riparian zone as indicated by LF0021. The shallow borehole LF002B indicates a large river loss to the northern bank, although the deeper hard rock aquifer seems to be detached from it.

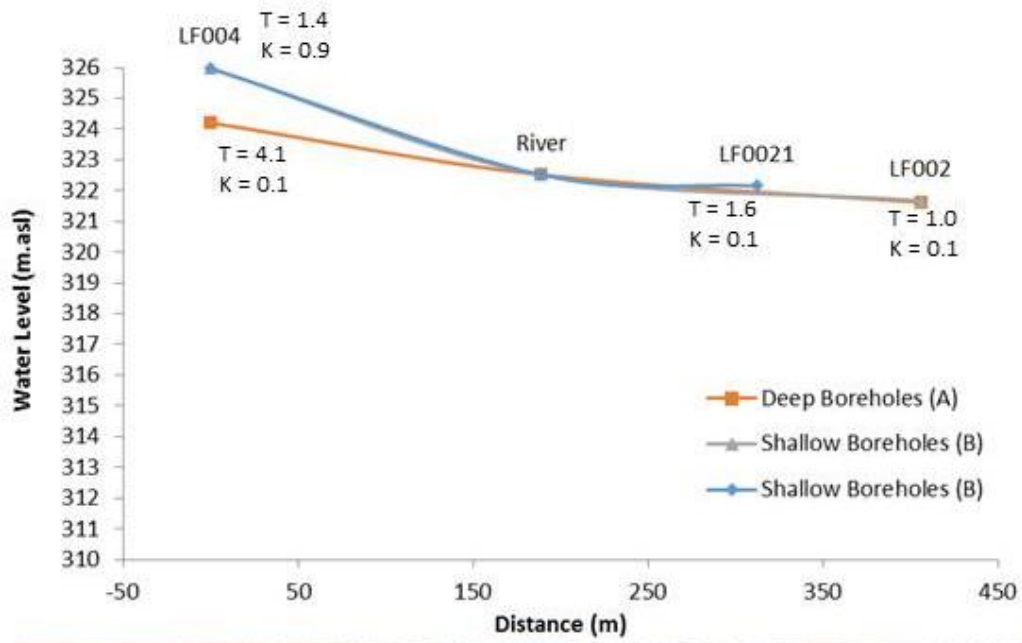


Figure 61: Cross-section plot of transect LF004 to LF002, February 2016

Figure 62 indicates the hydraulic gradient from north (LF0031) to south (LF0051). There is a definitive loss to the aquifer from the river on the southern bank in the weathered and hard rock, which is indicated by a high hydraulic gradient. LF003 seems to be an anomaly and might be disconnected from the regional aquifer as it indicates very low flow from the T values. A possible explanation could be that the water still flows from north to south but, because there is an increase in the hard rock elevation as seen in the geophysics, it “pinches” the water at LF003, thus increasing the hydraulic gradient a smaller scale, inducing flow and “pushing” the groundwater over the elevated hard rock.

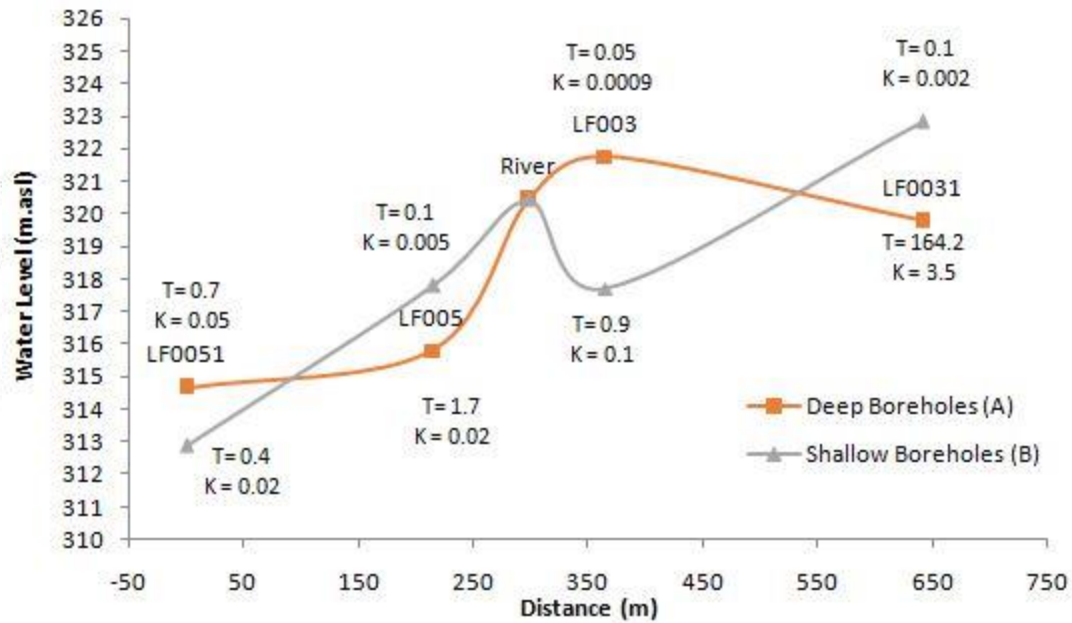


Figure 62: Cross-section plot of transect LF0051 to LF0031, February 2016

In Figure 63 it appears that the groundwater flows from the northern bank to the southern bank. The deep hard rock aquifer does not appear to be largely affected by the intersection of the river. From the T values it seems as if the deep hard rock aquifer is detached from the river with almost no change in values.

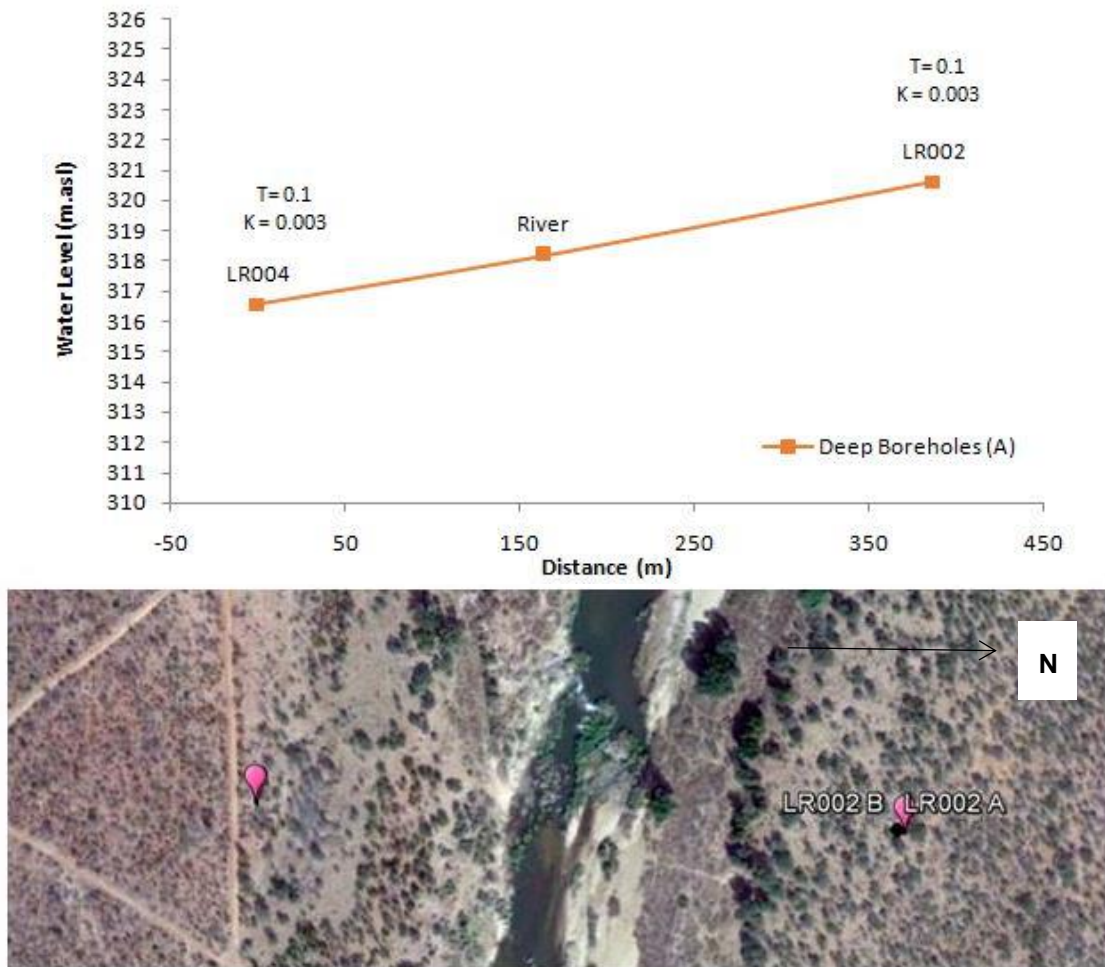


Figure 63: Cross-section plot of transect LR004 to LR002, February 2016

In Figure 64 both the deep hard rock aquifer and the shallow weathered aquifer display a large potential contribution from the groundwater to the river from both the south and north. It is likely that the shallow weathered aquifer contributes much more than the hard rock aquifer, although this will be impacted by riparian vegetation transpiration. Throughflow of the aquifer is not displayed in this transect like it is as in all the other transects, although there is a dolerite dyke running through the river between these two borehole positions in a north–east and south–west direction. It is therefore possible that this dyke might be separating two contributing aquifers.

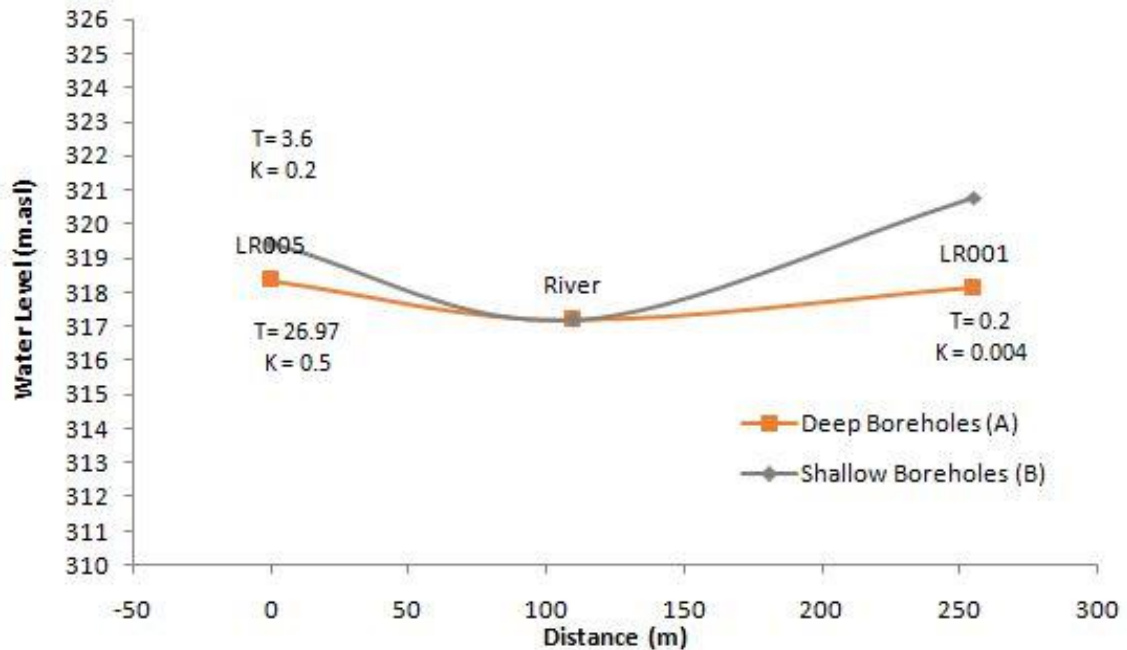


Figure 64: Cross-section plot of transect LR005 to LR001, February 2016

The hydraulic gradients in Figure 65 suggest a throughflow of the deep hard rock aquifer with a large contribution from the southern bank to the river, which is depicted by the T values. This throughflow is similar to the other transects and might indicate that the dolerite dyke does in fact separate the aquifer from LR001. The shallow weathered aquifer from the northern bank does not show a large loss to the river drainage (but this still requires hydraulic data characterisation), which can also be seen in the manual water levels where only small fluctuations occurred in the water level during the season.

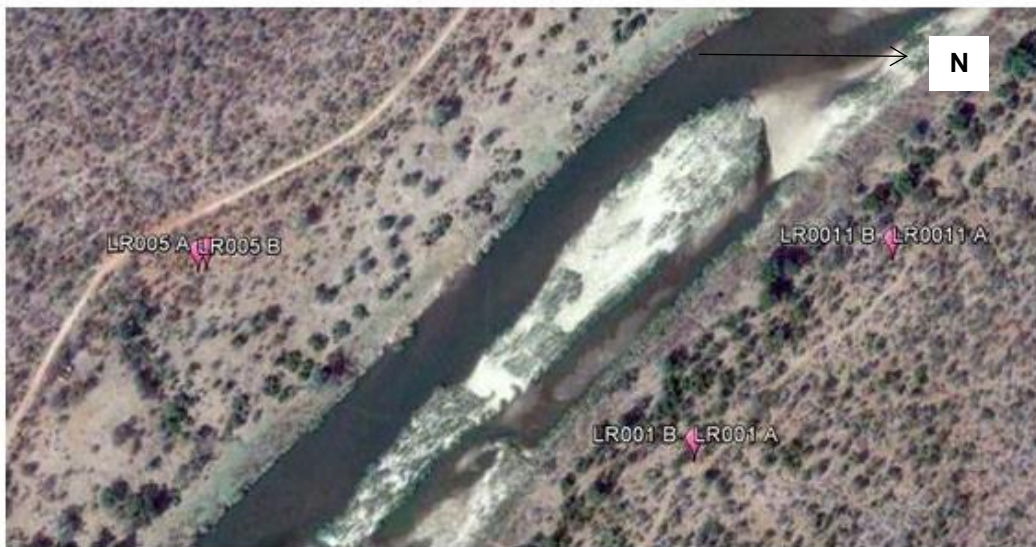
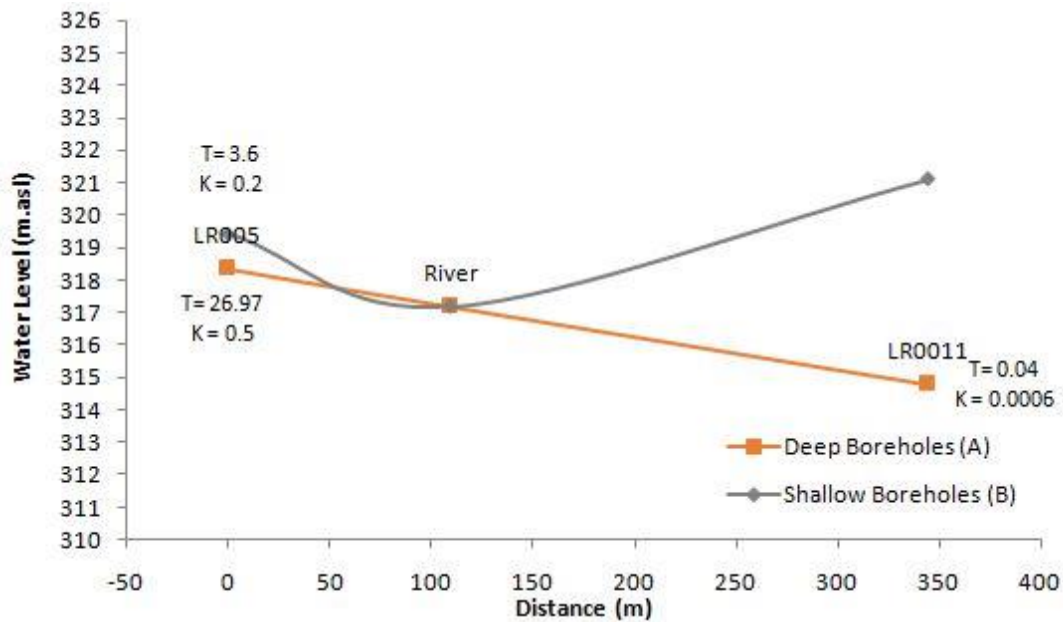


Figure 65: Cross-section plot of transect LR005 to LR0011, February 2016

5.3 Initial Transmission Loss Estimation

Following the groundwater hydraulic characterisation (Table 9), an initial transmission loss estimate can be made for the section of river as related to the groundwater component.

Table 9: Hydraulic characteristics of boreholes at study site

BOREHOL E	Slug K (m/day)	Depth	Storativity	Q L/s	Final T (m ² /day)
LF0021	0.00	15.00	0.04	0.17	0.030
LF002A	0.02	48.20	0.00	0.15	0.080
LF002B	to high for slug		0.50	0.70	18.000
LF0031A	3.54		0.00	STEP	164.200
LF0031B	0.00	6.60		SLUG	0.003
LF003A	0.13	60.00	0.01	0.22	0.050
LF003B	0.12		0.04	0.40	1.000
LF004A	0.02	58.00	0.00	0.15	0.870
LF004B	0.41	1.63		SLUG	0.668
LF0051A	0.35	39.00	0.00	1.00	13.650
LF0051B	0.02	15.00	0.00	0.15	0.300
LF005A	0.02	59.00	0.00	0.15	1.180
LF005B	0.00	29.00	0.00	0.10	0.058
LF005C	0.14	1.20		SLUG	0.168
LR0011A	0.01	61.00	0.00	0.11	0.305
LR001A	0.02	49.00	0.02	0.41	0.980
LR002A	0.01	31.00	0.00	0.10	0.155
LR003A	0.00	3.60	0.00	0.10	0.014
LR004A	0.02	40.00	0.00	0.16	0.680
LR004B	0.17	12.00	0.00	0.33	2.040
LR005A	0.53		0.05	1.60	26.970
LR005B	0.27	14.20	0.14	0.71	3.834

In accordance with the four geohydrological transects described, an estimate was made of the approximate river reach lengths represented by the surrounding aquifers, which divide the river between Mahale and Letaba Ranch into four representative river reaches (Figure 66). Using these, the interaction between the river and the aquifer can be estimated in terms of either gains or losses from the watercourse.



Figure 66: Assumed river reaches between Mahale and Letaba Ranch Weirs associated with geohydrological transects (green represents farming areas and yellow the protected areas)

Transmission losses along a river can be estimated using the following equation:

$$\text{Equation 6} \quad Q = TiL$$

Where:

Q is discharge (m^3);

T is transmissivity;

i is the hydraulic gradient between the river and the surrounding aquifer (dimensionless); and

L is the length of river reach (m).

This equation was applied to each river reach distinguishing between hydraulic parameters for deep and shallow boreholes and applied to the hydraulic gradients determined for the study site as depicted Table 9.

It is interesting to note that based on Table 10 there appears to be a nett loss from the river to the surrounding aquifer in the transects representing the farming areas, and this is potentially greater into the deeper hard rock zone. Moreover, there is a marginal decrease at the hydraulic gradient that reduces over time. Meanwhile, further downstream in the protected areas there is a potential flow gain from the surrounding aquifer especially in the deep hard rock zone. Here there is a noticeable decrease in potential gain from the aquifer to the river comparing February to September.

It is therefore important to take this into context of the prevailing hydrology for the study period in which the upstream Mahale Weir was discharging only through low flow outlets with an estimated flow of from $0.4\text{--}0.5 m^3/s$ or from $34\ 560\text{--}43\ 200 m^3/day$. Hydrocensus information for river abstractions (surface water only) between these two weirs allows for an estimate of total daily abstractions of $52 m^3/day$.

Table 10: Transmission loss parameters determined for the Letaba River study site comparing wet season (15 February 2016) with dry season (16 September 2016) (yellow highlighted values mean borehole (BH) properties could not be determined for the shallow boreholes due to insufficient head, so these values were inferred from the deep boreholes)

				15/02/2016			16/09/2016		
		River Section	Actual Section Length (L)	T m/day	i	Q m ³ /day	i	Q m ³ /day	
Deep BH data (A)	Farms	LF002	2200	0.08	-0.004	-0.72	-0.004	-0.78	
		LF004	2200	0.87	0.009	17.03	0.008	16.20	
		LF003	2180	0.05	0.020	2.19	0.020	2.19	
		LF005	2180	1.18	-0.055	-142.00	-0.055	-140.58	
		Total					-123.49		-122.97
	Reserves	LR002	1580	0.155	0.011	2.67	0.011	2.65	
		LR004	1580	0.68	-0.010	-10.64	-0.011	-12.33	
		LR001	880	0.98	0.006	5.52	0.006	5.44	
		LR005	880	3.834	0.011	35.76	0.008	27.98	
	Total					33.32	Total	23.74	
Shallow BH data (B)	Farms	LF002	2200	18	-0.003	-114.84	-0.003	-119.72	
		LF004	2200	0.6683	0.018	26.91	0.018	26.06	
		LF003	2180	1	-0.041	-88.94	-0.041	-89.37	
		LF005	2180	0.058	-0.032	-3.98	-0.031	-3.95	
		Total					-180.86		-186.98
	Reserves	LR002	1580	0.155	-0.001	-0.24	0.015	3.78	
		LR004	1580	2.04	-0.015	-47.38	-0.016	-52.55	
		LR001	880	0.98	0.025	21.22	0.024	20.35	
		LR005	880	3.834	0.020	68.83	0.018	62.02	
	Total					42.42	Total	33.59	

This information is integrated into a time series (Figure 67 and Figure 68), which suggests a sustained contribution from the deep regional aquifer of approximately +14.2 m³/day, although one observes that the hydraulic gradient to the river decreases toward the end of the reporting period in September (further data to be incorporated for the final version of the report). However, there is a potential drawdown of the river toward the unconsolidated shallow aquifer throughout the study period, which potentially averages -25.5 m³/day.

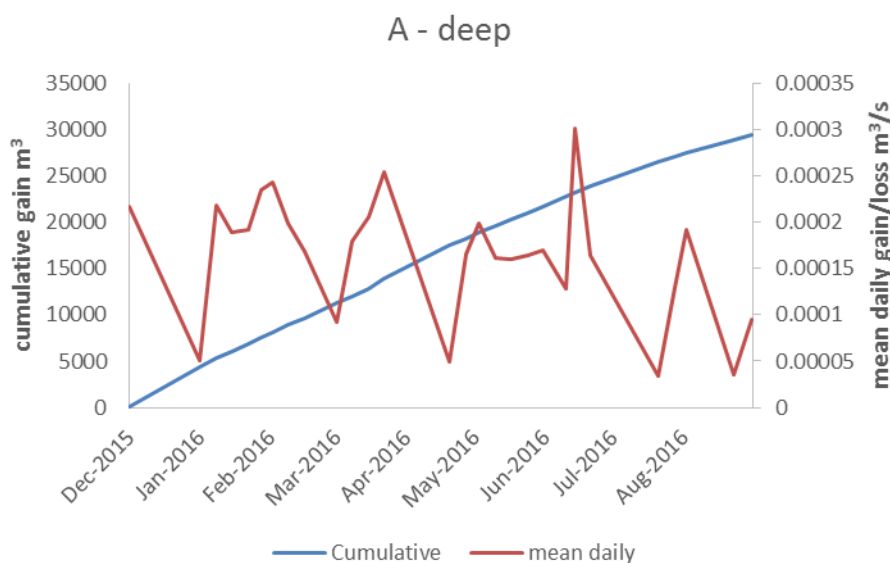


Figure 67: Time series of potential gains/losses along the study site (related to deep hard rock aquifer)

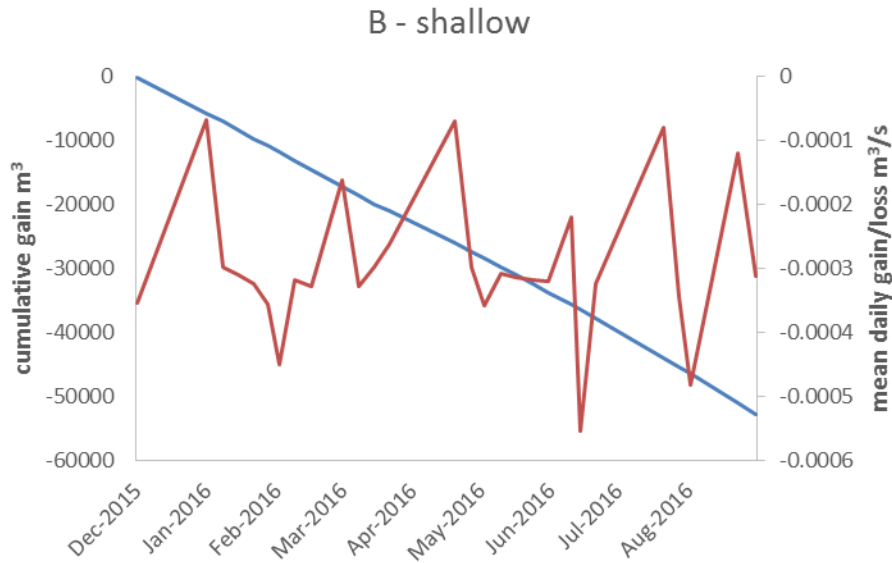


Figure 68: Time series of potential gains/losses along the study site (related to shallow unconsolidated aquifer)

5.4 Updated Conceptual Model: Groundwater/Surface Water Interaction

The data presented on borehole fluid logging and hydraulic gradients toward the river was used to derive a conceptual model of groundwater/surface water interactions along the study site reaches of the Letaba River. Further valuable information was derived from the single large streamflow event that occurred at site during the drought during the March 2016 flood (Figure 15). These will be discussed according to transect names (Figure 30).

5.4.1 Assessing peak flow transmission losses

Transect 1

Transect 1 includes borehole nests LF002, LF0021 and LF004. This studies the initial conceptual model, which is supported by the hydraulic gradient data interpreted that showed that groundwater was moving from LF004A in the south toward the river with water being lost from the river to LF002 and LF0021 on the northern bank. This assertion was supported by the boreholes' reaction to the March 2016 peak flows. Both LF002 and LF0021 displayed (Figure 69) a subtle delayed response, whereas LF004 did not display any reaction (not plotted). This data suggests that water was lost to the northern bank at Transect 1; although at a relative slow rate. The fluid logging supports this with a lower electrical conductivity found in these boreholes on the northern bank from the loss of river water to the groundwater.

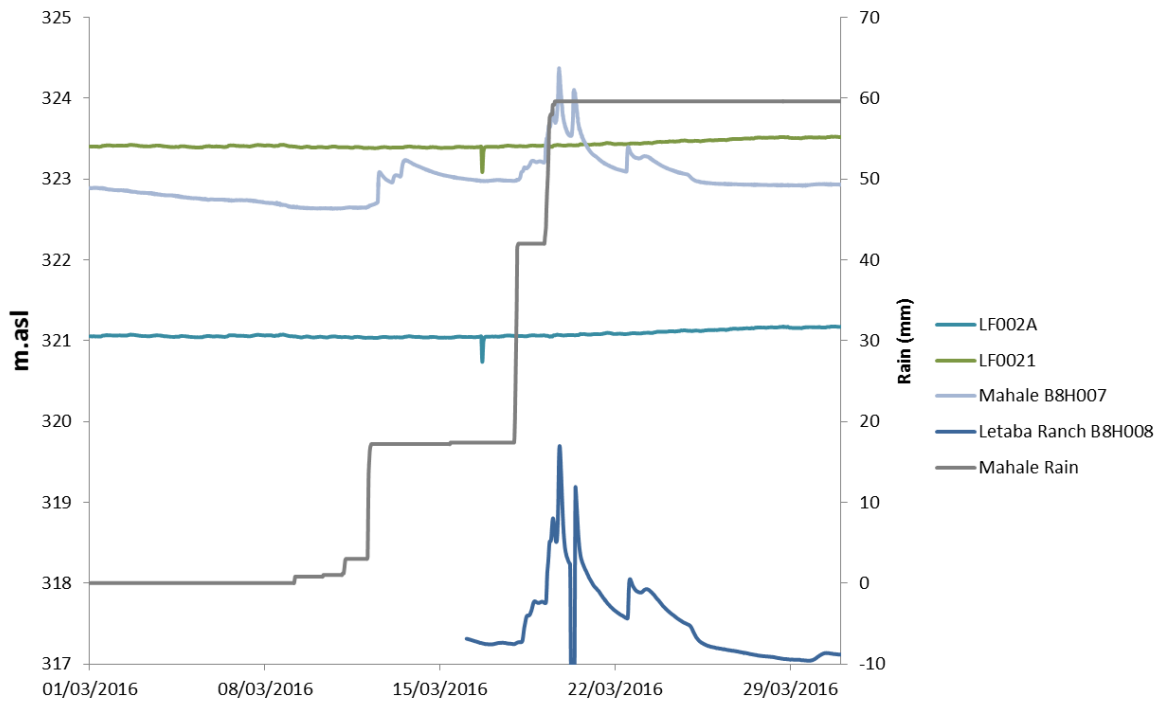


Figure 69: Key responses to March 2016 rain and peak flow along Transect 1 (stream stages plotted against datum at upstream and downstream sites for reference)

Transect 2

Transect 2 includes boreholes LF0031 and LF003 on the northern bank, and LF005 and LF0051 on the southern bank. Both deep and shallow holes at LF005 displayed (Figure 70) a quick and definite response to the flood. The water level in LF0051A further to the south only started responding on 19 March 2016, which indicated a delayed rainfall response. The previous conceptual model interpreted that groundwater was moving from the northern bank, intersecting the river before losing water to the southern bank, with the deeper aquifer possibly being detached from the river. This was supported in that neither borehole at LF003 displayed a reaction to the March 2016 peak flow with little reaction to the rain events (not plotted).

Flow within the unconsolidated to consolidated zone through the boreholes on this transect was indicated by all the boreholes with a decrease in temperature with depth. The temperature also suggested movement of groundwater within all the boreholes. An electrical conductivity of around 4000 uS is found within most of the boreholes (supporting the theory), except for LF0051A and LF0051B.

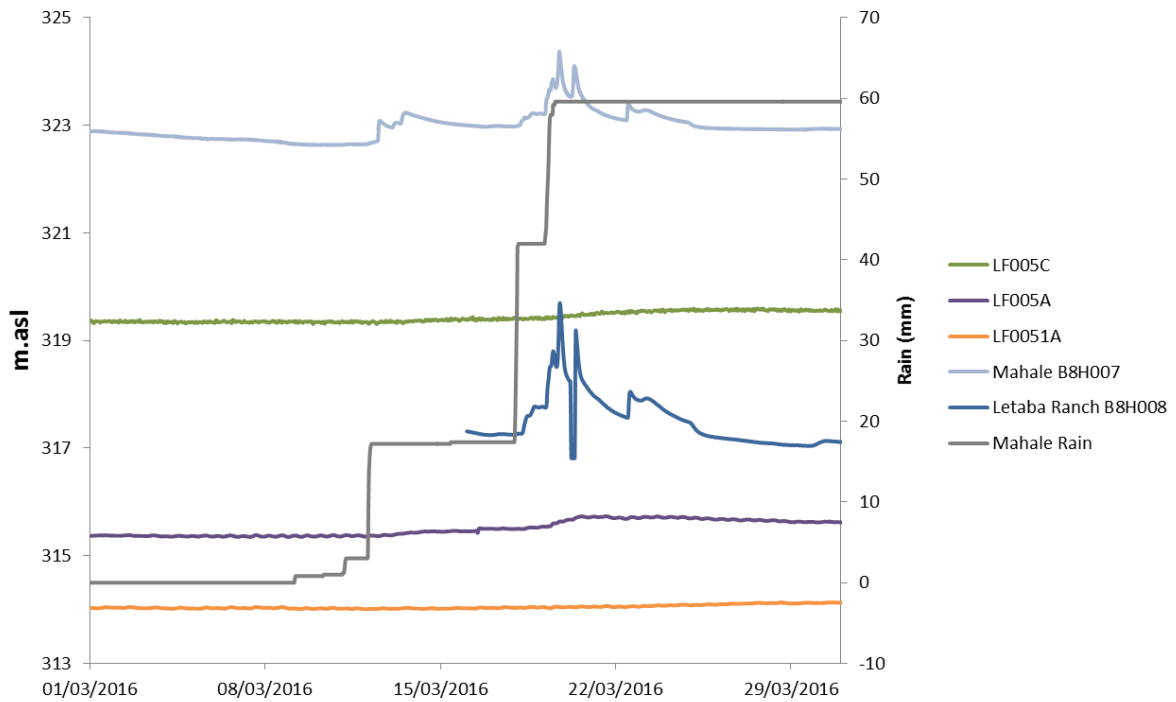


Figure 70: Key responses to March 2016 rain and peak flow along Transect 2 (stream stages plotted against datum at upstream and downstream sites for reference)

Transect 3

Transect 3 includes borehole nests at LR002 on the northern bank and LR004 on the southern bank, with the initial conceptual model suggesting that groundwater was moving from the northern bank to the southern bank as result of the hydraulic gradient across the transect. The March 2016 peak flow reactions only partially suggest this theory, because both LR002A and LR004A/B reacted to the flood on the same day (13 March 2016), see Figure 71. LR004A/B are located almost twice the distance from the river when it is in flood, which indicates that water is definitely being lost to the southern bank while water is only lost to the northern bank when the river is in flood or during high flow situations. During base flow situations, water continues to flow from the northern bank to the southern bank. The fluid log supports this theory with the temperature displaying a good flow within all the boreholes and a higher electrical conductivity of around 3000 uS in LR002A and lower electrical conductivity of around 1500 uS within both shallow and deep boreholes at LR004, suggesting that water is being lost from the river to the southern bank.

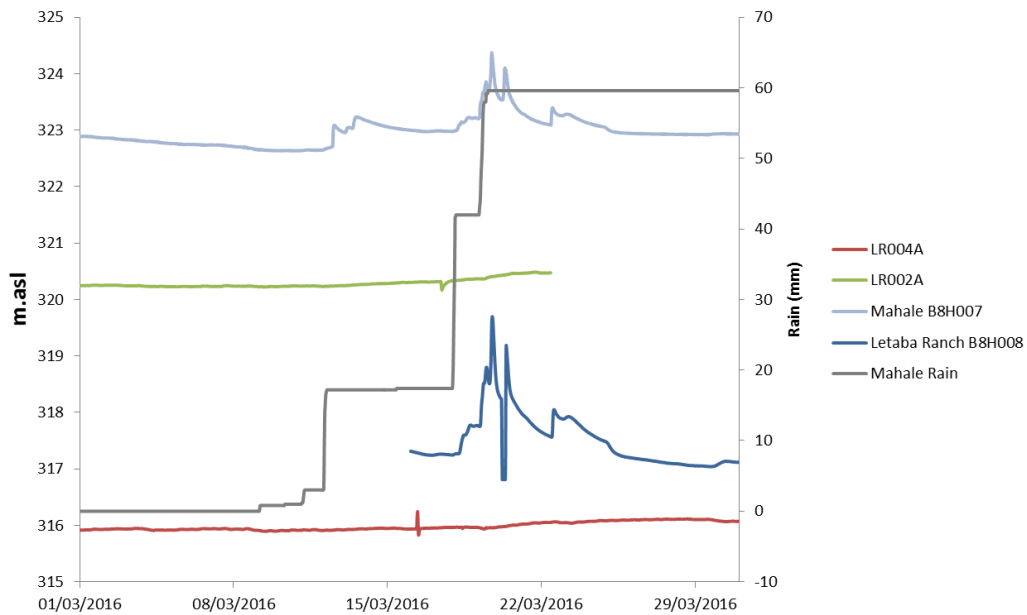


Figure 71: Key responses to March 2016 rain and peak flow along Transect 3 (stream stages plotted against datum at upstream and downstream sites for reference)

Transect 4

Transect 4 includes boreholes at LR001 on the northern bank and LR005 on the southern bank (see Figure 72). The hydraulic gradients across this transect suggest that groundwater moves from both north and south toward the river. The peak flow events of March 2016 suggest that this reverses to bank storage/recharge from the river as both LR005A and LR001A respond to the streamflow hydrograph, which is particularly obvious at LR001A. This indicates that the groundwater is contributing to the river from both sides during base flow. During flood conditions, the river contributes to the groundwater. The fluid log supports this theory with good flow indicated within all the boreholes, as well as water flowing through the unconsolidated zone into the boreholes noted from the decrease in temperature with depth.

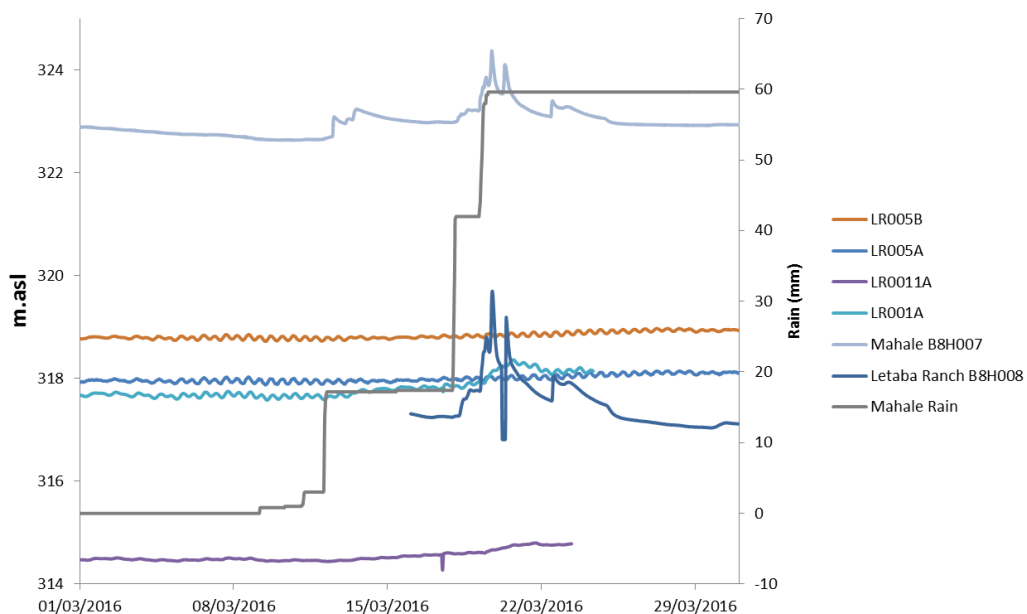


Figure 72: Key responses to March 2016 rain and peak flow along Transect 4 (stream stages plotted against datum at upstream and downstream sites for reference)

5.4.2 Groundwater flow direction from hydraulic heads

The hydraulic heads of all the boreholes were plotted as contours in Surfer™ to integrate groundwater movement in relation to the Letaba River. This focused on understanding groundwater movement before and after the flood/rains of March 2016 (Figure 74 and Figure 75) as well as a dry and wet season comparison (Figure 73 to Figure 76).

Transect 1

As discussed in the section above and supported by the hydraulic heads, the groundwater moves toward the northern bank of Traverse 1 (Figure 73). A small difference could be seen between the hydraulic heads before and after the March 2016 events. Greater hydraulic heads were observed on the northern bank but not on the southern bank, which supports the theory of transmission loss to the northern bank from the river. No large differences were observed between the hydraulic heads of the wet and dry season, although this can be assigned to the very little rainfall that occurred between these periods.

Transect 2

The discussion above is supported by the hydraulic head distribution where the groundwater is moving from the northern bank to the southern bank intersecting the river (Figure 73). The difference in hydraulic heads before and after the March 2016 peak flows displayed only a slight increase in hydraulic head on the southern bank again supporting the theory. This slight reaction might indicate that the fractured rock aquifer is detached from the system. Again, no big differences were observed between the wet and dry season due to little rainfall that occurred.

Transect 3

The discussion above is supported by the hydraulic head distribution where the groundwater is moving from the northern bank to the southern bank (Figure 73). An increase in hydraulic heads is observed on the southern bank and the northern bank. This indicates that during peak flows water is lost to both banks and during low flows only to the southern bank. A visible decrease in hydraulic heads was observed between the wet and dry season this was anticipated due to the drought conditions.

Transect 4

The groundwater is moving from both banks toward the river. An increase in hydraulic heads are observed after the March 2016 flood, which supports the theory that the river contributes to the groundwater during peak flow, while this process is reversed during low flow periods. A slight decrease in hydraulic head is observed in the dry season (Figure 76) as anticipated due to the little rain that fell within this period.

These processes as described are all captured visually in the conceptual model of the site in Figure 82.

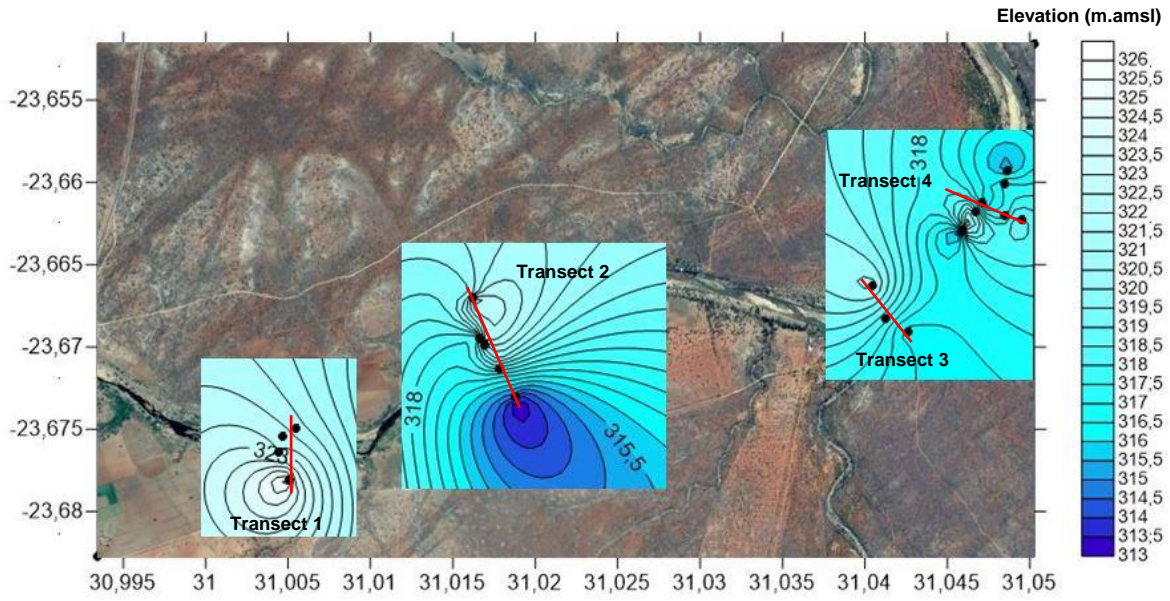


Figure 73: Borehole and river heads before the flood event (30 November 2015)

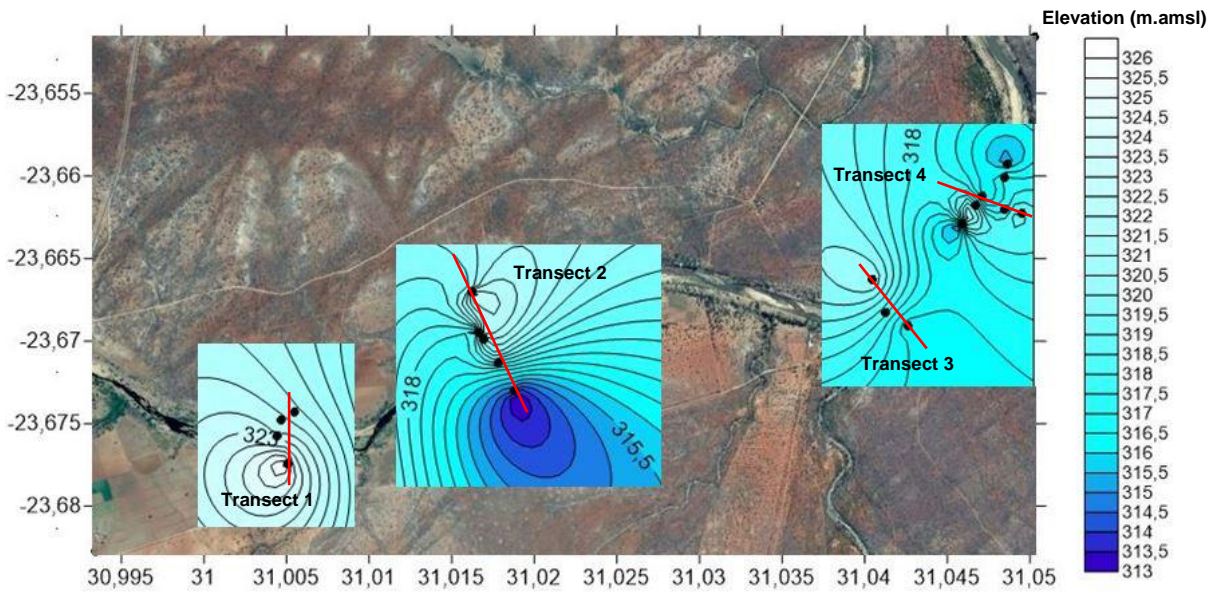


Figure 74: Borehole and river heads before the flood event (15 February 2016)

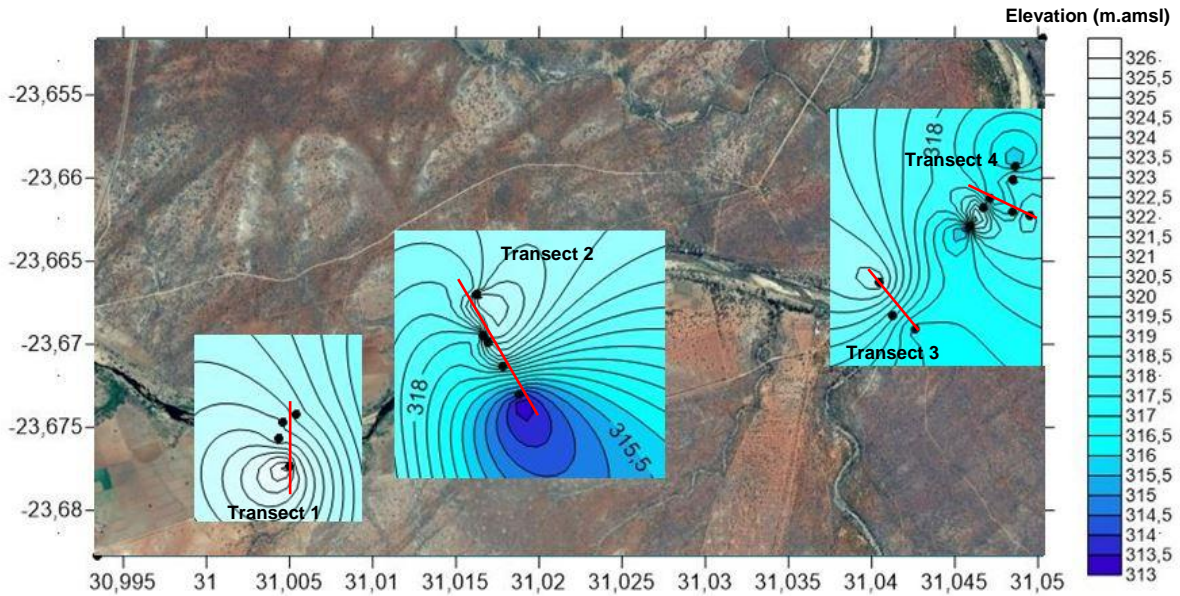


Figure 75: Borehole and river heads after the flood event (28 March 2016)

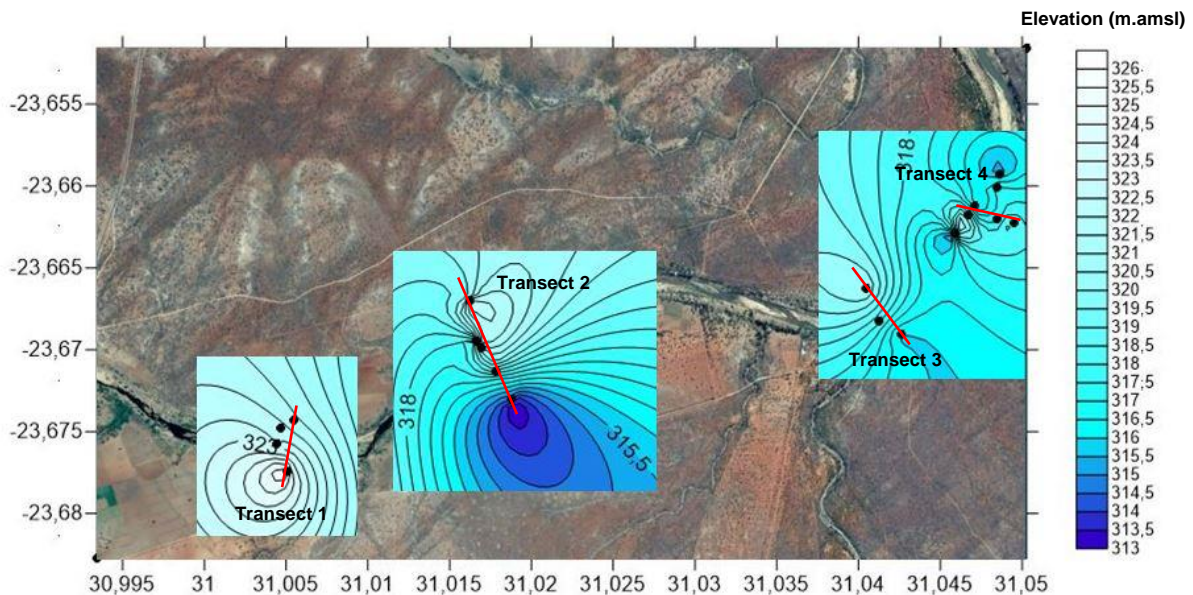


Figure 76: Borehole and river heads after the flood event (8 August 2016)

Groundwater stream flow process across dolerite dyke

LRW002 is located on the southern side (upstream) of a dolerite dyke with LRW001 located on the northern side (downstream) (see Figure 77). This is described briefly here in terms of the responses of these boreholes within the active river macro-channel. The first indication of the flood event on 13 March 2016 was indicated at the Mahale Weir upstream. The second indication was by LRW002, with a delayed response in LRW001. The reason being the dolerite dyke interrupts the groundwater moving through the unconsolidated/consolidated zone. This is supported by the fluid logging with LRW002 displaying lower temperatures of around 22°C from the interaction with river water, compared to LRW001 with a temperature between 24°C and 26°C. The electrical conductivity also supports this with a low electrical conductivity of around 1500 uS from mixing with river water, compared to LRW001 with a high electrical conductivity of around 7000 uS.

After the second peak of the flood, the two boreholes acted similarly as the river had now created connectivity over the dolerite dyke. After the flood passed, LRW002 displayed a faster decrease in water level due to a continual drawdown toward the river. The result was a steadier decrease in water level for LRW001.

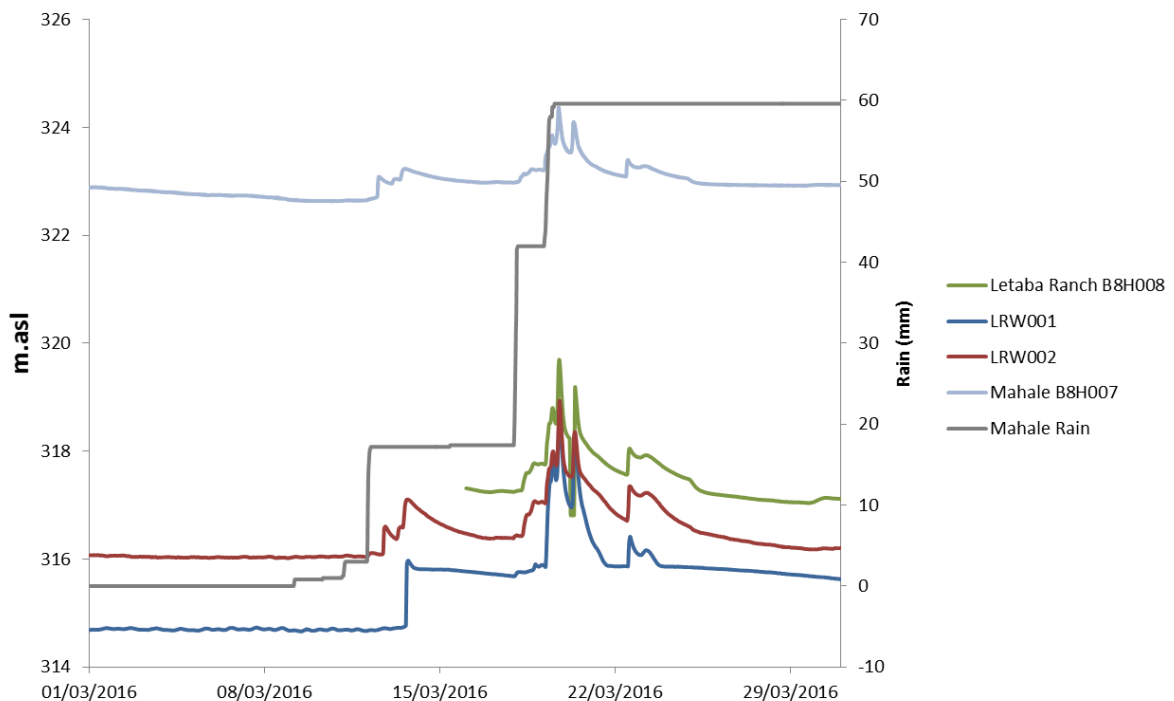


Figure 77: Groundwater-streamflow processes across dolerite dyke (Note: The dyke also has concrete wall built upon it as part of the rating structure for the Letaba Ranch gauge B8H008)

5.4.3 Conceptual model

The conceptual model of the Letaba River area illustrates the variation in earth materials – both vertically and spatially, which is important in inferring the spatial distribution of hydrological parameters, including the fluid logging data. The study area consists mainly of a two-layer system: the shallow, weathered-fractured unit with a thickness of approximately 10 m, and the deeper, unweathered fractured and faulted granitic unit (Figure 78 to Figure 81). The transition zone from weathered to unweathered is depicted with a black dotted line in the conceptual models that follow.

The hydraulic conductivity of the deep unweathered zone ranges between 0.0015 m/d and 0.002 m/d and is regarded as low yielding. The high salinity of this zone (electrical conductivity ranges from 5000–17 000 μS) suggests limited throughflow.

The weathered-fractured zone unit (above the dotted line in Figure 79) shows slightly higher yields with hydraulic conductivity values ranging between 0.17 m/d and 0.41 m/d. This higher yielding weathered zone shows freshening out after rainfall events, which suggests infiltration and throughflow. Furthermore, the general electrical conductivity values measured within the weathered zone (1500–4000 μS) are fairly low in relation to the higher electrical conductivity values (toward 17 000 μS) in the unweathered zone. The groundwater levels are fairly flat with a difference in height of less than 2 m on both sides of the river as seen in the conceptual model in Figure 78.

The weathered zone illustrated in the conceptual cross sections of the Letaba River varies in depth from the farming and natural reserve areas toward the river. The general depth of the weathered zone is 10 m, which gets shallower toward the river channel. However, there are some anomalies as seen from the following geophysics interpretations where the weathered zone is as deep as 30 at specific points.

The weathering depths on the cross-section for Transect 1 (Figure 78) are deepest where the boreholes were drilled and gets shallower toward the river as it flattens out at a depth of approximately 10 m. The weathering depth correlates with the riverbed.

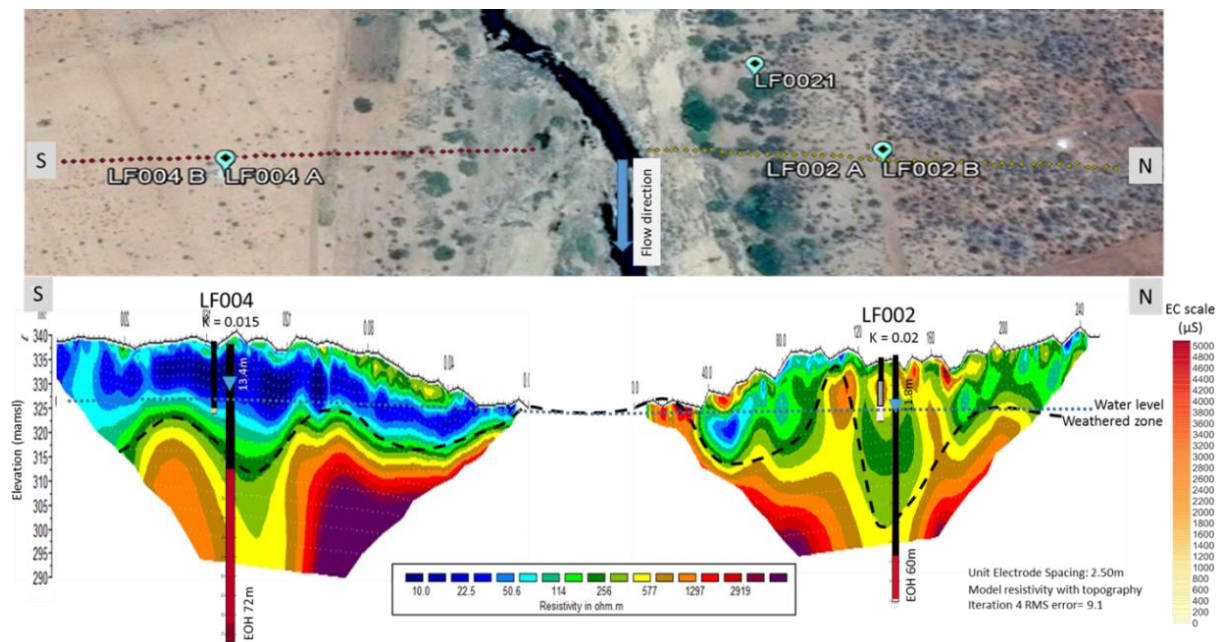


Figure 78: Conceptual model of cross-section LF004–LF002 (Transect 1 – see Figure 30)

Weathering depths in the cross-section of Transect 2 (Figure 79) are generally deeper than in the cross-section of Transect 1. The calculated hydraulic conductivity at each borehole is higher with lower electrical conductivity values.

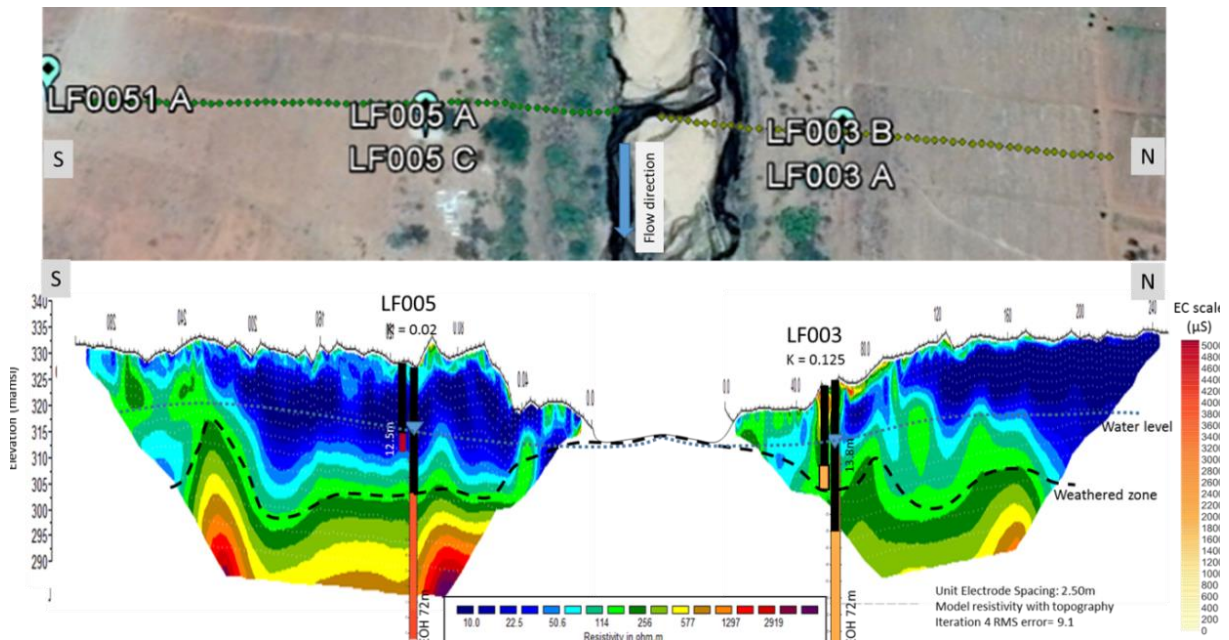


Figure 79: Conceptual model of cross-section LF005-LF003 (Transect 2 – see Figure 30)

At Transect 4 (Figure 80), the weathering depths are approximately 20 m on the southern side of the river with high yields and low electrical conductivity values, whereas weathering on the northern side of the river ranges between 5–10 m depth. High electrical conductivity values suggest limited throughflow.

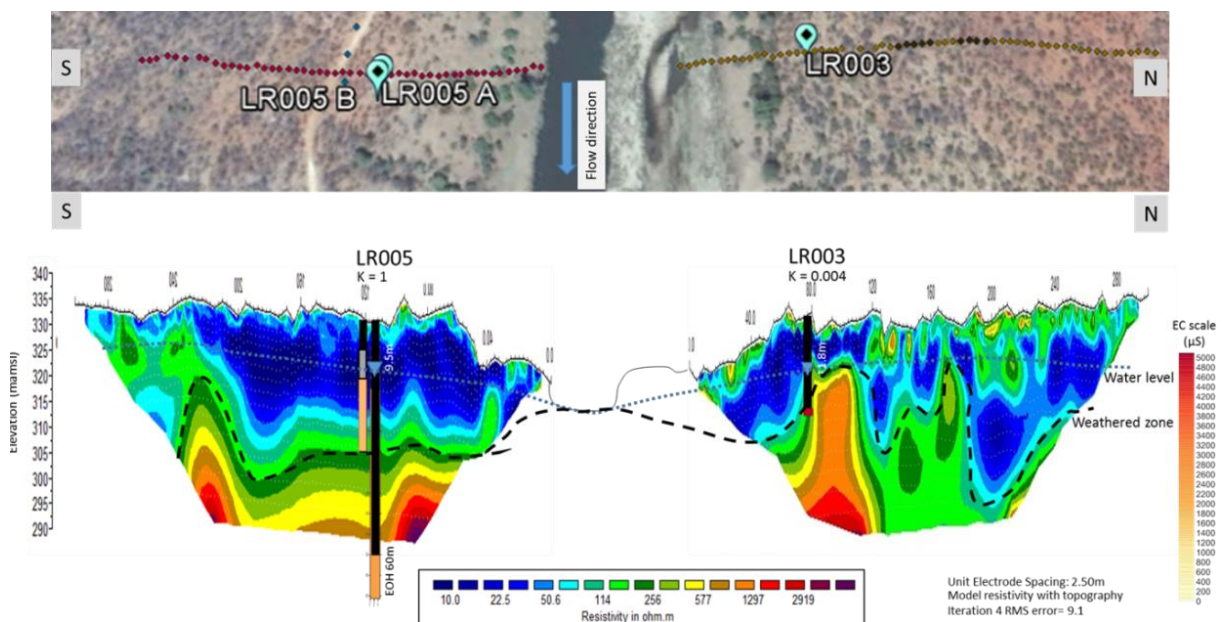


Figure 80: Conceptual model of cross-section LR005-LR003 (Transect 4 – see Figure 30)

The general weathering depths at the cross-section of Figure 81 are shallow and range between 5 m and 10 m. The deepest weathered depth is 15 m. The electrical conductivity values are fairly low, which suggest higher throughflow although the calculated hydraulic conductivity appears to be low.

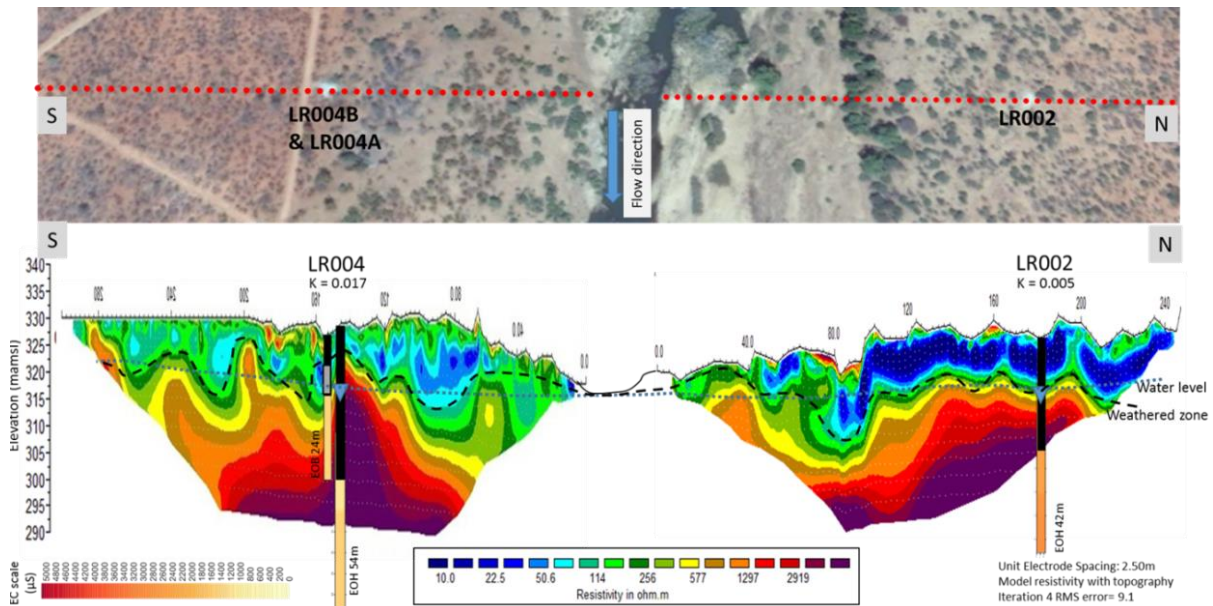


Figure 81: Conceptual model of cross-section LR004–LR002 (Transect 3 – see Figure 30)

The previous sections have detailed the hydrometric results from the piezometric borehole network. Based on this and the fluid logging results from the boreholes, hydrometric time series, and three longitudinal hydrochemical profiles of the entire river reach (Figure 11), it is possible to present a conceptual model for the study site from a geohydrological perspective (Figure 82).

Figure 11 compares the survey of November 2014, which can be considered representative of the dry season, but following a wet cycle climatically. The October 2015 survey (also in the dry season) also follows a significantly below-average rainfall year. This figure reveals two interesting aspects. The first being the apparently lower electrical conductivity in the November 2014 survey, with a clear increase in electrical conductivity in the river reach represented by the LF003–LF005 transect in the farming area, which then returns to a lower electrical conductivity further downstream. This contrasts with the higher electrical conductivity throughout in October 2015 with no electrical conductivity elevation at the LF003–LF005 transect. By the time of the third survey in April 2016, electrical conductivity had lowered significantly and remained so throughout the longitudinal profile.

Two factors may explain this: low flows in the Letaba River were significantly lower in the 2015 survey (<0.5 m³ at Letaba Ranch) compared to the former in 2014 (~1.0 m³ at Letaba Ranch), which are therefore subject to greater concentration of salts from natural processes as well as anthropogenic activities (the low electrical conductivity values in the April 2016 survey are likely a result of the March 2016 flood event). The year 2014–2015 being a low rainfall year may have prevented a significant hydraulic gradient from the weathered zone and disturbed landscapes of the farming region on the northern bank of the river (LF003–LF0031). This hydraulic gradient would have reduced during the very dry period of 2015–2016. This is of course speculative as we have no groundwater observations to verify for the early period, but certainly an aspect to consider in long-term monitoring of the site.

Meanwhile, other aspects to consider from the fluid logging include the low electrical conductivity readings for LF002, which suggest continuous connection to river surface water at least in the November 2015 survey. This implies losses to the northern bank in the most upstream part of the study and the hydraulic gradient data supports this. Moreover, LF004 on the southern side of the river shows increasing electrical conductivity to a depth of 30 m with corresponding increase in temperature with depth. This is seen in both fluid logging surveys, suggesting sustained groundwater contributions from elsewhere in the landscape.

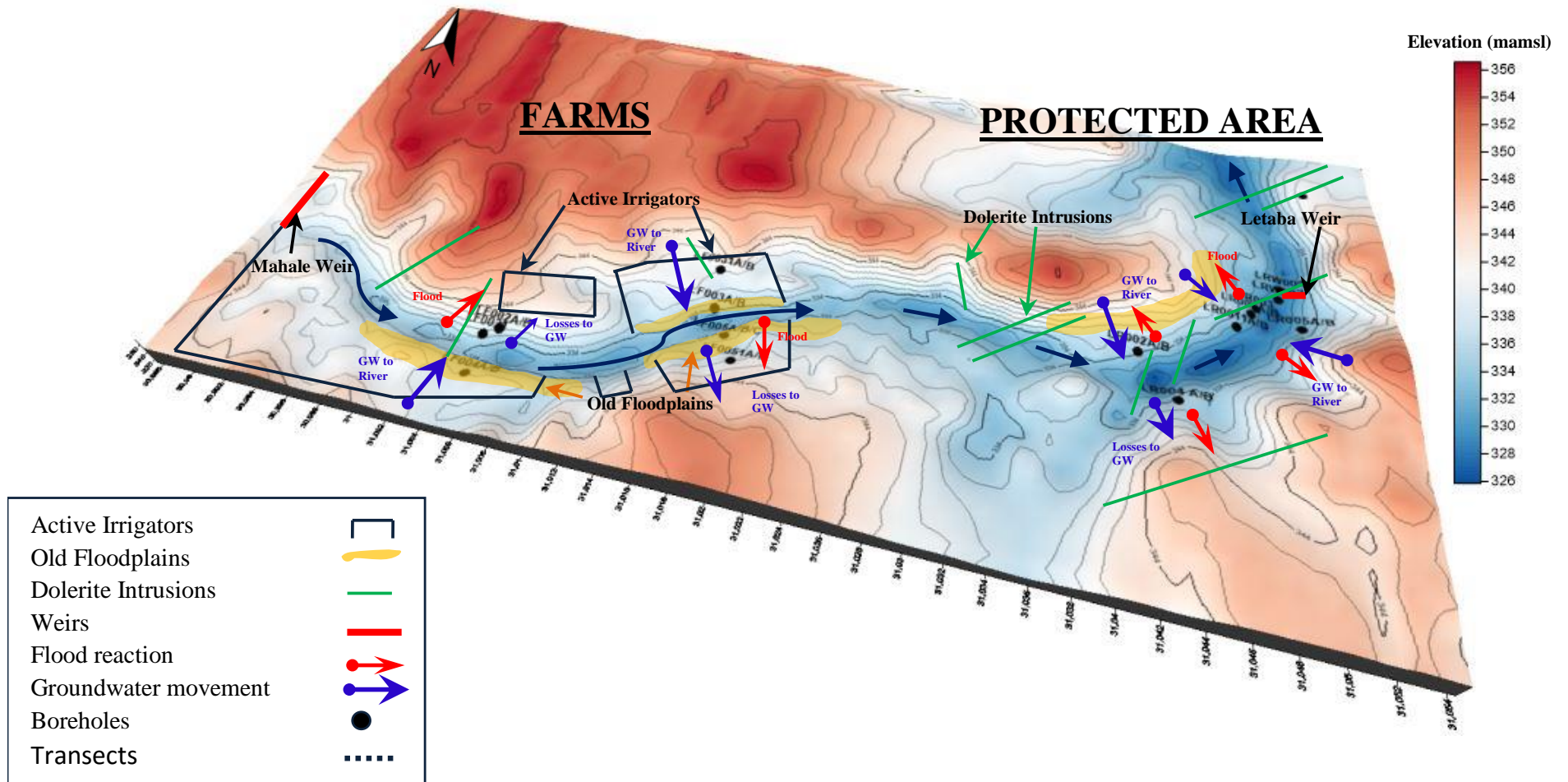


Figure 82: Conceptual model of gehydrological process connectivity along the Groot Letaba River study site

At the lowest end of the study site, the fluid logs suggest that there is a sustained groundwater contribution from the northerly directions into the river channel, as suggested by decreasing temperature and stable electrical conductivity with depth at LR001. Similar observations in the boreholes at LR005 also support sustained groundwater contributions to surface flow in the river from a southerly direction. The new data from the flood event of March 2016 also suggests that the river recharge from the groundwater can be reversed during peak flow especially at the lower end of the study site within the protected areas.

5.5 Stable Isotopes in the Riparian Zone

5.5.1 Isotopic composition of rainfall

The $\delta^2\text{H}$ in rainfall ranged from -22.9‰ to 15.3‰ , with a mean value of 0.2‰ ($\pm 11.6\text{‰}$). However, $\delta^{18}\text{O}$ in rainfall ranged from -4.3‰ to 0.9‰ , with a mean value of -1.7‰ ($\pm 1.6\text{‰}$). The LMWL for our study site, as shown in Figure 83, was established as $\delta^2\text{H} = 7.06\delta^{18}\text{O} + 12.13$, with an R^2 value of 0.89. The slope of the LMWL is lower than the slope of the global meteoric water line (GMWL), which were described respectively by Craig (1961) and Liu et al. (2014) as $\delta^2\text{H} = 8\delta^{18}\text{O} + 10$ and $\delta^2\text{H} = 7.94\delta^{18}\text{O} + 3.92$.

The lower slope of the LMWL can be attributed to rapid evaporation of falling raindrops (Ma & Song, 2016), which would be expected in this semi-arid region. It is also quite clear that the rainfall during the study period was dominated by convective rainfall with lighter isotopes – the exception being the rain of March 2016, which had a much more depleted signature.

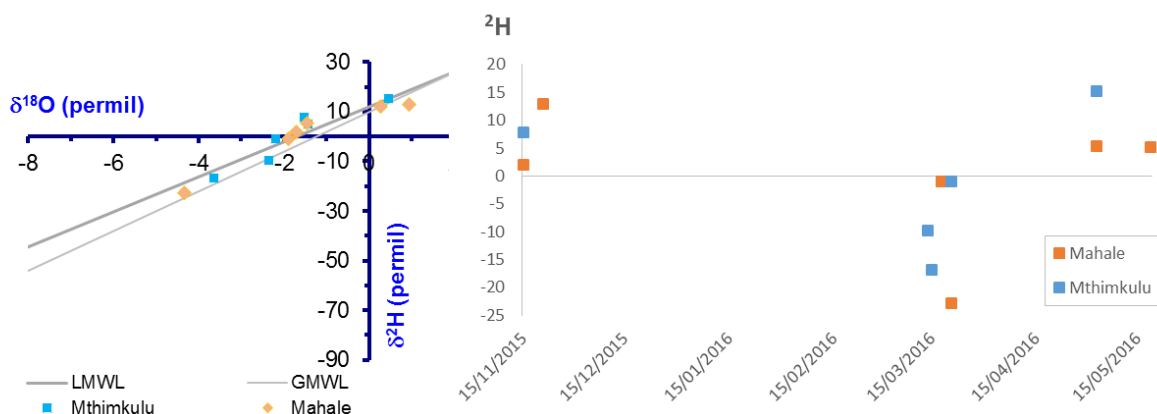


Figure 83: Stable isotopes of rainfall during the study period against GMWL (left) and time series (right)

5.5.2 Isotopic composition of riparian zone water

The $\delta^2\text{H}$ in rainfall ranged from -22.9‰ to 15.3‰ , with a mean value of 0.2‰ ($\pm 11.6\text{‰}$). However, $\delta^{18}\text{O}$ in rainfall ranged from -4.3‰ to 0.9‰ , with a mean value of -1.7‰ ($\pm 1.6\text{‰}$). The LMWL for our study site, as shown in Figure 84, was established as $\delta^2\text{H} = 7.06\delta^{18}\text{O} + 12.13$, with an R^2 value of 0.89. The slope of the LMWL is lower than the slope of the GMWL, described respectively in Craig (1961) and Liu et al. (2014), as $\delta^2\text{H} = 8\delta^{18}\text{O} + 10$ and $\delta^2\text{H} = 7.94\delta^{18}\text{O} + 3.92$.

The lower slope of the LMWL can be attributed to rapid evaporation of falling raindrops (Ma & Song, 2016), which would be expected in this semi-arid region. Rainfall during the study period was generally dominated by convective rainfall with lighter isotopes.

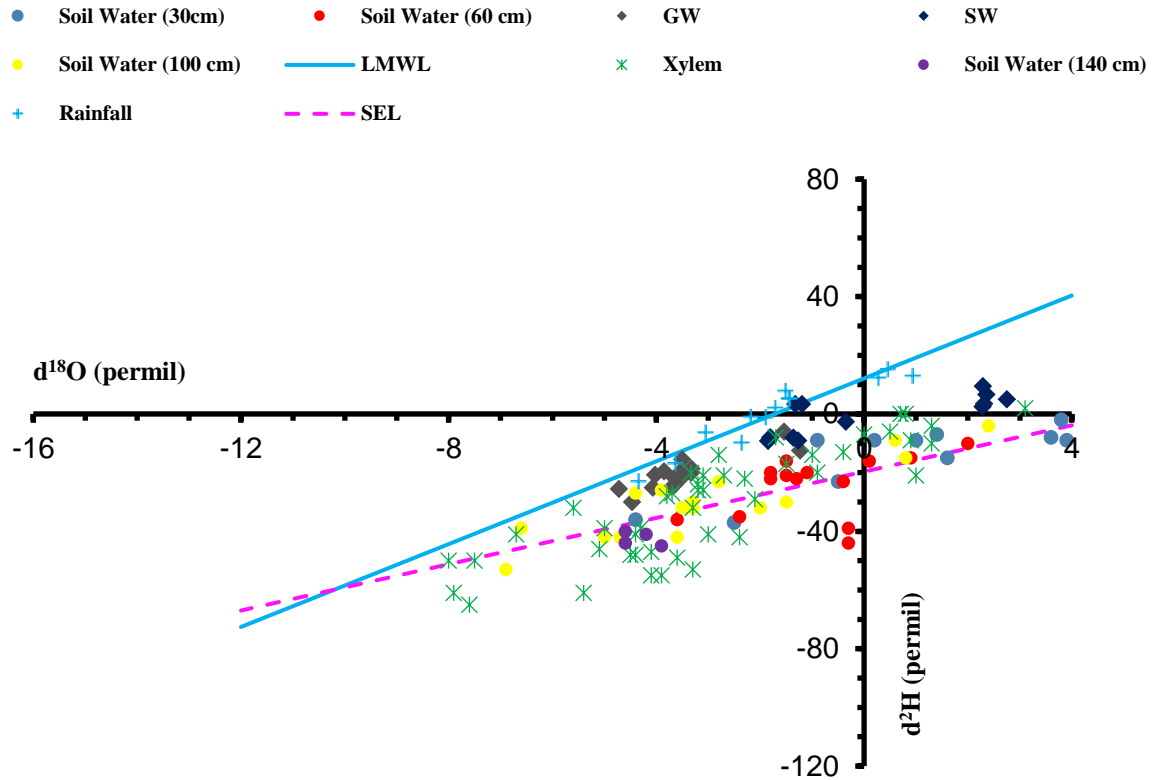


Figure 84: A plot of the relationship between $\delta^2\text{H}$ and $\delta^{18}\text{O}$ values for all the study samples

GW = groundwater; SW = stream water

The $\delta^2\text{H}$ and $\delta^{18}\text{O}$ of streamflow, soil water and xylem water plot below the LMWL that show evaporative enrichment in these samples relative to rainfall are shown in Figure 3. The $\delta^2\text{H}$ and $\delta^{18}\text{O}$ values for groundwater plot closest to the LMWL providing evidence that precipitation is one of the principal sources contributing to groundwater. $\delta^2\text{H}$ in-stream water ranged from -9.16‰ to 9.48‰ , with a mean value of -1.32‰ ($\pm 6.78\text{‰}$). However, $\delta^{18}\text{O}$ in-stream water ranged from -1.85‰ to 2.75‰ , with a mean value of 0.19 ($\pm 1.79\text{‰}$). The $\delta^{18}\text{O}$ and $\delta^2\text{H}$ in-stream water are generally relatively enriched in comparison to the other samples, which indicates a strong evaporation effect.

The $\delta^2\text{H}$ in soil water (30 cm, 60 cm, 100 cm and 140 cm) ranged from -53‰ to 7‰ , with a mean value of -23.95‰ ($\pm 14.89\text{‰}$). The $\delta^{18}\text{O}$ in soil water (30 cm, 60 cm, 100 cm and 140 cm) ranged from -6.9‰ to 7.9‰ with a mean value of -1.06‰ ($\pm 3.25\text{‰}$). The $\delta^2\text{H}$ and $\delta^{18}\text{O}$ in soil water were enriched in the top soil layers and generally depleted with depth. Mean $\delta^2\text{H}$ and $\delta^{18}\text{O}$ values for soil water in the upper soil layers (between 0 cm and 60 cm) were -17.77‰ ($\pm 12.91\text{‰}$) and 0.41‰ ($\pm 2.93\text{‰}$), respectively. Mean $\delta^2\text{H}$ and $\delta^{18}\text{O}$ values for soil water in the deeper soil layers (between 60 cm and 140 cm) were more negative with $\delta^2\text{H}$ of -33.23 ($\pm 12.66\text{‰}$) and $\delta^{18}\text{O}$ of -3.27 ($\pm 2.35\text{‰}$), respectively. The lower slope of the fitting line of the soil water $\delta^2\text{H}$ and $\delta^{18}\text{O}$ (SEL) relationship in comparison to the LMWL as shown in Figure 3, is indicative of the strong evaporation effect on soil moisture

The $\delta^2\text{H}$ in xylem water ranged from -65.0‰ to -6.0‰ , with a mean value of -28.7‰ ($\pm 19.66\text{‰}$). The $\delta^{18}\text{O}$ in xylem water ranged from -8.0‰ to 6.2‰ , with a mean value of -2.51‰ ($\pm 3.17\text{‰}$). The $\delta^2\text{H}$ and $\delta^{18}\text{O}$ values of xylem water generally plot closer to the SEL relationship, which indicate that soil water is one of the main contributors to vegetation during transpiration.

5.5.3 Proportional contribution of potential water sources to plant water use during transpiration

In this study, Simmr was proposed to quantify the proportional contribution of the various water sources to plant water uptake during transpiration. The isotopic composition of soil water at the various sampling depths were generally distinguishable; therefore, the measured $\delta^2\text{H}$ and $\delta^{18}\text{O}$ values at each depth were treated as separate sources. The input data to Simmr was the measured $\delta^2\text{H}$ and $\delta^{18}\text{O}$ for xylem water, soil water (30 cm, 60 cm, 100 cm and 140 cm), groundwater and stream water. According to Philips (2012), the isotopic composition of $\delta^2\text{H}$ and $\delta^{18}\text{O}$ in the xylem water must fall between those of the potential water source end members in order to be explained as a mixture of them.

The model is able to compute a mathematical solution of the proportion of sources that sum to 1 if the aforementioned condition is not met. The proportion of one of the sources will be negative, while the proportion of one of the remaining sources will be greater than 1; neither of which is hydrologically possible (Philips, 2012). According to Philips (2012), all possible water sources must be accounted for during the analysis of proportional use through the implementation of a mixing model. Failure to do so will bias the apparent proportions of water from the other sources.

Furthermore, this may even result in no combinations of the included sources that are consistent with the isotopic composition of the xylem water (Philips, 2012). In such circumstances it is highly probable that there is an additional source that has not been considered, or a degree of uncertainty associated with the isotopic composition of $\delta^2\text{H}$ and $\delta^{18}\text{O}$ in the xylem water or the sources remains.

In general, the $\delta^2\text{H}$ and $\delta^{18}\text{O}$ in the xylem water of our samples fall between those of the potential water source end members in order to be explained as a mixture of them. This is shown in the simple end member plot Figure 86. Only the $\delta^2\text{H}$ and $\delta^{18}\text{O}$ values pertaining to the xylem water that fell between those of the potential water source end members were used as inputs to Simmr in order to quantify the potential contribution of water from a particular source at these particular sampling points during plant water uptake. The average contribution of soil water (30 cm, 60 cm, 100 cm and 140 cm), groundwater and stream water to plant water uptake for each of the aforementioned tree species, estimated at the 50th percentile is given in Table 11.

Deeper soil water (100 cm to 140 cm) has been shown to be the major contributing source to plant water uptake during the period of investigation. There is a clear change in the water use strategies of vegetation in the study area as the seasons progress, as shown in Table 12.

In addition to the seasonal changes in the water use strategies of vegetation in the study area, there were also noticeable differences in water use dynamics of vegetation at the various sampling locations, as well as according to the individual vegetation species, as indicated in Table 11 and Table 12.

The results shown in Figure 85, Figure 86 and Table 11 indicate that during the investigation period, deeper soil water was the major contributing source to plant water uptake and accounted for approximately 95% of water during transpiration.

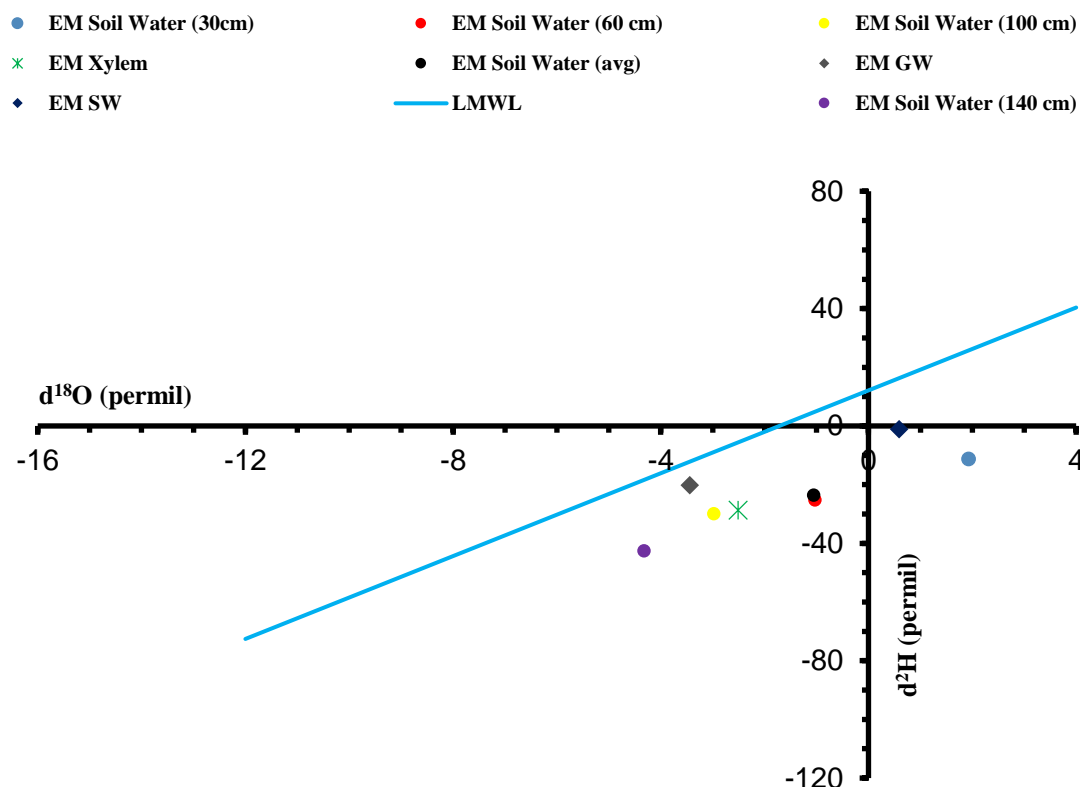


Figure 85: A plot of the relationship between $\delta^2\text{H}$ and $\delta^{18}\text{O}$ simple end member values for all study samples

GW = groundwater; SW = stream water

Table 11: Average contribution of sources to plant water uptake investigation period (May to October 2017)

Period	Ground-water	Surface water	Soil water (30 cm)	Soil water (60 cm)	Soil water (100 cm)	Soil water (140 cm)
May–October 2016	1.50%	1.70%	1.70%	1.80%	68.30%	24.00%

Deeper soil water (100 cm to 140 cm) has been shown to be the major contributing source to plant water uptake during the period of investigation. There is a clear change in the water use strategies of vegetation in the study area as the seasons progress, as shown in Table 12.

Table 12: Contribution of sources to plant water uptake under different environmental conditions (during each field campaign), estimated at the 50th percentile

Period	Ground-water	Surface water	Soil water (30 cm)	Soil water (60 cm)	Soil water (100 cm)	Soil water (140 cm)
May (Late Autumn)	0.10%	0.10%	0.10%	0.10%	46.40%	53.10%
Aug (Late Winter)	10.00%	6.00%	12.00%	17.00%	38.40%	13.00%
Oct (Early Spring)	8.00%	7.00%	8.00%	9.00%	10.00%	54.40%

In addition to the seasonal changes in the water use strategies of vegetation in the study area, there were also noticeable differences in water use dynamics of vegetation at the various sampling locations, as well as according to the individual vegetation species, as indicated in Table 13 and Table 14.

Table 13: Average contribution of sources to plant water uptake at each sampling location during the period of investigation (May to Oct 2017)

Sampling location	Ground-water	Surface water	Soil water (30 cm)	Soil water (60 cm)	Soil water (100 cm)	Soil water (140 cm)
1	2.40%	1.80%	2.70%	3.90%	62.70%	24.40%
2	3.70%	2.60%	4.30%	4.20%	80.60%	2.70%
3	0.50%	0.40%	0.50%	0.60%	2.50%	95.00%
4	1.30%	1.70%	1.40%	1.50%	56.70%	36.40%
5	0.20%	0.20%	0.20%	0.30%	52.20%	46.70%
6	3.40%	1.90%	4.60%	55.51%	5.00%	27.50%

Table 14: Average contribution of sources to individual plant species during the period of investigation (May to October 2017)

Tree species	Ground-water	Surface water	Soil water (30 cm)	Soil water (60 cm)	Soil water (100 cm)	Soil water (140 cm)
<i>F. sycomorus</i>	1.50%	1.70%	1.60%	1.70%	72.40%	20.20%
<i>P. violacea</i>	4.40%	3.50%	4.90%	5.60%	73.60%	5.40%
<i>D. mespiliformis</i>	2.30%	2.90%	2.60%	2.80%	70.00%	17.50%
<i>C. mopane</i>	1.10%	0.70%	1.50%	2.00%	3.80%	89.50%
<i>C. microphyllum</i>	1.20%	0.90%	1.50%	1.90%	16.10%	77.50%
<i>G. senegalensis</i>	1.50%	1.70%	1.60%	1.80%	67.00%	25.40%
<i>Z. mucronata</i>	1.10%	0.60%	1.50%	2.00%	3.30%	90.00%
<i>P. mauritanus</i>	N/A	8.50%	66.50%	5.70%	10.40%	6.10%

The $\delta^2\text{H}$ and $\delta^{18}\text{O}$ values for soil water were enriched in the upper soil layers (between 0 cm and 60 cm) and generally depleted with depth. The higher levels of enrichment associated with the $\delta^2\text{H}$ and $\delta^{18}\text{O}$ values of soil water in the upper soil layers are due to the effects of evaporation. Higher levels of depletion generally associated with the $\delta^2\text{H}$ and $\delta^{18}\text{O}$ values of soil water deeper down the profile could presumably be attributed to isotopically depleted heavy rainfall events that have not been accounted for during sampling, or which fell prior to the commencement of sampling. Infiltration and subsequent deep percolation of this rainfall will influence the isotopic composition of soil water throughout the soil profile (Gazis & Feng, 2004).

In the deeper soil profile, rainfall may enter by travelling vertically down the profile through piston flow, in which older soil water (has not mixed proportionally) is forced to move further downwards under the influence of rainfall from recent precipitation events (Gazis & Feng, 2004). Additionally, rainfall may move along preferential flow paths without interacting with most of the mobile soil water in the soil profile (Gazis & Feng, 2004). Consequently, isotopically depleted heavy rainfall events may have resulted in the depleted isotopic composition of water in deeper soils, while water in the upper soil layers remain enriched due to the influence of evaporation at the surface.

The isotopic composition of $\delta^2\text{H}$ and $\delta^{18}\text{O}$ in the xylem water were shown to generally plot closest to the SEL, indicating that soil water is one of the main contributors to the vegetation during transpiration. The $\delta^2\text{H}$ and $\delta^{18}\text{O}$ values of xylem water were generally concentrated around an uptake depth between

100 cm and 140 cm. The results of implementing the Simmr model to determine the proportional contribution of sources to transpiration indicated that riparian vegetation predominantly used soil water during the study period, with marginal contributions from stream water and groundwater. Soil water at depths of 100 cm and 140 cm were found to be the dominant contributing sources to plant water uptake.

Soil water at these depths was a major contributor to the water use requirements of the tree species sampled in this study. It is evident that over the course of the three sampling campaigns, there has been a change in the water use strategies of the riparian vegetation. There is a noticeable increase in the proportional contribution of groundwater to plant water uptake as the dry season progresses, which indicates that during unfavourable environmental conditions, riparian vegetation accesses alternate sources if available in order to fulfil a portion of their daily water requirements.

In addition to the influence of environmental conditions, the species of riparian vegetation and their respective locations also showed variability in the use of groundwater during plant water uptake. Groundwater may represent a potential water source to plant water uptake, especially during periods in which there is insufficient soil moisture to meet daily water requirements. The accessibility of this resource for consumption is largely controlled by the physical adaptations of the plant/tree species. Furthermore, the depth to groundwater, as well as the physical properties of the soil and underlying aquifer at a particular location, may further influence the accessibility of this resource. Therefore, while groundwater is potentially available for plant water uptake, the aforementioned factors will significantly influence how much of this resource is utilised.

5.6 Total Evaporation

5.6.1 Inter-annual comparison of EC_{ET} for 2015 and 2016

The results presented below discuss the inter-annual comparisons of EC_{ET} measurements. Only those EC_{ET} measurements for the corresponding dates, namely, 17 June to 17 October are presented and discussed. Furthermore, the FAO 56 Penman–Monteith reference evaporation is included in the graphical illustrations and statistical analyses to compare if the ranges of the EC_{ET} measurements are within a similar magnitude as ET_0 .

The results presented in Table 15 and the graphical illustration shown in Figure 86 indicate that the EC_{ET} for 2016 is significantly higher than the EC_{ET} for 2015. The ET measured in 2016 has approximately increased by a factor of 1.7 when compared with the ET measured in 2015 during this period.

The root mean square error (RMSE) indicates that on average the EC_{ET} for 2016 is $1.76 \text{ mm}\cdot\text{d}^{-1}$ higher than the EC_{ET} for 2015. The result of the analysis of variance (ANOVA) test at the 95% confidence level reaffirms that there is a significant difference between the 2015 and 2016 EC_{ET} .

Table 15: Statistical comparison of ET_0 and EC_{ET} for 2015 and 2016

	ET_0 2015	EC_{ET} 2015	ET_0 2016	EC_{ET} 2016
Total	337.72	203.83	357.55	338.51
Average	2.99	1.80	3.16	3.00
Maximum	5.65	4.97	5.80	5.45
Minimum	0.41	0.46	0.27	0.77
Median	2.65	1.08	3.10	2.88
Variance	1.17	1.56	1.07	1.37
Standard deviation	1.08	1.25	1.03	1.17
RMSE				1.76
ANOVA p value				0.00

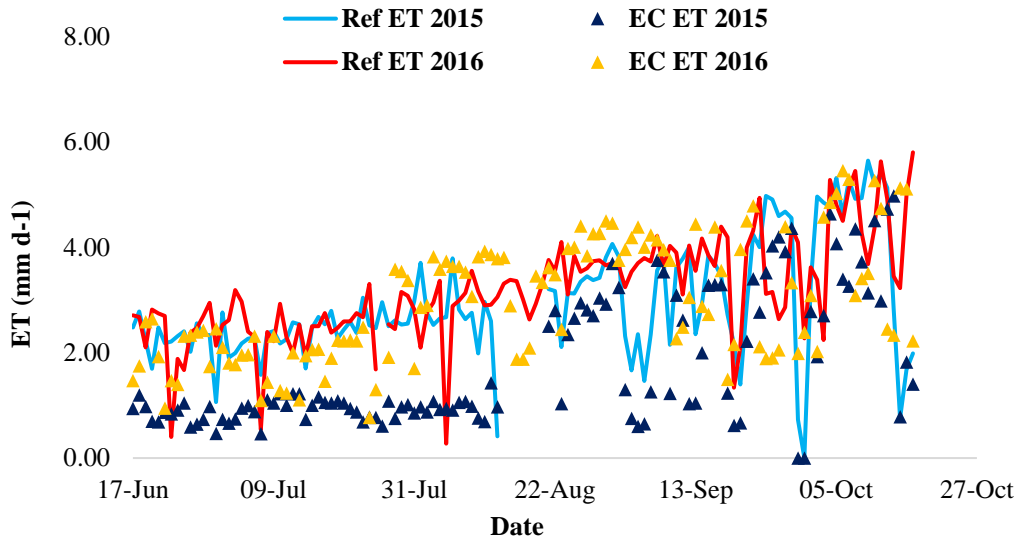


Figure 86: A comparison of ET_0 and EC_{ET} for 2015 and 2016

5.6.2 A comparison of satellite-derived evaporative fraction (EF) and ET against EF and ET measured *in situ* for the period 17 June to 22 October 2015

In order to assess if the evaporative scaling factor for SEBS ($SEBS_{ESF}$) improves the estimation of ET during conditions of water stress, EF and ET computed from electrical conductivity measurements were compared with modelled EF and ET estimates acquired from implementing $SEBS_0$ and $SEBS_{ESF}$ at both the MODIS and Landsat resolutions.

The results of the statistical comparisons (presented in Table 16) indicate that there is a clear overestimation of the $SEBS_0$ EF when compared with the eddy covariance EF (EC_{EF}) – especially for Site 1. However, the implementation of $SEBS_{ESF}$ resulted in a marginally improved agreement overall between the modelled EF and EC_{EF} . The relative volume error (RVE) indicates that, on average, $SEBS_{ESF}$ underestimated the EF by approximately 30% and 20% for Landsat and MODIS, respectively, when compared to the EC_{EF} .

Although the results of the statistical comparisons presented in Table 16 generally show a marginal improvement in the modelled EF when implementing $SEBS_{ESF}$, the modelled EF is now generally underestimated when compared to the EC_{EF} .

Table 16: Statistical comparison of $SEBS_0$ and $SEBS_{ESF}$ EF estimates derived using Landsat and MODIS against EC_{EF} from 17 June to 22 October 2015

	Landsat		MODIS			
	17 June to 22 October 2015	$SEBS_0$ EF	$SEBS_{ESF}$ EF	17 June to 22 October 2015	$SEBS_0$ EF	$SEBS_{ESF}$ EF
RVE		-65.30	29.96	RVE	-76.41	19.63
MAD		0.33	0.23	MAD	-0.19	0.14
RMSE		0.39	0.28	RMSE	0.38	0.24
Kruskal-Wallis (p value)		0.52	0.03	ANOVA (p value)	0.00	0.00
R ²		0.09	0.41	R ²	0.02	0.33
Nash-Sutcliffe		-1.63	-0.42	Nash-Sutcliffe	-2.20	-0.24

The marginal improvement in the modelled EF through the implementation of $SEBS_{ESF}$ subsequently resulted in improved agreement between the modelled ET and EC_{ET} as indicated by the improved imagery.

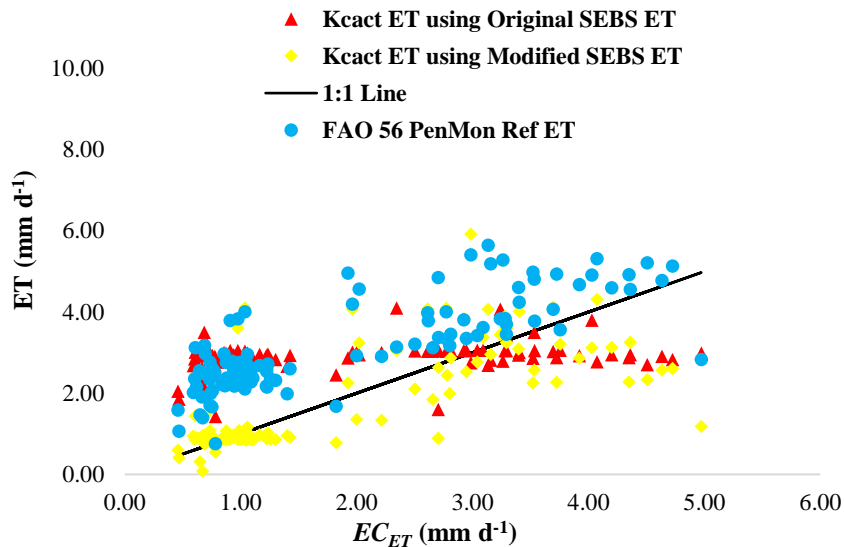


Figure 88 and the results of the statistical comparisons presented in Table 17 indicate that there is an improved agreement overall between the modelled ET and EC_{ET} . The $SEBS_{ESF}$ was able to better capture the ET for Site 1. It is able to capture the ET for Site 2 within a similar level of accuracy as $SEBS_0$.

The R^2 and RMSE values for ET estimates derived using Landsat data in $SEBS_{ESF}$ for the entire period of study improved to 0.65 $\text{mm}\cdot\text{d}^{-1}$ and 0.90 $\text{mm}\cdot\text{d}^{-1}$, respectively, when compared to EC_{ET} . Furthermore, the results of the Kruskal–Wallis test at the 95% confidence level, as well as the R^2 and Nash–Sutcliffe efficiency values, indicate that there is an improved correlation between the EC_{ET} and the ET estimates derived using Landsat data in $SEBS_{ESF}$.

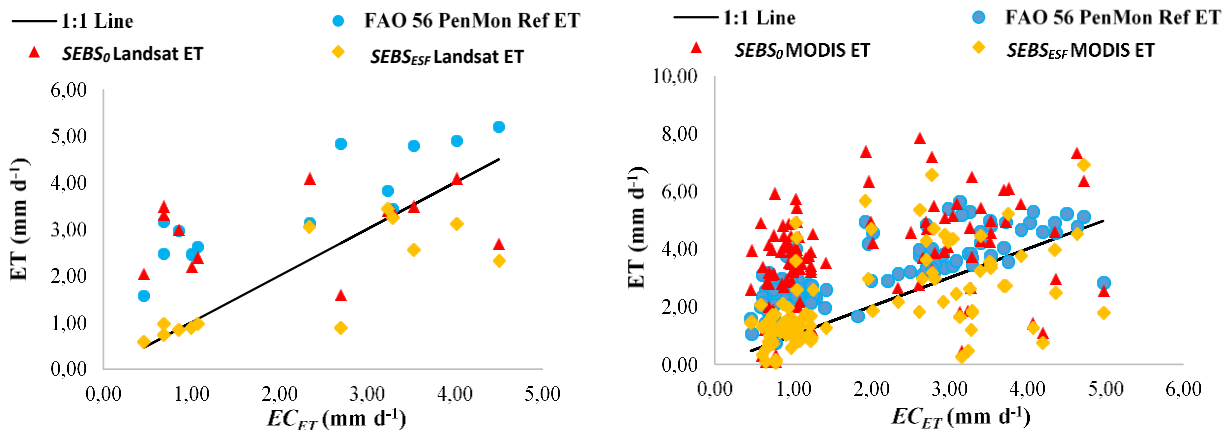


Figure 87: A comparison of the $SEBS_0$ and $SEBS_{ESF}$ derived ET against EC_{ET} from 17 June to 22 October 2015

The R^2 and RMSE values for ET estimates derived using MODIS data in $SEBS_{ESF}$ for the entire period of study improved to 0.31 $\text{mm}\cdot\text{d}^{-1}$ and 1.31 $\text{mm}\cdot\text{d}^{-1}$, respectively, when compared to EC_{ET} . Although the results of the ANOVA test at the 95% confidence level indicate that there is still a significant difference between the EC_{ET} and the ET estimates derived using MODIS data in the modified version of SEBS, the discrepancies between the SEBS ET and EC_{ET} has now decreased as indicated by the increase in the Nash–Sutcliffe efficiency values.

Table 17: Statistical comparison of $SEBS_0$ and $SEBS_{ESF}$ ET estimates derived using Landsat and MODIS against EC_{EF} from 17 June to 22 October 2015

Landsat			MODIS		
Site 1	$SEBS_0$ ET	$SEBS_{ESF}$ ET	Site 1	$SEBS_0$ ET	$SEBS_{ESF}$ ET
RVE	-272.69	-10.34	RVE	-293.24	-46.10
MAD	1.95	0.12	MAD	2.57	0.46
RMSE	2.05	0.29	RMSE	2.74	0.57
Kruskall–Wallis (p value)	0.00	0.75	ANOVA (p value)	0.00	0.28
R ²	0.02	0.58	R ²	0.01	0.01
Nash–Sutcliffe	-96.03	0.52	Nash–Sutcliffe	-194.68	-7.34
Site 2	$SEBS_0$ ET	$SEBS_{ESF}$ ET	Site 2	$SEBS_0$ ET	$SEBS_{ESF}$ ET
RVE	-0.51	18.51	RVE	-65.49	-20.11
MAD	0.72	0.97	MAD	1.98	1.39
RMSE	1.04	1.21	RMSE	2.39	1.80
Kruskall–Wallis (p value)	0.95	0.11	ANOVA (p value)	0.00	0.55
R ²	0.01	0.02	R ²	0.05	0.04
Nash–Sutcliffe	-1.32	-2.05	Nash–Sutcliffe	-3.77	-1.72
17 June to 22 October 2015	$SEBS_0$ ET	$SEBS_{ESF}$ ET	17 June to 22 October 2015	$SEBS_0$ ET	$SEBS_{ESF}$ ET
RVE	-126.14	5.20	RVE	-186.52	-33.51
MAD	1.29	0.58	MAD	2.29	0.89
RMSE	1.59	0.90	RMSE	2.58	1.31
Kruskall–Wallis (p value)	0.13	0.52	ANOVA (p value)	0.00	0.04
R ²	0.10	0.65	R ²	0.09	0.31
Nash–Sutcliffe	-0.31	0.58	Nash–Sutcliffe	-3.38	-0.13

5.6.3 A comparison of downscaled and infilled ET against ET measured *in situ* from 17 June to 22 October 2015

The $K_{C_{act}}$ and output downscaling with linear regression approaches were used to derive ET at an MSR and HTR resolution during the period from 17 June to 22 October 2015. The modelled ET obtained from implementing $SEBS_{ESF}$ was used to provide the requisite input data required for the application of the aforementioned procedures. These estimates were then compared against the EC_{ET} , as well as the previously determined MSR and HTR ET estimates obtained from implementing the $SEBS_0$ formulation.

The comparisons between $K_{C_{act}}$ ET estimates, which were derived from the implementation of the $SEBS_0$ and $SEBS_{ESF}$ against the EC_{ET} , indicated that there was a clear improvement in the

MAD	1.93	0.28
RMSE	1.95	0.59
ANOVA (p value)	0.00	0.16
R ²	0.06	0.01
Nash–Sutcliffe	-97.40	-7.97
Site 2	<i>K_{Cact}</i> ET derived from <i>SEBS₀</i> ET	<i>K_{Cact}</i> ET derived from <i>SEBS_{ESF}</i> ET
RVE	-42.52	2.19
MAD	0.92	0.86
RMSE	1.12	1.17
ANOVA (p value)	0.14	0.20
R ²	0.12	0.31
Nash–Sutcliffe	0.09	0.01
17 June to 22nd Oct 2015	<i>K_{Cact}</i> ET derived from <i>SEBS₀</i> ET	<i>K_{Cact}</i> ET derived from <i>SEBS_{ESF}</i> ET
RVE	-127.98	-6.67
MAD	1.39	0.59
RMSE	1.56	0.95
ANOVA (p value)	0.00	0.00
R ²	0.10	0.51
Nash–Sutcliffe	-0.56	0.43

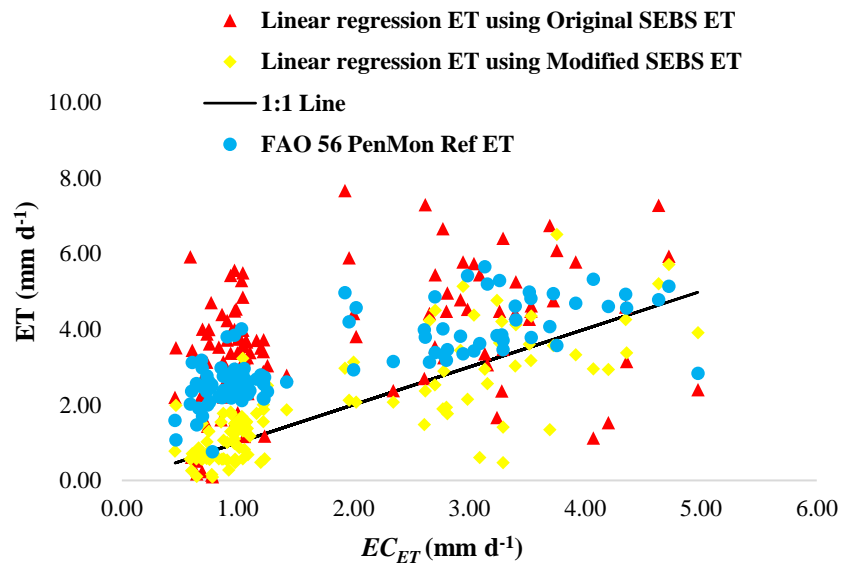


Figure 89 and Table 19, respectively, there is a clear improvement in the performance of the output downscaling with linear regression approach when ET estimates obtained from implementing *SEBS_{ESF}* were utilised.

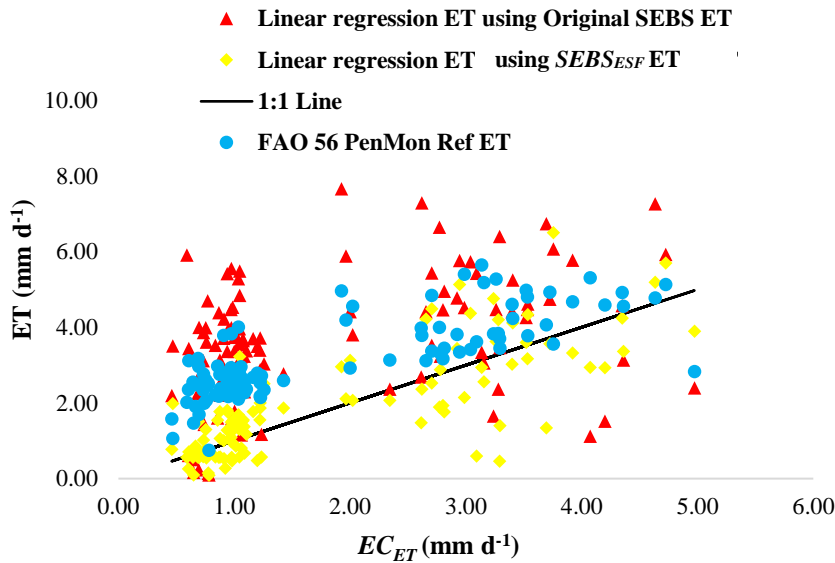


Figure 89: A comparison of the downscaled ET estimates derived from the implementation of $SEBS_0$ and $SEBS_{ESF}$ against EC_{ET} from 17 June to 22 October 2015

The R^2 and RMSE values for the downscaled ET derived from implementing $SEBS_{ESF}$ for the entire period of study improved to $0.59 \text{ mm}\cdot\text{d}^{-1}$ and $0.91 \text{ mm}\cdot\text{d}^{-1}$, respectively, showing a much better agreement with the EC_{ET} . Furthermore, the results of the ANOVA test at the 95% confidence level and Nash–Sutcliffe efficiency values indicate that there is a significant improvement in the correlation between the EC_{ET} and the ET estimates derived using MODIS data in $SEBS_{ESF}$.

In general, the results of the various investigations indicated that the use of ET estimates emanating from $SEBS_{ESF}$ in the Kc_{act} and output downscaling with linear regression approaches results in a considerable improvement to the performance of both these approaches for the estimation of ET at a MSR and HTR over the entire period of study. Therefore, $SEBS_{ESF}$ rather than $SEBS_0$ was implemented to quantify riparian ET in the study area for the 2016 dry season.

Table 19: Statistical comparison of the Kc_{act} ET estimates against EC_{ET} from 17 June to 22 October 2015

Site 1	Downscaled ET derived from $SEBS_0$ ET	Downscaled ET derived from $SEBS_{ESF}$ ET
RVE	-267.27	-21.97
MAD	2.36	0.41
RMSE	2.60	0.51
ANOVA (p value)	0.00	0.01
R^2	0.02	0.17
Nash–Sutcliffe	-175.54	-5.83
Site 2	Downscaled ET derived from $SEBS_0$ ET	Downscaled ET derived from $SEBS_{ESF}$ ET
RVE	-64.50	-5.35
MAD	1.85	0.97
RMSE	2.28	1.20
ANOVA (p value)	0.00	0.92
R^2	0.08	0.34
Nash–Sutcliffe	-3.35	-0.21

17 June to 22 October 2015	Downscaled ET derived from $SEBS_0$ ET	Downscaled ET derived from $SEBS_{ESF}$ ET
RVE	-170.62	-14.05
MAD	2.12	0.67
RMSE	2.45	0.91
ANOVA (p value)	0.00	0.24
R ²	0.14	0.59
Nash–Sutcliffe	-2.97	0.46

5.6.4 A comparison of satellite-derived ET against EC_{ET} from 19 May to 11 November 2016

As shown in Figure 90 and Table 20, the implementation of $SEBS_{ESF}$ results in a marginal improvement in the overall agreement between the modelled ET and EC_{ET} . The R² and RMSE values for ET estimates derived using Landsat data in $SEBS_{ESF}$ for the entire period of study improved to 0.26 mm·d⁻¹ and 1.12 mm·d⁻¹, respectively, when compared to EC_{ET} .

The R² and RMSE values for ET estimates derived using MODIS data in $SEBS_{ESF}$ for the entire period of the study improved to 0.27 mm·d⁻¹ and 1.26 mm·d⁻¹, when compared to EC_{ET} . Furthermore, the results of the Kruskal–Wallis and ANOVA test at the 95% confidence level, as well as the increase in Nash–Sutcliffe efficiency values, indicate that the discrepancies between the EC_{ET} and the modelled ET estimates have decreased marginally.

Table 20: Statistical comparison of $SEBS_0$ and $SEBS_{ESF}$ ET estimates derived using Landsat and MODIS against EC_{ET} from 19 May to 11 November 2016

Landsat			MODIS		
19 May to 11 November 2016	$SEBS_0$ ET	$SEBS_{ESF}$ ET	19 May to 11 November 2016	$SEBS_0$ ET	$SEBS_{ESF}$ ET
RVE	-8.69	-1.95	RVE	-24.60	0.49
MAD	0.93	0.86	MAD	1.26	0.99
RMSE	1.16	1.12	RMSE	1.55	1.26
Kruskal–Wallis (p value)	0.85	0.87	ANOVA (p value)	0.01	0.17
R ²	0.24	0.26	R ²	0.08	0.27
Nash–Sutcliffe	0.02	0.10	Nash–Sutcliffe	-0.89	-0.24

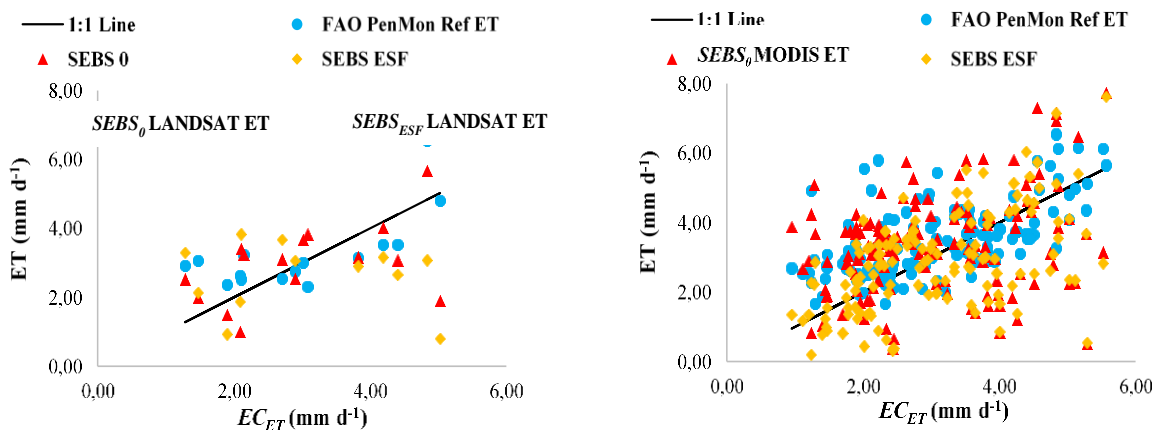


Figure 90: A comparison of the $SEBS_0$ and $SEBS_{ESF}$ derived ET against EC_{ET} from 19 May to 11 November 2016

The results shown in Table 21 indicate that while the implementation of $SEBS_{ESF}$ marginally improved the K_{act} ET estimated at Site 1, there was a marginal increase in the discrepancies between the EC_{ET} and modelled ET for Site 2, as well as over the entire study period. However, the results of the ANOVA test at the 95% confidence interval for the entire study period show that there is no significant difference between the EC_{ET} and K_{act} ET estimates.

Table 21: Statistical comparison of K_{act} ET estimates against EC_{ET} from 19 May to 11 November 2016

Site 1	K_{act} ET derived from $SEBS_0$ ET	K_{act} ET derived from $SEBS_{ESF}$ ET
RVE	-33.60	-25.50
MAD	0.87	0.72
RMSE	0.97	0.89
ANOVA (p value)	0.00	0.00
R ²	0.34	0.37
Nash–Sutcliffe	-1.82	-0.81
Site 2	K_{act} ET derived from $SEBS_0$ ET	K_{act} ET derived from $SEBS_{ESF}$ ET
RVE	-8.50	2.39
MAD	0.82	0.95
RMSE	1.07	1.22
ANOVA (p value)	0.36	0.02
R ²	0.18	0.04
Nash–Sutcliffe	-0.13	-0.47
19 May to 11 November 2016	K_{act} ET derived from $SEBS_0$ ET	K_{act} ET derived from $SEBS_{ESF}$ ET
RVE	-19.20	-9.52
MAD	0.84	0.85
RMSE	1.09	1.09
ANOVA (p value)	0.00	0.94
R ²	0.34	0.22
Nash–Sutcliffe	0.07	0.07

The results shown in Table 22 indicate that while the implementation of $SEBS_{ESF}$ only marginally improved downscaled ET estimates at Site 1, there was a significant improvement between the EC_{ET} and modelled ET for Site 2, as well as over the entire study period.

The R² and RMSE values for the downscaled ET derived from implementing $SEBS_{ESF}$ for the entire period of study improved to 0.43 mm·d⁻¹ and 1.12 mm·d⁻¹, respectively, showing a much better agreement with the EC_{ET} . However, the results of the ANOVA test at the 95% confidence interval show that there is still a significant difference between the downscaled ET estimates and EC_{ET} over the entire study period.

Table 22: Statistical comparison of the K_{cact} ET estimates against EC_{ET} from 17 June to 22 October 2015

Site 1	Downscaled ET derived from $SEBS_0$ ET	Downscaled ET derived from $SEBS_{ESF}$ ET
RVE	-60.40	-28.30
MAD	1.15	0.97
RMSE	1.43	1.03
ANOVA (p value)	0.00	0.00
R ²	0.01	0.12
Nash–Sutcliffe	-3.61	-1.40
Site 2	Downscaled ET derived from $SEBS_0$ ET	Downscaled ET derived from $SEBS_{ESF}$ ET
RVE	-7.64	-0.05
MAD	1.24	0.87
RMSE	1.55	1.19
ANOVA (p value)	0.37	0.74
R ²	0.01	0.12
Nash–Sutcliffe	-1.36	-0.40
19 May to 11 November 2016	Downscaled ET derived from $SEBS_0$ ET	Downscaled ET derived from $SEBS_{ESF}$ ET
RVE	-30.20	-12.10
MAD	1.20	0.93
RMSE	1.50	1.12
ANOVA (p value)	0.00	0.01
R ²	0.16	0.43
Nash–Sutcliffe	-0.75	0.01

5.6.5 Discussion

In order to understand the inter-annual variations seen in the measured ET, the climatic factors that drive ET were analysed to identify any specific trends that may have contributed to the differences in the 2015 and 2016 EC_{ET} values. As ET is mainly a physical process driven by radiation and the vapour pressure deficit (VPD) (Penman, 1948; Xu et al., 2014), measurements of these variables for 2015 and 2016 during the period 17 June to 17 October were compared.

These are shown in Figure 91 to

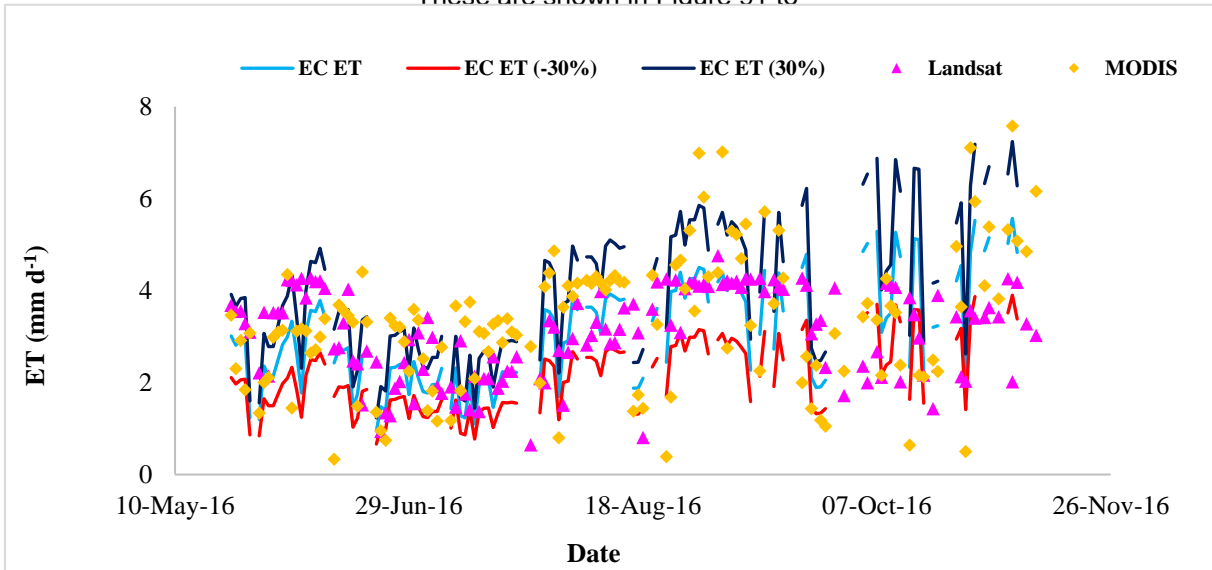


Figure 95. In addition, average temperature measurements during the aforementioned period are shown in Figure 12. The EC_{ET} and FAO 56 Penman–Monteith reference ET values measured at Site 2 were generally higher than at Site 1 for both 2015 and 2016. This is largely due to the influence of climatic factors during this period of investigation. According to Xu et al. (2014), ET is generally positively correlated to climatic factors (radiation, VPD and temperature) and responds rapidly to variations in radiation and VPD (Monteith, 1965). As shown in Figure 91 to

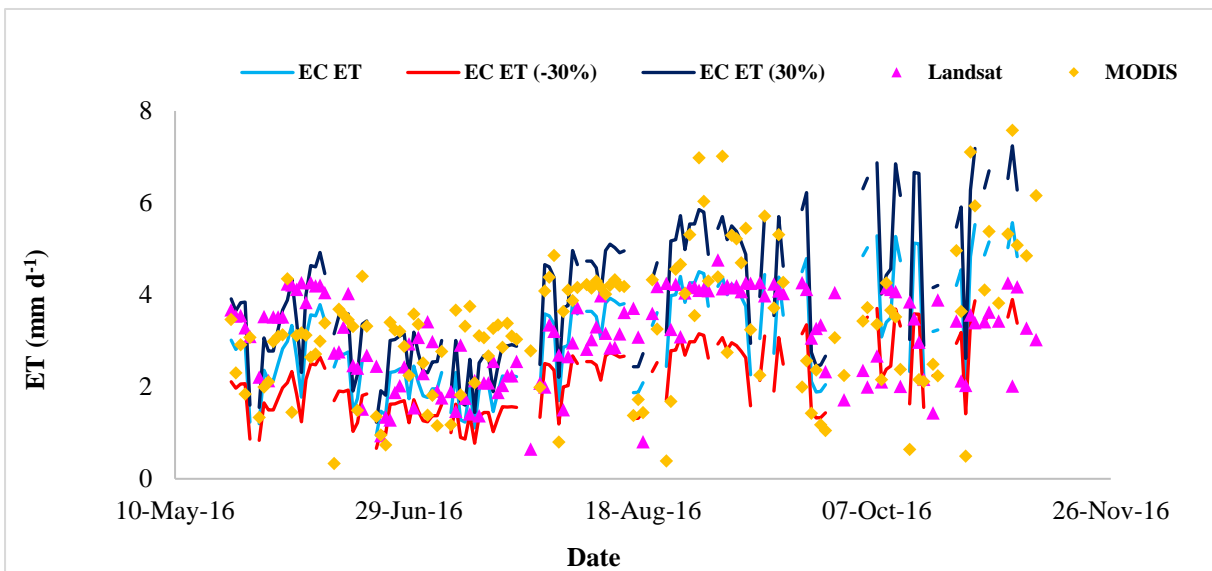


Figure 95, the values for these climatic factors are generally higher for Site 2.

In addition to climatic factors, biotic factors such as leaf area index and stomatal conductance of the canopy, *inter alia*, play a substantial role in driving ET (Bernier et al., 2006; Bucci et al., 2008; Monteith, 1965; Pejam et al., 2006). Assuming that the stomatal conductance of the canopy at both sites is similar (tree species and age of the vegetation is similar for both sites), the greater canopy coverage for Site 2, as well as the higher values associated with the climatic variables at this site, subsequently resulted in a higher daily ET.

The intra-annual variability for 2016 EC_{ET} follows a similar trend to the 2015 EC_{ET} . There is a significant increase in EC_{ET} for 2016. Comparisons between the 2015 and 2016 solar radiation, nett radiation, VPD and temperature (shown in Figure 91 to

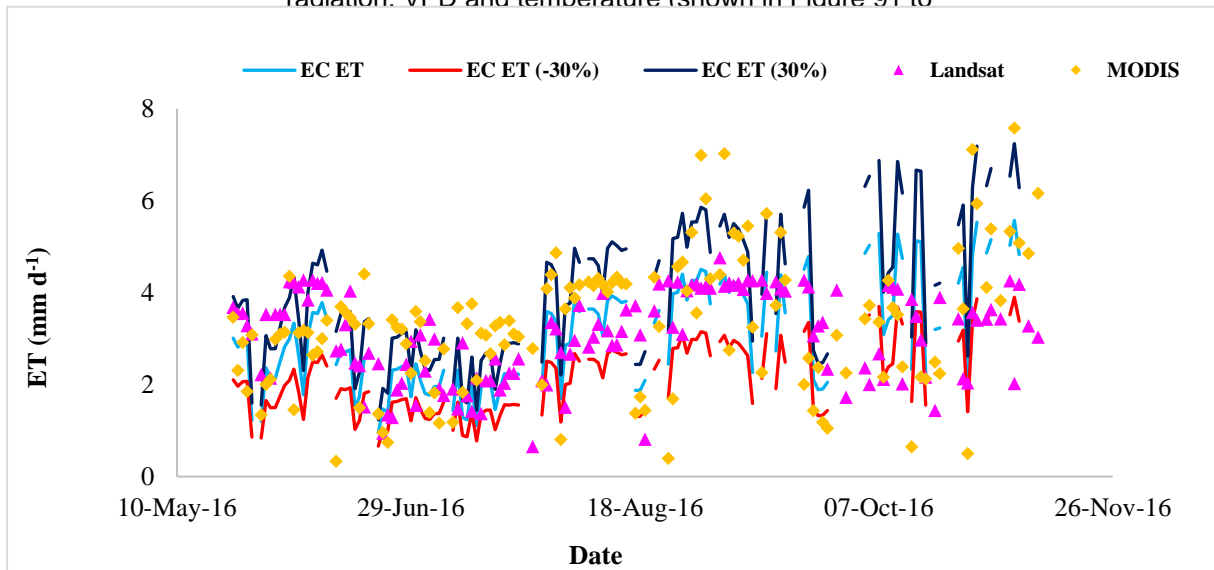


Figure 95) illustrate that in general there are no significant differences in the daily solar radiation, nett radiation and temperature for 2015 and 2016.

However, the daily VPD is significantly higher in 2016. These observations are reaffirmed by the results of the ANOVA test at the 95% confidence interval, shown in Table 23. While there is a significant increase in the VPD for 2016, the 2016 VPD is generally only higher than the 2015 VPD at Site 2.

Table 23: ANOVA test at 95% confidence interval, comparing changes in 2015 and 2016 climatic drivers of ET

	Solar Radiation	Nett Radiation	VPD	Temperature
ANOVA p value	0.61	0.32	0.00	0.94

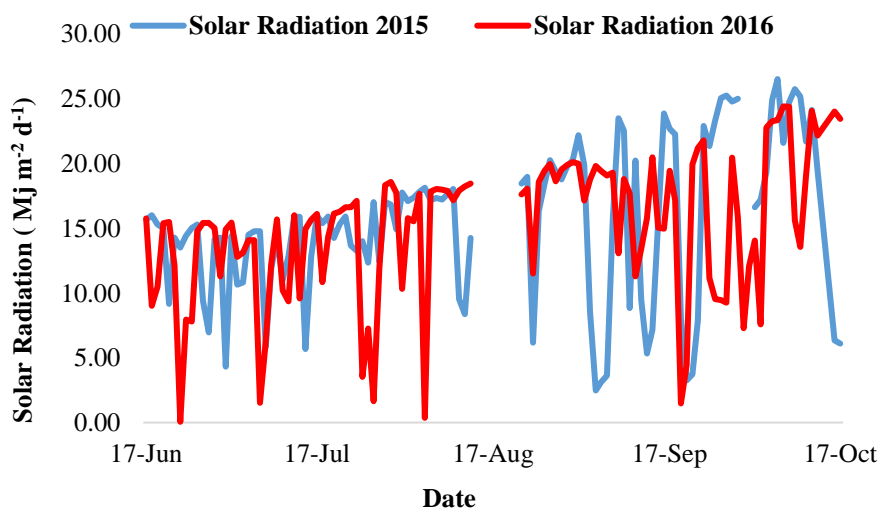


Figure 91: A comparison of solar radiation for 2015 and 2016 from 17 June to 17 October

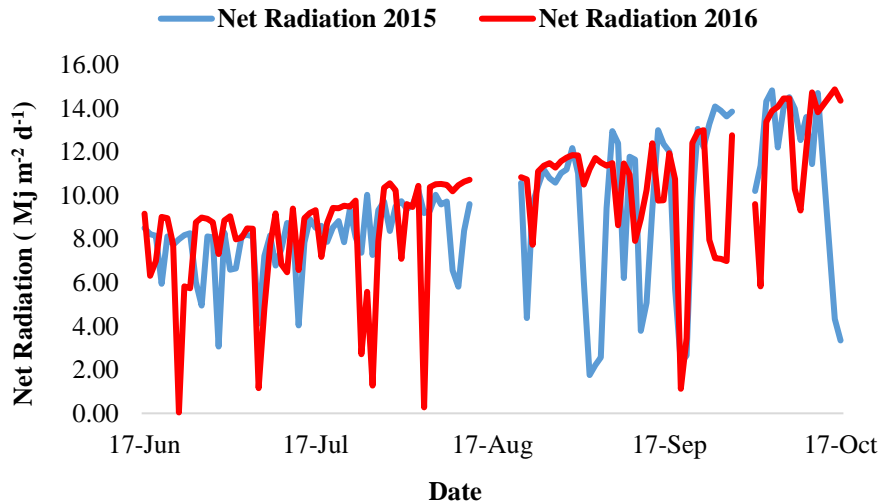


Figure 92: A comparison of nett radiation for 2015 and 2016 from 17 June to 17 October

With respect to the increasing rates of ET for 2016, the absolute difference in EC_{ET} at Site 2 is 53.6 mm. The absolute difference in EC_{ET} at Site 1 is 80.07 mm. Climatic and biotic factors are generally the factors which control ET; however, during periods of water stress, soil water content becomes the main controlling factor of ET (Alfieri et al., 2007). The electrical conductivity system was situated at Site 1 during the dry season (winter) and then moved to Site 2 just prior to the beginning of the wet season (spring).

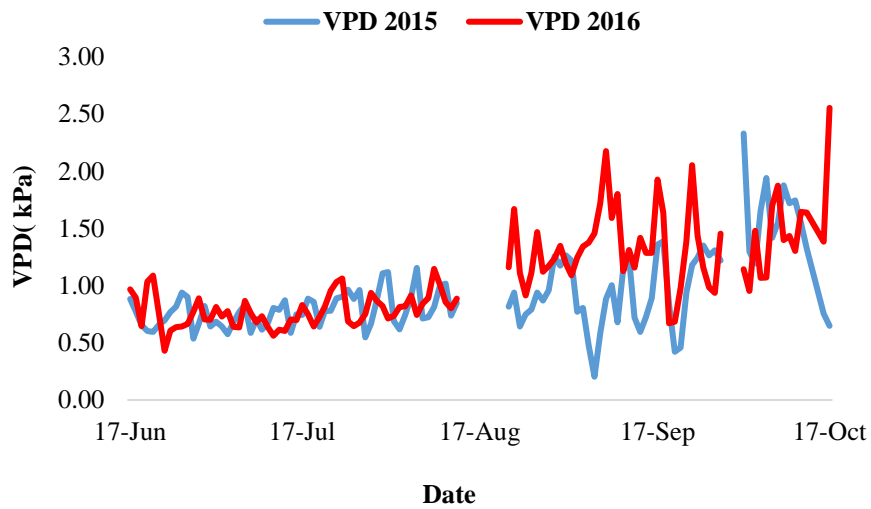


Figure 93: A comparison of VPD for 2015 and 2016 from 17 June to 17 October

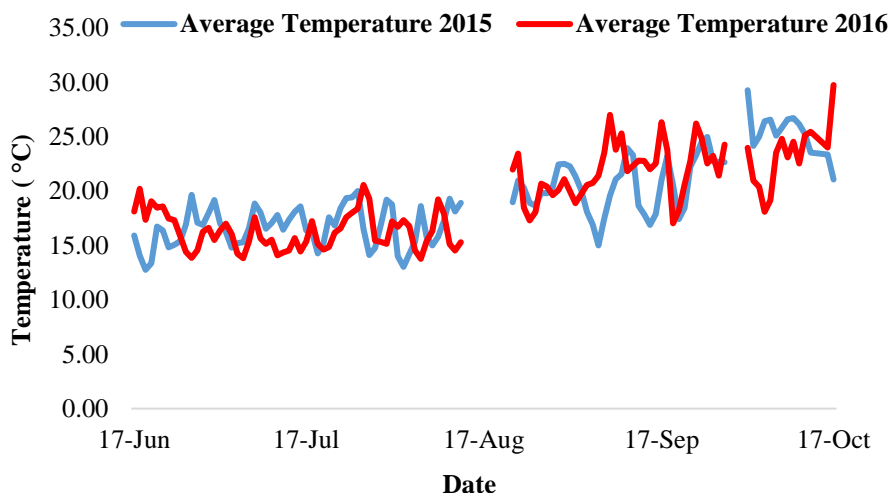


Figure 94: A comparison of temperature for 2015 and 2016 from 17 June to 17 October

During the wet season ET is limited by available energy, while during the dry season, ET is limited by water availability. At the time of the study, the greater study area was experiencing one of the most severe droughts in decades. While the study site is situated within a riparian environment, water availability is quite variable along the portion of river that was studied and has been further impacted by the drought.

During the measurement period in 2015, there were a few minor precipitation events that would have contributed to soil water recharge. However, the single high precipitation event of March 2016 would have contributed a much higher volume of water to soil water recharge than the rest of the study period. Considering ET is controlled by soil water availability during periods of water stress, the increase in soil moisture via these precipitation events could have potentially resulted in the higher EC_{ET} for 2016 – especially at Site 1.

As discussed previously, the SEBS model does not explicitly account for soil moisture and biophysical parameters during the derivation of surface fluxes and ET. As a result, SEBS may overestimate the EF and the latent heat flux for semi-arid and arid environments in which the availability of water is the limiting for ET (Huang et al., 2015). This in turn may have potentially contributed to the overestimation of ET by $SEBS_0$ in this study. Furthermore, Gokmen et al. (2012) and Pardo et al. (2014) note that the overestimation of EF and the latent heat in SEBS may be markedly higher for drier soils lacking vegetation coverage – an observation that has been reaffirmed by the results presented previously.

The $SEBS_{ESF}$ formulation was applied as a means to address this limitation. The results presented for the 2015 and 2016 study period have shown that the implementation of $SEBS_{ESF}$ was able to marginally improve the estimation of ET for the study period. Furthermore, the use of ET estimates emanating from $SEBS_{ESF}$ in the $K_{C_{act}}$ and output downscaling with linear regression approaches, resulted in a performance of both these approaches for the estimation of ET at a MSR and HTR over the entire period of study.

The use of ET estimates emanating from $SEBS_{ESF}$ in the $K_{C_{act}}$ and output downscaling with linear regression approaches were shown to generally improve the estimation of ET. The performance of this approach was found to be poorer for the 2016 study period. This occurrence can largely be attributed to the relationship identified between the EC_{ET} and ET_0 .

During the 2016 study period, there were numerous instances where the ET_0 was lower or approximately equal to the EC_{ET} measurements, as illustrated in Figure 7. Subsequently, the ESF estimated for these instances will be close to or greater than 1, resulting in minimal to no reduction in the ET estimated through the implementation of $SEBS_{ESF}$.

The lower estimates of ET_0 in comparison to EC_{ET} may possibly due to the ET_0 estimates for 2016 not adequately representing the maximum ET associated with the vegetation in the study area. During 2015 when water availability was a considerable limiting factor to ET, it was conceivable that the ET associated with a hypothetical grass reference surface experiencing no water stress (ET_0) was higher than the ET associated with the vegetation in the study area.

However, as water availability marginally increased in 2016 due to the abovementioned precipitation events, the water use associated with the vegetation in the study area would have increased. Consequently, the use of ET_0 to represent the maximum ET for a given day during these conditions was an inadequate representation of the upper limit of ET. Moreover, unidentified errors during the measurement of EC_{ET} or an increase in the open water evaporation rates captured by the electrical conductivity system, could have also contributed to the discrepancy.

The implementation of $SEBS_{ESF}$ was not able to considerably improve the correlation between modelled and measured ET during the 2016 study period. The implementation of $SEBS_{ESF}$ ET estimates as inputs to the downscaling and infilling techniques was able to produce ET estimates that were consistently within an acceptable accuracy range ($\pm 30\%$) when compared with EC_{ET} , as shown in

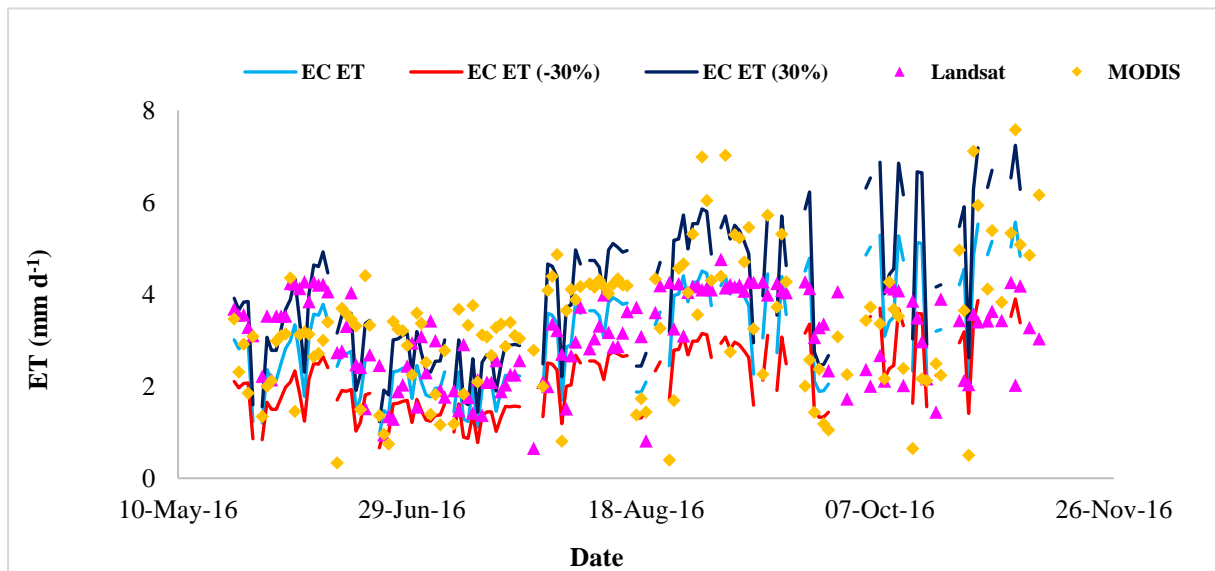


Figure 95. Of the $K_{C_{act}}$ ET estimates, 88% fell within an acceptable accuracy range of $\pm 30\%$, with 57% of these values falling within an accuracy range of $\pm 15\%$. Of the downscaled ET estimates, 78% fell within an acceptable accuracy range of $\pm 30\%$, with 48% of these values falling within an accuracy range of $\pm 15\%$.

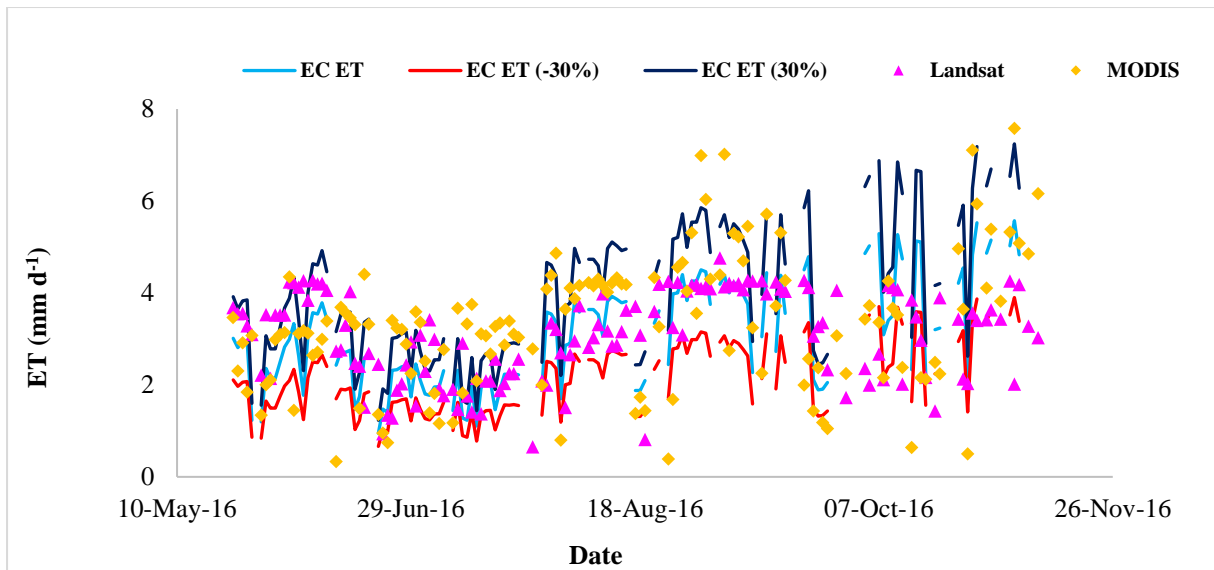


Figure 95: A comparison of the $SEBS_{ESF}$ derived ET against EC_{ET} within acceptable accuracy ranges from 19 May to 11 November 2016

5.6.6 Estimation of losses due to ET

The ET data and isotope data presented in the previous sections, and the soil water ($0.15 \text{ mm}\cdot\text{d}^{-1}$ and $0.65 \text{ mm}\cdot\text{d}^{-1}$, for winter and summer respectively) and open water evaporation rates ($2.14 \text{ mm}\cdot\text{d}^{-1}$ and $3.73 \text{ mm}\cdot\text{d}^{-1}$, for winter and summer respectively) previously determined in Deliverable 4 of this project, were used to provide an estimate of the losses in the system that can be attributed to ET and open water evaporation. The total area of the river channel and riparian zone contributing to ET was estimated to be approximately $980\,000 \text{ m}^2$. This was calculated by summing the width of the river channel (approximately 60 m) and riparian zone (40 m on either side of the channel) and multiplying it by the longitudinal distance of the portion of river reach studied (7000 m). The section of river channel studied during the collection of ET data approximately constitutes 50% vegetation, 30% bare soil and 20% open water.

Groundwater and stream water were shown to contribute to approximately 16% of plant water uptake to riparian vegetation situated on either side of the river channel during late winter and early spring. Stream water contributes to 75% of the plant water uptake to *P. mauritianus* (assuming that soil water in the upper 30 cm is actually surface water).

Using the aforementioned data, the estimated losses in the system as a result of ET and open water evaporation were calculated and are presented in Table 24 to Table 26. The ET values used here represent the average ET values for winter and summer respectively and correspond with the ET values used during the MODFLOW modelling for a winter, summer and extreme summer scenario. It should be noted that values used to determine losses in the summer were kept constant when determining ET losses for the extreme summer scenario as there was no measured data available to adequately represent such an event, only the ET was changed from $5 \text{ mm}\cdot\text{d}^{-1}$ to $7 \text{ mm}\cdot\text{d}^{-1}$.

The results presented in these tables show that the combined losses of water to ET and open water evaporation in the study area were approximately $1.01 \text{ mm}\cdot\text{d}^{-1}$ for winter, $1.87 \text{ mm}\cdot\text{d}^{-1}$ for summer and $2.34 \text{ mm}\cdot\text{d}^{-1}$ for extreme summer conditions.

Table 24: Estimated losses due to ET (3 mm·d⁻¹) and open water evaporation in winter

	Area (m ²)	Transpiration (m ³ ·d ⁻¹)	Soil water evaporation (m ³ ·d ⁻¹)	Open water evaporation (m ³ ·d ⁻¹)	Total (m ³ d)
Riparian Banks	560 000	255.36	84.00		339.36
River Channel	420 000	448.88	18.90	179.76	647.54
					986.90

Table 25: Estimated losses due to ET (5 mm·d⁻¹) and open water evaporation in summer

	Area (m ²)	Transpiration (m ³ ·d ⁻¹)	Soil water evaporation (m ³ ·d ⁻¹)	Open water evaporation (m ³ ·d ⁻¹)	Total (m ³ d)
Riparian Banks	560 000	389.76	364.00		753.76
River Channel	420 000	685.13	81.90	313.32	1080.35
					1834.11

Table 26: Estimated losses due to ET (7 mm·d⁻¹) and open water evaporation in summer

	Area (m ²)	Transpiration (m ³ ·d ⁻¹)	Soil water evaporation (m ³ ·d ⁻¹)	Open water evaporation (m ³ ·d ⁻¹)	Total (m ³ d)
Riparian Banks	560 000	568.96	364.00		932.96
River Channel	420 000	1000.13	81.90	313.32	1395.35
					2328.31

6 NUMERICAL FLOW MODEL

6.1 Objective of the Model

The objective of the model is to evaluate river flows and transmission losses under different conditions. A realistic baseline model was established and used to conduct scenario modelling to run different scenarios in the natural environment or anthropogenic inputs.

These scenario conditions included:

- Low, medium, high and extremely high flows.
- Summer conditions: high ET and recharge rates for farms vs. reserves.
- Winter conditions: low ET and recharge rates for farms vs. reserves.
- Extreme summer conditions: Very high ET rates for farms vs. reserves.

The results of the modelling are aimed at providing information that may be used to implement an efficient water resource and ecological management plan for the catchment.

6.2 Governing Equations

The numerical model for the project was constructed using Groundwater Vistas Version 6 (GV6), a pre- and post-processing package for the modelling code MODFLOW-USG. MODFLOW-USG Advanced version (Panday et al., 2013) and the xMD solver for unstructured grids were used in the simulation of the Letaba River study site transmission loss numerical groundwater flow model.

MODFLOW-USG is based on an underlying control volume finite difference (CVFD) formulation in which a cell can be connected to an arbitrary number of adjacent cells. MODFLOW-USG includes a groundwater flow (GWF) process based on the GWF Process in MODFLOW–2005, as well as a new connected linear network (CLN) process representing the Letaba River in this model. The CLN process is tightly coupled with the GWF process in that the equations from both processes are formulated into one matrix equation and solved simultaneously. This robustness results from using an unstructured grid with unstructured matrix storage and solution schemes.

The numerical model was based on the findings of the fieldwork investigations, the hydrogeological information interpreted as part of this study, and the conceptual model developed (see p. 76).

MODFLOW-USG provides a framework for tightly coupling multiple hydrologic processes. The tight coupling occurs through the formulation of a global conductance matrix that includes the cells for all processes. The framework allows individual MODFLOW-USG processes to add to the global conductance matrix in order to represent fluxes between cells within a process as well as with cells of other processes. The global conductance matrix can be symmetric or asymmetric and is unstructured, indicating that an individual cell may have an arbitrary number of connections with other cells. The CVFD formulation accommodates this unstructured framework of tightly coupling flow processes as well as of allowing flexibility in cell geometry and connectivity within processes. Following is the general form of a CVFD balance equation for cell n :

$$\text{Equation 7: } \sum_{m \in \epsilon_n} C_{nm} (h_m - h_n) + HCOF_n(h_n) = RHS_n$$

Where:

- C_{nm} is the inter-cell conductance between cells n and m ;
- h_n and h_m are the hydraulic heads at cells n and m ;
- $HCOF_n$ is the sum of all terms that are coefficients of h_n in the balance equation for cell n ; and
- RHS_n is the right-hand side value of the balance equation.

6.3 Boundary Conditions

Boundary conditions express the way in which the considered domain interacts with its environment. In other words, they express the conditions of known water flux, or known variables, such as the hydraulic head. Different boundary conditions result in different solutions, hence the importance of stating the correct boundary conditions. Boundary condition options in MODFLOW can be specified as:

- Specified head or Dirichlet; or
- Specified flux or Neumann; or
- Mixed or Cauchy boundary conditions.

From the conceptual point of view, it was essential to meet two criteria to the maximum extent possible:

- The modelled area should be defined by natural geological and hydrogeological boundary conditions, i.e. the model domain should preferably encompass the entire hydrogeological structure.
- The mesh size of model grid has to correspond to the nature of the problem being addressed with the model.

Local sub-catchment hydraulic boundaries were identified for model boundaries. They were represented by no-flow boundaries and delineated the entire model domain. These hydraulic boundaries were selected far enough from the area of investigation to not influence the numerical model behaviour in an artificial manner.

Figure 96 shows the model area and unstructured grid for the Letaba model. Table 27 provides a summary of the boundaries, boundary descriptions and boundary conditions specified in the hydrogeological model.

Table 27: Identification of the real-world local boundaries and the adopted model boundary conditions

Boundary	Boundary Description	Boundary Condition
Top	Top surface of water table	Mixed type: CLN cells for Letaba River and side streams. Recharge to the water table. SUDEM ⁶ data was used for the top layer topography
Bottom	Very low hydraulic conductivities in fractured aquifer	No flow at bottom layer
North, South	Local sub-catchment boundary	No flow
East	Letaba Ranch outflow	Drain in CLN removing water from model
West	Mahale Weir inflow	Specified flux within the CLN

⁶ <http://www.innovus.co.za/pages/english/technology/our-technologies-and-spin-out-companies/physical-sciences/stellenbosch-university-digital-elevation-model-28sudem29.php>

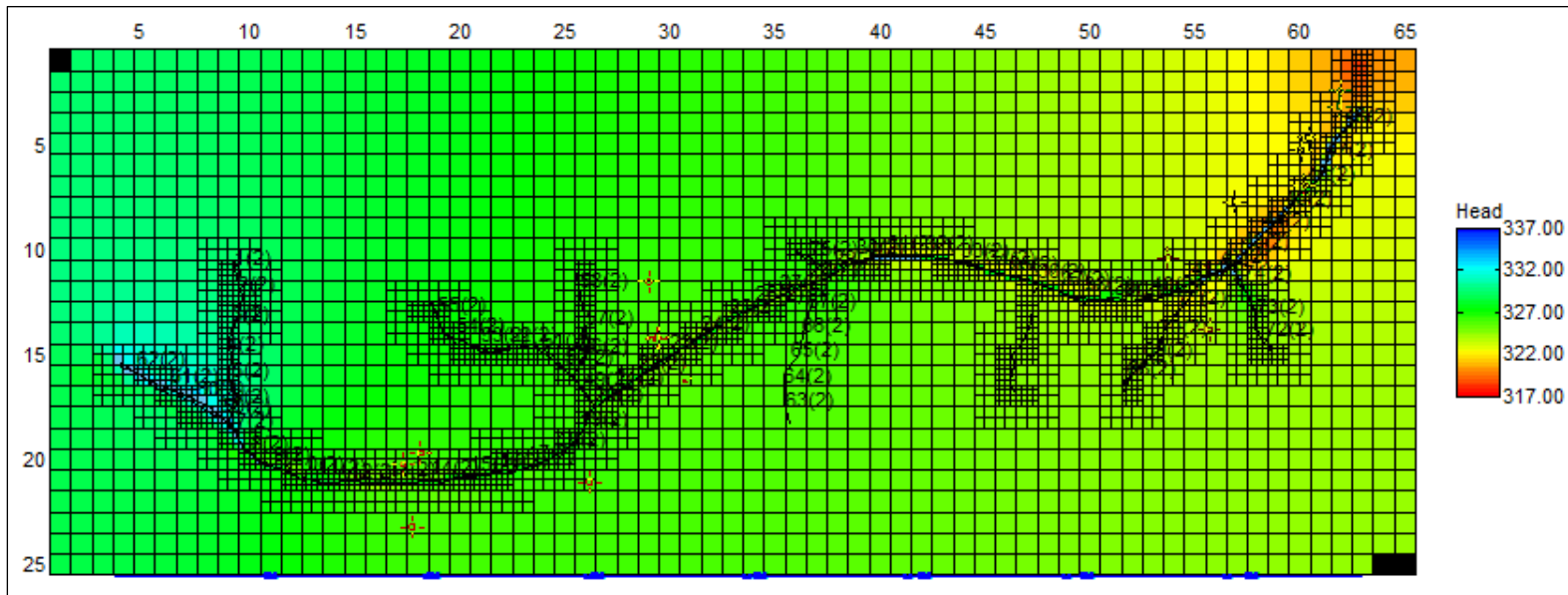


Figure 96: Model area, unstructured grid and steady-state water levels of the Letaba groundwater model (head = above mean sea level)

6.4 Construction of the Finite Difference Grid

Compilation of the finite difference grid using the Groundwater Vistas graphic user interface facilitated the construction of an unstructured quadtree grid, as well as vertical geometry provided for each of the layers. The rectangular grid consisted of two layers with a total of 9052 cells ($25 \times 65 \times 2$ layers). The positions of the river and stream boundaries are incorporated in the modelling grid.

Smaller cell sizes were specified along the Letaba Riverbanks, where a more accurate solution of the groundwater flow equation is required. These smaller cells consisted of 814 quadtree cells (Figure 97). Slightly larger cell sizes were specified in other areas. Cell size refinement across the model domain did not exceed 0.5 times the neighbouring cells.

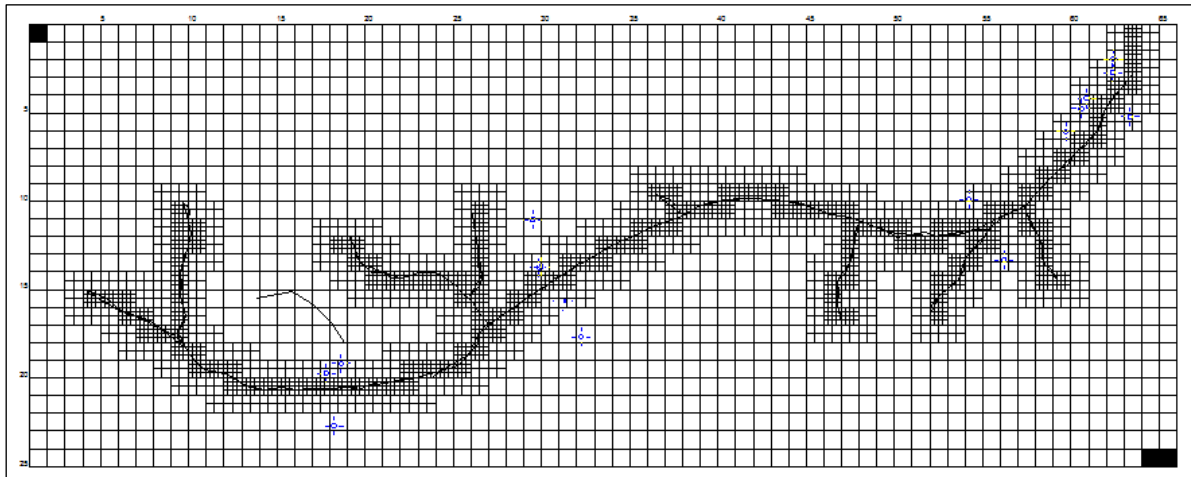


Figure 97: A picture representing the aerial view of the finite difference grid

6.5 Vertical Discretization

Along the vertical direction, the steady-state hydrogeological model is structured in two model layers (Figure 98). The layer positions were selected to best incorporate the weathering depth and vertical hydraulic gradients along the Letaba River. The grid and layer definitions are seen below.

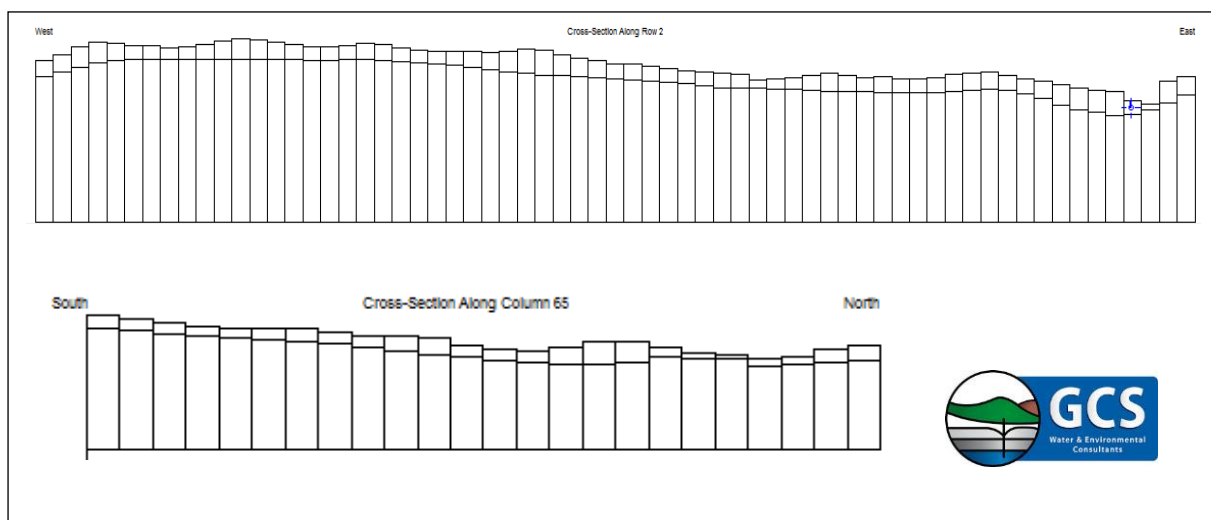


Figure 98: NW-SE and NE-SW cross-section through grid at the Letaba Catchment site showing grid and layer definition used in numerical model

6.6 Input Parameters

Model input parameters for these flow models are divided into two groups:

- Variable river flow rates.
- Realistic seasonal conditions.

The initial estimates for hydraulic properties were assigned based on the aquifer test results. The initial head conditions, specified in the steady-state model, were estimated from topography and borehole data.

6.7 Aquifer Hydraulic Conductivity

Initial estimates of the hydraulic conductivity of the different geological units were obtained from prior aquifer test data used as part of this investigation. These hydraulic conductivity values were assigned to the two layers of the model: the shallow weathered-fractured unit with a thickness of approximately 20–40 m and the deeper unweathered fractured and faulted granite units. The horizontal conductivity of the two different layers are seen in Figure 99 and the hydraulic conductivity values for the x-, y- and z-axis are tabulated in Table 28.

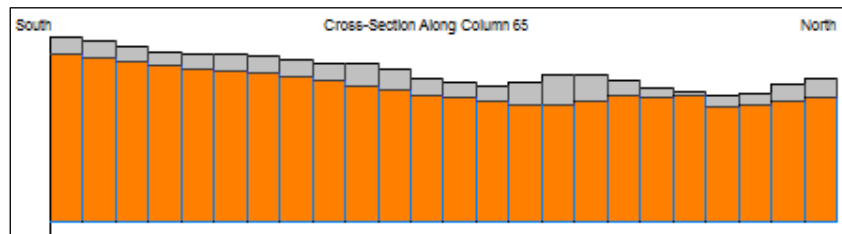


Figure 99: A south–north cross-section displaying the two layers of different hydraulic conductivities

Table 28: Values of horizontal and vertical hydraulic conductivities

Zone/layer	X-axis (Horizontal)	Y-axis (Vertical)	Z-axis
1	0.08	0.08	0.08
2	0.05	0.05	0.05

6.8 Recharge

Recharge values were estimated at 10% of the average rainfall in the catchment. The first four models (Model 1–4) were tested against a uniform recharge rate of 0.001 m/day. These simplified recharge models enabled clarity on the effect of variable flow rates for the catchment. The rest of the model scenarios (Model 5–7) contain recharge zones specified for the farms and reserves under seasonal variation. In summer (December–March), the recharge rates for the farm lands were 0.0002 m/day due to summer rainfall contribution. In winter (May–August), the recharge rates for the farms were 0.0001 m/day. Under both seasons, the reserves recharge rates remained constant at 0.000001 m/day.

The two recharge zones used for different scenarios are displayed in Figure 100.

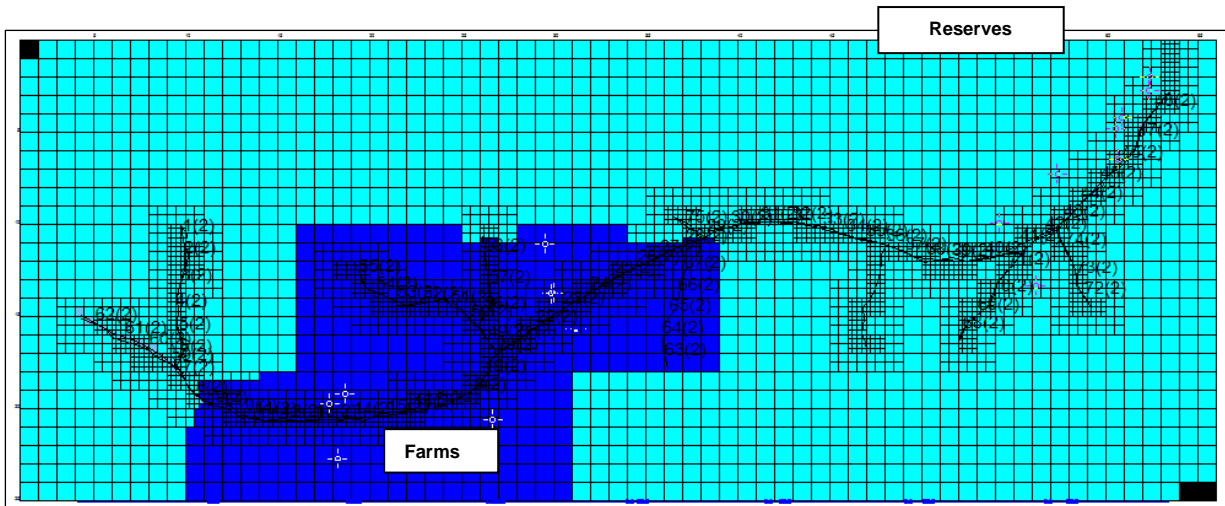


Figure 100: A model representation of two recharge zones (farms and reserves)

6.9 Evapotranspiration

ET values were obtained from the data collected as part of the study. This ET data was measured at the site by an electrical conductivity system, as well as the FAO Penman–Monteith reference evaporation. All models consist of two ET zones to represent the difference in farms and the reserves:

- Model scenarios 1–4 include summer ET rates of 0.014 m/day and 0.007 m/day for farmlands and reserves respectively.
- Model 5 attains summer ET rates of 0.0042 m/day and 0.007 m/day for the farms and reserves respectively.
- Model 6 displays winter ET rates of 0.0027 m/day and 0.003 m/day for the farms and reserves respectively.
- Model 7 represents extreme summer conditions with high ET rates of 0.014 m/day and 0.007 m/day respectively.

All the above models attain an ET extinction rooting depth of 2 m, whereas the reserves have a longer rooting extinction depth of 5 m due to deeper rooted trees. The two ET zones that are applicable for Models 5–7 are indicated in Figure 101.

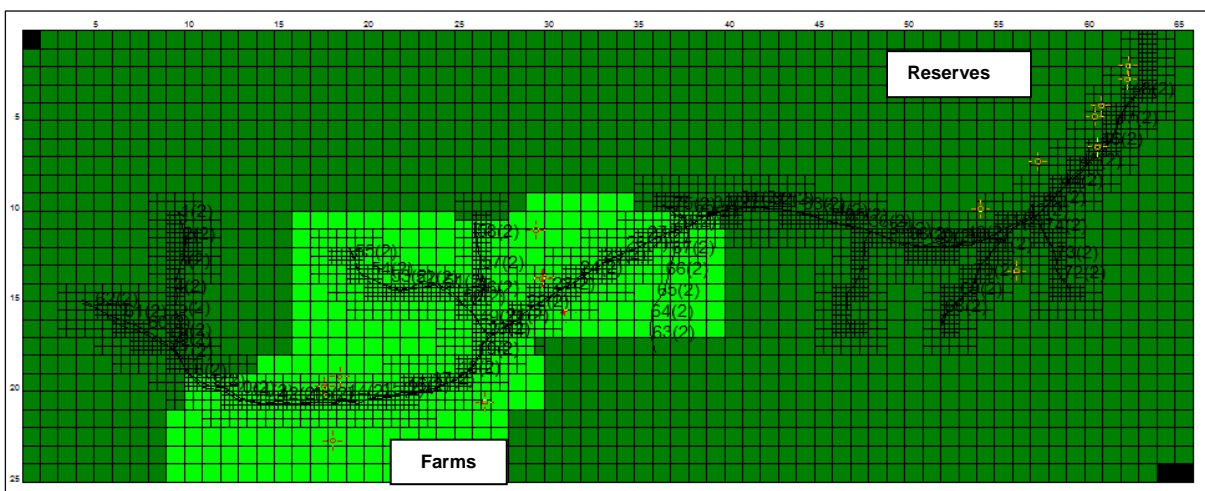


Figure 101: A model representation of the two ET zones (farms and reserves)

6.10 Time Discretization

Steady-state groundwater flow models were used to gain a basic understanding of how the catchment functions under different conditions.

6.11 Flow Rates

Letaba River flow rates are based on data recorded as part of this study as well as the Letaba Ranch Weir with the DWS data logging network. The simulated flow rates were divided into low, medium, high and extremely high rates to predict the way the transmission losses will respond in different conditions. These flow rates are tabulated in Table 29 with a representation of the medium flow rate heads in Figure 102.

Table 29: Four values of the flow rates per category

Flow	Flow rate per second (m ³ /s)	Flow rate per day (m ³ /day)
Low (Mahale Weir Baseflow)	0.5	43 200
Medium	1.0	86 400
High	1.5	129 600
Extremely High	23.0	2 000 000

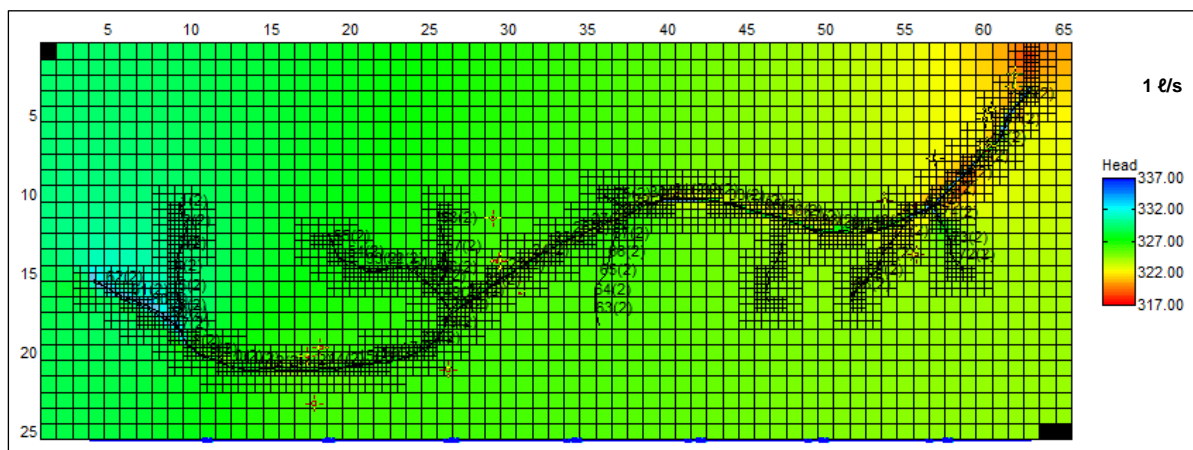


Figure 102: A model representation of the hydraulic head distribution under medium flow conditions (1 l/s)

6.12 Model Results

6.12.1 Evaluation of river flows

Seven different models were produced to test the response of the Letaba River under variable flow and seasonal conditions.

The first four models analyse flow conditions valued at 0.5 m³/s, 1 m³/s, 1.5 m³/s and 23 m³/s for model 1, 2, 3 and 4 respectively. All other input parameters remain constant throughout the four models. These in parameters include:

1. ET rates, which vary between the two zones (farms vs. reserves).
2. Hydraulic conductivity values, which vary for the two layers. The top layer is the shallow weathered-fractured unit and the bottom layer is the deeper unweathered faulted granitic unit.
3. Uniform recharge at 0.001 mm/day.

The last three models (Models 5, 6 and 7) examine the catchments response to seasonal variation under farm and reserve conditions. Model 5 depicts a summer scenario (December to March) with a higher ET and recharge rates due to summer rainfall. Model 6 depicts a winter scenario (May to August) with a lower ET and recharge rates due to drier winters. Model 7 depicts extreme summer conditions with very high ET rates to understand the effect that crop water consumption has within the catchment. In all three models, hydraulic conductivity and flow rates remain constant.

A summary of the seven models input parameters are tabulated in Table 30.

Table 30: Input parameters for the constructed seven models

Model no.	Scenario description	ET (m/day)	Hydraulic conductivity (m/day)	Recharge (m/day)	River flow rate (m ³ /s)
1 2 3 4	Standard model input parameters with variable flow rates.	Farms = 0.014 Reserves = 0.007	Unweathered = 0.08 Weathered = 0.05	0.000001	0.5 1 1.5 23
5	Summer conditions with high ET and increased summer farm irrigation.	Farms = 0.0042 Reserves = 0.007	Unweathered = 0.08 Weathered = 0.05	Farms = 0.0002 Reserves = 0.000001	0.5
6	Winter conditions with low ET rates and higher rainfall.	Farms = 0.0027 Reserves = 0.003	Unweathered = 0.08 Weathered = 0.05	Farms = 0.0001 Reserves = 0.000001	0.5
7	Extreme summer conditions with very high ET and increased summer farm irrigation.	Farms = 0.014 Reserves = 0.007	Unweathered = 0.08 Weathered = 0.05	Farms = 0.0002 Reserves = 0.000001	0.5

In Figure 103 to Figure 109 (Model 1–6), it is observed that the Letaba River at the study reach responds similarly for all models under variable flow rates and seasonal variations. The general trend of the catchment indicates that the Letaba River decreases in flow rate along the river length. Observing the distance to flow rate relationship, it is evident that there is a relatively steep decline in flow rate, which is attributed to a 10 m gradual decrease in topographic gradient. Thereafter, the river intercepts the Mahale Weir. The weir tends to sustain a relatively stable flow rate until the river meets a meander.

The flow rate decreases at the meander due to groundwater infiltration at the meander cut bank (approximate position of Transect 2). The flow continues to steadily decline until it is approximately 800 m away from the lower weir (Letaba Ranch B8H008). Thereafter, it experiences a sharp decline in flow rate due to the stream bed flowing over a deeply weathered zone. The weathered zone has a lower topography with increased hydraulic conductivity; therefore, acting as a small reservoir by slowing down the flow rate and increasing the groundwater contribution. Thereafter, a steady decline in flow rate is observed due to the lower weir restricting the hydraulic gradient.

Although the models seem to follow the same general trends, it is noted that under summer conditions (Model 7, Figure 109) there is a sudden increase in flow rate within the weathered zone.

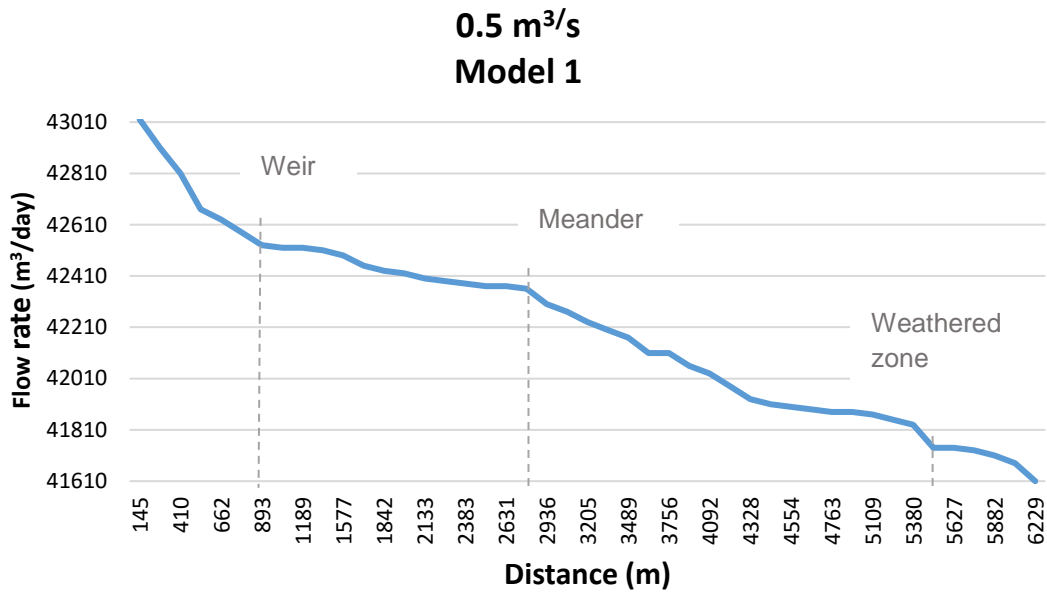


Figure 103: Model 1: Response of Letaba River against distance with a flow rate of 43 200 m³/day (0.5 m³/s)

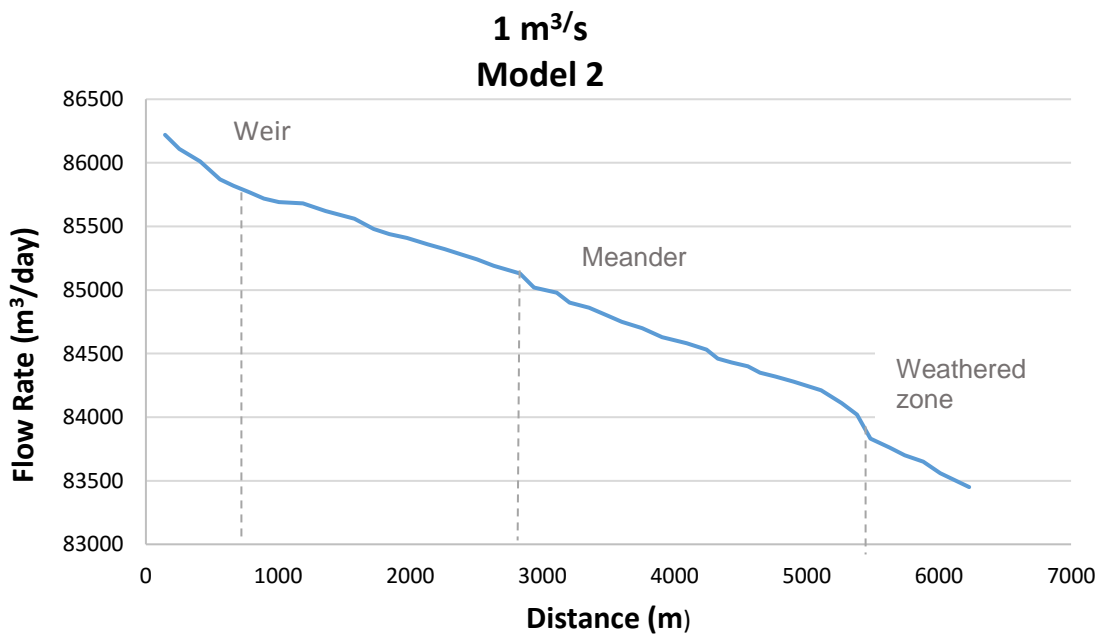


Figure 104: Model 2: Response of Letaba River against distance with a flow rate of 86 400 m³/day (1 m³/s)

**1.5 m³/s
Model 3**

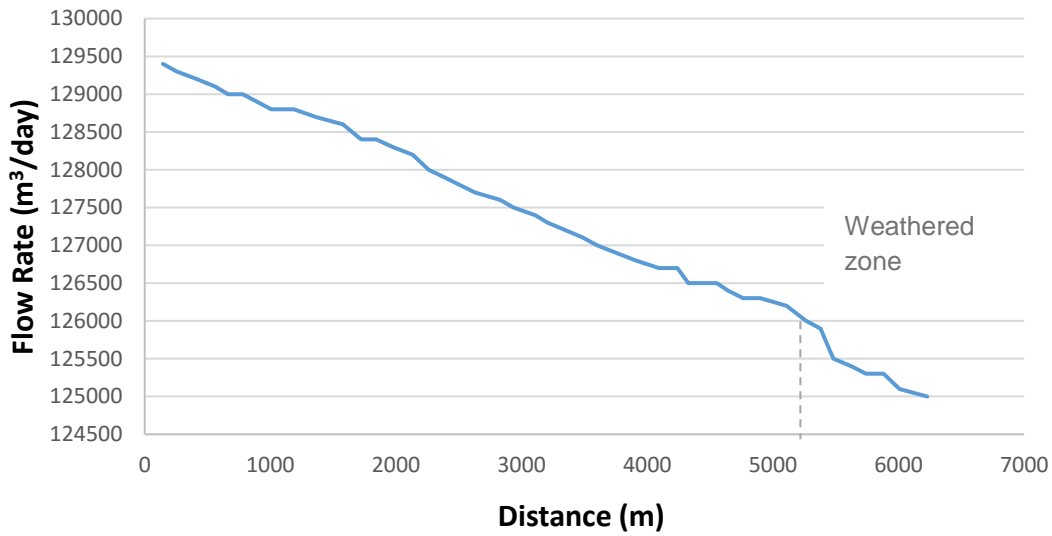


Figure 105: Model 3: Response of Letaba River against distance with a flow rate of 129 600 m³/day (1.5 m³/s)

**23 m³/s
Model 4**

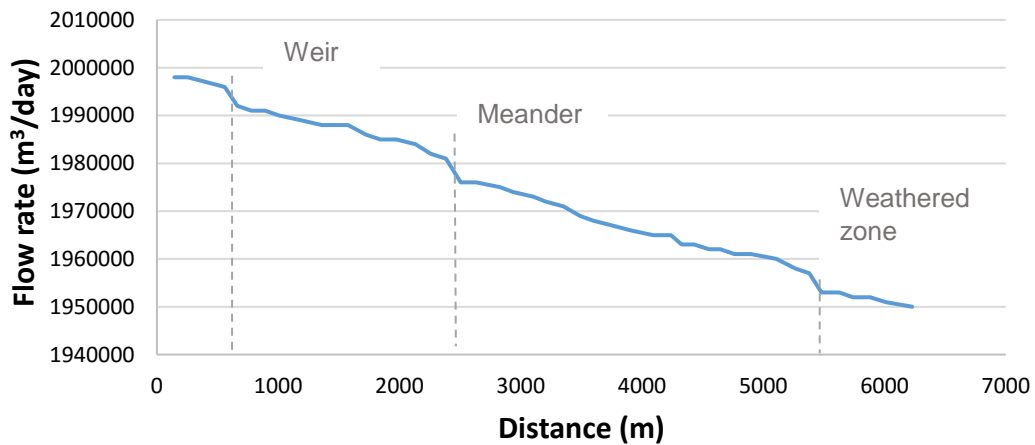


Figure 106: Model 4: Response of Letaba River against distance with a flow rate of 2 000 000 m³/day (23 m³/s)

Summer, 0.5 m³/s Model 5

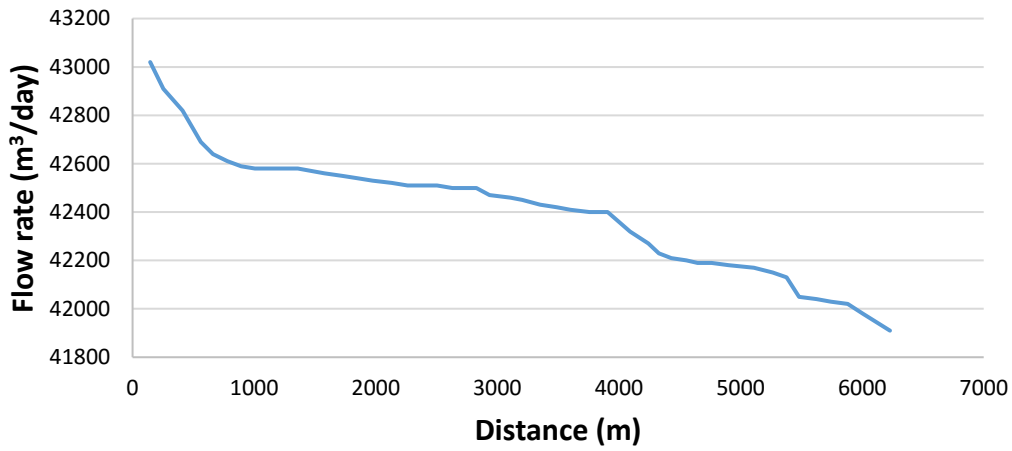


Figure 107: Model 5: Response of Letaba River under realistic summer conditions at 0.5 m³/s

Winter recharge, 0.5 m³/s Model 6

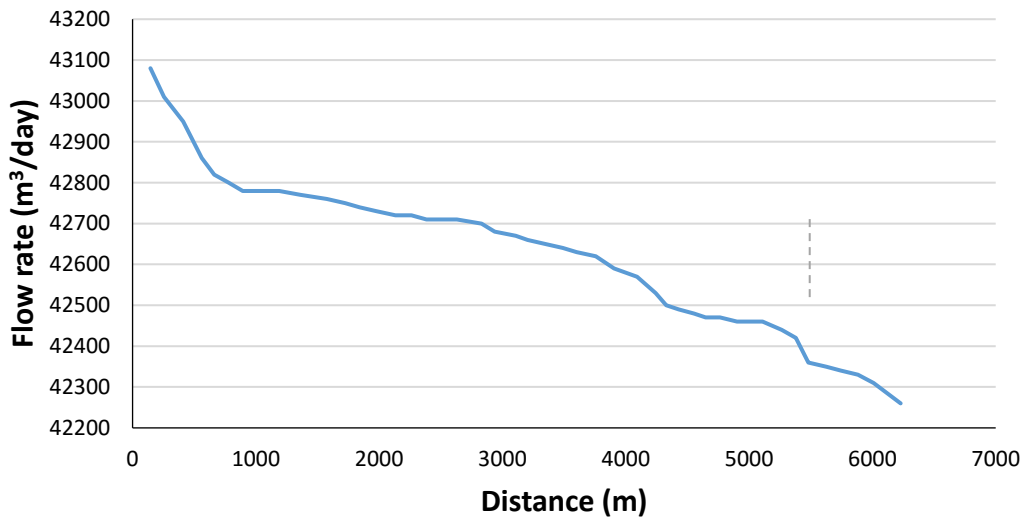


Figure 108: Model 6: Response of Letaba River in winter conditions at 0.5 m³/s

**Summer, 0.5 m³/s
Model 7**

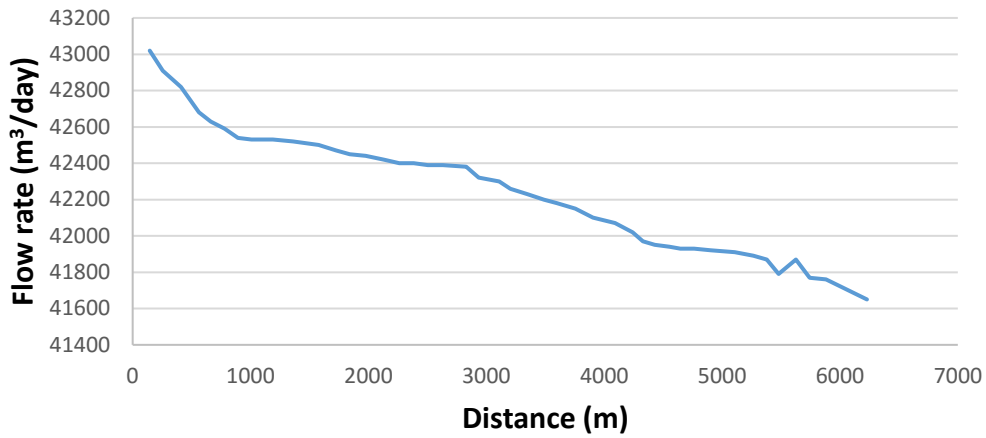


Figure 109: Model 7: Response of Letaba River in extreme summer conditions at 0.5 m³/s

6.12.2 Transmission losses

The same seven models were evaluated to determine transmission losses along the simulated Letaba River length under variable flow and seasonal conditions.

Letaba River topography

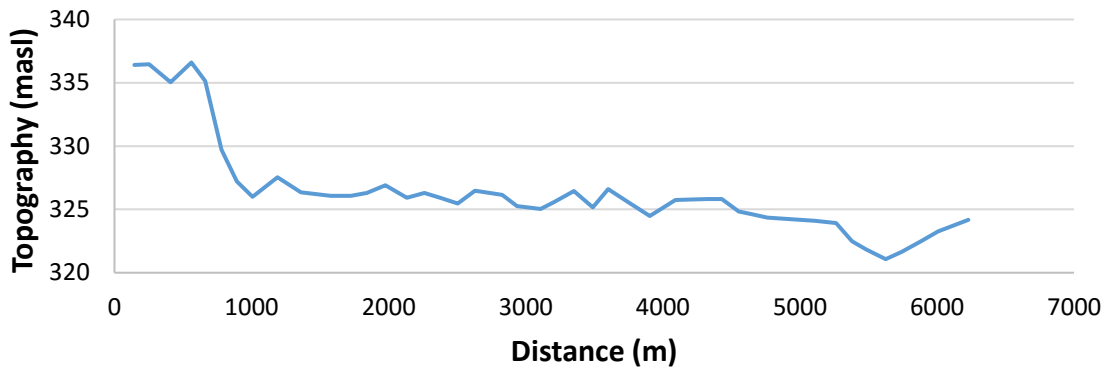


Figure 110: Graph indicating transmission losses of the Letaba River against topography

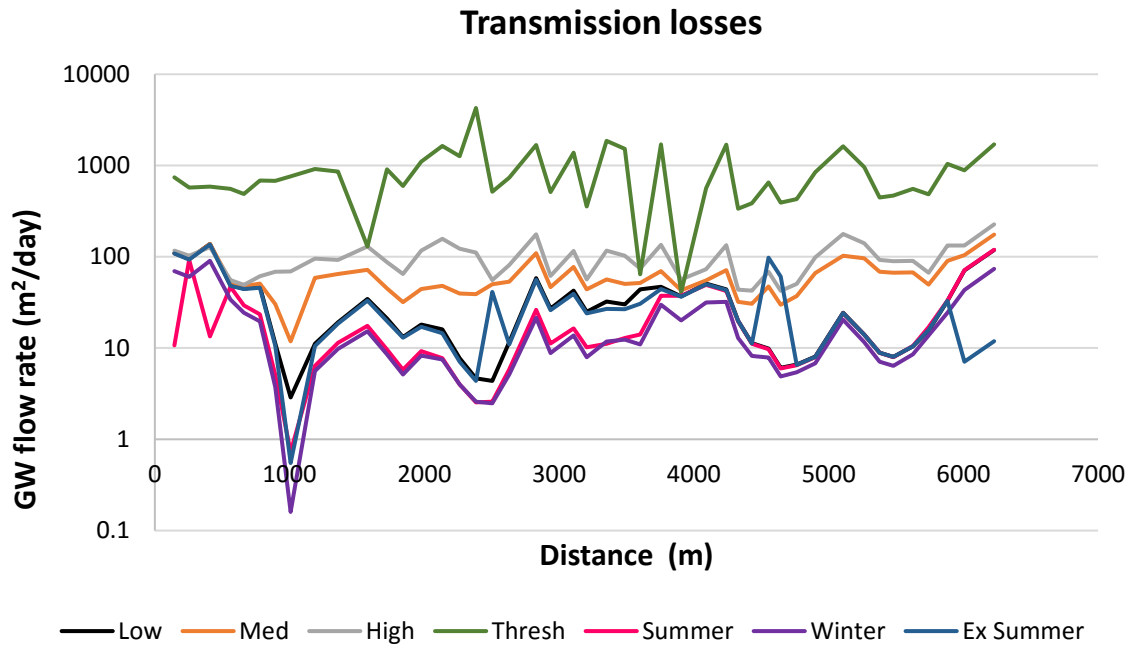


Figure 111: Graph indicating transmission losses of the Letaba River against distance

Figure 110 and Figure 111 display a complex system of transmission losses and groundwater inflow for the Letaba reach. For explanatory purposes, Models 1, 2, 3, 5, 6 and 7 will be annotated jointly due to observed similar transmission loss trends. Model 4 will be described separately.

In Models 1, 2, 3, 5, 6 and 7, it is evident that all models display similar transmission loss relationships pertaining to the reach. At the start of the reach, 200 m downstream, a minor transmission gain occurs. At 1000 m into the reach, the groundwater flow rate sharply declines. This is attributed to a sudden 10 m drop in river elevation. Thereafter, a fairly steady transmission loss is obtained until 2500 m into the reach whereby a slight decrease in transmission loss occurs, which is also attributed to river topography. At 3000 m into the reach, high transmission losses occur, which is attributed to a meandering stream bed. The meandering of the river contributes to a deeper weathered zone that increases groundwater recharge, thus increasing transmission losses. Thereafter, transmission losses remain fairly constant at a rate of 100 m³/day. From 5000 m, higher transmission losses are evident, which is due a deeper weathered zone as well as deeper rooted trees consuming larger quantities in the reserves (?). Thereafter, at approximately 5060 m, the increase and decrease in transmission losses is attributed to a 4 m topography change.

When analysing the seasonal variation in ET rates between Model 5–7, it is evident that ET does not influence the catchments responses drastically. This is evident in Figure 107 to Figure 111 above whereby the summer, winter and extreme summer scenarios display similar results. This is attributed to the shallow extinction rooting depth of the farm lands being at 2 m below the surface as well as the reserve rooting depth being applied at a deeper, natural 7 m below ground level.

In Model 5 (Figure 107) it is evident that there are extreme fluctuations in transmission losses. These fluctuations are not dependent on the river topography, but instead act differently due to the severely high flow rate of 23 m³/s. This high flow rate induces higher transmission losses due to bank storage processes where the river water recharges the weathered aquifer adjacent the river. The trees surrounding the river will consume this water at a higher rate thus increasing transmission losses.

6.12.3 Water Balances

Table 31 displays water balances of the various models. These water balances represent the flow of water in and out of the Letaba Catchment. In Models 1, 2, 4 and 5, it is evident that there is an excess of water flowing through the Letaba River. However, in Model 3, 6 and 7 there is a deficit of water in the Letaba River. These are accurate representations as low to medium flows generally lose less river water to groundwater, whereas higher realistic river flows (1.5 m³/s) saturate riverbanks, thus increasing transmission losses due to groundwater recharge. In Model 4, which is the extreme flow rate (23 m³/s), it is evident that there is an excess of water flowing through the catchment, although a large volume of water is contributed to groundwater recharge.

The realistic summer scenario (Model 5) displays that water flows out of the catchment even though higher ET rates are apparent. This is attributed to summer rainfall, increasing recharge rates, thus increasing surface water contribution. The winter scenario (Model 6) displays that water is at a deficit in the Letaba River due to lower recharge rates with moderate ET rates. The extreme summer scenario (Model 7) displays a water deficit. This is sensible as high ET rates are apparent, thus increasing transmission losses.

Table 31: Water balances for the seven models

	Model 1, 0.5 m³/s	Model 2, 1 m³/s	Model 3, 1.5 m³/s	Model 4, 23 m³/s	Model 5, summer	Model 6, winter	Model 7, ext. summer
Wells (River Inflow)	43 200	86 400	129 600	2 000 000	43 200	43 200	43 200
Recharge	16	16	16	16	653	333	653
Drains (River Outflow)	-41 488	-83 269	-124 764	-1 948 241	-41 788	-42 188.95	-41 562
ET	-1 728	-3 147	-4 852	-51 750	-2 065	-1 344	-2 291
	4.44E-05	8.98E-04	-9.88E-04	2.55E+01	3.27E-04	-7.64E-04	-3.21E-04

7 CONCLUSIONS

The uncertainty associated regarding system losses via transmission loss remains a constraint to the effective planning and management of water resources in arid and semi-arid environments and, more specifically, to the implementation of ecological reserve flows. To remedy this situation, it is imperative that the effects of transmission loss at various spatial and temporal scales are quantified. The use of conceptual models and time series analysis may perhaps allow for the reliable prediction of transmission loss for regions possessing long time series of streamflow data. However, in arid and semi-arid environments, the routine monitoring of streamflow is generally limited. For such circumstances, the use of process-orientated models, which are parameterized using representative measurements of hydrological parameters, represent the most suitable tool for quantifying transmission loss, which in turn may facilitate the improved management of ecological reserve flows.

In order to achieve this objective, the aim of this study was to close the gap in knowledge on the Letaba River's hydrology through the detailed characterisation of hydrological processes along a 10 km reach of the lower Groot Letaba. It was envisaged that the improved hydrological understanding gained from this can then be used to inform OWRM of the system. This involved a comprehensive hydrological process determination phase, which was centred around quantifying the rapport between subsurface water storage processes in parallel with the measurement of total evaporation, so as to gain a conceptual understanding of the system. Subsequently, this data was integrated into a numeric groundwater flow model of the study area to quantify the dominant elements of the water balance at the scale of the study area. This reduced some of the uncertainty with the estimation of transmission loss in the Letaba system in an attempt to improve the environmental flow allocations along the Groot Letaba River.

Total evaporation was determined for the riparian zone during periods when the active channel was accessible; this being during winter to spring. This coincided with the low flow management period in this river system. The analysis developed a time series of downscaled SEBS modelled actual ET, cross-referenced with *in situ* measurements determinations of daily ET using an eddy covariance system. Initial investigation revealed poor model performance of SEBS, especially under sparse vegetation conditions (outside the protected areas reed beds were heavily grazed).

This was overcome by introducing an $SEBS_{ESF}$, which corrected for the overestimation of the EF and latent heat flux. The new approach showed a marginal improvement for the modelled EF and ET in the case of Site 1, while the EF at Site 2 was captured within a similar level of accuracy as $SEBS_0$. The $K_{C_{act}}$ and output downscaling with linear regression approaches were applied using the ET estimates generated from implementing the $SEBS_0$ and $SEBS_{ESF}$. The results indicated that the use of ET estimates emanating from $SEBS_{ESF}$ in the $K_{C_{act}}$ and output downscaling with linear regression approaches resulted in a considerable improvement to the performance of both these approaches for the estimation of ET at a MSR and HTR during the 2015 study period.

However, the performance of this approach was found to be poorer for the 2016 study period. The implementation of $SEBS_{ESF}$ was not able to considerably improve the correlation between modelled and measured ET during the 2016 study period. The implementation of $SEBS_{ESF}$ ET estimates as inputs to the downscaling and infilling techniques was able to produce ET estimates that were consistently within an acceptable accuracy range ($\pm 30\%$) when compared with EC_{ET} .

Dual stable isotope analysis and the Simmr model were used to determine the proportions of water used from a particular source by riparian vegetation during plant water uptake along a portion of the Groot Letaba River. The results of the dual stable isotope analysis indicated that δ^2H and $\delta^{18}O$ values of xylem water generally plot closest to the SEL, which indicates that soil water is one of the main contributors to the vegetation during transpiration. The isotopic composition of the xylem water generally fell between those of the potential water source end members. Simmr was subsequently applied, using the measured δ^2H and $\delta^{18}O$ for xylem water, soil water (30 cm, 60 cm, 100 cm and 140 cm), groundwater and stream water as inputs to determine the proportion of water used from these various sources, during plant water uptake.

The results of the investigations indicated that the tree species sampled in this study display quite dynamic water uptake patterns during different periods of the year. In general, soil water at depths of 100 cm and 140 cm were shown to be the dominant contributing source during plant water uptake during the period of investigation. Contributions from groundwater and stream water to plant water uptake increased as the dry season progressed.

Continuous monitoring of the groundwater phreatic surface and hydraulic characterisation of aquifer properties enabled baseline calculations of losses and gains along the river to be determined. This in turn facilitated the development of a conceptual model of spatially variable interactions between the river and adjacent aquifer. The western-most reaches of the river within the study site, within the agricultural areas, show a throughflow system of the regional aquifer to the river from the south to the north, which then reverses further downstream.

At the most eastern part of the study site, within the protected areas, the river sees potential gains from the regional aquifer. However, this is complicated by the rivers interactions with the shallow/unconsolidated aquifer which appears to have a predominantly negative gradient away from the river during low flows. This was further supported through bank-full recharge events during the one major peak flow of March 2016. The Lower Letaba River is therefore both a geohydrologically losing and gaining river depending on the spatial scale of analysis.

The numerical model for the study was run using MODFLOW-USG under steady-state conditions and applying two distinct recharge and evaporative zones, which were informed by the conceptual model development. In general, the model results point to a linear relationship between inflow and transmission losses, which can be explained due to the head-driven process between the river and the surrounding aquifer based on its hydraulic characteristics.

Higher flow rates have been shown to induce higher transmission losses due to bank storage processes. The influence of total evaporation on losses in the study area should not be discounted. For winter and summer scenarios (Model 6 and 7) using the representative flow rate of the study area, it is evident that there is a deficit in the water balance. The evaporative losses are estimated to approximately reduce the flow in the river by 3.07% and 5.22% for summer and winter, respectively.

The findings presented in this study indicate that transmission loss only accounts for approximately 3% of the flow in the river system. This is a rather conservative estimate when compared to some of the findings reported in published literature (approximately 30%) loss. This estimate is similar to that obtained by Seago et al. (2011), in which transmission losses were estimated to account for approximately 5% of the available flow.

It should be noted that the results presented herein are representative of only a small segment of the entire river reach. Therefore, it is possible that losses along the entire river system are potentially higher. Assuming that similar hydrogeological and ecohydrological characteristics of the riparian zone exist up toward the next upstream gauge, it is possible that estimated losses are in the order magnitude of 20% when extrapolated over a 44 km reach of river. Unfortunately, since the commencement of this study the gauging in the Letaba River has deteriorated and the Prieska Weir is no longer operational to verify this estimate.

Further testing and validation of the approaches applied in this study is recommended in other environmental settings to estimate transmission losses. The results presented in this study indicate that it would prove to be advantageous to integrate the MODFLOW routines developed in this study into any future operational model modifications or re-development. This in turn can prove to be extremely beneficial in furthering our understanding of surface water and groundwater interactions and how these influences the natural functioning of ecosystems. Subsequently providing an opportunity to facilitate the improved management of our limited water resources, especially in arid and semi-arid environments.

Overall, the study has detailed key hydrological processes influencing transmission losses along the Letaba River. While the study site was extensively gauged/monitored during the duration of this study, these observations/measurements only provide an understanding of the system for a limited period in time. Therefore, it would prove to be advantageous to continue longer term monitoring at that site, which may facilitate an improved understanding of the system under changing environmental conditions, as well as allowing for a reduction in the assumptions and related uncertainties that had to be factored into the analysis.

8 REFERENCES

- Alidoost, F, Sharifi, MA and Stein, A. 2015. Region and pixel-based image fusion for disaggregation of actual evapotranspiration. *International Journal of Image and Data Fusion*, 216–231. DOI: 10.1080/19479832.2015.1055834.
- Allen, R, Bastiaanssen, W and Waters, R. 2002. SEBAL Expert Training Tutorial, August 19–23, 2002. Personal communication. The Idaho Department of Water Resources, Idaho State University.
- Allen, R, Tasumi, M, Morse, A, Trezza, R, Wright, J, Bastiaanssen, W, Kramber, W, Lorite, I and Robison, C. 2007. Satellite-based energy balance for Mapping Evapotranspiration with Internalized Calibration (METRIC): Applications. *Journal of Irrigation and Drainage Engineering*, 1334: 395–406.
- Allen, RG, Pereira LS, Raes D and Smith, M. 1998. Crop evaporation: Guidelines for computing crop water requirements, FAO Irrigation and Drainage Paper No. 56. Food and Agriculture Organization of the United Nations, Rome, Italy. ISBN 92-5-104219-5.
- Allen, RG, Pereira, LS, Smith, M, Raes, D and Wright JL. 2005. FAO-56 dual crop coefficient method for estimating evaporation from soil and application extensions. *Journal of Irrigation and Drainage Engineering ASCE*, 1311:2–13.
- Allen, RG, Pruitt, WO, Wright, JL, Howell, TA, Ventura, F, Snyder, R, Itenfis, D, Steduto, P, Berengena, J, Yrisarry, JB, Smith, M, Pereira, LS, Raes, D, Perrier, A, Alves, I, Walter, I and Elliott, R. 2006. A recommendation on standardized surface resistance for hourly calculation of reference ETo by the FAO56 Penman–Monteith method. *Agricultural Water Management*, 81:1–22.
- Arthington, A.H., et al. 2006. The challenge of providing environmental flow rules to sustain river ecosystems. *Ecological Applications*, 16:4, 1311–1318.
- Bhattarai, N, Quackenbush, LJ, Dougherty, M and Marzen, LJ. 2015. A simple Landsat–MODIS fusion approach for monitoring seasonal evapotranspiration at 30 m spatial resolution. *International Journal of Remote Sensing*, 361: 115-143.
- Bierkens, MFP, Finke, PA and Willigen, DE. 2000. *Upscaling and Downscaling Methods for Environmental Research*. Dordrecht: Wageningen University and Research Centre, Kluwer Academic.
- Boroto, J and Görgens, AHM. 2003. Limpopo River: An overview of alternative methods for estimating transmission losses. Hydrology of Mediterranean and Semiarid Regions, Proceedings of the Montpellier Conference. IAHS Publ. 278.
- Cataldo, J, Behr, C, Montalto, F and Pierce, RJ. 2010. Prediction of transmission losses in ephemeral streams, western USA. *The Open Hydrology Journal*, 4:19–34.
- Cooper, HH and Jacob, CE. 1946. A generalized graphical method for evaluating formation constants and summarizing well field history. *American Geophysical Union Transactions*, 27:526–534.
- Costa, AC, Foerster, S, De Araujo, JC and Bronstert, A. 2013. Analysis of channel transmission losses in a dryland river reach in north-eastern Brazil using streamflow series, groundwater level series and multi-temporal satellite data. *Hydrological Processes*, 27:1046–1060.
- Costelloe, JF, Grayson, RB, Argent, RM, and McMahon, TA. 2003. Modelling the flow regime of an arid zone floodplain river, Diamantina River, Australia. *Environmental Modelling and Software*, 18:693–703.
- Department of Water Affairs (DWA). 2011 Development of operating rules for the integration of the Blyde and Olifants River Systems. DWA Report No. P WMA O4/B60/00/8510.

- Department of Water Affairs (DWA). 2013. Classification of water resources and determination of the resource quality objectives in the Letaba Catchment. Ecological Water Requirements. Prepared by: Rivers for Africa eFlows Consulting (Pty) Ltd. DWA Report, RDM/WMA02/00/CON/CLA/0313.
- Department of Water Affairs (DWA). 2014. Development of a reconciliation strategy for the Luvuvhu and Letaba water supply system: Reconciliation strategy. Report No. P WMA 02/B810/00/1412/10.
- Department of Water Affairs and Forestry (DWAf). 2006. Letaba River system annual operating analysis. DWAf Report No: WMA 02/000/00/0406.
- Everson CS. 2001. The water balance of a first order catchment in the montane grasslands of South Africa. *Journal of Hydrology*, 241:110–123.
- Ghorbani, A, Mossivand, MA and Ouri, AE. 2012. Utility of the normalised difference vegetation index (NDVI) for land/canopy cover mapping in Khalkhal County (Iran). *Annals of Biological Research*, 3(12):5494–5503.
- Gokmen, M, Vekerdy, Z, Verhoef, A, Verhoef, A, Batelaan, O and Tol, C. 2012. Integration of soil moisture in SEBS for improving evapotranspiration estimation under water stress conditions. *Remote Sensing of Environment*, 121:261–274. DOI: 10.1016/j.rse.2012.02.003.
- Ha, W, Gowda, PH and Howell, TA. 2013. A review of downscaling methods for remote sensing-based irrigation management: Part I. *Irrigation Science*, 31:831–850.
- Hacker, F. 2005. Model for water availability in semi-arid environments (WASA): Estimation of transmission losses by infiltration at rivers in the semi-arid federal state of Ceara Brazil. MSc Thesis, University of Potsdam, Germany.
- Heritage, GL, Moon, BP and Large, ARG. 2001. The February 2000 floods on the Letaba River, South Africa: An examination of magnitude and frequency. *Koedoe*, 44 2:1–6.
- Hong, S, Hendrickx, JMH and Borchers, B. 2011. Down-scaling of SEBAL derived evapotranspiration maps from MODIS 250 m to Landsat 30 m scales. *International Journal of Remote Sensing*, 3221:6457–6477.
- Hughes, DA. 1999. Towards the incorporation of magnitude-frequency concepts into the Building Block Methodology used for quantifying ecological flow requirements of South African rivers. *Water SA*, 25(3):279–284.
- Hughes, DA. 2001. Providing hydrological information and data analysis tools for the determination of ecological instream flow requirements for South African rivers. *Journal of Hydrology*, 241: 140–151.
- Hughes, DA, Mallory, SJL and Louw, D. 2008. Methods and software for the real-time implementation of the ecological reserve-explanations and user manual. Water Research Commission Report No. 1582/1/08. Water Research Commission, Pretoria.
- Hughes, DA and Sami, K. 1992. Transmission losses to alluvium and associated moisture dynamics in a semi-arid ephemeral channel system in southern Africa. *Hydrological Processes*, 6:45–53.
- Jarmain, C, Everson, CS, Savage, MJ, Mengistu, MG, Clulow, AD, Walker, S and Gush, MB. 2009. Refining tools for evaporation monitoring in support of water resources management. Water Research Commission Report No. 1567/1/08. Water Research Commission, Pretoria. ISBN 978-1-77005-798-2.
- Katambara, Z and Ndiritu, JG. 2010. A hybrid conceptual-fuzzy inference streamflow modelling for the Letaba River system in South Africa. *Physics and Chemistry of the Earth*, 3513–14: 582–595.

- King, JM and Louw, MD. 1998. Instream flow assessments for regulated rivers in South Africa using the Building Block Methodology. *Aquatic Ecosystem Health and Management*, 1:109–124.
- Kongo et al. 2007.
- Kruseman, G and De Ridder, N. 1994. *Analysis and Evaluation of Pumping Test Data*. 2nd ed.
- Lane, LJ. 1990. Transmission losses, flood peaks and groundwater recharge. Hydraulics/hydrology of Arid Lands H2AL, Proceedings of the International Society of Civil Engineers, Hydraulics Division.
- Lange, J. 2005. Dynamics of transmission losses in a large arid stream channel. *Journal of Hydrology*, 306:112–126.
- Li, Y, Zhou, J, Wang, H, Li, D, Jin, R, Zhou, Y and Zhou, Q. 2015. Integrating soil moisture retrieved from L-band microwave radiation into an energy balance model to improve evapotranspiration estimation on the irrigated oases of arid regions in northwest China. *Agricultural and Forest Meteorology*, 214–215:306–318.
- Liang, S. 2004. *Quantitative Remote Sensing of Land Surfaces*. New York, NY: John Wiley.
- Liou, Y and Kar, SK. 2014. Evapotranspiration estimation with remote sensing and various surface energy balance algorithm: A review. *Energies*, 7:2821–2849.
- Loke, MH. 1999. Electrical imaging surveys for environmental and engineering studies: A practical guide to 2-D and 3-D surveys. www.terrajp.co.jp/lokenote.pdf.
- Malan and Day. 2003.
- McLoughlin, CA, Deacon, A, Sithole H and Gyedu-Ababio, T. 2011. History, rationale, and lessons learned: Thresholds of potential concern in Kruger National Park river adaptive management. *Koedoe*, 53(2):1–27.
- Molle, F, Wester, P and Hirsch, P. 2010. River basin closure: Processes, implications and responses. *Agricultural Water Management*, 97:569–577.
- Moon, BP and Heritage, GL. 2001. The contemporary geomorphology of the Letaba River in the Kruger National Park. *Koedoe*, 44(1):45–55.
- O’Keeffe. 2008.
- Pardo, N, Sanchez, LM, Timmermans, J, Su, Z, Perez, IA and Garcia, MA. 2014. SEBS validation in a Spanish rotating crop. *Agricultural and Forest Meteorology*, 195–196:132–142.
- Poff, NL et al. 2009. The ecological limits of hydrologic alteration (ELOHA): A new framework for developing regional environmental flow standards. *Freshwater Biology*, 55(1):147–170.
- Pollard, S and Du Toit D. 2011a. Towards adaptive integrated water resources management in southern Africa: The role of self-organisation and multi-scale feedbacks for learning and responsiveness in the Letaba and Crocodile Catchments. *Water Resources Management*, 25(15):4019–4035.
- Pollard, S and Du Toit, D. 2011b. Towards the sustainability of freshwater systems in South Africa: An exploration of factors that enable and constrain meeting the ecological reserve within the context of Integrated Water Resources Management in the catchments of the Lowveld. Water Research Commission Report No. K8/1711. Water Research Commission, Pretoria.
- Pollard et al. 2012. Through a historical contextual assessment of compliance.
- Ramsey, RD, Wright (Jr), DL and McGinty, C. 2004. Enhanced thematic mapper to monitor vegetation cover in shrub-steppe environments. *Geocarto International*, 19(2):39–47.
- Riddell, ES, Pollard, SR, Mallory, S and Sawunyama, T. 2014. A methodology for historical assessment of compliance with environmental water allocations: Lessons from the Crocodile (East River), South Africa. *Hydrological Sciences Journal*, 831–843.

- Robinson, DA, Campbell, CS, Hopmans, JW, Hornbuckle, BK, Jones, SB, Knight, R, Ogden, F, Selker, J and Wendroth, O. 2008. Soil moisture measurement for ecological and hydrological watershed-scale observatories: A review. *Vadose Zone Journal*, 7:358–389.
- Santos, C, Lorite, IJ, Tasumi, M, Allen, RG and Fereres, E. 2008. Integrating satellite-based evapotranspiration with simulation models for irrigation management at the scheme level. *Irrigation Science*, 263:277–288.
- Sawunyama, T and Hughes, DA. 2010. Using satellite-based rainfall data to support the implementation of environmental water requirements in South Africa. *Water SA*, 364.
- Seneviratne, SI, Luthi, D, Litschi, M and Schar, C. 2006. Land-atmosphere coupling and climate change in Europe. *Nature*, 443:205–209.
- Shanafield, M and Cook, PG. 2014. Transmission losses, infiltration and groundwater recharge through ephemeral and intermittent streambeds: A review of applied methods. *Journal of Hydrology*, 511: 518–529.
- Singh, RK, Senay, GB, Velpuri, NM, Bohms, S and Verdin, JP. 2014. On the downscaling of actual evapotranspiration maps based on combination of MODIS and Landsat-based actual evapotranspiration estimates. *Remote Sensing*, 6:10483–10509.
- Spiliotopolous, M, Adaktylou, N, Loukas, A, Michalopoulou, H, Mylopoulos, N and Toullos, L. 2013. A spatial downscaling procedure of MODIS derived actual evapotranspiration using Landsat images at central Greece. Proceedings of SPIE, The International Society for Optical Engineering, August 2013. DOI: 10.1117/12.2027536.
- Su, Z. 2002. The surface balance energy system (SEBS) for estimating turbulent heat fluxes. *Hydrology and Earth System Sciences*, 61:85–99.
- Su, Z, Pelgrum, H and Menenti, M. 1999. Aggregation effects of surface heterogeneity in land surface processes. *Hydrology Earth System Science*, 34:549–563.
- Uhlenbrook, S, Wenninger, J and Lorentz, S. 2005. What happens after the catchment caught the storm? Hydrological processes at the small, semi-arid Weatherley catchment, South Africa. *Advances in Geosciences*, 2: 237–241.
- Vlok, W and Engelbrecht, JS. 2000. Some aspects of the ecology of the Groot Letaba River in the Northern Province, South Africa. *African Journal of Aquatic Science*, 25(1):76–83.
- Walters, MO 1990. Transmission losses in arid regions. *Journal of Hydraulic Engineering ASCE* 116:129-38.
- Water Research Commission (WRC). 2001. State of the Rivers Report: Letaba and Luvuvhu Rivers Systems. Water Research Commission Report No. TT 165/01, Water Research Commission, Pretoria.
- Wenninger, J, Uhlenbrook, S, Lorentz, S and Leibundgut, C. 2008. Identification of runoff generation processes using combined hydrometric, tracer and geophysical methods in a headwater catchment in South Africa. *Hydrological Sciences Journal*, 53(1) 65–80.
- Wu, X, Zhou, J, Wang, H, Li, Y and Zhong, B. 2014. Evaluation of irrigation water use efficiency using remote sensing in the middle reach of the Heihe river, in the semi-arid Northwestern China. *Hydrol Process* 2014. DOI: 10.1002/hyp.10365.
- Yang, D, Chen, H and Lei, H. 2010. Estimation of evapotranspiration using a remote sensing model over agricultural land in the North China Plain. *International Journal of Remote Sensing*, 3114:3783–3798.
- Zhuo, G, Ba, L, Ciren, P and Bu, L. 2014. Study on daily surface evapotranspiration with SEBS in Tibet Autonomous Region. *Journal of Geographical Sciences*, 241:113–128.

Appendix I: Letaba River Transmissions Losses Maps

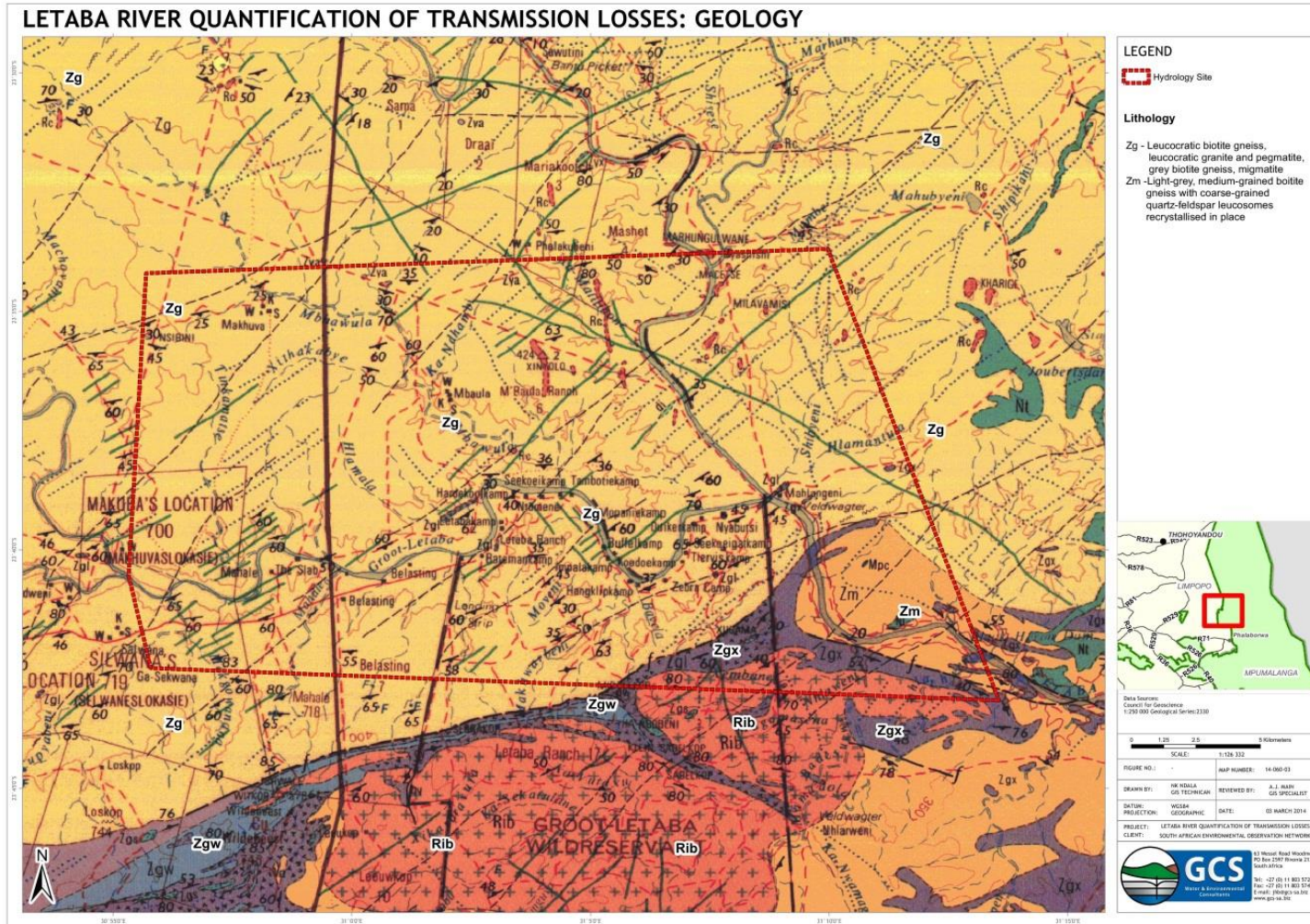


Figure 112: Geology of the site illustrating the dominant geology and dykes

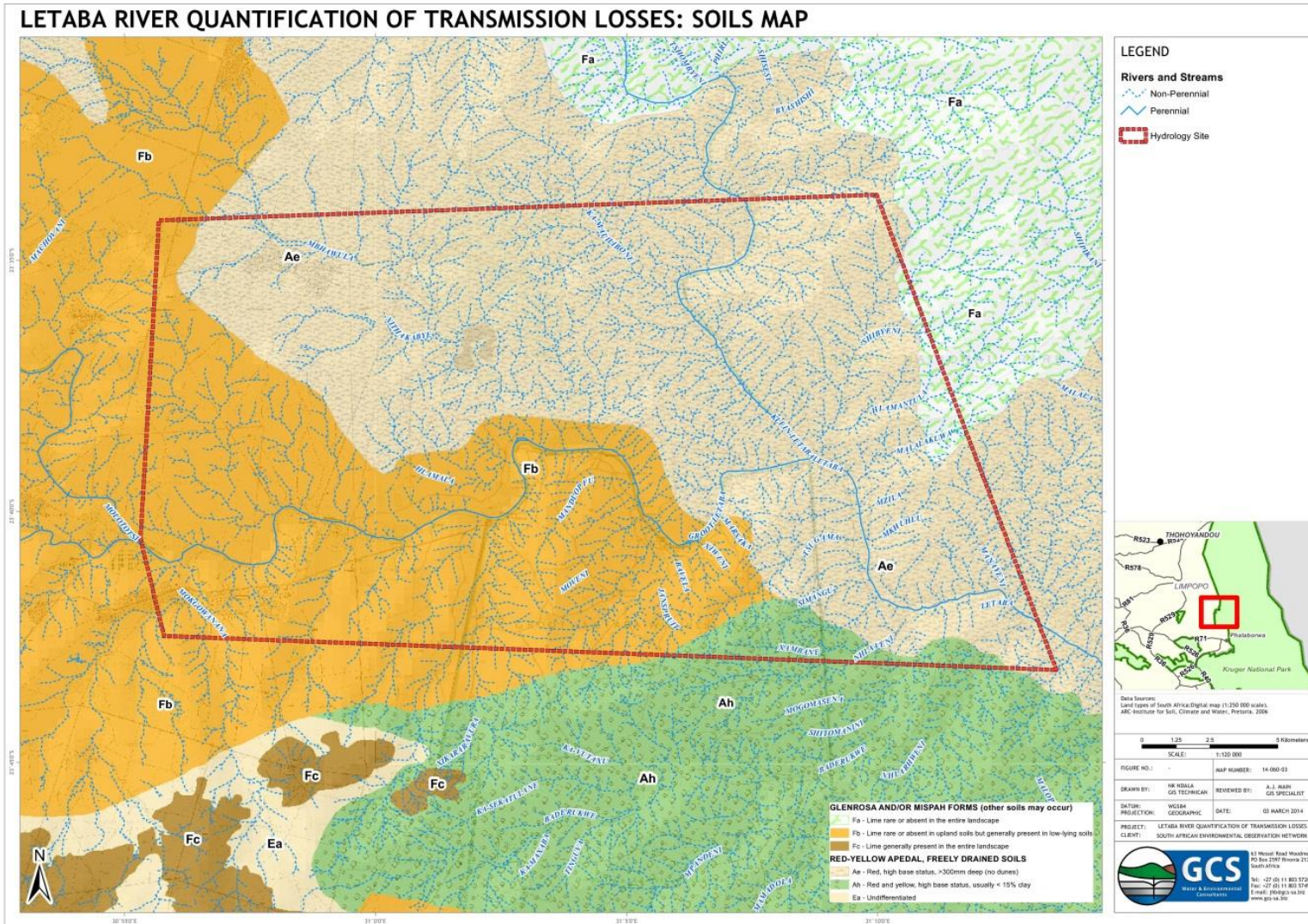


Figure 113: The dominant soil types and perennial/non-perennial streams

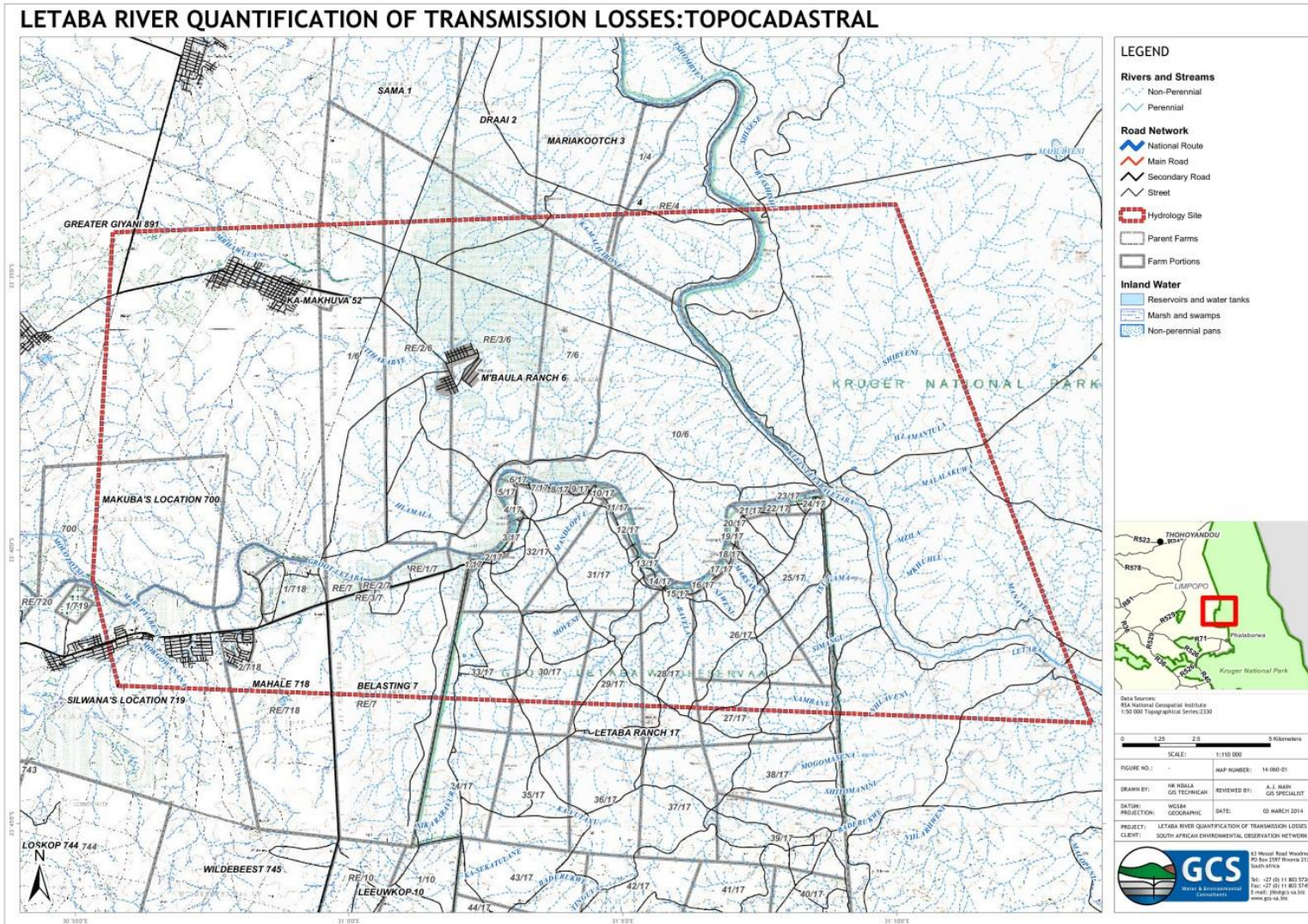


Figure 114: Topocadastral map of the study site delineating farms, ranches and rural communities

LETABA RIVER QUANTIFICATION OF TRANSMISSION LOSSES: TOPOGRAPHY

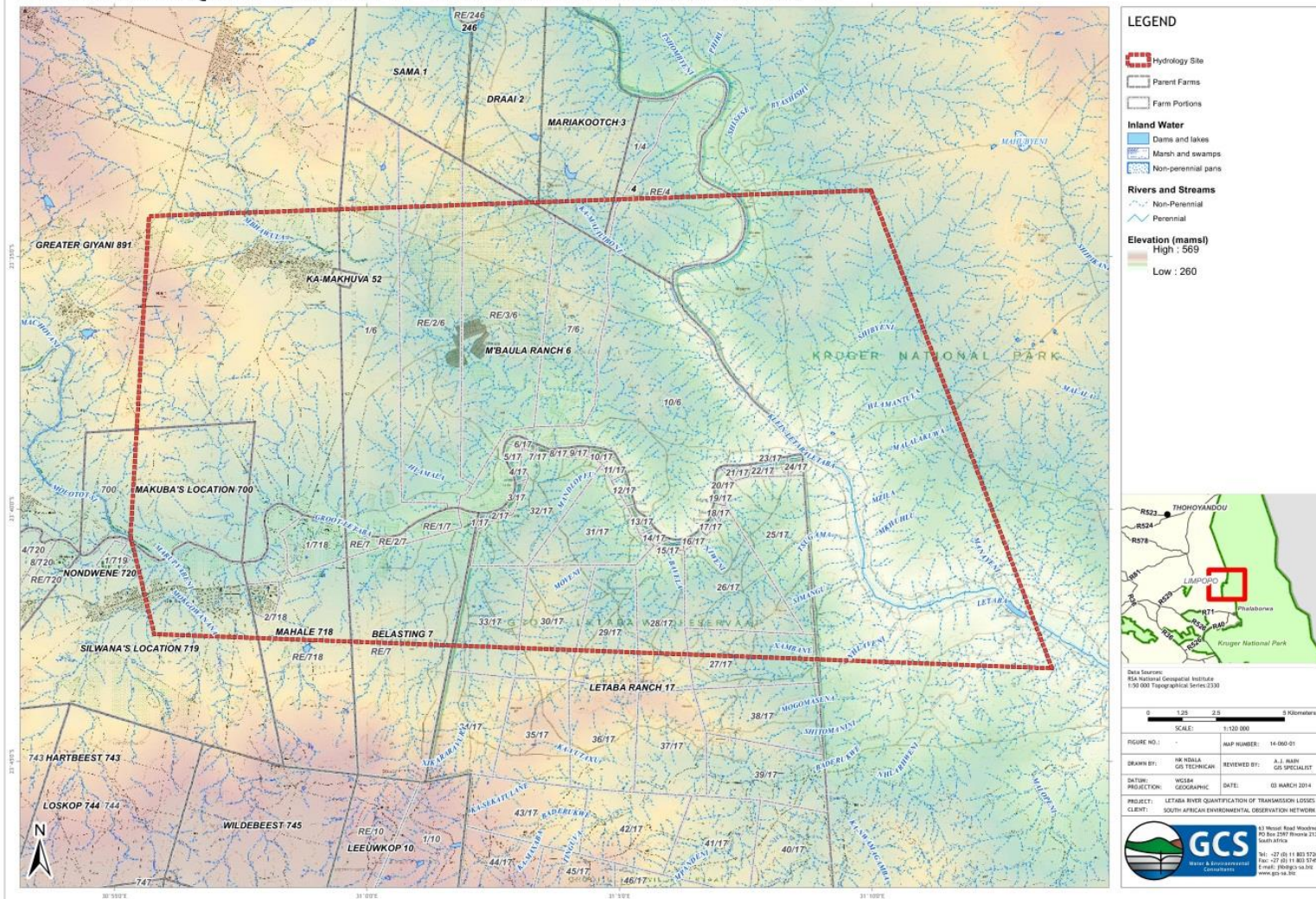
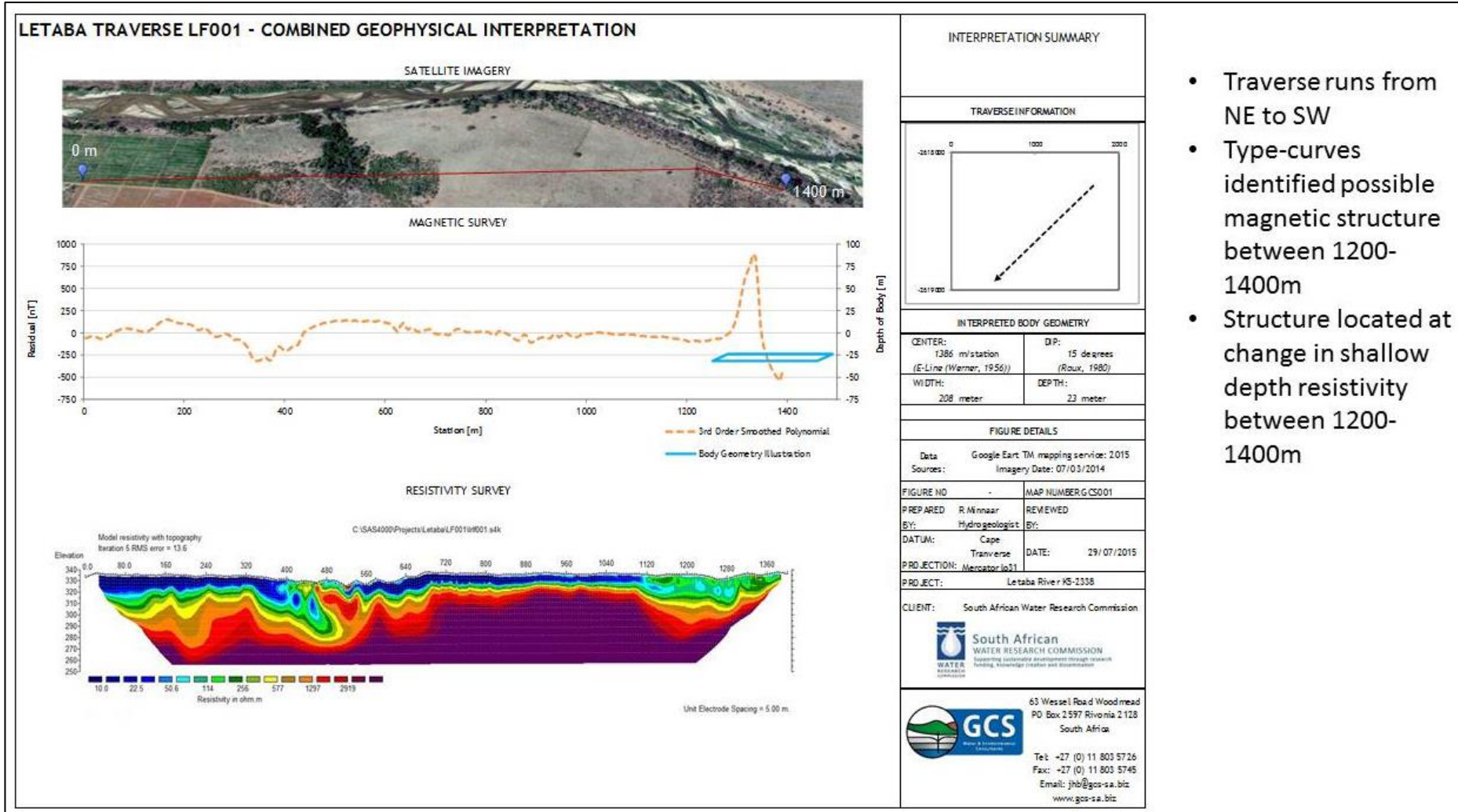


Figure 115: Topographical map of the study site

Appendix II: Magnetic Surveys

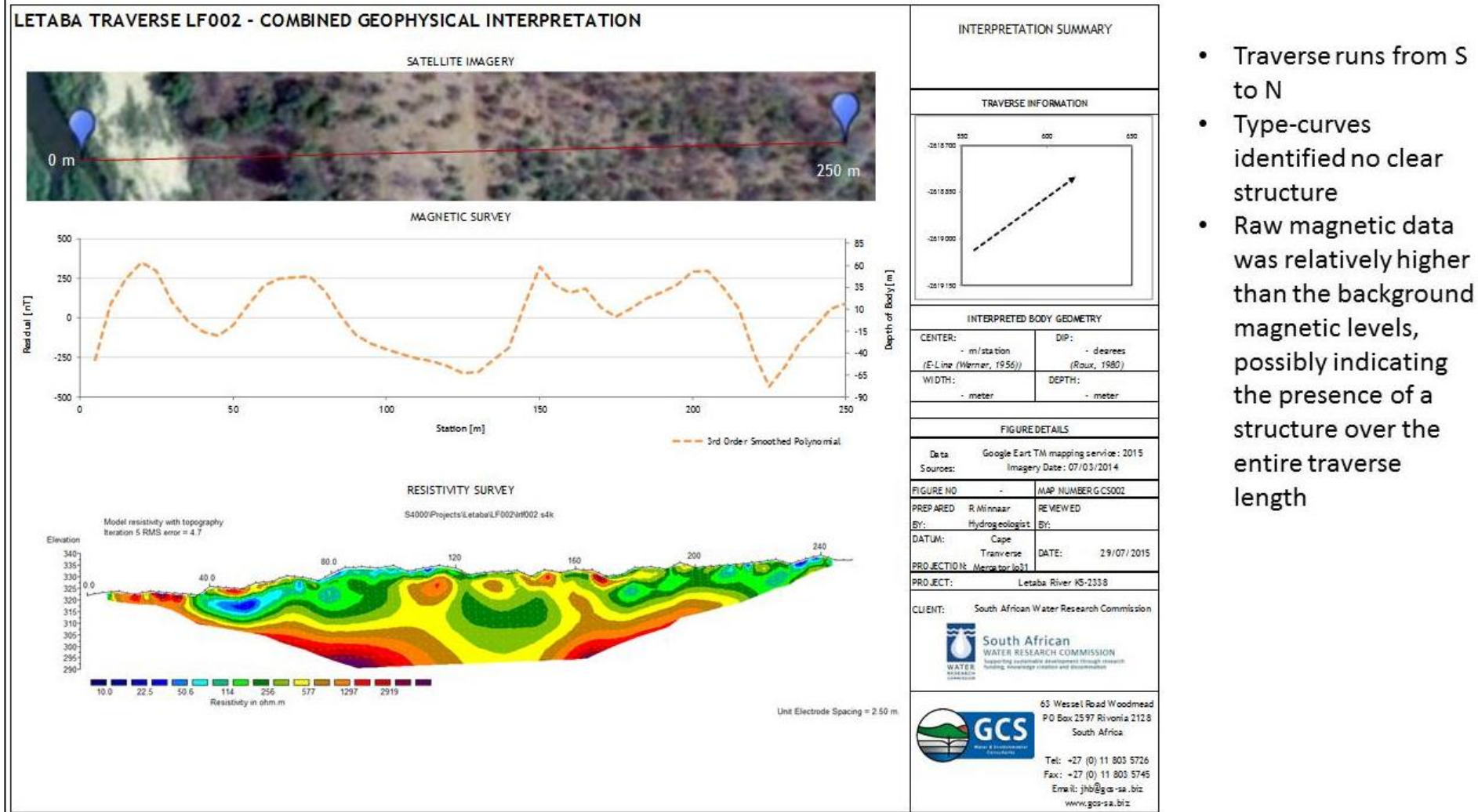
Magnetic surveys

Magnetic surveys are applied in many fields, such as geological mapping and geohydrological surveys. During a field campaign conducted in June 2015, magnetic surveys were used to characterise and confirm the presence of structural intrusions (or magnetic dykes) along the Letaba River. Geophysics transects conducted in 2014 using ERT were resurveyed using a Geotron Proton Magnetometer (G5 Model). The magnetic survey data was coupled and overlaid with the geophysics survey data to verify the presence of possible dyke intrusions that were recorded during the ERT surveys.



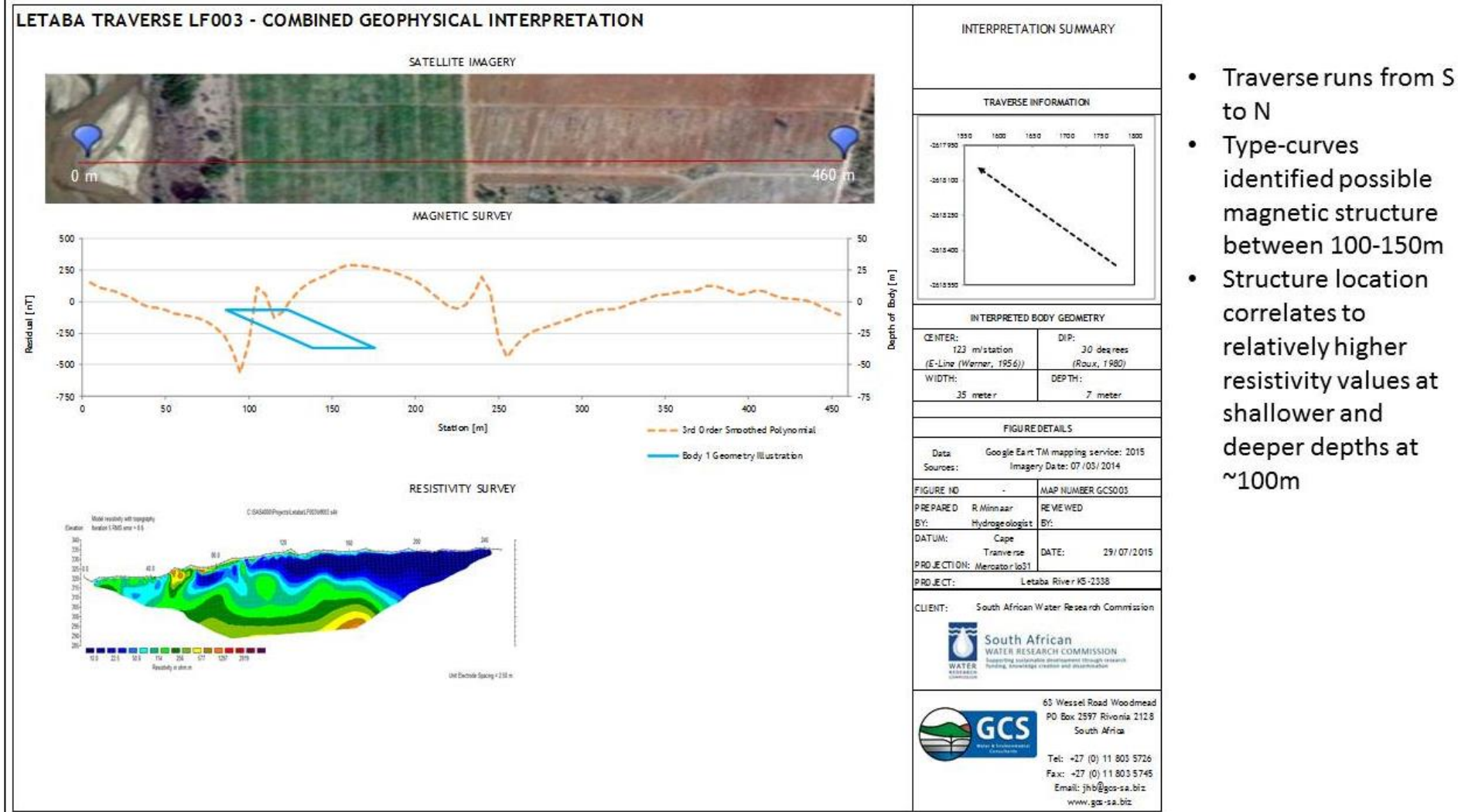
- Traverse runs from NE to SW
- Type-curves identified possible magnetic structure between 1200-1400m
- Structure located at change in shallow depth resistivity between 1200-1400m

Figure 116: Combined geophysical interpretation LF001



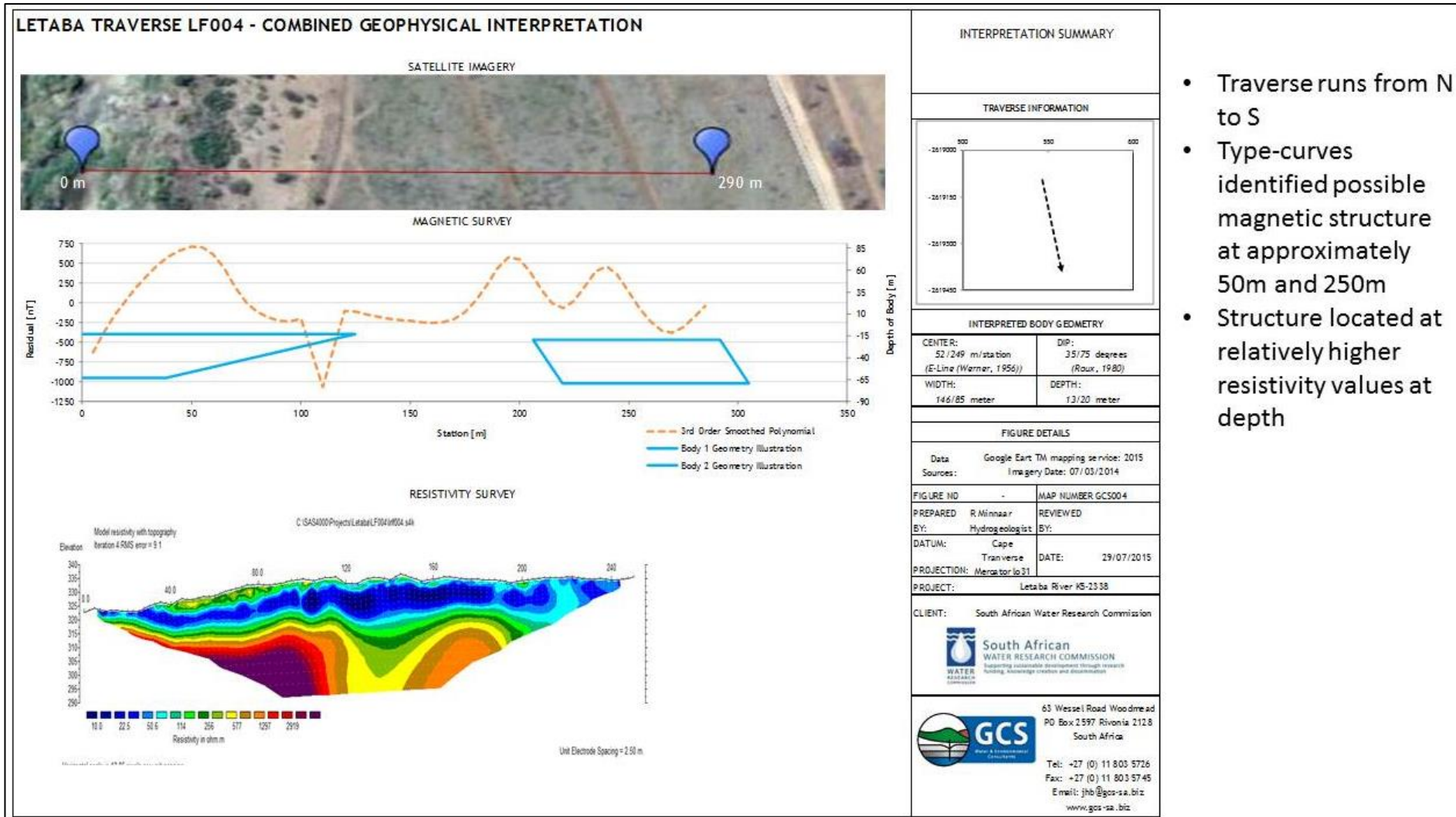
- Traverse runs from S to N
- Type-curves identified no clear structure
- Raw magnetic data was relatively higher than the background magnetic levels, possibly indicating the presence of a structure over the entire traverse length

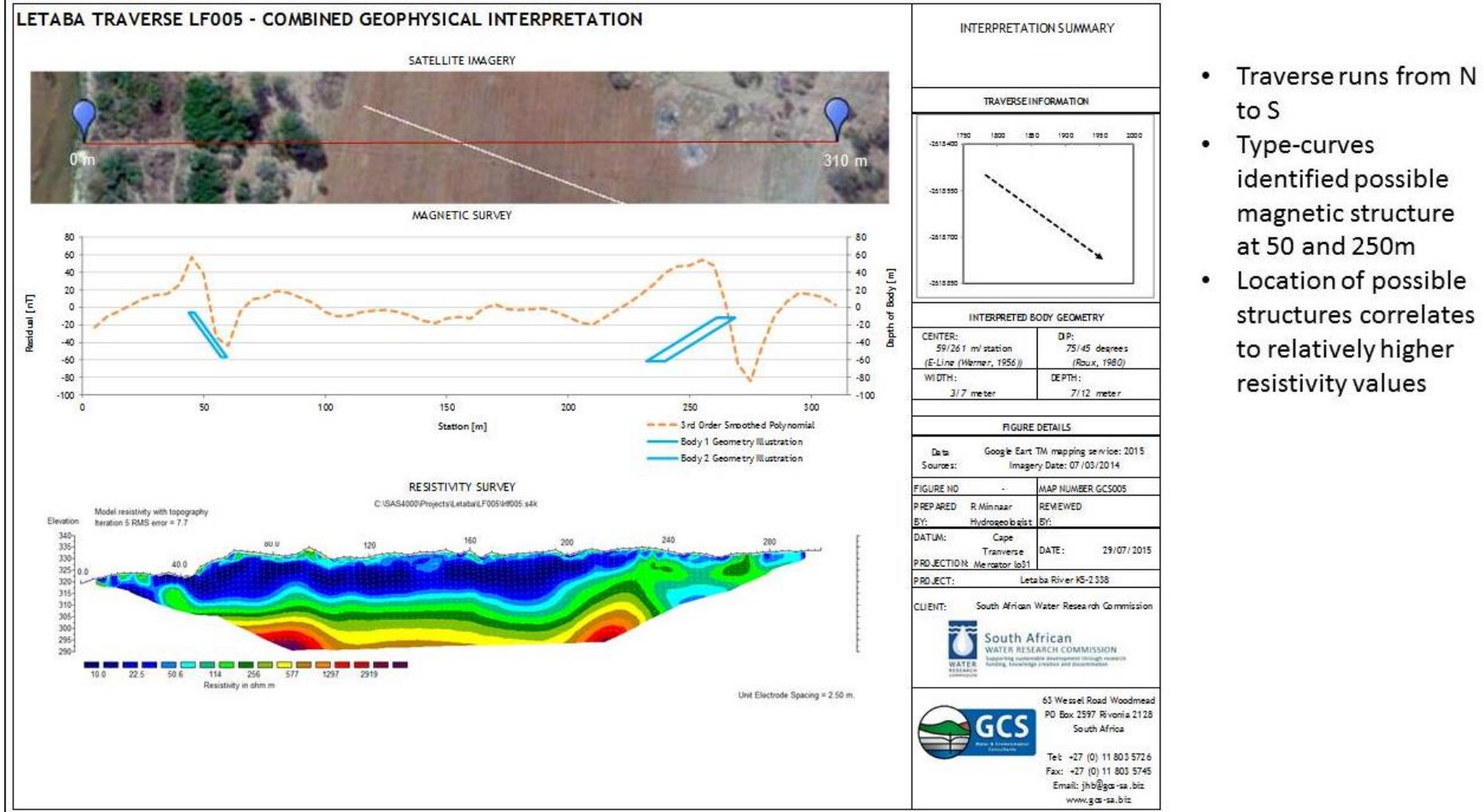
Figure 117: Combined geophysical interpretation LF002



- Traverse runs from S to N
- Type-curves identified possible magnetic structure between 100-150m
- Structure location correlates to relatively higher resistivity values at shallower and deeper depths at ~100m

Figure 118: Combined geophysical interpretation LF003





- Traverse runs from N to S
- Type-curves identified possible magnetic structure at 50 and 250m
- Location of possible structures correlates to relatively higher resistivity values

Figure 120: Combined geophysical interpretation LF005

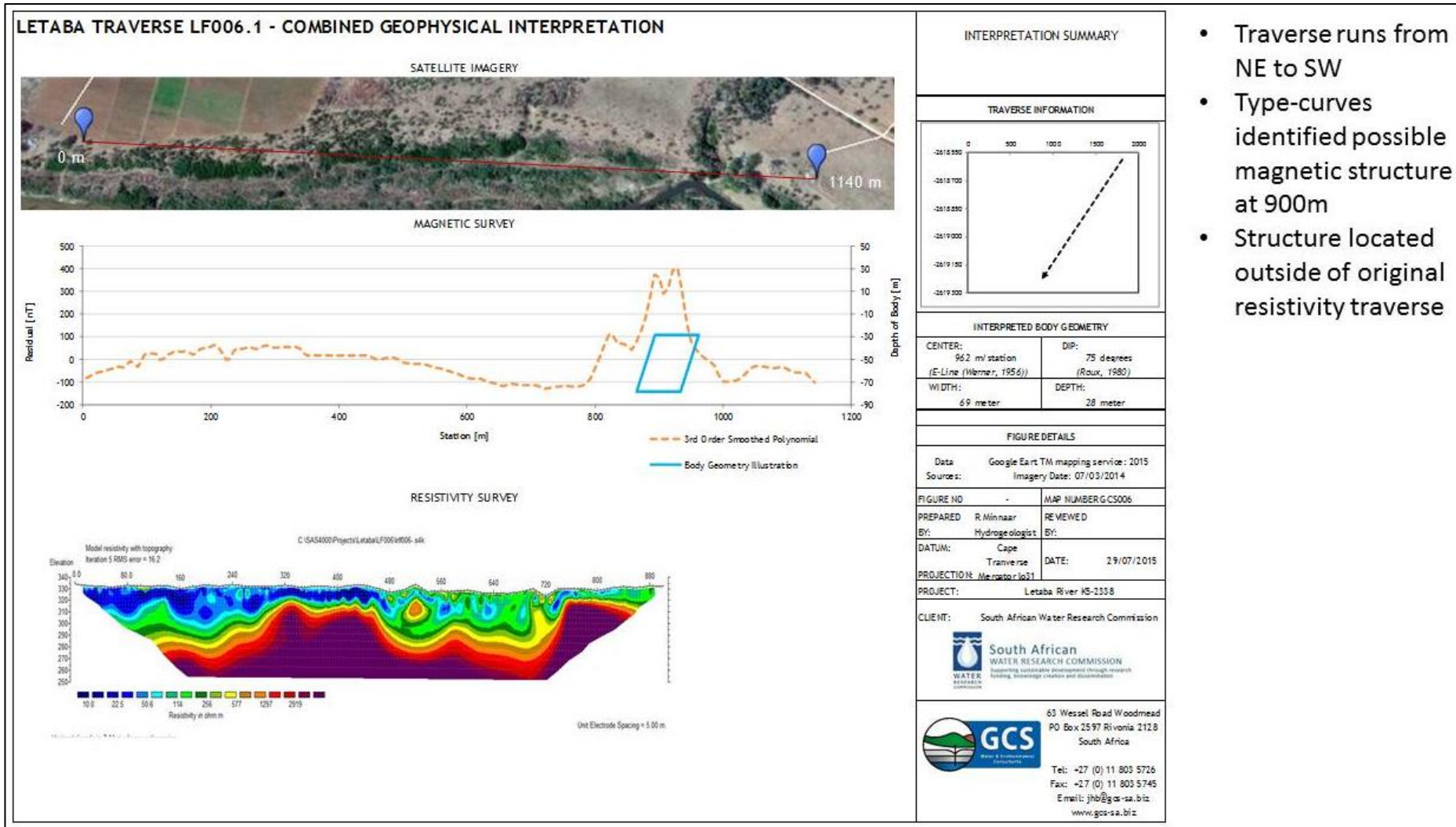
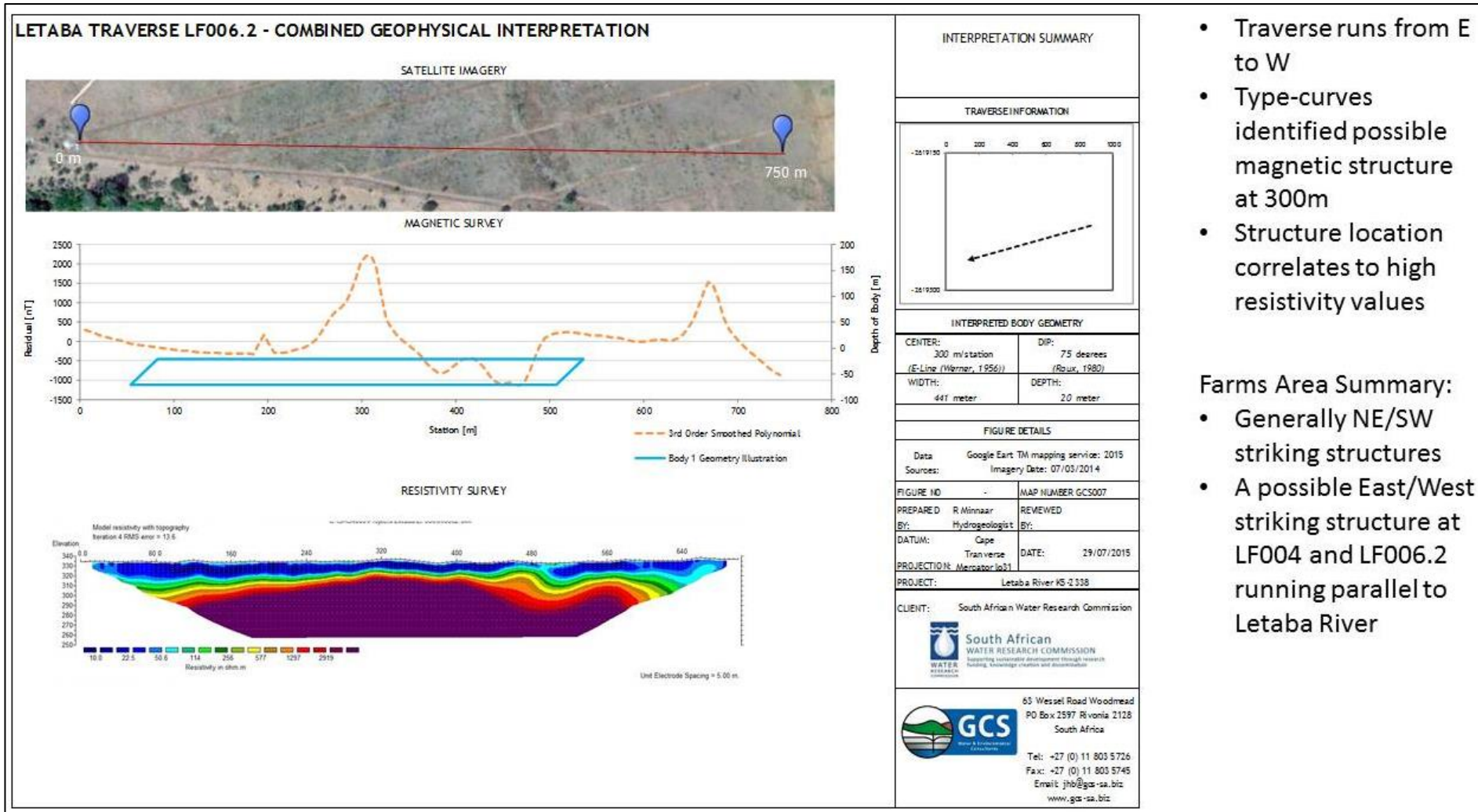


Figure 121: Combined geophysical interpretation LF006.1

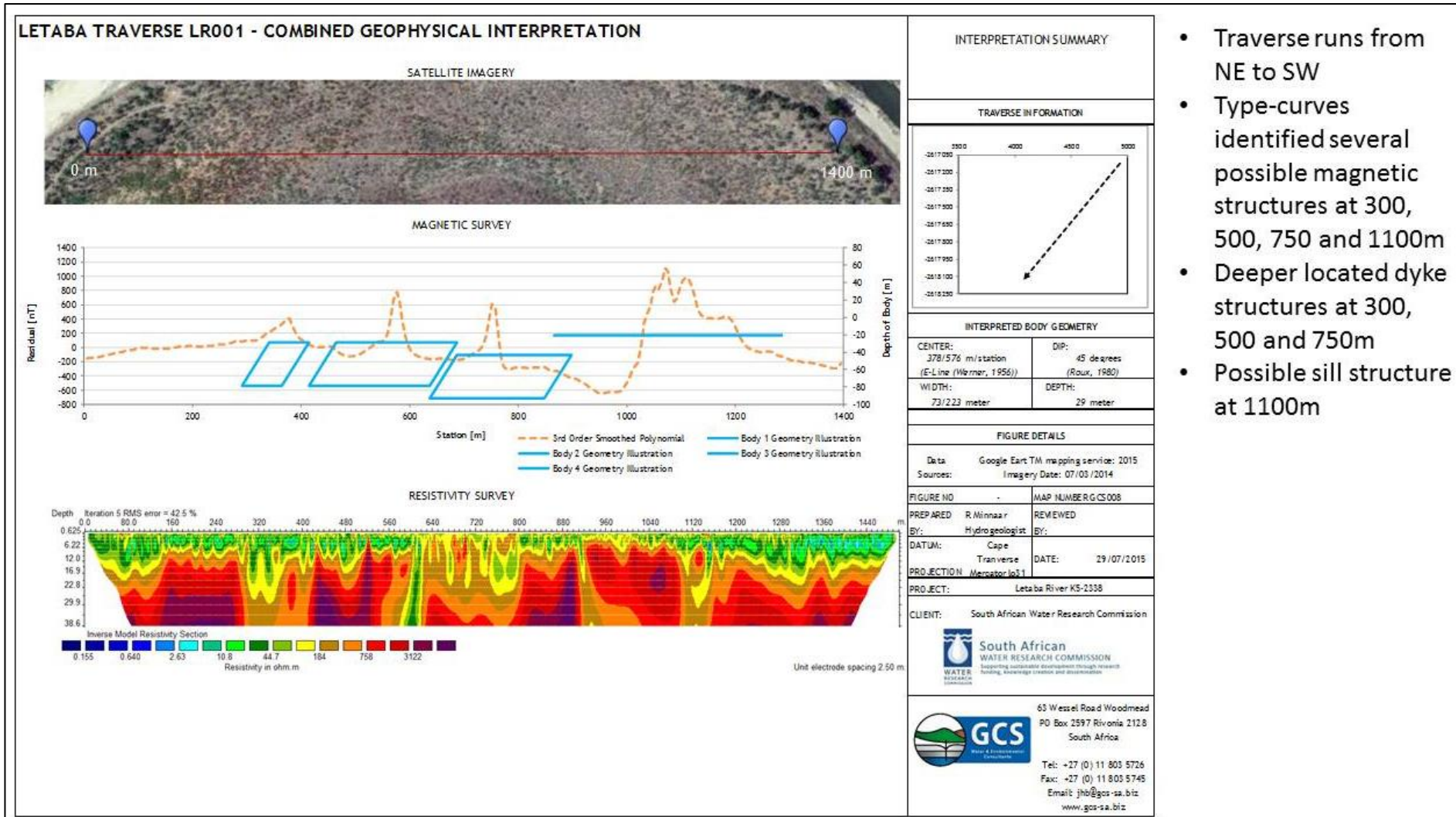


- Traverse runs from E to W
- Type-curves identified possible magnetic structure at 300m
- Structure location correlates to high resistivity values

Farms Area Summary:

- Generally NE/SW striking structures
- A possible East/West striking structure at LF004 and LF006.2 running parallel to Letaba River

Figure 122: Combined geophysical interpretation LF006.2



- Traverse runs from NE to SW
- Type-curves identified several possible magnetic structures at 300, 500, 750 and 1100m
- Deeper located dyke structures at 300, 500 and 750m
- Possible sill structure at 1100m

Figure 123: Combined geophysical interpretation LR001

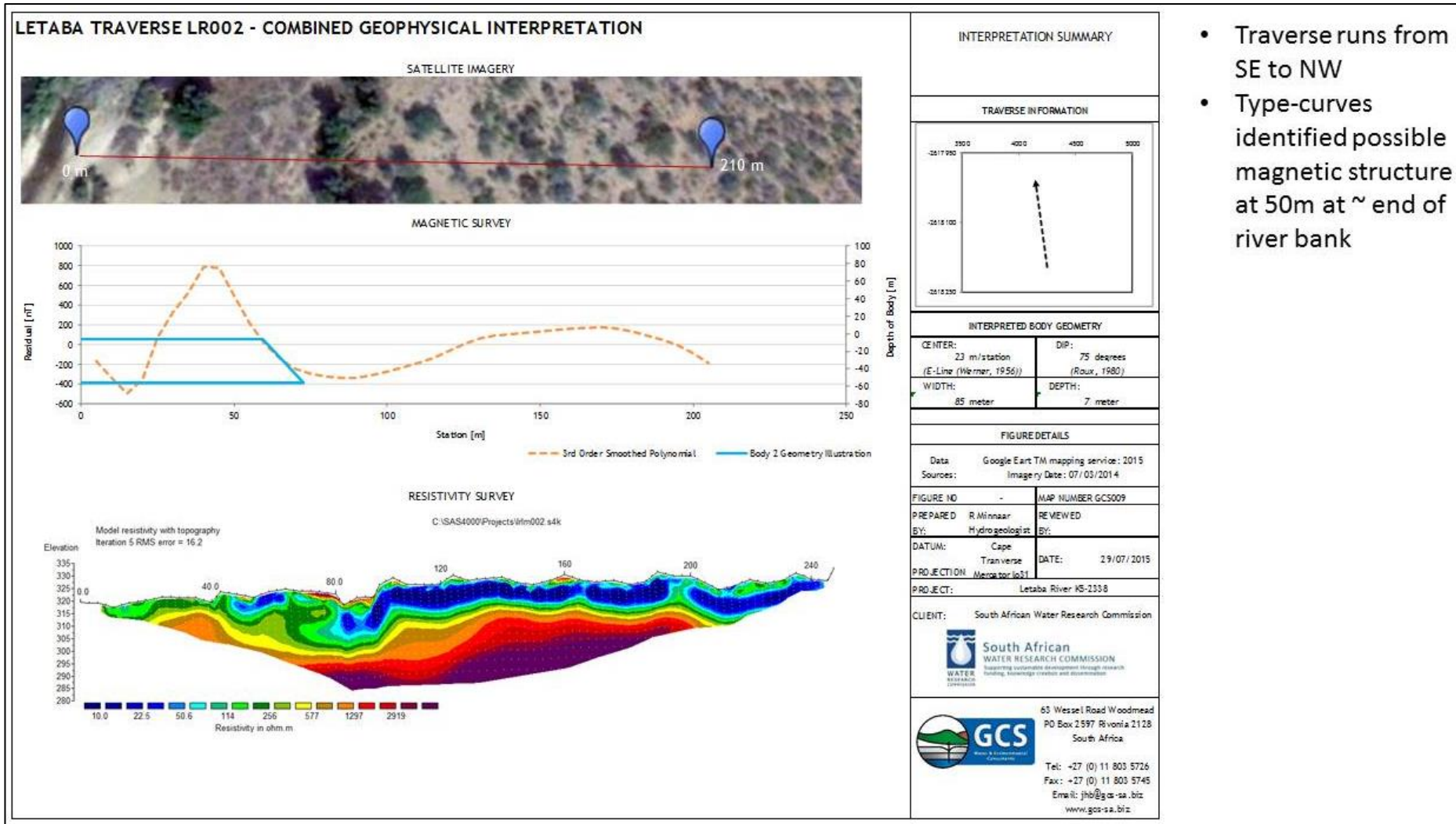
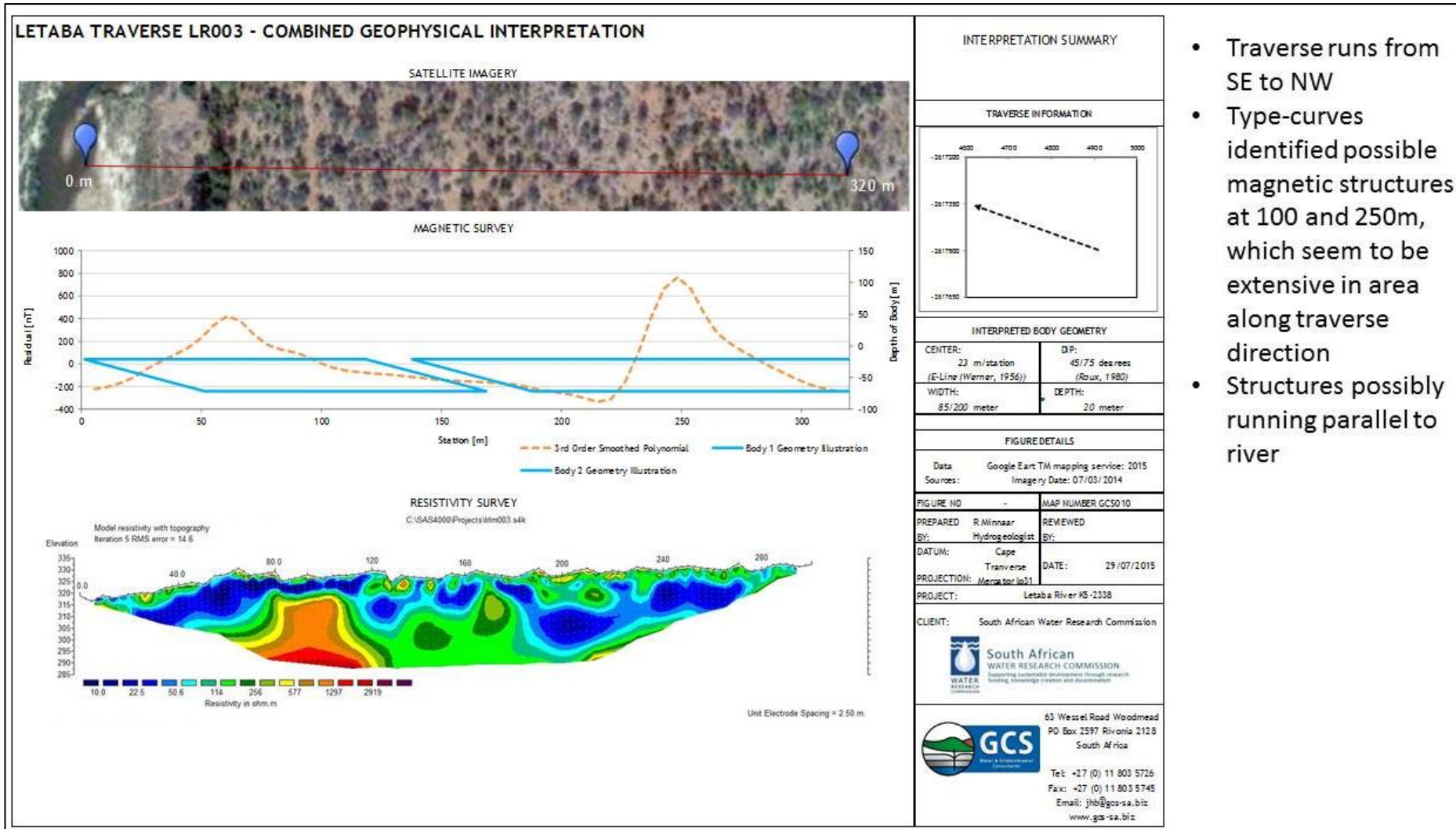
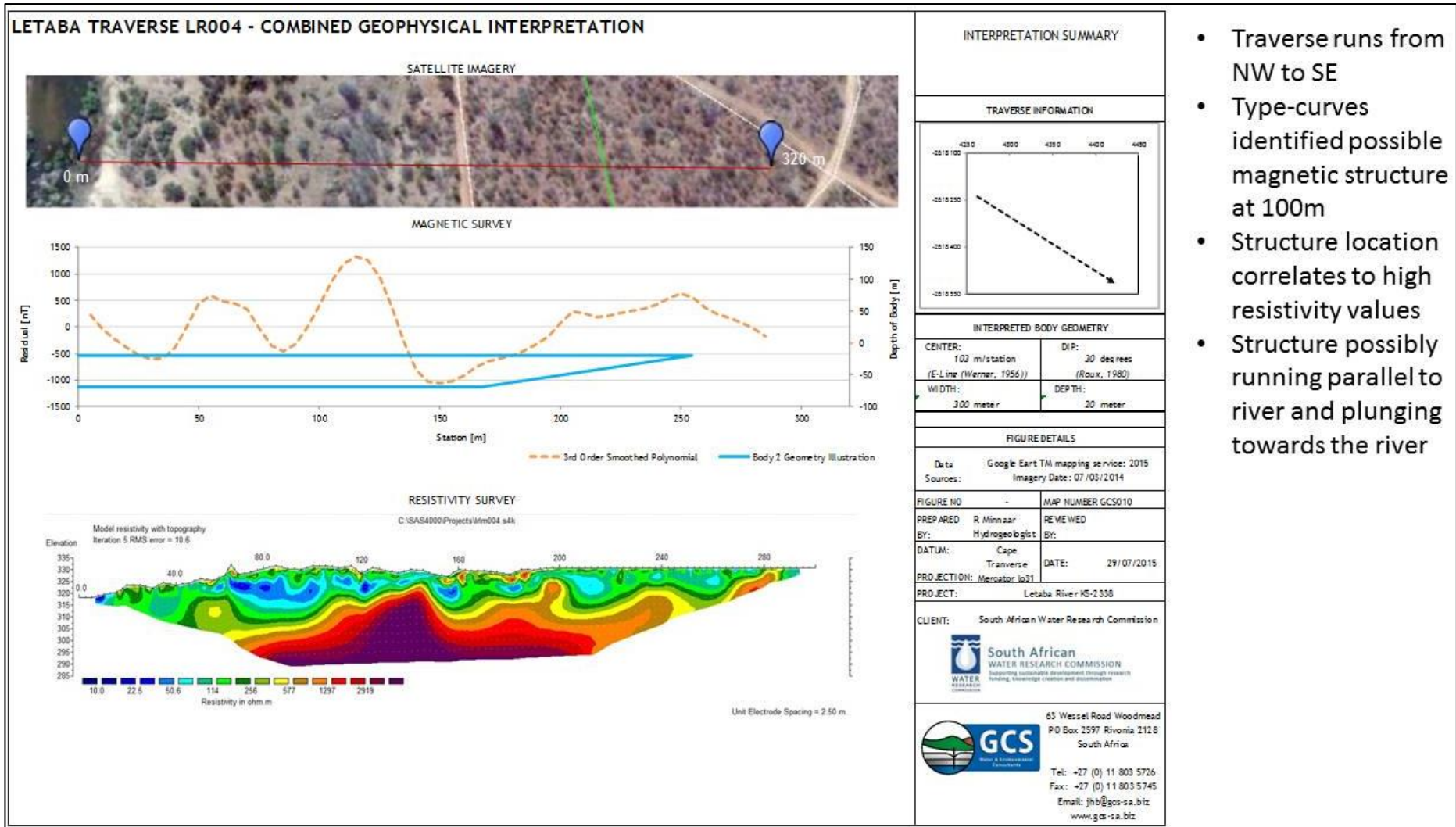


Figure 124: Combined geophysical interpretation LR002



- Traverse runs from SE to NW
- Type-curves identified possible magnetic structures at 100 and 250m, which seem to be extensive in area along traverse direction
- Structures possibly running parallel to river

Figure 125: Combined geophysical interpretation LR003



- Traverse runs from NW to SE
- Type-curves identified possible magnetic structure at 100m
- Structure location correlates to high resistivity values
- Structure possibly running parallel to river and plunging towards the river

Figure 126: Combined geophysical interpretation LR004

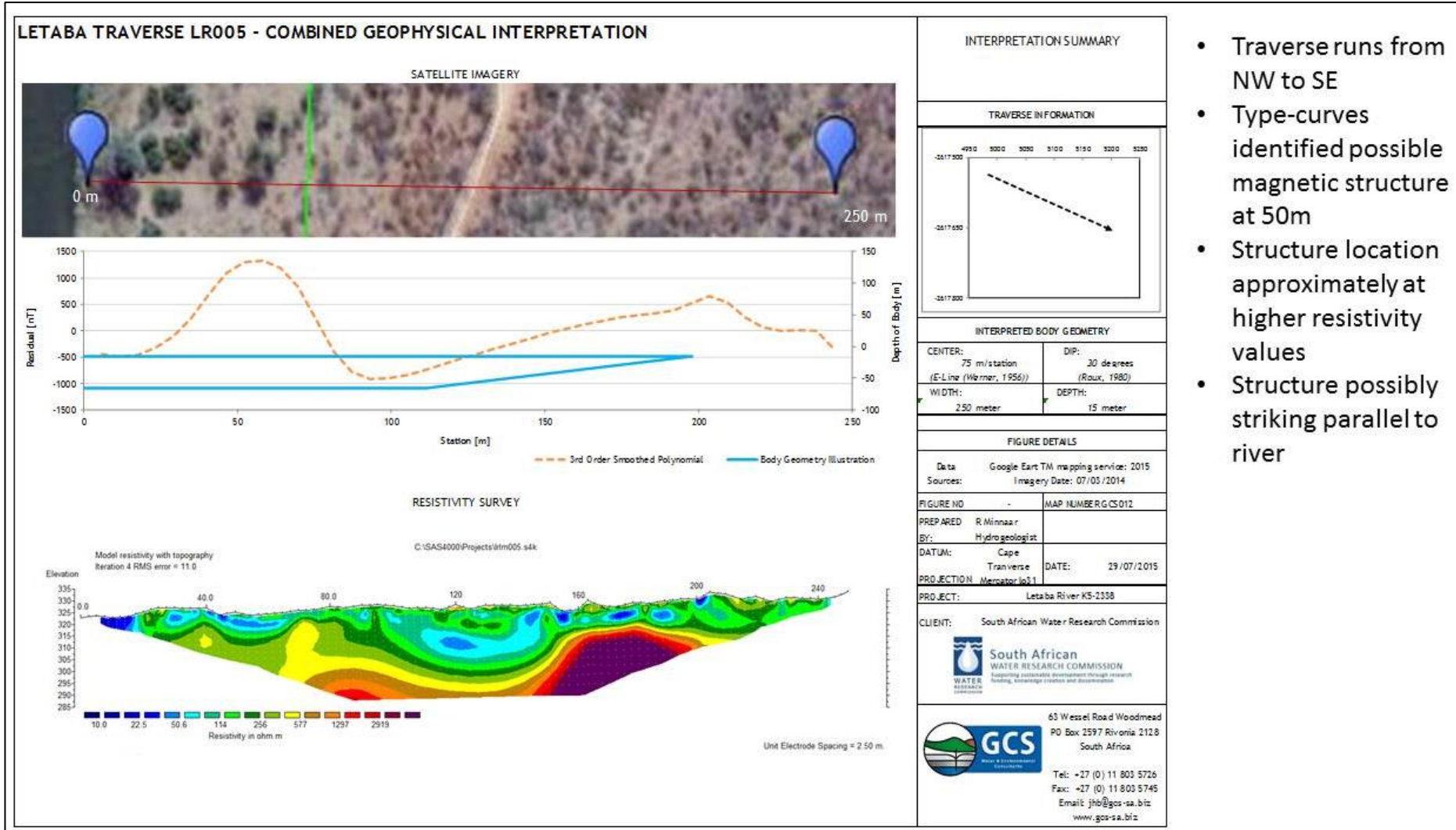
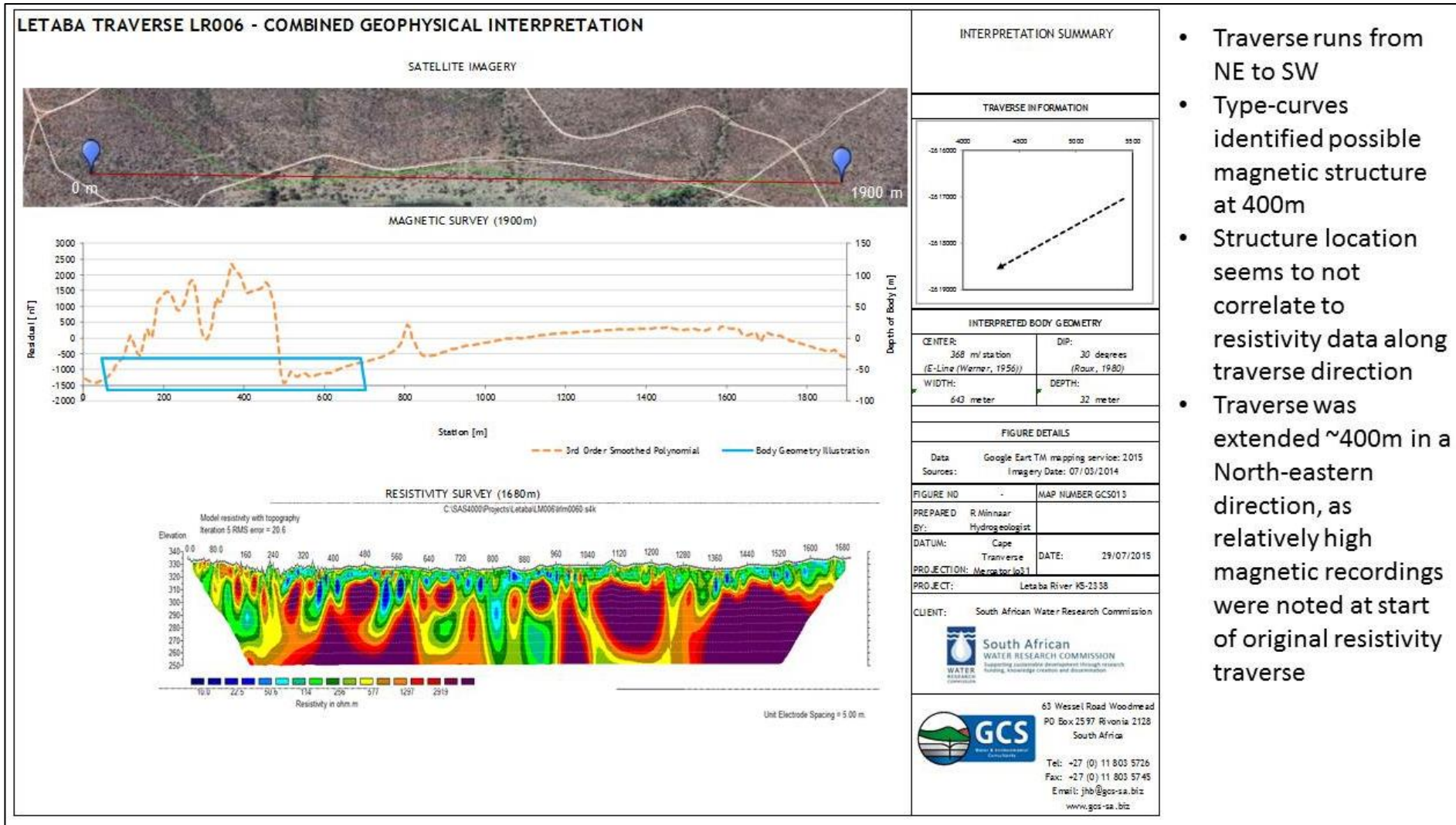


Figure 127: Combined geophysical interpretation LR005



- Traverse runs from NE to SW
- Type-curves identified possible magnetic structure at 400m
- Structure location seems to not correlate to resistivity data along traverse direction
- Traverse was extended ~400m in a North-eastern direction, as relatively high magnetic recordings were noted at start of original resistivity traverse

Figure 128: Combined geophysical interpretation LR006